SAND2017-10749R

Evaluation of Spent Fuel Disposition Crystalline Rocks: FY17 Progress Report

Spent Fuel and Waste Disposition

Prepared for
US Department of Energy
Spent Fuel and Waste Science Technology

Y. Wang, T. Hadgu, E. Kalinina
Sandia National Laboratories
J. Jerden, V. K. Gattu, W. Ebert
Argonne National Laboratory
H. Viswanathan, J. Hyman, S. Karra, N. Knapp,
N. Makendonska, P. Reimus, K. Telfeyan
Los Alamos National Laboratory
P. M. Fox, P. S. Nico
Lawrence Berkeley National Laboraotory
M. Zavarin, E. Balboni, C. Atkins-Duffin
Lawrence Livermore National Laboratory

September, 2017
SFWD-SFWST-2017-000007

Sandia National Laboratories is a multi-mission laboratory managed and operated by National Technology andEngineering Solutions of Sandia, LLC., a wholly owned subsidiary of Honeywell International, Inc., for the U.S. Department of Energy's National Nuclear Security Administration under contract DE-NA0003525

Sandia
National
Laboratories

Revision 4
07/05/2017

APPENDIX E

NTRD DOCUMENT COVER SHEET [1]

Name/Title of Deliverable/Milestone/Revision No.	Evaluation of Spent Fuel Disposition in Crystalline Rocks: FY17 Progress Report M2FT-17SN010302011
Work Package Title and Number	Crystalline Disposal R&D – SNL SF-17SN01030201
Work Package WBS Number	1.08.01.03.02
Responsible Work Package Manager	Yifeng Wang (signature on file) (Name/Signature)

Date Submitted 8/18/2017

Quality Rigor Level for Deliverable/Milestone[2]	☐ QRL-1 ☐ Nuclear Data	☐ QRL-2	X QRL-3	☐ QRL 4 Lab-specific

This deliverable was prepared in accordance with Lawrence Berkeley National Laboratory (LBNL)
(Participant/National Laboratory Name)

QA program which meets the requirements of
X DOE Order 414.1 ☐ NQA-1 ☐ Other

This Deliverable was subjected to:

☐ Technical Review	☐ Peer Review
Technical Review (TR)	**Peer Review (PR)**
Review Documentation Provided	**Review Documentation Provided**
☐ Signed TR Report or,	☐ Signed PR Report or,
☐ Signed TR Concurrence Sheet or,	☐ Signed PR Concurrence Sheet or,
X Signature of TR Reviewer(s) below	☐ Signature of PR Reviewer(s) below
Name and Signature of Reviewers	**Name and Signature of Reviewers**
Carlos Jove-Colon (signature on file)	

NOTE 1: *Appendix E should be filled out and submitted with each deliverable. Or, if the PICS: NE system permits, completely enter all applicable information in the PICS: NE Deliverable Form. The requirement is to ensure that all applicable information is entered either in the PICS: NE system or by using the NTRD Document Cover Sheet.*

- *In some cases there may be a milestone where an item is being fabricated, maintenance is being performed on a facility, or a document is being issued through a formal document control process where it specifically calls out a formal review of the document. In these cases, documentation (e.g., inspection report, maintenance request, work planning package documentation or the documented review of the issued document through the document control process) of the completion of the activity, along with the Document Cover Sheet, is sufficient to demonstrate achieving the milestone.*

NOTE 2: *If QRL 1, 2, or 3 is not assigned, then the QRL 4 box must be checked, and the work is understood to be performed using laboratory specific QA requirements. This includes any deliverable developed in conformance with the respective National Laboratory Participant, DOE or NNSA-approved QA Program.*

This page left blank intentionally

EXCUTIVE SUMMARY

The U.S. Department of Energy Office of Spent Fuel Waste Disposition (SFWD) established in fiscal year 2010 (FY10) the Spent Fuel Waste Science & Technology (SFWST) Program (formerly the Used Fuel Disposition Campaign - UFDC) program to conduct the research and development (R&D) activities related to storage, transportation and disposal of used nuclear fuel and high level nuclear waste. The Mission of the SFWST is:

> *To identify alternatives and conduct scientific research and technology development to enable storage, transportation and disposal of used nuclear fuel and wastes generated by existing and future nuclear fuel cycles*.

The work package of Crystalline Disposal R&D directly supports the following SFWST objectives:

- Develop a fundamental understanding of disposal system performance in a range of environments for potential wastes that could arise from future nuclear fuel cycle alternatives through theory, simulation, testing, and experimentation.
- Develop a computational modeling capability for the performance of storage and disposal options for a range of fuel cycle alternatives, evolving from generic models to more robust models of performance assessment.

The objective of the Crystalline Disposal R&D control account is to advance our understanding of long-term disposal of used fuel in crystalline rocks and to develop necessary experimental and computational capabilities to evaluate various disposal concepts in such media.

Significant progress has been made in FY17 in both experimental and modeling arenas in evaluation of used fuel disposal in crystalline rocks, especially in model demonstration using field data. The work covers a wide range of research topics identified in the R&D plan. The major accomplishments are summarized below:

- **Model development for spent fuel degradation and its coupling with metal corrosion:** Both experimental and modeling studies show that H_2 plays an important role in determining the dissolution rate of UO_2 fuel, and that even moderate H_2 concentrations suppress the oxidative dissolution of spent fuel. The major source of H_2 within a breached waste package in low-oxygen environments will be anoxic corrosion of the various steels used as containers and structural components. The steel corrosion and H_2 generation reactions are coupled redox reactions that proceed at equal rates under anoxic conditions. Therefore, a steel corrosion model was added to the fuel matrix degradation (FMD) model to represent the primary kinetic source of H_2 (and Fe^{2+}) in a breached waste container. Once it is fully calibrated, the steel corrosion model can be used to calculate the corrosion rates of various metals under the environmental conditions in a breached waste package as a function of temperature, Eh, pH and solution chemistry to provide the H_2 concentrations controlling the fuel degradation rate. We identified the processes through which steel corrosion kinetics is coupled with the fuel degradation kinetics in the FMD model and summarized the sensitivity of the calculated fuel degradation rate to the range of corrosion rates that could occur for different steels expected to be present in a waste package. We also identified information gaps that need to be filled in order to further develop, parameterize, and calibrate the

steel corrosion model for the range of environmental conditions that could occur in a breached waste package.

- **Model development for glass waste form degradation:** The reactivity of silicate glasses and minerals is important to numerous engineering applications including nuclear waste disposal. The dissolution process has long been considered to be controlled by a leached surface layer in which cations in the silicate framework are gradually leached out and replaced by protons from the solution. This view has recently been challenged by observations of extremely sharp corrosion fronts and oscillatory zonings in altered rims of the materials, suggesting that corrosion of these materials may proceed directly through congruent dissolution followed by secondary mineral precipitation. We have shown that complex silicate material dissolution behaviors can emerge from a simple positive feedback between dissolution-induced cation release and cation-enhanced dissolution kinetics. This self-accelerating mechanism enables a systematic prediction of the occurrence of sharp dissolution fronts (vs. leached surface layers), oscillatory dissolution behaviors and multiple stages of glass dissolution (in particular the alteration resumption at a late stage of a corrosion process). Our work provides a new perspective for predicting long-term silicate weathering rates in actual geochemical systems and developing durable silicate materials for nuclear waste disposal.
- **Understanding uranium interactions with bentonite materials:** This work is designed to test the effect of bentonite heating on U(VI) adsorption. U(VI) adsorption onto bentonite samples from the FEBEX *in situ* experiment, which were subjected to 18 years of heating at temperatures of 45-100 °C, was compared to adsorption onto original FEBEX bentonite and cold-zone FEBEX bentonite from the *in situ* experiment. The experimental results show that kinetics of U(VI) adsorption appear to be very fast, reaching equilibrium in less than 8 hours, while DIC concentrations reach equilibrium in 48 hours. U(VI) adsorption onto unpurified FEBEX bentonite samples which experienced sustained temperatures of approximately 95 °C was lower than adsorption onto original unheated and cold-zone (20 °C) FEBEX bentonite over a range of chemical conditions (pH 7-8, Ca = 0.1 and 2.0 mM) relevant to nuclear waste disposal. U(VI) adsorption onto unpurified FEBEX bentonite which experienced more moderate temperatures (approximately 45 °C) was *not* lower than unheated FEBEX bentonite for the single chemical condition tested (0.05 M NaCl, pH 7.5, 0.1 mM Ca). The difference in U(VI) adsorption between heated (95 °C) and cold-zone (20 °C) FEBEX bentonite persisted over the range of chemical conditions tested when the bentonite samples were purified to remove mineral impurities such as calcite, quartz, and feldspars. This suggests that the decrease in U(VI) adsorption was due to alteration of the clay mineral structure, and *not* due to a change in the pore water chemistry or amount and type of accessory minerals. This may reflect illitization of the montomorillonite; however, further clay characterization is needed to verify this hypothesis. These results provide key information necessary for performance assessment of HLW disposal scenarios. The decreased adsorption observed in this study as a result of bentonite heating may impact the diffusion of U(VI) through engineered clay barriers. Because the decreased U(VI) adsorption was due to changes in the clay mineral structure and *not* to aqueous U(VI) speciation, other radionuclides may be similarly affected
- **Understanding radionuclide interactions with metal corrosion products:** The main interest in radionuclide sequestration by corrosion products stems from (1) the potential for this process to significant inhibit radionuclide release during canister breaching and (2) from the absence of such processes in most repository performance assessments. The objective of this work is to quantify radionuclide sequestration as a result of canister breaching and near field corrosion processes. We have evaluated this process from both an experimental and modeling perspective. Experimentally, we developed methodologies to grow various iron oxides phases (goethite, hematite, magnetite) in the presence of radionuclides. We performed a small number of binary (RN-mineral) coprecipitation experiments to test radionuclide (Pu, Am, Np, and U) partitioning. Experiments are aimed to quantify coprecipitation partitioning and also examine the effects of aging and the

potential iron oxide recrystallization effects associated with the presence of aqueous phase Fe(II). The exprimental results reveal that (1) upon aging of a Pu-doped ferrihydrite precorsor into more crystalline phase, plutonium associates more strongly with goethite (FeOOH) than hematite (Fe_2O_3); and (2) the timing of Pu addition in the synthetic procedures affects the final form of plutonium associated with goethite.

- **Understanding colloid-facilitated Cs transport in granitic materials:** Transport experiments using two mini-columns were conducted to interrogate the colloid-facilitated transport of ^{137}Cs through crushed Grimsel granodiorite. Water from the Chancellor nuclear test cavity at the Nevada Nuclear Security Site was selected because ^{137}Cs is strongly associated with the colloidal fraction, and ^{3}HHO is present in high concentrations and therefore acts as a conservative tracer. Column eluent was measured for ^{3}HHO, ^{137}Cs, and turbidity (as a proxy for colloid concentration). After one pore volume eluted through the first column, both the ^{3}HHO and turbidity reached Chancellor water values, suggesting that no colloids were filtered by the granodiorite. ^{137}Cs breakthrough occurred concurrently with the ^{3}HHO and turbidity breakthroughs but in concentrations less than the injection solution. The initial breakthrough consisted almost entirely of colloidal ^{137}Cs. Solute concentrations of ^{137}Cs were negligible initially and rose steadily along with the colloid-associated ^{137}Cs until about 50 pore volumes, after which both solute and colloid-associated ^{137}Cs eluted through the column at the same concentration and partitioning as the injection solution, suggesting that the granodiorite's adsorption capacity had been exhausted. Eluent samples from the first ~26 pore volumes that were not used for analysis were combined and injected into a second column. Analyses indicated that the granodiorite in the first column had adsorbed most of the ^{137}Cs in the solute phase and over half of the ^{137}Cs that was associated colloids during the first 26 pore volumes. Thus, the injection solution into the second column consisted mainly of ^{137}Cs strongly bound to colloid surfaces that outcompeted the sites of the granodiorite. The results from the second column reflect the much stronger association between the ^{137}Cs and the strong sites of the colloids. In contrast to the results from the first column, where only about 45% of the ^{137}Cs initially associated with colloids remained associated with colloids, about 90% of the colloid-associated ^{137}Cs remained associated with colloids in the second column. The results from both column experiments were simultaneously matched by a two-adsorption-site model in which the first site is weaker than the second but has greater abundance. These experiments demonstrate how the sequential column technique can provide well-constrained model parameterizations of the adsorption and desorption behavior of a radionuclide on colloids in the presence of competing immobile surfaces. The method is especially well suited to interrogate the slower desorption rate constants of radionuclides from colloids that will dictate the magnitude of colloid-facilitated radionuclide transport over the long time and distance scales relevant to nuclear waste repository systems.
- **Compaison of discrete fracture and equivalent continuum approaches for modeling flow and transport in fractured media:** One of the major challenges of simulating flow and transport in the far field of a geologic repository in crystalline host rock is related to reproducing the properties of the fracture network over the large volume of rock with sparse fracture characterization data. Various approaches have been developed to simulate flow and transport through the fractured rock. The approaches can be broadly divided into Discrete Fracture Network (DFN) and Equivalent Continuum Model (ECM). The DFN explicitly represents individual fractures, while the ECM uses fracture properties to determine equivalent continuum parameters. We compared DFN and ECM in terms of upscaled observed transport properties through generic fracture networks. The major effort was directed on making the DFN and ECM approaches similar in their conceptual representations. This allows for separating differences related to the interpretation of the test conditions and parameters from the differences between the DFN and ECM approaches. The two

models were compared using a benchmark test problem that is constructed to represent the far field (1x1x1 km^3) of a hypothetical repository in fractured crystalline rock. The test problem setting uses generic fracture properties that can be expected in crystalline rocks. The models were compared in terms of the: 1) effective permeability of the domain, and 2) nonreactive solute breakthrough curves through the domain. The principal differences between the models are mesh size, network connectivity, matrix diffusion and anisotropy. We demonstrated how these differences affect the flow and transport. We identify the factors that should be taken in consideration when selecting an approach most suitable for the site-specific conditions.

- **Understanding solute dispersion and mixing in fracture networks:** Using the DFN model, we performed dispersion and mixing simulations on three dimensional fracture networks. The new capability was developed to calculate and analyze subsurface transport dispersion. We designed two synthetic networks to isolate the influence of structure and disorder at the macro-scale and then compared its importance relative to moderate levels of hydraulic heterogeneity. Our study shows that, as hydraulic heterogeneity increased, both longitudinal and traverse dispersion also increased; the less mechanical dispersion observed in the structured network appeared to be linked to the higher levels of connectivity than in the poorly connected random network; for moderate levels of hydraulic heterogeneity, fracture network structure is the principal control on transport times and dispersion within fracture networks. We applied a DFN model to interpret tracer diffusion data obtained from the Long Term Sorption Diffusion Experiments conducted in Sweden. Experiments were focused on tracer transport in the stagnant pore water of the rock matrix. Analyzing the shape of the tracer penetration profiles observed in the experiment and comparing it to the predicted general shape of a 1D diffusion model, vastly different behavior was observed for the natural fracture surfaces and for the unaltered rock matrix. The micro fractures were observed in different slices of the sample core. Several slices of the individual cores had micro fractures that were fresh and consequently they were likely newly formed, i.e. induced by drilling or stress release. Our study focuses on understanding how micro fractures, which provide faster transport paths, affect the penetration profile. The DFN model was used to investigate, how the thickness of fractured layer affects the penetration profile of tracer driven by pure diffusion. The obtained results emphasize the importance of including heterogeneity into the simulation process. Micro fractured surface contributes to initial fast decrease of concentration followed by a slower penetration as tracer gets into homogeneous medium.
- **Synthesis of field data into a flow and transport model:** Through the Development of Coupled Models and their Validation against Experiments (DECOVALEX-2019) project, we obtained a comprehensive set of hydrologic and chemical data from a research tunnel at 500 m depth, at the Japan Atomic Energy Agency (JAEA) Mizunami Underground Research Laboratory (MIU). The objectives of this work is to develop a general workflow or methodology to synthesize field observations and measurements into a flow and transport model. Fracture data analysis and preliminary modeling analysis were performed. The fracture data analysis utilizes fracture data collected in the research tunnel and monitoring borehole 12MI33. A discrete fracture model was developed based on fracture orientation, size and intensity derived from the fracture data analysis. The discrete model was then upscaled to an effective continuum model that could be used for flow and transport simulations. A preliminary modeling analysis was conducted to predict inflows into the inclined drift and the Closure Test Drift (CTD) as a function of the extent of tunnel excavation. The predicted inflow rates are comparable to field measurements.

Based on the work accomplished in FY17 and the prior years, the future work is recommended to:

- Continue to focus on two key topics related to deep geologic disposal of spent fuel in crystalline rocks: better characterization and understanding of fractured media and fluid flow and transport in such media, and designing effective engineered barrier systems (EBS) for waste isolation. Specific attention will be given to the development of next-generation buffer materials for waste isolation and to a mechanistic understanding of alteration products (e.g. iron oxides) of EBS components as secondary waste forms for radionuclide retention.

- Help the generic disposal system analysis (GDSA) team to develop a total system performance assessment (PA) model and provide the parameter feeds to the model. One goal of this effort is to have a PA model matured enough over next two years to be able to simulate a typical thermal-hydrologic-chemical evolution history of a repository in a crystalline medium. Once such as a model becomes available, various disposal concepts will be explored.
- Continue to synthesize technical results obtained in FY17 and prior years in a few selected areas to demonstrate tangible progress in the research. The focus areas will include thermal limits of bentonite and smectite illitization and modeling approaches of fluid flow and transport in fractured geologic media.
- The modeling work will move towards model demonstrations and applications using actual field data. For the process model development, an emphasis will be placed on the integration with total system model development.
- Fully leverage international collaborations, especially with Sweden Underground Research Lab and DECOVALEX.

This page left intentionally blank

CONTENTS

ACRONYMS

ADE	Advection-diffusion equation
ANL	Argonne National Laboratory
DECOVALEX	Development of Coupled Models and their Validation against Experiments
DFN	Discrete fracture network
DIC	Dissolved inorganic carbon
DOC	Dissolved organic carbon
DOE	U.S. Department of Energy
ECM	Equivalent continuum model
ENRESA	Empresa Nacional de Residuos Radiactivos
FEBEX	Full-Scale Engineered Barriers Experiment
FMD	Fuel matrix degradation
FMDM	Fuel matrix degradation model
GDSA	Generic Disposal System Analysis
HLW	High-level radioactive waste
IC	Inorganic carbon
ICP-MS	Inductively coupled plasma mass spectrometry
JAEA	Japan Atomic Energy Agency (JAEA)
LBNL	Lawrence Berkeley National Laboratory
LLNL	Lawrence Livermore National Laboratory
LANL	Los Alamos National Laboratory
LLW	Low-level radioactive waste
MIU	Mizunami Underground Research Laboratory
OC	Organic carbon
PA	Performance assessment
SNL	Sandia National Laboratories
SFWD	Spent Fuel Waste Disposition
SFWST	Spent Fuel Waste Science & Technology
UMTRA	Uranium Mill Tailings Remedial Action
XRD	X-ray diffraction

This page is intentionally left blank.

1. GOALS AND OUTLINE

The U.S. Department of Energy Office of Spent Fuel Waste Disposition (SFWD) established in fiscal year 2010 (FY10) the Spent Fuel Waste Science & Technology (SFWST) Program (formerly the Used Fuel Disposition Campaign - UFDC) program to conduct the research and development (R&D) activities related to storage, transportation and disposal of used nuclear fuel and high level nuclear waste. The Mission of the SFWST is:

> *To identify alternatives and conduct scientific research and technology development to enable storage, transportation and disposal of used nuclear fuel and wastes generated by existing and future nuclear fuel cycles*.

The work package of Crystalline Disposal R&D directly supports the following SFWST objectives:

- Develop a fundamental understanding of disposal system performance in a range of environments for potential wastes that could arise from future nuclear fuel cycle alternatives through theory, simulation, testing, and experimentation.
- Develop a computational modeling capability for the performance of storage and disposal options for a range of fuel cycle alternatives, evolving from generic models to more robust models of performance assessment.

The objective of the Crystalline Disposal R&D control account is to advance our understanding of long-term disposal of used fuel in crystalline rocks and to develop necessary experimental and computational capabilities to evaluate various disposal concepts in such media. The main research topics identified for this control account are summarized in a research plan developed by Wang et al. (2014). FY17 work is aligned with the following considerations and project goals:

- This control account would focus on two key topics related to deep geologic disposal of spent fuel in crystalline rocks: (1) better characterization and understanding of fractured media and fluid flow and transport in such media, and (2) designing effective engineered barrier systems (EBS) for waste isolation. Specific attention would be given to the development of next-generation buffer materials for waste isolation and to a mechanistic understanding of alteration products (e.g. iron oxides) of EBS components as secondary waste forms for radionuclide retention.
- This control account would help the generic disposal system analysis control account to develop a total system performance assessment model and provide the parameter feeds to the model. One goal of this effort is to have a PA model matured enough over next two years to be able to simulate a typical thermal-hydrologic-chemical evolution history of a repository in a crystalline medium. Once such as a model becomes available, various disposal concepts will be explored.
- FY17 would continue to synthesize technical results obtained in FY17 and prior years in a few selected areas to demonstrate tangible progress in the research. The focus areas will include (1) thermal limits of bentonite and smectite illitization and (2) modeling approaches of fluid flow and transport in fractured geologic media. The former would joint with Argillite control account.
- The modeling work would move towards model demonstrations and applications using actual field data. For the process model development, an emphasis will be placed on the integration with total system model development.
- The work planned for this control account would fully leverage international collaborations, especially with Sweden Underground Research Lab and DECOVALEX.
- Closely collaborate and integrate with other work packages, especially those on disposal in argillite, deep borehole disposal, and DOE-managed HLW and SNF Research.

The FY17 work for the Crystalline Disposal R&D control account is structured into the following tasks:

- Task 1: (SNL, LANL) Support to develop of a total system performance assessment model for crystalline media. FY17 activity will help the GDSA work package to improve the existing PA model for crystalline rocks. The potential improvements will include an upgraded far field transport model for multiple realizations and an improved Engineered Barrier System (EBS) model with a preliminary representation of waste package degradation and failure.
- Task 2: (ANL) Development of spent fuel degradation and waste package degradation model: This task will continue the development of the fuel degradation model and initiate the waste package degradation model that includes both overpack and canister materials. Due to the budget constraint, this activity will be jointed with the similar effort for the argillite work package.
- Task 3: (LBNL, LANL, SNL) Synthesis of the work on bentonite thermal limits and illitization: The work will synthesize both literature and SFWST data on the engineering specifications of bentonite buffer materials (e.g., swelling pressure), phase stability of smectite under relevant repository conditions, and thermal limits of bentonite as a buffer material. This work will joint with the Argillite Work Package, and it will be documented.
- Task 4: (LANL, SNL) Modeling of fluid flow and transport in fractured crystalline rocks: The task will continue to demonstrate the potential application of the discrete fracture network model and the fracture continuum model to actual field testing data obtained from international collaborations. Develop a strategy to integrate these types of process models into a total system performance assessment model.
- Task 5: (LANL, LLNL, SNL, LBNL) Experimental investigation of radionuclide interactions with natural and engineered materials: Continue the work on actinide sorption and diffusion in clays and in granitic materials, with an aim to a comprehensive process model for total system performance assessment and to maintain certain levels of experimental activities. The effort will also include the development of next-generation buffer materials for waste isolation.
- Task 6: (LANL, LLNL, SNL, LBNL) International collaborations: International collaborations are crucial for the activities proposed for this work package. These collaborations will include: SKB-BRIE tests, DECOVALEX, Mont Terri and FEBX-DP tests.

This report summarizes work accomplished in FY17 for the Crystalline Disposal R&D control account. The report is outlined as follows, covering topics from near-field waste form degradation, to engineered barrier material performance, and finally to far-field flow and transport:

- Chapter 2 documents the model development for fuel matrix degradation (FMD) and its coupling with package material degradation. The work documented is a jointed effort between the Crystalline and the Argillite control accounts. (Research topics addressed: S2, S3 and P19; see Wang et al., 2014).
- Chapter 3 presents a new model for aqueous degradation of silicate glasses and minerals by considering nonlinear dynamics of the process. (S2, S3 and P19).
- Chapter 4 summarizes an investigation of uranium interaction with FEBEX bentonite. (P10)
- Chapter 5 presents a preliminary result on radionuclide sorption sequestration by metal corrosion products. (P20 and P22)
- Chapter 6 provides a summary of colloid-facilitated Cs transport in granitic materials (P10 and P11).
- Chapter 7 provides a comparison between two modeling approaches for flow and transport in fractured crystalline rocks: DFN model and Fracture Continuum Model (FCM). (P1, P8, P9 and P12)
- Chapter 8 presents the understanding of solute dispersion and mixing in fracture networks. (P1, P8, and P9)

- Chapter 9 provides a demonstration about how to synthesize field data into a flow and transport model.
- Chapter 10 provides an overall summary of FY17 accomplishment for Crystalline Disposal R&D control account.

It should be pointed out that the results documented in this report represents the major portion of the work conducted in FY17 for the Crystalline Disposal R&D control account but not all the work. The work not documented here includes the experimental study of smectite-to-illite conversion and the development of a new generation of buffer materials. Either being at an early stage of data synthesis or due to the sensitivity of intellectual properties involved, the results from these studies will be reported later as they become appropriate for public release.

Wang Y. et al., (2014) *Used Fuel Disposal in Crystalline Rocks: Status and FY14 Progress*, FCRD-UFD-2014-000060, SAND2014, Sandia National Laboratories, Albuquerque, NM.

2. SPENT FUEL DEGRADATION AND ITS COUPLING WITH PACKAGE MATERIAL CORROSION

2.1 Introduction

Science-based predictive models of waste form corrosion rates are being developed to provide reliable radionuclide source terms for use in repository performance assessments. Demonstrating that there is a fundamental scientific basis for the waste form degradation models is a key aspect for building confidence in the long-term predictions used for the repository safety case.

The purpose of this project is to develop, test and implement a fundamentals-based process model for the degradation rate of spent nuclear fuel that can be readily incorporated into the generic disposal system analyses (GDSA) performance assessment (PA) code to provide reliable radionuclide source terms throughout the service life of a repository. The fuel matrix degradation (FMD) model (or FMDM) is based on the Canadian Mixed Potential Model (King and Kolar, 2003), but has been expanded and customized for application in the ongoing spent fuel and waste science and technology (SFWS) campaign.

The continuing development and implementation of the FMD model also address two high level Features, Events, and Processes (FEPs) that are recognized as high R&D priorities for the SFWS campaign (Wang et al., 2014). The FEPs addressed by this model are 2.1.02 (waste form) and 2.1.03 (waste container), which correspond to the high priority research topics P19 (Development of waste form degradation model) and P20 (Development of new waste package concepts and models for evaluation of waste package performance for long-term disposal) identified by Wang et al. (2014).

The flow of information within the integrated FMDM – GDSA-PA model is summarized in Figure 2-1

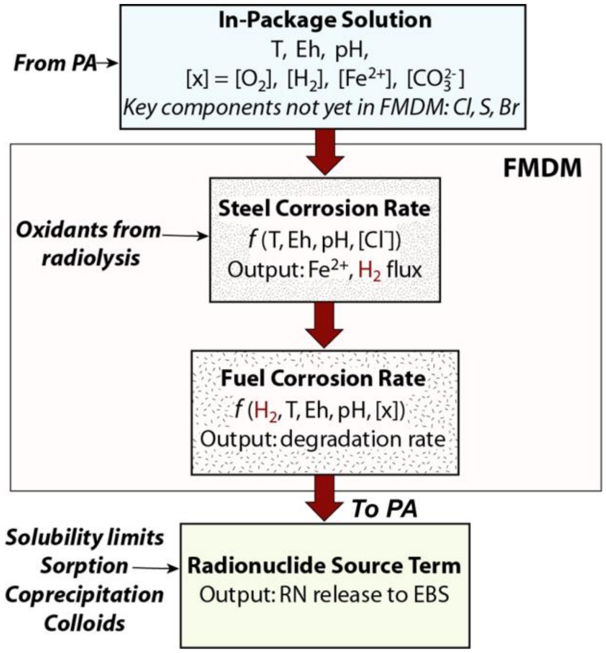

Figure 2-1. Summary figure showing the context of the FMDM within the source term calculation information flow (adapted from Jerden et al., 2017)

The FMD model calculates the degradation rate of UO_2 fuel under the environmental conditions in a breached waste package. The degradation rate will be used to calculate radionuclide source term values for use in reactive transport calculations through the EBS and host geology to demonstrate regulated dose limits will be met throughout the service life of the repository.

The FMD model calculates the dissolution rate of spent fuel as a function of the interfacial corrosion potential (E_{corr}), at which all of the anodic and cathodic half reactions occurring at the fuel/solution boundary under the environmental conditions are kinetically balanced and there is no net electron transfer. The dissolution rate (which generates an anodic current due to the oxidation of U^{4+} to U^{6+}) is relatively high under oxidizing conditions above the U(IV)/U(VI) threshold potential, but significantly lower at potentials where only solubility-limited chemical dissolution of U^{4+} occurs. The threshold potential for U(IV)/U(VI) oxidative dissolution depends on pH, as shown in Figure 2-2, and on the water chemistry. Under the reducing conditions envisioned in argillite and crystalline rock repositories (the region in Figure 2 labeled Repository Groundwater), the Eh of the solution will be well below the U(IV)/U(VI) threshold. However, the radiolysis of water by spent fuel to form H_2O_2 and O_2 can cause localized oxidizing conditions that drive the Eh far above the threshold for oxidative dissolution of the fuel, i.e., into the U(VI) stability field. The shaded area in Figure 2 shows the possible range of in-package conditions due to radiolysis (which affects Eh) and the corrosion of steel components (which affects Eh and pH). This shows the FMD model must address a range of pH from about 4 to 11 and Eh values spanning the range of water stability.

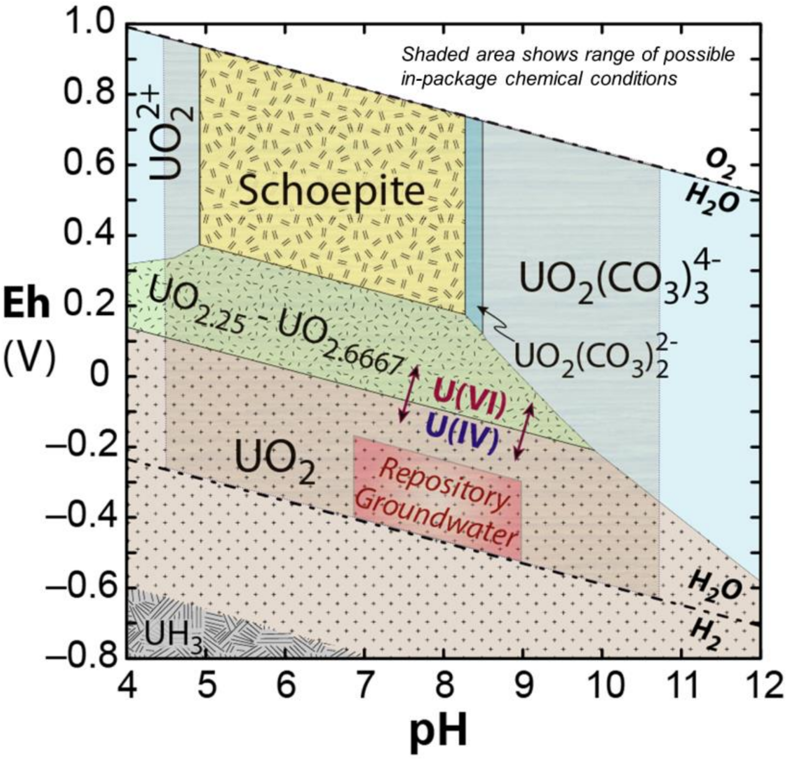

Figure 2-2. Eh – pH diagram for U speciation showing the conditions expected for groundwaters in a reducing crystalline rock or argillite repository (from Laaksoharju, et al., 2008). This diagram was drawn for a solution with $1x10^{-6}$ molar uranium and $1x10^{-4}$ molar carbonate.

A number of experimental and modeling studies have shown that the radiolytic oxidative dissolution of spent fuel in anoxic environments is counteracted by the catalyzed oxidation of H_2 on fission product alloy phases referred to as Ru ε-phases or noble metal particles (NMP). What we refer to as the H_2 effect has been shown qualitatively to decrease spent fuel dissolution rates by 4 orders of magnitude from the maximum rates attained in the absence of H_2, so the H_2 effect must be taken into account in scientifically based performance assessment calculations (e.g., Shoesmith, 2008, Grambow, et al., 2010, Jerden et al., 2015). The major goal of the ongoing FMD model development work is to implement an accurate model that quantifies the generation of H_2 and its effect on spent fuel degradation rates. This report presents results from a new version of the FMD model (FMDM v.3) that incorporates a steel corrosion module to quantify the source of H_2 in a breached waste package or near field environment. (Note that the steel corrosion module is used to represent the corrosion of all metals to generate H_2, not only steel.) This report builds on the more extensive FMD model sensitivity runs discussed in Jerden et al. (2017).

One of the main findings is that future work for this project needs to address the extensive coupling between the corrosion of waste package components and the spent UO_2 fuel. As shown in examples below, the Eh and pH conditions within a breached waste package will evolve with time due to coupled reactions of alloy corrosion, radiolysis, and spent fuel dissolution. The latest FMD model accounts for radiolysis and takes a step towards accounting for coupled processes by linking steel corrosion kinetics and fuel degradation rates; however, more extensive experimental and modeling work is needed to accurately model the fuel dissolution rate as the in-package solution chemistry evolves due to the corrosion of engineering materials.

A schematic diagram showing the key materials and generalized key reactions within a breached spent fuel waste package is shown in Figure 3, which highlights the spatial context and key processes that are being taken into account in the FMD model. As shown schematically in Figure 2-3, the spent fuel assemblies will be surrounded by (and in close proximity to) steel components within the waste package and disposal canister, which may include low carbon steels (C-steel), borated stainless steels and 316 stainless steel. Another important material from the prospective of H_2 production in the repository is the Zircaloy cladding surrounding the fuel pellets. No credit is taken for Zircaloy as a physical barrier in the current FMD or GDSA PA models, but it will probably be beneficial to include Zircaloy corrosion as a source of H_2 the FMD model.

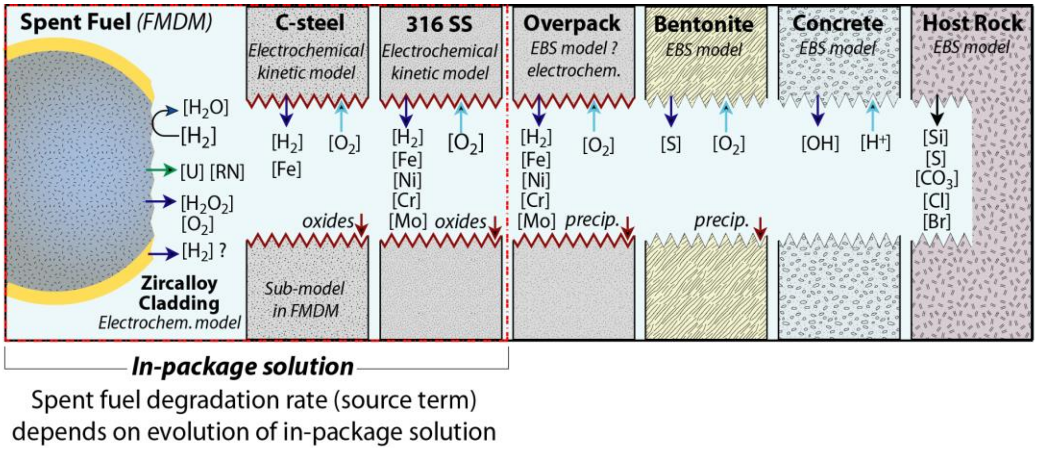

Figure 2-3. Schematic diagram depicting the interdependent chemical relationships between spent fuel, in-package alloy components and engineered barrier materials within a breached waste package.

2.2 Fuel Matrix Degradation Model and Its Integration with Generic Disposal System Analyses (GDSA) Model

The key processes represented in the latest version of the FMD model (FMDM.V3) are:

- generation of radiolytic oxidants as a function of fuel burn-up,
- NMP-catalyzed oxidation of H_2, which protects the fuel from oxidative dissolution,
- precipitation of U-bearing secondary phases,
- complexation of uranyl by carbonate,
- oxidation of ferrous iron,
- temperature variations of reaction rates (by Arrhenius equations),
- one-dimensional diffusion of all chemical species to and from the fuel and steel surfaces,
- anoxic corrosion of steel components to generate dissolved H_2 and ferrous iron.

Of these processes, the effect of H_2 oxidation is the most important in determining the fuel dissolution rate and thus the radionuclides source term (Jerden et al. 2015). The second most important effect is the oxidative dissolution of the fuel by the radiolytic oxidant H_2O_2 and its decomposition product O_2. In the FMD model, the H_2O_2 concentration is calculated using an analytical form of the radiolysis model developed at PNNL (Buck et al., 2014) and the burn-up/dose rate function. Fuel oxidation is counteracted by the catalytic oxidation of H_2 on NMP sites that are present on the fuel surface as a distinct Ru-Mo-Pd-Rh-Tc phase. The FMD model calculates the net effect of all redox reactions occurring in the system based on the fuel corrosion potential (E_{corr}) by using mixed potential theory. Steel corrosion at the E_{corr} value established by a particular environmental condition (Eh, pH, chemistry), will stabilize at a particular rate that will depend on whether it corrodes actively or passivates. The rate can be measured electrochemically as a corrosion current, which can be converted to a surface area-normalized mass dissolution rate by using Faraday’s law for implementation in the FMD model.

The reaction scheme and layout of the FMD model is shown in Figure 2-4.

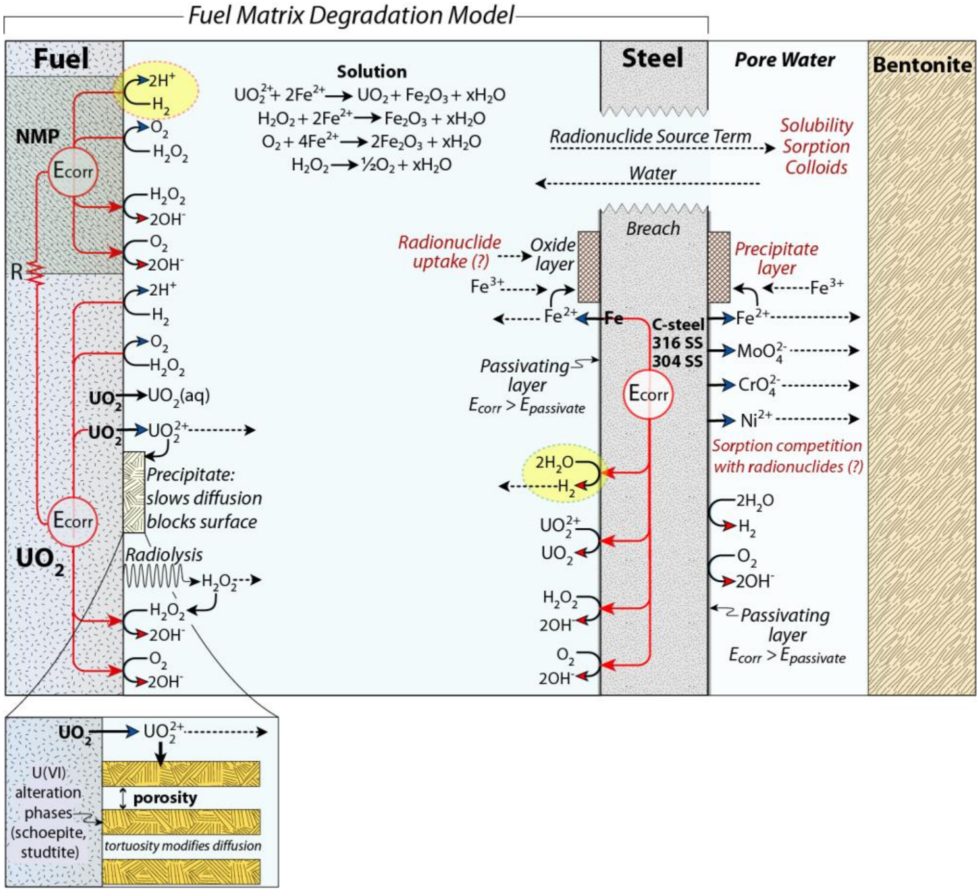

Figure 2-4. Schematic showing the reaction scheme for the fuel matrix degradation model and identifying other key processes that influence in-package chemistry and radionuclide mobilization. This report focuses on the reactions that are highlighted in yellow: H_2 generation during steel corrosion and H_2 oxidation on the fuel surface (adapted from Jerden et al., 2017).

In the absence of oxidative dissolution, the fuel degrades by solubility-limited chemical dissolution, which is much slower than oxidative dissolution (e.g., Röllin et al., 2001). It was shown in Jerden et al., 2015 that the FMD model accurately reproduces the experimental observation that even relatively low concentrations of dissolved H_2 (~0.1 mM) can measurably inhibit the oxidative dissolution of the fuel. In 2017, the FMD model was successfully integrated with the GDSA PA code PFLOTRAN. A set of sensitivity runs using the integrated code were performed at Sandia National Laboratory by Dr. Jennifer Fredricks to demonstrate that the H_2 effect represented in the stand-alone FMD model is accurately captured in the integrated model. Results from this sensitivity study, which are shown in Figure 5, indicate that the integrated code accurately accounts for the effect of H_2 and is consistent with experimental results indicated by the ovals.

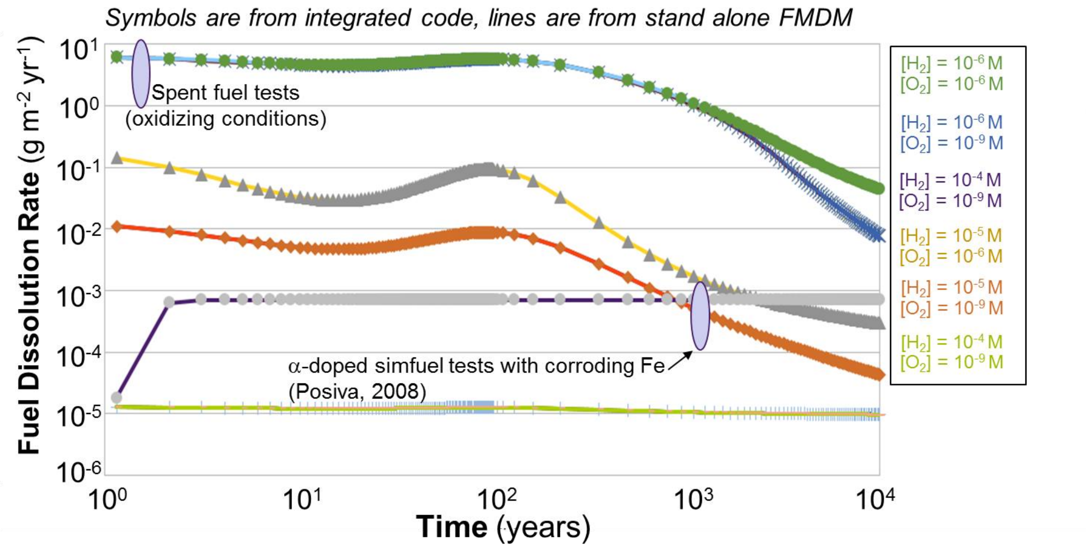

Figure 2-5. Comparison of results from the integrated FMDM-PFLOTRAN model (symbols) with the stand-alone FMD model (solid lines), and experimental results (ovals) for a range of H_2 and O_2 concentrations.

Figure 2-5 shows that the FMD model predicts that H_2 concentrations as low as 0.1mM will inhibit the oxidative dissolution of the fuel and limit degradation to the slow chemical dissolution rate (bottom green line), which is more than 4 orders of magnitude lower than the oxidative dissolution rate (blue line with green symbols). These runs also confirm that the results from the FMD model are consistent with data from batch dissolution studies of spent fuel (Cunnane 2004 - gray oval in top left of diagram) and from simfuel dissolution studies (Posiva, 2008).

The stand-alone FMD model was further developed in the 2016 – 2017 timeframe by the addition of a corroding steel surface to the modelled system to provide a kinetic source of H_2 within the model (Figure 2-4). The addition of a corroding steel surface in the FMD model is an initial step for representing the important coupling between the corrosion of waste package components and waste forms. The environmental dependencies of the steel corrosion rate remain to be added. Results from sensitivity runs with the FMD model containing the steel corrosion module presented in this report and in Jerden et al., 2017 indicate the sensitivity of the fuel dissolution rate to the steel corrosion rate.

The specific steps involved in radionuclide release from spent fuel that are or will be represented in the FMD model are as follows: in a breached waste package, groundwater will infiltrate open spaces within the canister and begin to corrode steel components. This will set up a reaction front of corrosion products in the seepage water that will eventually contact the fuel rods. The steel will corrode and produce H_2 even when the infiltrating groundwaters are electrochemically reducing with respect to the fuel. This is because the stability fields of carbon steels and stainless steels lie below the stability field of water, as shown in the iron Eh-pH diagram in Figure 2-6. Assuming that the Zircaloy cladding has failed, the fuel will begin degrading when contacted by seepage water by either relatively rapid oxidative dissolution or by relatively slow chemical dissolution, depending on the Eh and pH of the seepage water and the dissolved concentration of H_2. The dominant dissolution mechanism will be determined by the fuel surface potential that is established by the solution Eh. The shaded area in Figure 6 shows the possible range of in-package conditions due to radiolysis (which affects Eh) and the corrosion of steel components (which affects Eh and pH).

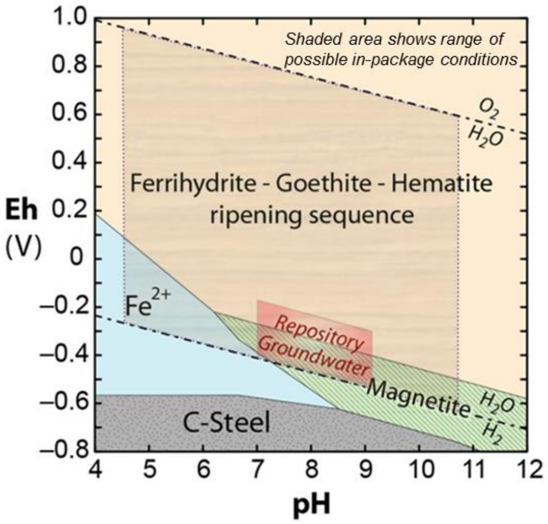

Figure 2-6. Eh – pH diagram showing the conditions expected for groundwaters in a reducing crystalline rock or argillite repository (from Laaksoharju, et al., 2008), drawn for 1x10^{-3} molar iron.

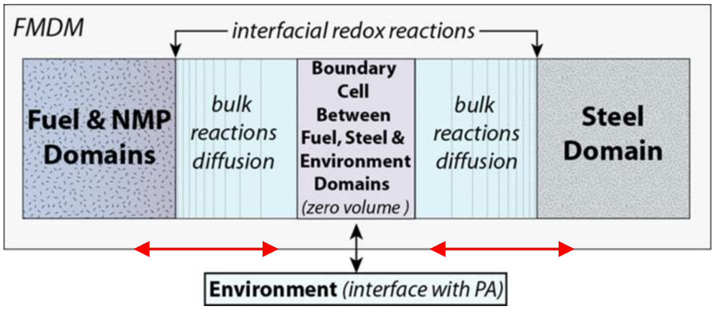

Figure 2-7. Schematic diagram showing how steel surface corrosion is represented in the FMDM.

Figure 2-7 shows how three solution domains used in the FMD model are coupled. The half of the bulk solution contacting the steel surface is coupled to the other half of the bulk solution contacting the fuel surface through a zero-volume interstitial domain. The interstitial domain is used as a boundary mixing cell to exchange mass generated the fuel and steel surfaces that diffused through the seepage water in the breached waste package and with pore water in the adjacent near field environment define fluxes passing to the other surface. No chemistry occurs in the interstitial domain or environment; those regions are zero-volume and only serve to provide an interface between the fuel and steel domains used to model diffusion and the environment. It is possible to control the interaction between the steel and fuel domains by altering (1) the environmental concentrations, (2) the relative areas of the two reactive domains, and (3) the leak rate from the interstitial domain into the near field environment. The boundary cell serves as the input/output interface with the GDSA performance assessment model.

The addition of the steel corrosion module directly into the FMD model has the downside of potentially slowing down execution of the code. However, this possible challenge is outweighed by the technical benefits of having the steel and fuel corrosion directly coupled in the same code. The specific technical advantages include the following:

- The direct coupling of fuel and steel corrosion is necessary to quantify the H_2 effect on the fuel corrosion rate, as it has been shown that H_2 produced from the anoxic corrosion of steel can decrease the fuel dissolution rate by over four orders of magnitude (Jerden et al., 2015).

- The common environment couples the steel and fuel corrosion rates. Directly coupling the fuel and steel degradation kinetics allows for the quantification of redox fronts that develop within the waste container due to the diffusion of radiolytic oxidants away from the fuel surface and the reactions of these oxidants with the steel surface and the resulting aqueous Fe^{2+} and H_2. This is also important because these redox fronts represent the Eh of the seepage water contacting the waste form and waste container internal components to establish the surface potentials and corrosion rates.
- Direct coupling will allow the steel corrosion module to be readily implemented into the GDSA PA model. The version of FMDM that has already been integrated with PA can be replaced with the new version that includes the steel corrosion module, since all changes will occur within the FMDM without affecting the data exchange.

The details of the development and implementation of the steel corrosion module in the FMD model are discussed in Section 2-3 (starting on page 15) of Jerden et al. (2017.

As discussed in Jerden et al. (2017), a critical review of the parameter database used in the FMD model resulted in the identification of a number of important data gaps that need to be addressed. These data needs are identified in Table 1, which is adapted from Jerden et al. (2017).

Table 2-1. Summary of FMDM parameters and data gaps that need to be addressed in future work to improve the accuracy of the model (adapted from Jerden et al., 2017).

Parameter	Description	Data needs to improve accuracy
Dimension of fuel environment	(mm – cm)	To be updated when dimensions of waste package are known
Nodes in fuel environment	(log-space grid: fine-spacing near surface)	To be updated when dimensions of waste package are known
Fuel surface coverage by NMP	(~1%)	From literature
Dimension of steel environment	(mm – cm)	To be updated when dimensions of waste package are known
Nodes in steel environment	(log-space grid: fine-spacing near surface)	To be updated when dimensions of waste package are known
Number of FMDM time steps	(100 – 1000)	Use to optimize PA interface
Fuel alteration layer porosity	(~50%)	From literature
Fuel alteration layer tortuosity	(~0.01)	From literature
Fuel alteration layer radiolysis factor	(*not used*)	*Could be activated to account for radionuclide uptake by U secondary phases*
Alpha particle penetration depth	(35μm)	From literature
Fuel burnup	(25 – 75 GWd/MTU)	Input from PA
Age of fuel (time out of reactor)	30 – 100 yrs	Input from PA
Resistance between fuel and NMP domains	(10^{-3} Volts/Amp)	Interpretation of literature
Temperature history	function	Data need: needs to be input from PA – will depend on repository scenario
Dose rate history	function	Based on MCNPX results of Radulescu, 2011
Spatial dose rate	function (decrease in dose rate with distance from fuel)	Based on MCNPX results of Radulescu, 2011
Rate constants for interfacial reactions in fuel and steel domains	See Figure 8 for summary of specific reactions	Data need: experiments needed due to lacking or inconsistent data in current literature on H_2 reactions on fuel and NMP and steel corrosion under relevant conditions
Charge transfer coefficients for interfacial half-cell reactions in fuel and steel domains	See Figure 8 for summary of specific reactions	Data need: experiments needed due to lacking or inconsistent data in current literature on H_2 reactions on fuel and NMP
Activation energies	T dependence: See Figure 8 for summary of specific reactions	Data need: experiments needed due to lacking or inconsistent data in current literature on H_2 reactions on fuel and NMP and steel corrosion under relevant conditions

Table 2-1. Continued.

Parameter	Description	Data needs to improve accuracy
Standard potentials for interfacial half-cell reactions: fuel and steel	See Fig. 8 for reactions	From literature
Relative area of fuel domain	Default 1:1, depends on waste package design	To be updated when dimensions of waste package are known
Relative area of steel domain	Default 1:1, depends on waste package design	To be updated when dimensions of waste package are known
Environmental leak rate (diffusion barrier factor)	Depends on waste package design, breach	Interpretation of literature
Environmental concentrations	(O_2, H_2, CO_3^{2-}, Fe^{2+}, Cl^-)	Input from PA
Rate constants for bulk solution reactions in fuel, steel environments	See Figure 6 for summary of specific reactions	From literature
Activation energy for bulk solution reactions	T dependence, See Figure 8 for reactions	From literature
Passivation potential of steel surface	(75 V_{SCE}) as place-holder	Data need: experiments needed due to lacking or inconsistent data in current literature
Passivation corrosion current density	Calculated internally within FMDM	Data need: experiments needed due to lack of data in literature
Radiolytic oxidant (H_2O_2) generation value (G_{cond})	Analytical function for conditional G_{H2O2} value from PNNL radiolysis model	Values based on radiolysis model results, Buck et al., 2013. *Would need to be updated, expanded for brine solutions (Cl, Br)*

2.3 Results from Electrochemical Scoping Experiments to Parameterize the Steel Corrosion Module

2.3.1 Background

Establishing accurate steel corrosion rates for relevant disposal conditions is essential for source term modeling because of the dominant effect of H_2 on the spent fuel dissolution rate (as discussed in Section 2.2 above). The half-cell reactions of particular interest for H_2 generation are as follows:

$Fe^0 \rightarrow Fe^{2+} + 2e^-$ (Reaction 1)

$2H_2O + 2e^- \rightarrow H_2 + 2OH^-$ (Reaction 2a)
$2H^+ + 2e^- \rightarrow H_2$ (Reaction 2b)

with the overall anoxic steel corrosion reactions

$Fe + 2H_2O \rightarrow H_2 + Fe^{2+} + 2OH^-$ (Reaction 3a)
$Fe + 2H^+ \rightarrow H_2 + Fe^{2+}$ (Reaction 3b)

Reactions 3b and 3a provide the fundamental coupling between steel corrosion and H_2 generation in acidic and neutral or alkaline solutions. (Analogous reactions can be written for Zircaloy corrosion to form ZrO_2.) The oxidation of other steel constituents (e.g., Cr, Mo, Ni, and Mn) will contribute to the anodic current, but the oxidation of Fe will be dominant. The threshold potential and reaction rates will depend on the surface potential imposed by the seepage water.

As discussed in Jerden et al. (2017), there is a wealth of literature studies on steel corrosion but much of the previous work was not done under repository relevant conditions. Furthermore, those studies that were done using bentonite pore waters or relevant ground waters (see reviews by Johnson and King, 2003 and King, 2007) involved batch style immersion tests that provide average cumulative rates rather than the instantaneous corrosion rates that represent the H_2 generation rates and are needed to parameterize and validate the FMDM steel corrosion module.

Steel coupon immersion tests provide useful information on mineralogy and the evolution of the chemical system, but the Eh, pH and solution chemistry are not controlled and the surface conditions can change significantly over the test duration. Corrosion rates derived from immersion tests are based on cumulative mass loss measurements or corrosion layer thicknesses that do not indicate how the corrosion rate (and thus H_2 generation rate) varies with time or conditions (most importantly, with the solution Eh). Knowing these dependencies of the H_2 generation rate is essential for modeling spent fuel dissolution under evolving in-package chemical conditions.

In an immersion test with a passivating steel, most of the mass loss occurs before the steel surface is passivated. The average rate may be relatively high, but the actual instantaneous rate that controls H_2 generation could have been low for the majority of the test duration. We need to know how the rate changes as the conditions evolve to accurately represent the flux of H_2 in the FMD model. Electrochemical techniques allow us to measure instantaneous rates under carefully controlled conditions. The difference between the cumulative rates from immersion tests and instantaneous rates measured with electrochemical methods is illustrated in Figure 2-8, where the blue curve shows the actual mass loss during aa coupon corrosion test. At the end of the test duration, the corroded material is removed from coupon to measure the mass loss, which is represented by the blue circle, that is used to determine the average corrosion rate indicated by the dashed green line. The majority of mass loss that occurred prior to passive stabilization dominates the cumulative mass loss and is not well-represented by the average rate, which depends on the test duration. However, the instantaneous (kinetic) rate that is given by the slope of the curve decreases significantly as the surface stabilizes and becomes much lower than the average cumulative rate. Whereas a series of immersion tests can be conducted for different durations to derive the mass loss curve, the method will not be sufficiently sensitive to measure the mass loss of a passivated surface. Immersion tests with actively corroding materials may provide corrosion rates that can be used for modeling, but only at E_{corr}. The instantaneous rate that is measured directly as the corrosion current with electrochemical methods is needed to calculate the H_2 generation rate in the FMD model. Perhaps more important from the modeling perspective, the immersion tests do not provide indications of the solution Eh or surface potential at which the steel is corroding, and cannot be used to determine the dependence of the corrosion rate on the solution Eh. Electrochemical tests can be conducted to measure the corrosion rate at fixed potentials in solutions having known compositions.

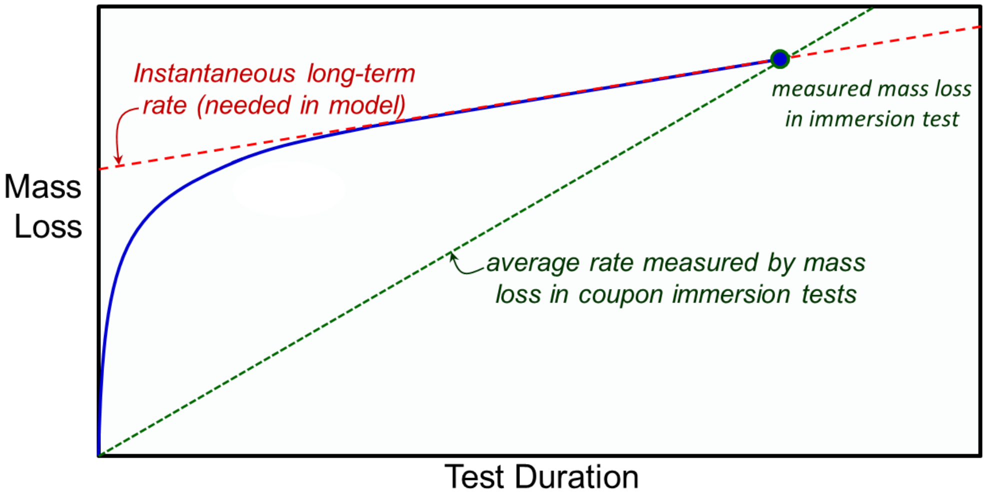

Figure 2-8. Conceptual diagram showing how mass loss measurements of steel corrosion rates yield rates that are significantly higher than the instantaneous rates relevant for repository process modeling (adapted from Jerden et al., 2017).

Electrochemical tests can also be used to quantify the effects of surface stabilization due to passivation and localized corrosion, such a pitting, that can only be observed in coupon immersion tests. Furthermore, electrochemical methods can measure rates on the order of nanograms cm^{-2} d^{-1}. The use of electrochemical methods would provide reliable corrosion rates for durable EBS materials (including Zircaloy cladding) and provide dependencies on environmental conditions that could be used to predict the long-term generation of H_2 and attenuation of fuel degradation rates as the seepage water composition evolves.

2.3.2. Method and Results

The standard three electrode method (Bard and Faulkner, 2001) was used to perform preliminary electrochemical tests on a carbon steel (4320) and a stainless steel (316L). The compositions of the steels are shown in Table 2-2. The three-electrode cell consisted of a 20 mL cell with a saturated calomel reference electrode a graphite counter electrode and a steel specimen working electrode. A typical electrochemical cell is shown in Figure 2-9. For these scoping experiments, an aggressive 10 mM NaCl solution adjusted to pH 4 with sulfuric acid was used as the electrolyte. This provides an extreme environment relative to the ranges shown in Figures 2-2 and 2-6.

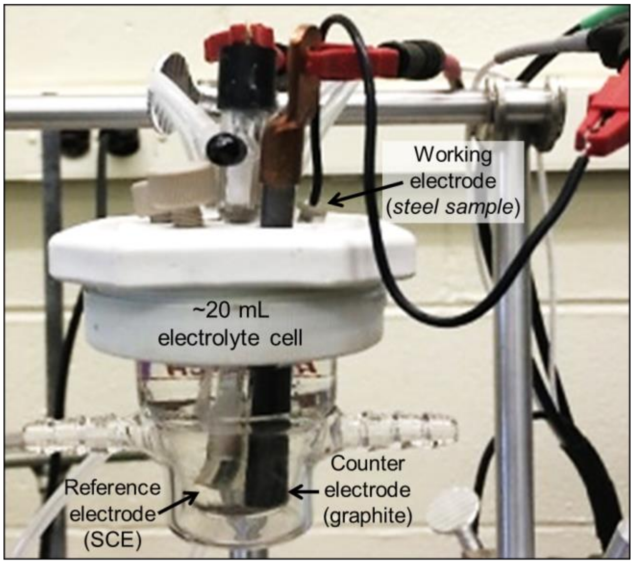

Figure 2-9. Three-electrode electrochemical cell used in ANL electrochemical experiments.

Table 2-2. Compositions of steels used in scoping experiments. These are nominal compositions from Azo Materials (https://www.azom.com/). The compositions of the particular electrodes used in the experiments has not yet been determined, but will likely be close to these nominal values.

Component	316 SS	4320 Steel
C	0.02	0.25
Mn	2.0	0.65
P	0.05	0.04
S	0.03	0.04
Si	0.75	0.12
Cr	17.0	0.60
Ni	12.0	2.0
Co	---	---
Mo	2.5	0.30
N	0.08	---
Fe	65.58	96.0
B	---	---

In the electrochemical tests, the electrolyte is used to impose chemical effects, including pH and Cl concentrations, and a potentiostat is used to impose a surface potential representing the solution Eh. The potentiostat can be used to impose a wide range of fixed potentials to efficiently determine the effect of the solution Eh on the steel corrosion and H_2 generation rate. In practice, a potentiodynamic scan is performed to measure E_{corr} for the surface in the test solution and identify regions of active and passive behavior to be studied in subsequent potentiostatic tests. The rapid scan rate used in potentiodynamic scan indicates the propensity for active or passive corrosion, but does not allow stable passive layers to form. Potentiostatic tests are conducted to measure the corrosion currents after stable passive layers have formed or constant (steady-state) rates are achieved with actively corroding metals. Figure 2-10 shows typical results for potentiodynamic (a) and potentiostatic (b) measurements on the 4320 carbon steel specimen in the pH 4 NaCl solution. The potentiodynamic response is typical of a non-passivating alloy as indicted by the continuously increasing current with increasing potential above E_{corr} (-0.45 V SCE). The electrode surface area-normalized currents (current densities) measured for potentiostatic holds at 0.10 V SCE (0.34 V SHE) and -0.45 SCE (-0.21 V SHE) in Figure 10b show the effect of the surface potential on the corrosion rates (calculated from the current densities using Faraday's law). The anodic current measured in the potentiostatic tests at (-0.45 V SCE) shows E_{corr} decreased as the surface corroded and stabilized within about 1 day at about 200 µA/cm^2. Using Faraday's law, the steel corrosion rate is 9×10^3 g m^{-2} yr^{-1}. The potentiostatic test at 0.10 V SCE results in a current density that is about 10-times higher and has not stabilized after 2 days. Series of potentiostatic tests will provide an analytical dependence of the corrosion rate as a function of Eh, pH, and Cl concentration.

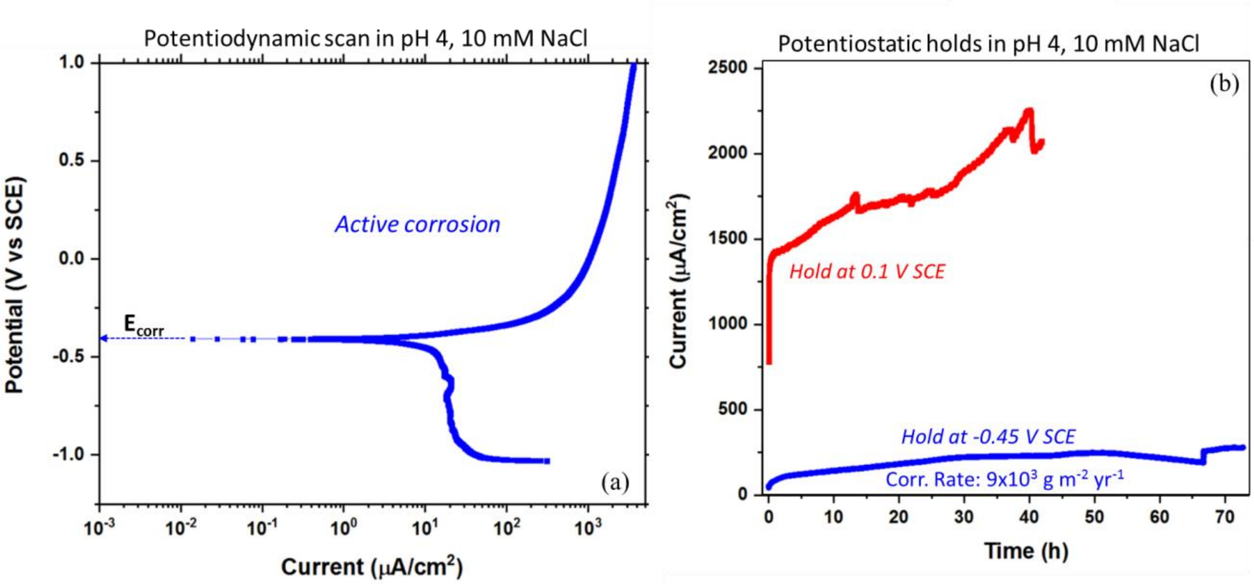

Figure 2-10. Results from potentiodynamic (a) and potentiostatic (b) tests on the 4320 carbon steel specimen in pH 4, 10 mM NaCl electrolyte.

Figure 2-11 shows potentiodynamic scans for a 316L stainless steel electrode in solutions with different NaCl concentrations. The results indicate that in pH 4, 10mM NaCl solution, 316L corrodes by relatively slow passive mechanism from around 0 V SCE up to around 0.9 V SCE. However, when the same electrode was reacted in 1 molar NaCl brine (after repolishing), the passive layer broke down above about 0 V SCE and the steel corroded actively. These experiments show the extreme dependence of stainless steel corrosion rates on the Cl concentration that must be captured in the FMD model.

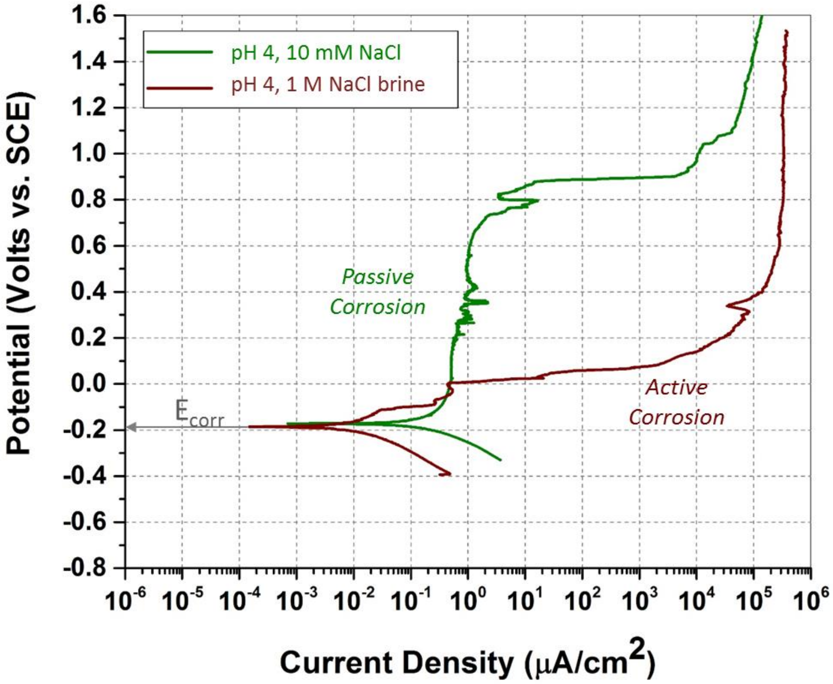

Figure 2-11. Results from potentiodynamic scans of a commercial 316L SS alloy in pH 4, 10 mM NaCl electrolyte (green) and pH 4, 1 M NaCl brine (brown).

Figure 2-12 shows results from a potentiostatic hold of 316L steel at 0.25 V SCE in the pH 4, 10 mM NaCl solution. This shows the rate decreases by a factor of ~150 within one day as the steel surface passivated and stabilized. The corrosion rate of of 0.6 g m^{-2} yr^{-1} for the stabilized surface represents the H_2 generation rate. As mentioned above, series of potentiostatic tests can be conducted to derive the analytical dependence of the steel corrosion rate on the Eh, pH, and Cl concentration (and any other key variable) to calculate the H_2 generation rate in the FMD model. Although the combined potential and solution compositions used in all potentiostatic tests may not represent an actual disposal condition, they provide the database required to determine the dependencies of the stabilized rates on the environmental variables. Results from a coupon immersion test would average the cumulative mass loss occurring during the first few hours over the duration of the experiment at the value of E_{corr}, which would evolve during the tests and not be known. That average rate would not represent the H_2 generation rate.

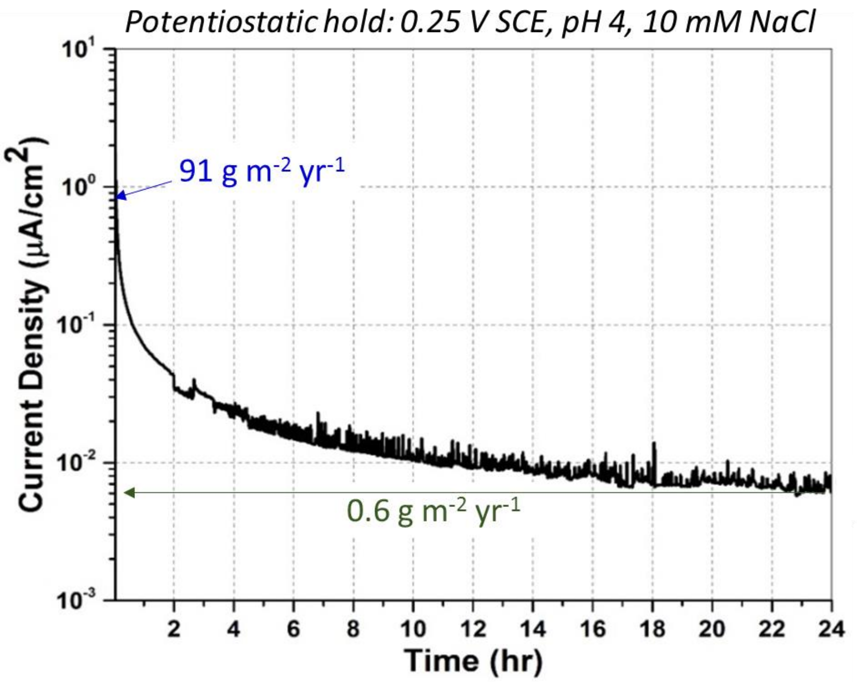

Figure 2-12. Results from potentiostatic test with commercial 316 stainless steel in pH 4, 10 mM NaCl electrolyte.

In the next Section, we demonstrate how the potentiodynamic and potentiostatic rate measurements can be used to calibrate kinetic fuel degradation and in-package chemistry models using the rates from Figures 2-10 – 2-12.

2.4 Example In-Package Chemistry Simulation and the Fuel Matrix Degradation Model: Role of Steel Corrosion

The reaction-path modeling code Gechemist's Workbench (Bethke, 2014) was used in series with the FMD model to investigate how the H_2 concentration may evolve as the carbon steel (4320), stainless steel (316L) and spent fuel within a failed canister all corrode simultaneously. The modeling approach is identical to that used in Jerden et al., 2017, except that the reactants in the present study are 4320 carbon steel and 316L stainless steel.

The thermodynamic database used for this model was thermo.com.V8.R6 (Johnson et al, 2000) to which the steel reactants were added. The masses of the different steel components and total solution volume were taken from the in-package chemistry model used for the YM TSPA (CRWMS, 2003). The compositions of the steel reactants are shown in Table 2-2 above, the masses used for this model are shown in Table 2-3, and the initial groundwater composition, which is typical of a crystalline rock repository environment, is shown in Table 2-4. The volume of solution used in the model was 4.1 m^3, which is based on the void volume within the spent fuel canister assumed in CRWMS, 2003.

Table 2-3. Values used in the Geochemist's Workbench steel titration model (from CRWMS, 2003).

Materials	**Total Mass** (kg)	**Specific Surface Area** (m^2 g^{-1})	**Total Area** (m^2)
316 SS	$5.9x10^3$	$4.1x10^{-6}$	24.2
C-steel: 4320	$2.1x10^3$	$8.7x10^{-5}$	180.5

Table 2-4. Initial solution composition used in Geochemist's Workbench steel titration model (from Posiva, 2012). This composition is typical of groundwater in a crystalline rock repository environment.

Component	**Concentration** (molar)
pH	8.2
Na	0.36
Ca	0.25
K	$4.9x10^{-4}$
Mg	$1.5x10^{-3}$
Sr	$1.1x10^{-3}$
Mn	$9.3x10^{-6}$
Fe	$3.8x10^{-7}$
Cl^-	0.86
SO_4^{2-}	$2.1x10^{-4}$
CO_3^{3-}	$4.0x10^{-5}$
SiO_2	$2.1x10^{-4}$

Six model runs were performed using the steel corrosion rates summarized in Table 2-5. In-package solution compositions based on the measured steel corrosion rates were calculated first and then manually input into the FMD model to calculate the fuel dissolution rates. Determination of the steel corrosion rates based on the seepage water composition, changes in the solution composition, and the resulting fuel dissolution rate will all be performed within a future version of the FMD model.

It should be emphasized that the scoping electrochemical experiments performed for the present study were on the aggressive end of the possible range of conditions with respect to steel corrosion. The low pH and relatively high chloride concentrations result in relatively high steel corrosion rates. Further work is needed to represent the effects of the full range of relevant conditions shown in the Eh – pH diagrams above (Figures 2-2 and 2-6).

Table 2-5. Steel corrosion rates used for the Geochemist's Workbench reaction path model.

Model Run	**4320 C-Steel** ($g\ m^{-2}\ yr^{-1}$)	**Source of Rate**	**316 Stainless Steel** ($g\ m^{-2}\ yr^{-1}$)	**Source of Rate**
1	91.0	Literature*	0.6	Present Study (Figure 12)
2	9000	Present Study (Figure 10b)	0.6	Present Study (Figure 12)
3	91	Literature*	91.0	Present Study PS# rate (Fig. 12)
4	91	Literature*	9.0	Present Study 10% PS# rate (Fig. 12)
5	9.0	Literature*	0.6	Present Study (Figure 12)
6	51.0	Literature*	0.6	Present Study (Figure 12)

*The literature reference used is Johnson and King, 2003, which provides rates for C-steel in general without specifying the exact composition. # PS stands for potentiostatic hold.

In each model run, the formation of radiolytic oxidants was simulated by the addition of O_2 to the solution over time. The rate of O_2 addition was initially $5x10^{-3}$ moles of O_2 per kg of water per year and decreased linearly with time. The initial O_2 concentration is based on a G-value for H_2O_2 of 1.0 molecules per 100eV (Pastina and LaVerne, 2001). The fuel burnup and dose rate assumptions are described below.

Each model run involved the following steps:

- The two steels (Table 2-2) in the proportions given in Table 3 were congruently reacted with the solution composition given in Table 4 at the rates specified in Table 5.
- Geochemist's Workbench was used to determine the evolution of the pH, Eh and speciation (solution and solids) of the simulated in-package solution corresponding to a given set of steel dissolution rates.
- Results from the in-package solution simulations were used as input to the FMD model, which was used to calculate the H_2 generation rate and corresponding spent fuel degradation rate.
    - Parameter values for the fuel environment (see Table 1) are from Jerden et al., 2015.
    - Parameter values for the steel environment (see Table 1) are from King and Kolar, 2003 (the actual values of these parameters need to be determined experimentally for relevant types of steels).

  - The environmental concentrations (constant concentration boundary) were $[H_2] = 1 \times 10^{-9}$ M, $[O_2] = 1 \times 10^{-9}$ M, $[Fe^{2+}] = 1 \times 10^{-9}$ M, $[CO_3^{2-}] = 1 \times 10^{-6}$ M.
  - Temperature was held constant at 25 ºC for all runs.
  - The fuel burnup was 60 GWd/tHM (gigawatt days per metric ton of initial heavy metal: U).
  - The age of the fuel for all model runs was 100 years out of reactor.

The results from model runs 1 – 6 (Table 2-5) are presented in Figures 2-13 to 2-21. The following trends are consistent for all six model runs:

- The initial Eh conditions fall within the U(VI) and ferric oxide stability fields due to the initially high O_2 production rate. However, once the initially accumulated O_2 is consumed, the solution becomes reducing with respect to the U^{4+}/U^{6+} and Fe^{2+}/Fe^{3+} couples. The time at which the Eh drop occurs varies depending on the steel corrosion rates used.

- In all model runs except Run 2 (Table 2-5), the pH evolution involves an initial decrease down to below pH 6 followed by a rebound to above pH 8. The initial pH decrease is caused by the oxidation of zero valent elements in the steel (reactions 4 and 6) and the subsequent pH increase is caused by reduction reactions that consume H^+ (reactions 7 – 9). The oxidation of iron to oxides involves both consumption and production of H^+ (reactions 10 – 11).

- The primary iron oxide phases in all model runs are ferric oxides and oxyhydroxides within the first few years of the simulation, but magnetite becomes the dominant oxide phase once the O_2 is depleted and will likely represent the main alteration phase formed on C-steel. Trevorite and chromite, nickel silicate, molybdenum oxide and nickel sulfide are predicted to form on the 316L SS.

- The third set of plots for each model run shows results from the FMD model based on the steel corrosion rates for each scenario. As the H_2 generation rate is directly proportional to the steel corrosion rates, the FMD model predicts lower fuel degradation rates during faster steel corrosion. Once the fast-corroding steel (4320 carbon steel in these runs) is consumed, the H_2 generation rate decreases to that of the lower steel corrosion rate (316L SS) and the fuel degradation rate increases accordingly. The dotted lines on these plots show the evolution of the spent fuel degradation rate if no H_2 is present (top dotted line) and for the case where spent fuel degrades solely by chemical dissolution (i.e., when oxidative dissolution is completely inhibited by the H_2 effect).

H^+ production reactions:
$S + H_2O + 1.5\ O_2(aq) \leftrightarrow 2\ H^+ + SO_4^{2-}$ (Reaction 4)
$C + H_2O + O_2(aq) \leftrightarrow H^+ + HCO_3^-$ (Reaction 5)
$P + 1.5\ H_2O + 1.25\ O_2(aq) \leftrightarrow 2\ H^+ + HPO_4^{2-}$ (Reaction 6)
H^+ consumption reactions:
$SO_4^{2-} + H^+ \leftrightarrow HS^- + 2\ O_2(aq)$ (Reaction 7)
$SO_4^{2-} + 2\ H^+ \leftrightarrow H_2S(aq) + 2\ O_2(aq)$ (Reaction 8)
$HCO_3^- + H^+ + H_2O \leftrightarrow CH_4 + 2\ O_2(aq)$ (Reaction 9)
Iron oxide formation reactions:
$Fe^0 + 2\ H^+ + 0.5\ O_2(aq) \leftrightarrow Fe^{2+} + H_2O$ (Reaction 10)
$3\ Fe^{2+} + 3\ H_2O + 0.5\ O_2(aq) \leftrightarrow Fe_3O_4 + 6\ H^+$ (Reaction 11)
$2\ Fe^{2+} + 2\ H_2O + 0.5\ O_2(aq) \leftrightarrow Fe_2O_3 + 6\ H^+$ (Reaction 12)

Figure 2-13 shows the Eh and pH evolution for model runs 1 and 2, which both use a measured rate for 316L SS corrosion and vary the 4320 steel corrosion rate between the measured value of 9000 g m^{-2} yr^{-1} for an Eh of -0.45 V SCE and a representative rate for higher pH and lower Eh (91 g m^{-2} yr^{-1}) (Johnson and King, 2003). Run 1 [Figure 13 (a) and (c)] shows an initial pH decrease from around pH 8 down to around pH 6 followed by an abrupt increase to pH 9.5 after 500 years caused by the consumption of O_2 as indicated by the Eh trend. Run 2 [Figure 2-13 (b) and (d)] indicates that for the fast corrosion rate of 9000 g m^{-2} yr^{-1} the initial pH decrease is not evident, presumably because all of the accumulated O_2 is consumed in the first time-step (within the first year) due to rapid steel corrosion. For both cases the Eh drops from 0.8 V (SHE) during the low pH interval down to -0.6 V (SHE) for the high pH interval.

Figure 2-14 shows how the masses of solids change over time for model runs 1 and 2 (Table 2-5). For both runs 316SS is present throughout the 10^5-year time-frame. For the moderate corrosion rate of 91 g m^{-2} yr^{-1} the model shows that the 4320 carbon steel will be entirely consumed in 8000 years [Figure 2-14(a)]. Using the higher corrosion rate of 9000 g m^{-2} yr^{-1} measured in the pH 4, 10mM NaCl for this study, the model predicts that all of the 4320 carbon steel will be consumed by year 60 [Figure 2-14(b)]. Plots (c) and (d) of Figure 2-14 show how the mineral assemblage on the corroding steels change over times (see bullets above).

Figure 2-21 shows the impacts that the steel corrosion kinetics have on the spent fuel degradation rates calculated by the FMD model. For the low 4320 steel corrosion rate [Figure 2-21(a)] used in Run 5, fuel degradation proceeds at a rate around a factor of 14 lower than the “no H_2” case for 40,000 years. Once all of the 4320 is consumed, the fuel degradation rate increases to a value that is a factor of 5 lower than the “no H_2” case, which corresponds to a H_2 generation rate equal the rate of 316 SS corrosion. For the higher 4320 steel corrosion rate [Figure 2-21(b)] used in Run 6, the fuel degradation rate is a factor of 250 lower than the “no H_2” for the first 2,000 years, after which it increases to a factor of 4 lower than the “no H_2” case due to 316L SS corrosion.

Figure 2-15 shows the Eh and pH evolution for model runs 3 and 4 (Table 2-5), which both use the relatively high 316 SS corrosion rates from the literature (Johnson and King, 2003). The 4320 steel corrosion rates for these runs were both set at the rate 91 g m^{-2} yr^{-1} found in the literature (Johnson and King, 2003). Run 3 [Figure 2-15 (a) and (c)] shows an initial pH decrease from around pH 8 down to around pH 5.6 within the first year followed by an abrupt increase to pH 10 in the first year caused by the consumption of accumulated $O_{2.}$ which is also indicated by the Eh trend. This trend is due to the relatively fast corrosion rate of 316 SS. The pH decrease extends to around 400 years in Run 4 with the lower corrosion rate. For both cases, the Eh drops from 0.8 V (SHE) during the low pH interval down to -0.6 V (SHE) for the high pH interval due to the O_2 consumption.

Figure 2-16 shows how the masses of solids change over time for model runs 3 and 4 (Table 5). Using the relatively high 4320 and 316 SS corrosion rates [Figure 2-16(a)] leads to the consumption of both steels within 4000 years. For the lower 316SS corrosion rate of (9 g m^{-2} yr^{-1}) in both runs, the model shows that the 4320 carbon steel will be entirely consumed in 4000 years [Figure 2-16(a)] but that the 316 SS will be present until the 40,000-year mark [Figure 2-16(b)]. Plots (c) and (d) of Figure 2-14 show how the mineral assemblage on the corroding steels change over times (see bullets above).

Figure 2-19 shows the Eh and pH evolution for model runs 5 and 6, which both use a measured rate for 316 SS corrosion and vary the 4320 steel corrosion rate between the relatively low rate of 9.0 g m^{-2} yr^{-1} and a rate of 51 g m^{-2} yr^{-1} (Johnson and King, 2003). Run 5 [Figure 2-19 (a) and (c)] shows an initial pH decrease from around pH 8.0 down to pH 5.6 followed by an abrupt increase at 5000 years caused by the consumption of accumulated O_2 as indicated by the Eh trends. Run 6 [Figure 2-19 (b) and (d)] indicates that the initial pH decrease only lasts until the 3000-year mark for the high corrosion rate of 4320. The Eh drops from 0.8 V (SHE) during the low pH interval down to -0.6 V (SHE) for the high pH interval in both cases.

Figure 2-20 shows how the masses of solids change over time for model runs 5 and 6 (Table 2-5). For both runs, 316 SS remains throughout the 10^5-year time-frame. For the low corrosion rate of 9 g m^{-2} yr^{-1} used in Run 5, the model shows that the 4320 carbon steel will last for 40,000 years [Figure 20(a)]. Using the higher corrosion rate of 91 g m^{-2} yr^{-1} in Run 6, the model predicts that all of the 4320 carbon steel will be consumed by year 2,000 [Figure 2-20(b)]. Plots (c) and (d) of Figure 2-14 show how the mineral assemblage on the corroding steels change over times (see bullets above).

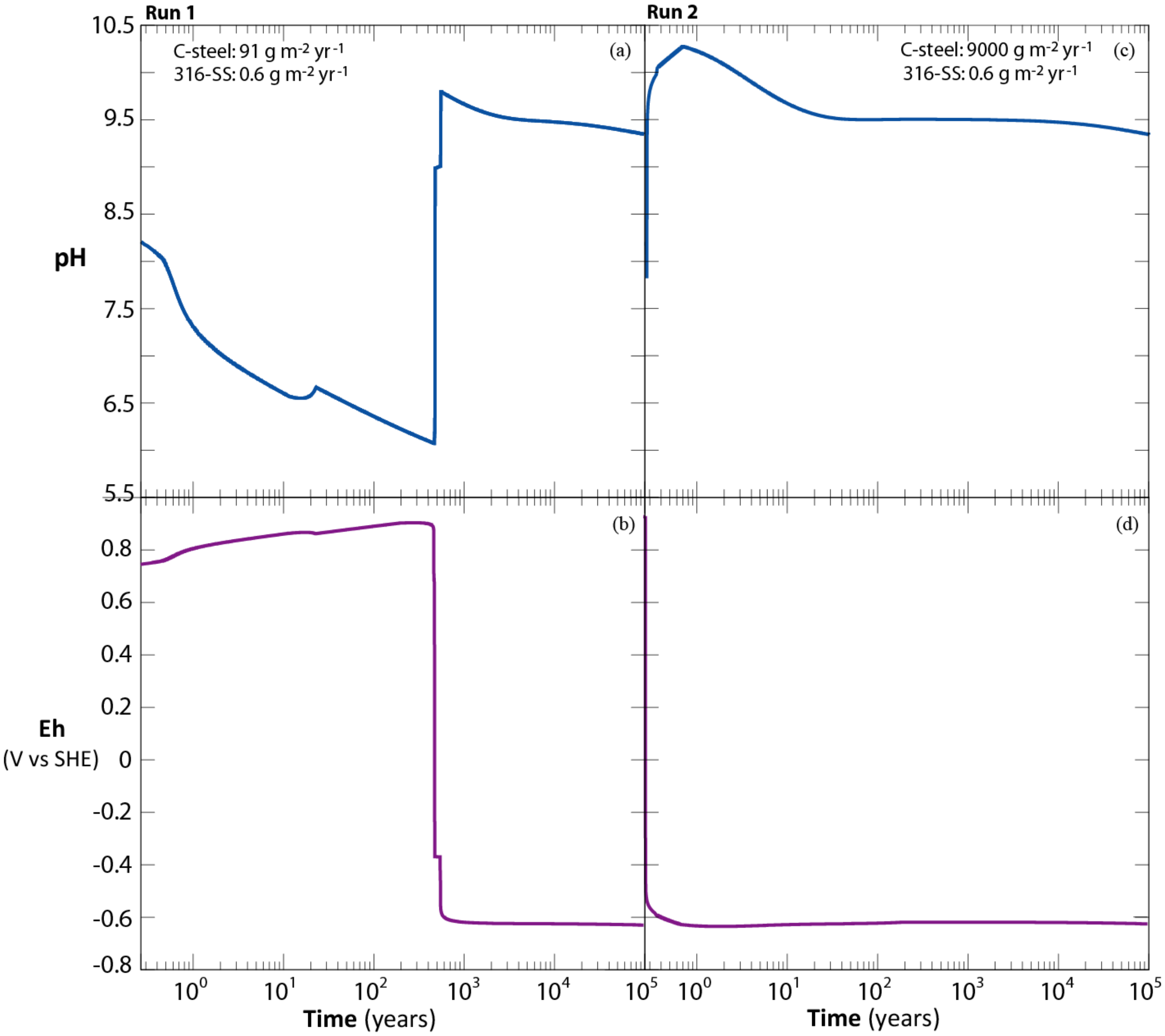

Figure 2-13. Results from simple in-package chemistry example model run using the reaction path code Geochemist's Workbench: (a) and (b) correspond to conditions for run 1 shown in Table 2-5 and (c) and (d) correspond to run 2 in Table 2-5.

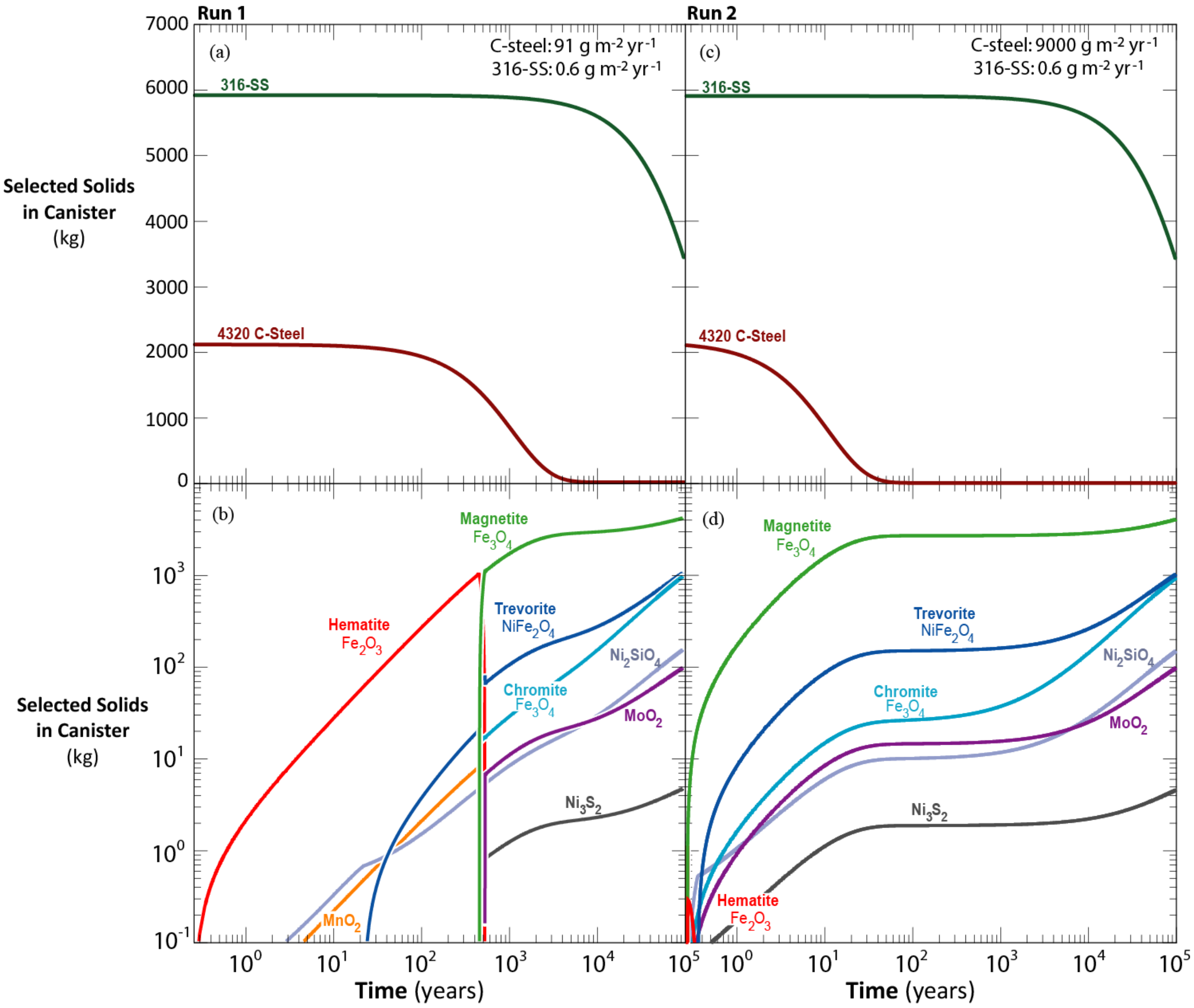

Figure 2-14. Results from Geochemist's Workbench in-package chemistry model: (a) and (b) correspond to conditions for run 1 shown in Table 2-5 and (c) and (d) correspond to run 2 in Table 2-5.

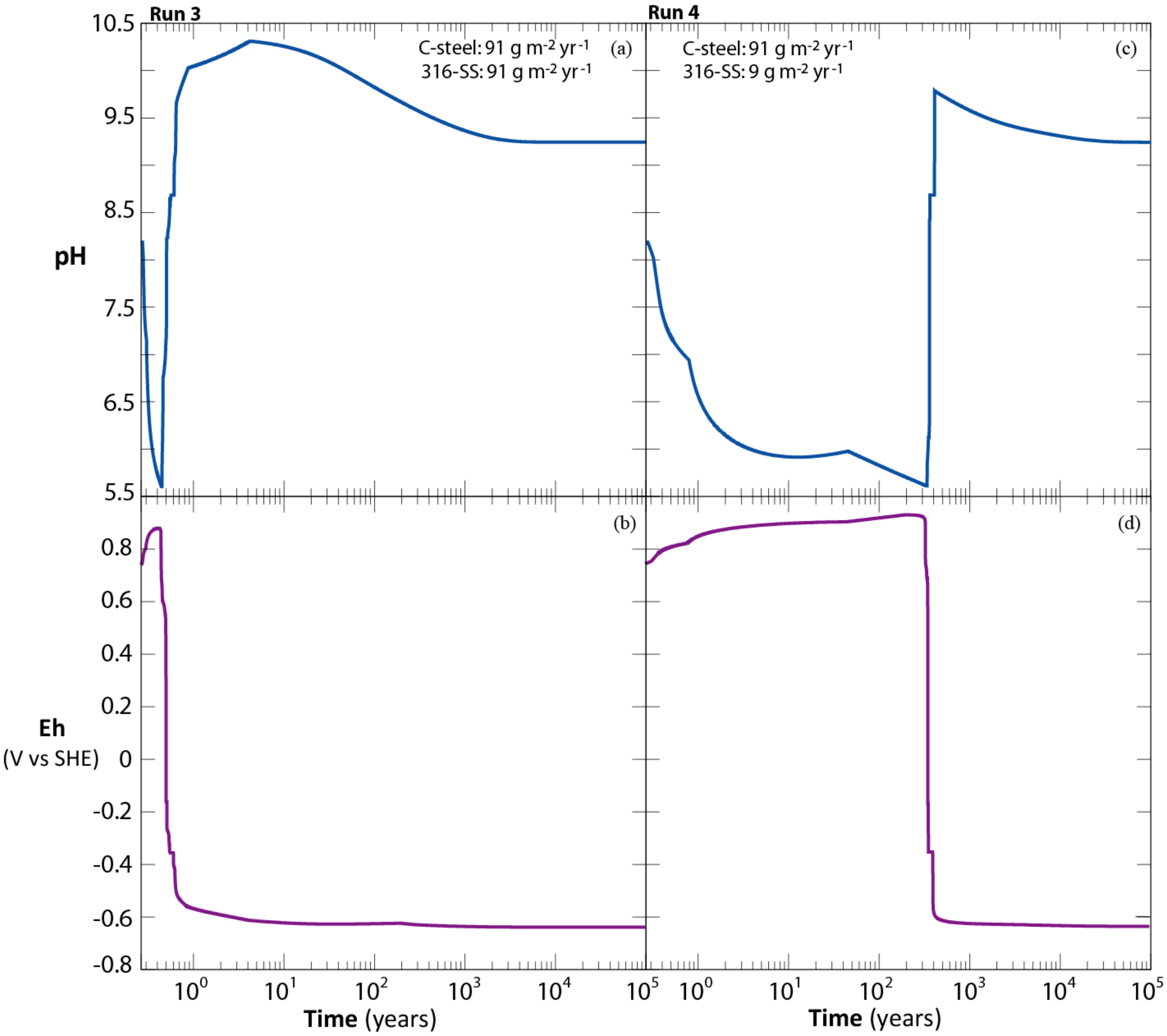

Figure 2-15. Results from simple in-package chemistry example model run using the reaction path code Geochemist's Workbench: (a) and (b) correspond to conditions for run 3 shown in Table 2-5 and (c) and (d) correspond to run 4 in Table 2-5.

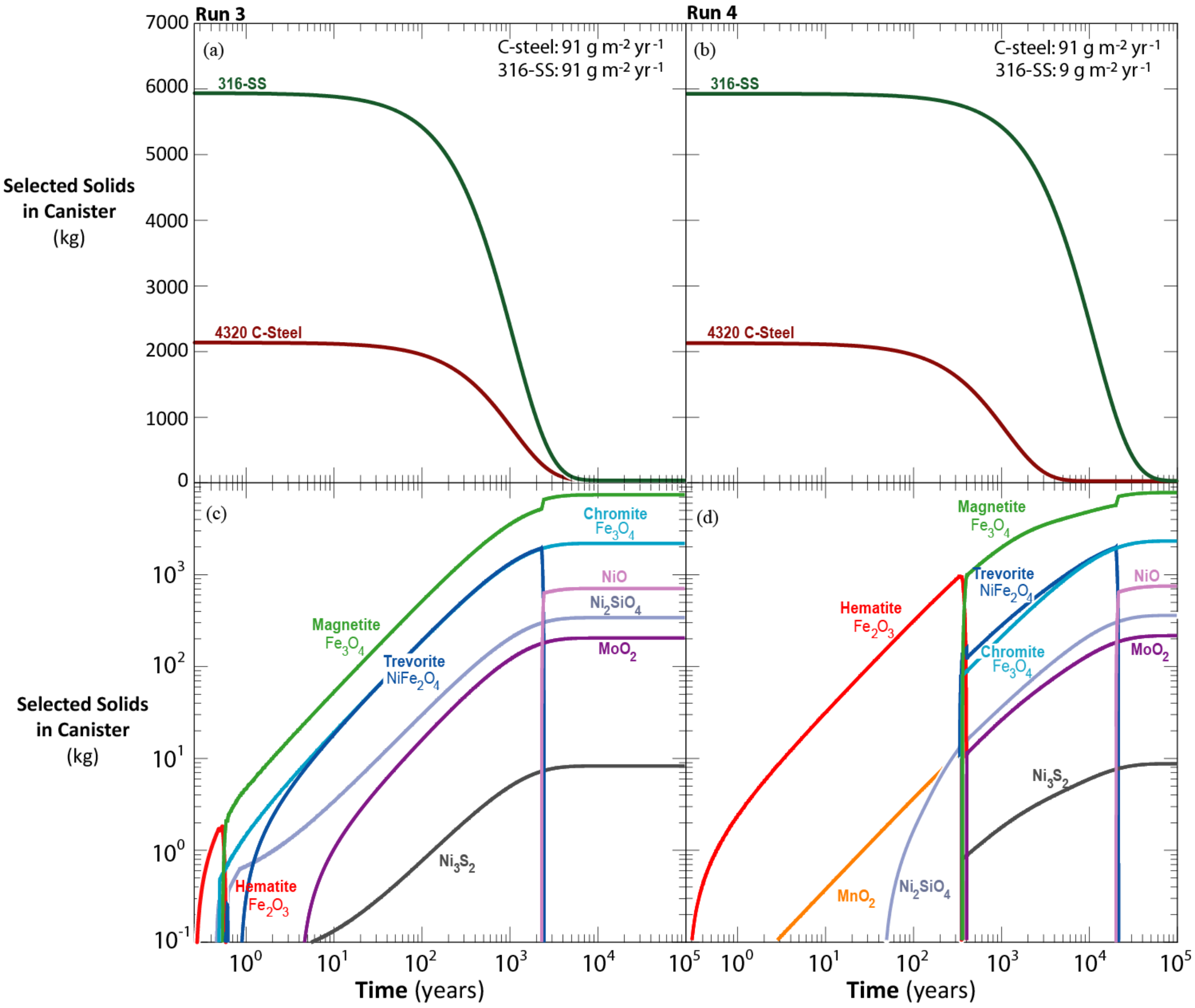

Figure 2-16. Results from Geochemist's Workbench in-package chemistry model: (a) and (b) correspond to conditions for run 3 shown in Table 2-5 and (c) and (d) correspond to run 4 in Table 2-5.

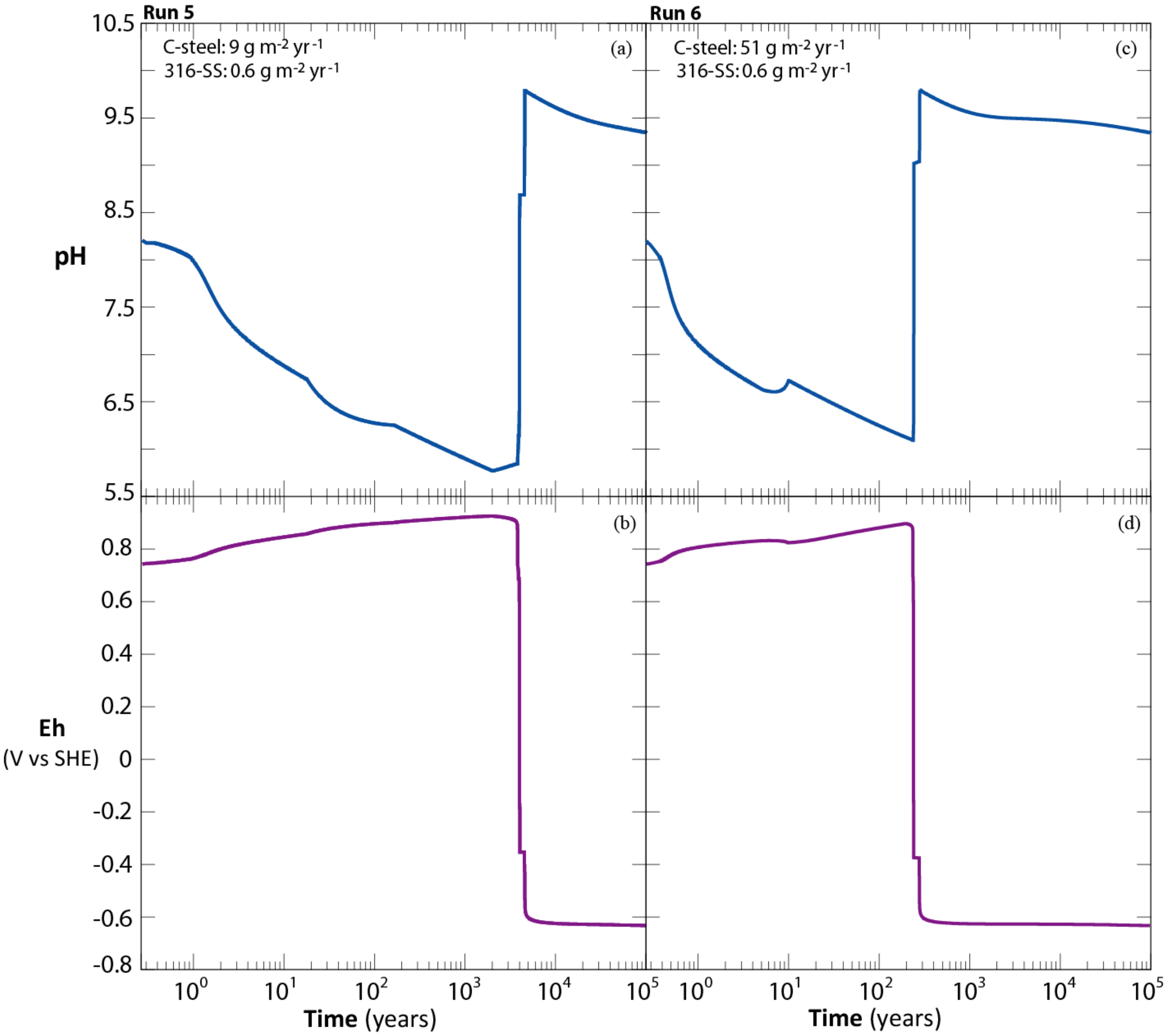

Figure 2-17. Results from simple in-package chemistry example model run using the reaction path code Geochemist's Workbench: (a) and (b) correspond to conditions for run 5 shown in Table 2-5 and (c) and (d) correspond to run 6 in Table 2-5.

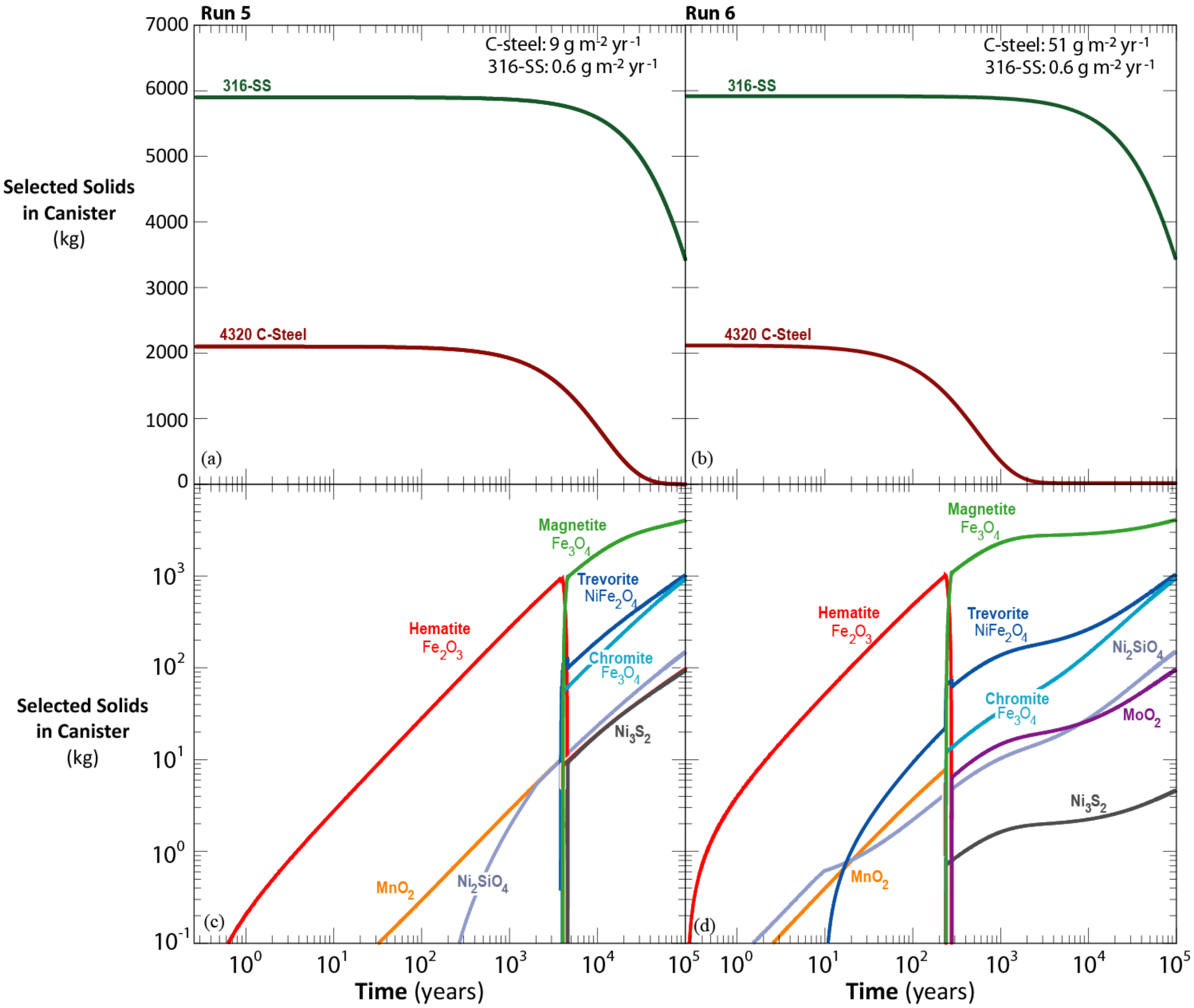

Figure 2-18. Results from Geochemist's Workbench in-package chemistry model: (a) and (b) correspond to conditions for run 5 shown in Table 2-5 and (c) and (d) correspond to run 6 in Table 2-5.

Figure 2-19 shows the impacts that the steel corrosion kinetics have on the spent fuel degradation rates as calculated by the FMD model. For the moderate 4320 steel corrosion rate [Figure 2-19(a)], fuel degradation proceeds at a rate around a factor of 60 lower than the "no H_2" case for 8000 years. Once all of the 4320 is consumed the fuel degradation rate increases to a value that is a factor of 4 lower than the "no H_2" case, which corresponds to the rate of 316 SS corrosions. For the high 4320 steel corrosion rate measured in the pH 4 solution [Figure 2-19(b)] the fuel degradation rate corresponds to the chemical dissolution rate due to high concentrations of H_2 suppressing oxidative dissolution (4 orders of magnitude lower than the "no H_2" case). However, due to the rapid corrosion rate, the 4320 steel is consumed by year 60 causing a corresponding dramatic increase in the fuel degradation rate.

For the relatively high 316 SS steel corrosion rate [Figure 2-19(c)] used in Run 3, fuel degradation proceeds at a rate that is around a factor of 250 lower than the "no H_2" case for 4000 years. Once all of the steel is consumed, the fuel degradation rate increases to the "no H_2" case. For the relatively low 316 SS corrosion rate [Figure 2-19(d)] used in Run 4, the fuel degradation rate is a factor of 250 lower than the "no H_2" case. At the 4000-year mark, the fuel degradation rate increases to a value corresponding the 316 SS corrosion rate and, the degradation rate increases back up to the "no H_2 case at the 40,000 year mark once all of the 316 is consumed.

For the low 4320 steel corrosion rate [Figure 2-19(e)] used in Run 5, fuel degradation proceeds at a rate around a factor of 14 lower than the "no H_2" case for 40,000 years. Once all of the 4320 is consumed, the fuel degradation rate increases to a value that is a factor of 5 lower than the "no H_2" case, which corresponds to the rate of 316 SS corrosion. For the higher 4320 steel corrosion rate [Figure 19(f)] used in Run 6, the fuel degradation rate is a factor of 250 lower than the "no H_2" for the first 2,000 years, after which it increases to a factor of 4 lower than the "no H_2" case due to 316L SS corrosion.

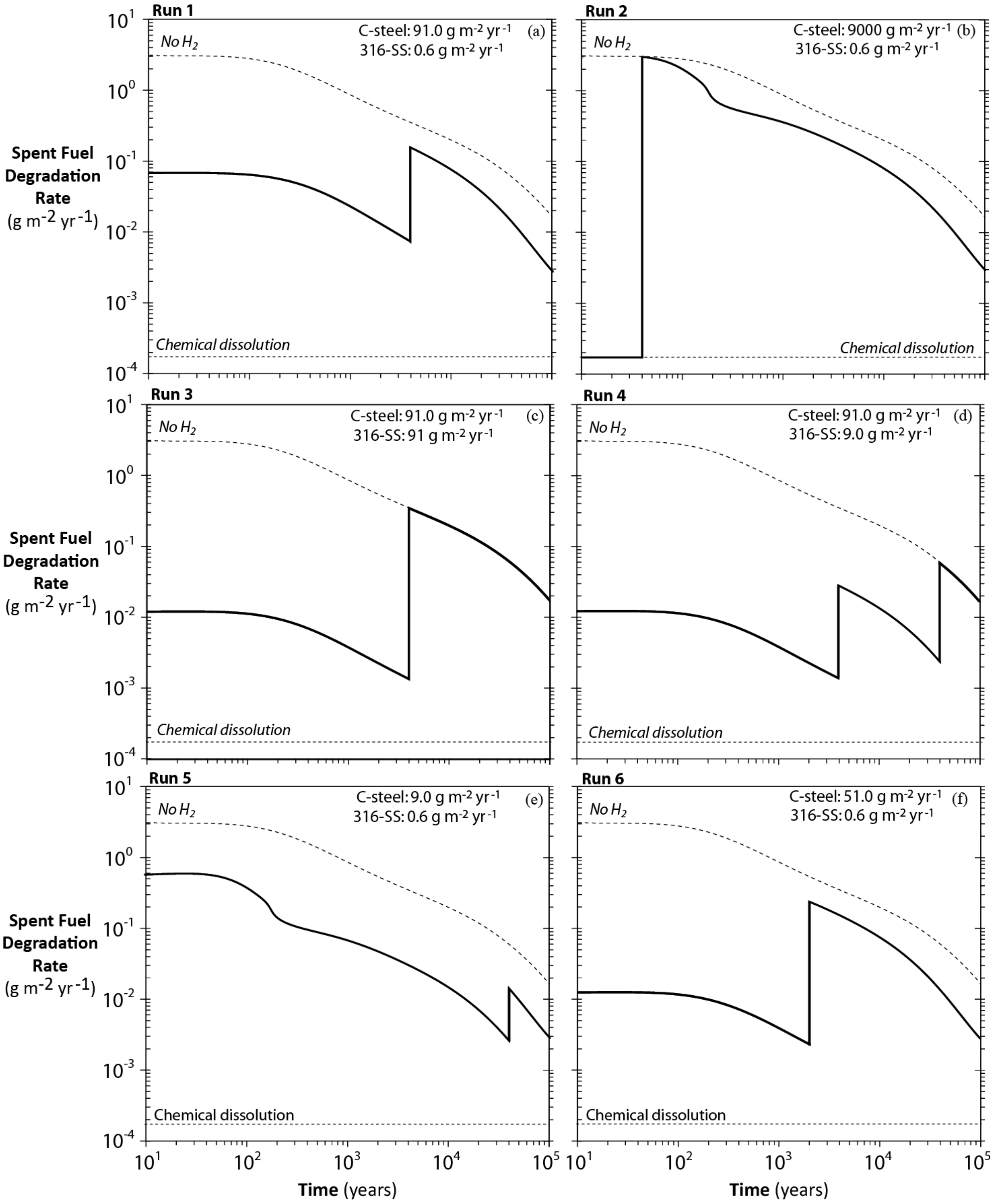

Figure 2-19. Results from FMD model accounting for variations in steel corrosion rates. These plots show how the degradation rate of the fuel changes over time with changes in the production rate of H_2, which is controlled by the steel corrosion rate.

2.5 Recommendations

The results of this study support the conclusions and recommendations that were identified and discussed in Jerden et al., 2017. Several information gaps were identified for modeling the anoxic corrosion behavior of relevant steels in repository-relevant conditions and the impact on spent fuel degradation rates. The magnitudes of the impacts of these processes were evident in Figures 2-15, 2-18 and 2-21, which show how the FMDM-predicted fuel degradation rates vary over a wide range of steel corrosion rates. Clearly, the environmental dependencies of steel (and Zircaloy) corrosion rates must be taken into account in the FMD model to represent the evolving conditions in a breached waste package. The high priority needs that were identified from the sensitivity runs discussed above are summarized in Table 6.

Table 6. Information gaps identified as part of the present work (adapted from Jerden et al., 2017).

Process	Issue and Data Needed	Experimental Approach
Long-term steel corrosion and H_2 generation rates at controlled Eh, pH, and and Cl^-.	Wide ranges of steel corrosion rates have been measured from mass loss in coupon tests under poorly controlled conditions; Those tests provide average rates that do not distinguish rates before and after passivation and do not identify the corrosion potential or provide a measure of the dependence of the corrosion rate on the Eh. Instantaneous steel corrosion rates with environmental dependencies (Eh, pH, Cl^-, T) are needed to calibrate and validate the H2 generation rate in the fuel matrix degradation model.	Electrochemical measurements of steel corrosion rates provide dependencies on T, Eh, pH, and Cl^- conditions for active corrosion and after passivation.
Dissolution rates of aged, high burn-up fuels in the presence H_2 from steel corrosion	Based on canister design characteristics, it is likely that much of the spent fuel in the repository will not be exposed to groundwater until more than 1000 years after repository closure. More studies are needed on the dissolution rates of actinide oxide materials that simulate “aged” ~1000 year old fuel in the presence and absence of H_2.	Synthesis of fission product and actinide doped simfuel, electrochemical measurements in the presence and absence of corroding steels
The roles that the porous corrosion layers (formed on the fuel and steel) play in the kinetics of spent fuel matrix degradation	Sensitivity runs performed with the FMDM indicate that the presence of a porous corrosion layer on the fuel surface will facilitate accumulation of oxidants and reductants (most importantly H_2) at the fuel/solution interface to enhance the attenuating effect. This process has not been confirmed or quantified experimentally.	Generation of corrosion product layers on simulated fuels and steels under controlled conditions (potentiostatic), corrosion rate measurements under controlled conditions with and without corrosion product layer coupled with solution analyses and microscopy.

Based on the sensitivity of the fuel degradation rate to an extreme range of steel corrosion rates demonstrated in Figures 2-13 to 2-21 above, it is recommended that the initial steel corrosion rate model be revised to include dependencies of steel and Zircaloy corrosion rates on key environmental variables. The scenario that needs to be studied involves post canister breaching conditions when the temperature will likely be 40 °C or lower (beyond 1000 years) with an initial solution composition similar to that shown in Table 2-4. The sensitivity of steel corrosion kinetics to environmental conditions is complex (including active and passive mechanisms at different Eh and pH conditions) and should be represented as accurately as possible in the FMD model. Corrosion rates of likely EBS materials should be measured under the anticipated range of relevant conditions to derive analytical functions for key variables (Eh, pH, and Cl^- concentration) that can be used in the FMDM.

2.6 Conclusions

The purpose of this study is to develop and test a process model for the degradation of uranium oxide spent fuel based on fundamental thermodynamics, kinetics, and electrochemistry that can be directly integrated into a repository performance assessment model. Because the model is based on fundamental principles, it can be applied with confidence over geologic time scales. The main features of the fuel degradation model discussed in this report are summarized in Figure 20, which is adapted from Jerden et al., 2017. The one-dimensional electrochemical/reactive transport FMD model was developed to meet this objective. The recent and on-going work described in Jerden et al., 2017 and this report involved quantifying the role of H_2 produced from the anoxic corrosion of steels in suppressing oxidative dissolution of the fuel. To this end, an electrokinetic mixed potential model for steel corrosion was added as a sub-model to the FMD model to calculate the amounts of H_2 generated as various metallic components in a waste package corrode. Sensitivity calculations relating the fuel degradation rate to the steel corrosion rates were performed to identify information gaps that need to be addressed to fully couple, calibrate, and validate the models.

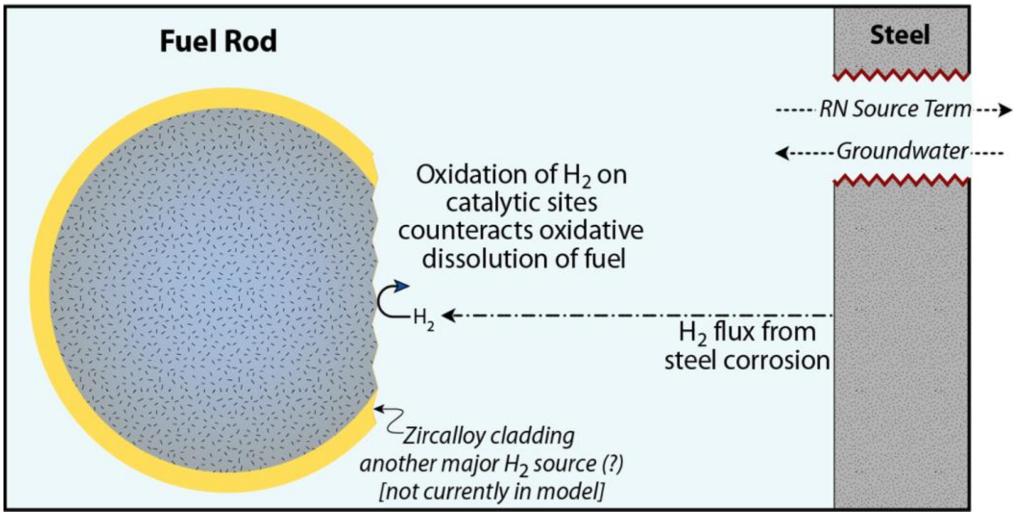

Figure 2-20. Conceptual summary of the FMDM highlighting the main features discussed in this report (adapted from Jerden et al., 2017).

The accomplishments and conclusions of this study are summarized as follows:

- The scoping experiments discussed in this report demonstrated a straightforward electrochemical method that provides the electrokinetic information needed for model parameterization and validation. Immersion tests can be used to provide information on mineralogy; however, they do not provide the quantitative, instantaneous corrosion rate data needed to calculate the H_2 generation rate.
- The FMD model was integrated with the GDSA PA code PFLOTRAN and the coupled model was tested over a range of H_2 concentrations to show that it accurately reproduces results from the stand-alone FMD model.

- An electro-kinetic mixed potential model for the corrosion of steels was coupled with the spent fuel dissolution reactions through the H_2 generation reactions. Modeling steel corrosion is a key part of the FMD model because it represents the main source of H_2 within the breached canister. Previous work has shown that less than 1 mM dissolved H_2 can suppress the oxidative dissolution of spent fuel under anticipated disposal conditions (Jerden et al., 2015, Wu et al., 2014)
- Sensitivity runs with the FMD model and new steel corrosion module show that enough H_2 is produced when the steel is corroding actively to inhibit the oxidative dissolution of the fuel and limit the rate of fuel degradation to the chemical dissolution rate (which is 3 to 4 orders of magnitude lower than the maximum oxidative dissolution rate).
    - Model results indicate lower steel corrosion rates due to passivation of the steel surface will allow for significantly higher spent fuel degradation rates. This is because, under anoxic conditions, the steel corrosion rate is directly proportional to the generation rate of H_2.
    - The amount of H_2 produced during passive steel corrosion is uncertain due to the lack of experimental data on steel corrosion rates in repository-relevant conditions where the Eh and pH are carefully controlled and monitored.
- The FMD model was applied to a series of in-package chemistry scenarios that were simulated using the reaction path code Geochemist's Workbench. The scenarios involve a breached spent fuel canister containing relevant masses of carbon-steel and 316 stainless steel. In the model, the steels were allowed to corrode in a groundwater typical of a crystalline rock repository. Various steel corrosion rates and starting oxidant concentrations were used and the Eh, pH and spent fuel corrosion rates were calculated.
    - It was found that the pH evolution is particularly sensitive to the starting O_2 concentration in the solution. If it was assumed that the solution contained ~10 mM O_2 (residual from canister emplacement and/or from the decomposition of radiolytic H_2O_2), the pH decreased from a starting value of pH 8.0 down to around pH 5.5, and then increased to pH 9.5 once the O_2 was consumed. The H^+ consuming and generating reactions responsible for this behavior are identified. The initial pH decrease does not occur when the starting O_2 concentration is in the μmolar range.
    - When the FMD model is applied using the steel titration model results, it shows that the fuel degradation rate will increase after carbon steel is consumed during the first few thousand years to decrease the H_2 concentration. This indicates that canisters containing relatively large amounts of carbon steel will likely provide low radionuclide source terms because they will maintain high H_2 concentrations for longer time periods.
- Comparison of the simple steel corrosion model currently used in the FMD model with recent electrochemical measurements indicates that the present model does not accurately represent long-term steel degradation. Electrochemical tests are needed to implement an improved steel passivation model in the FMD model by providing data sets with which the model can be calibrated for metals that will be present in the EBS and for key environmental variables. The model and test protocol developed at ANL for metal waste form degradation are probably suitable, but this should be verified.
- Simulations show how the presence of metals that corrode at different rates can extend the time over which H_2 generation will attenuate the fuel degradation rate. The materials used in the EBS can be selected to benefit the long-term performance of disposed fuel based on their measured corrosion behaviors and impacts on FMDM calculations.
- Preliminary electrochemical tests on the corrosion of Zircaloy-4 cladding suggest that this material will provide another important source of H_2 that is not currently accounted for in the FMDM. Including the H_2 generated during Zircaloy cladding corrosion on fuel degradation will benefit performance assessments. More experimental work is needed to confirm and conceptualize how

Zircaloy corrosion could influence spent fuel degradation rates and measure the dependence on environmental variables, particularly the chloride concentrations.

2.7 References

Bard, A., Faulkner, L., “Electrochemical methods: Fundamentals and Applications”, John Wiley and Sons, Inc., 2001

Buck E., Jerden, J., Ebert, W., Wittman, R., “Coupling the Mixed Potential and Radiolysis Models for Used Fuel Degradation,” FCRD-UFD-2013-000290, 2013.

Buck, E., Mausolf, E., McNamara, B., Soderquist, C., Schwantes, J., “Nanostructure of Metallic Particles in Light Water Reactor Used Nuclear,” *Journal of Nuclear Materials*, vol. 61, pp. 236–243, 2015.

Bethke, C.M., Yeakel, S. “The Geochemist's Workbench User's Guides, Version 10.0,” Aqueous Solutions LLC, Champaign, Illinois, 2014.

Caporuscio, F.A., Cheshire, M.C., Rearick, M.S., and Jove-Colon, C. “LANL Argillite EBS Experimental Program 2014,” FCRD-USED-2014-000491, 2014.

Caporuscio, F.A., Cheshire, M.C., Palaich, S., Norskog, K., Jove-Colon, C., “Argillite Disposal R&D-LANL 2015. Summary of baseline experiments for generic repository engineered barriers,” FCRD-UFD-2015-000356, LA-UR-15-26110, 2015.

Caporuscio, F.A., Norskog, K , Maner, J., Palaich S., Cheshire, M.C., Rearick, M.S., “LANL Argillite EBS Experimental Program 2016,” FCRD-UFD-2016-000620, LA-UR-16-25834, 2016.

CRWMS M&O 2003, “In-Package Chemistry Abstraction,” ANL-EBS-MD-000037 REV 02., Las Vegas, Nevada: CRWMS M&O. ACC: MOL.20000418.0818, 2003.

Cunnane, J.C., 2004, “CSNF Waste Form Degradation: Summary Abstraction,” Bechtel SAIC Company LLC Technical Report, ANL-EBS-MD-000015 REV 02, August 2004.

Debruyn, W., J. Dresselaers, Ph. Vermieren, J. Kelchtermans and H. Tas. “Corrosion of container and infrastructure materials under clay repository conditions,” Commission of the European Communities Report, EUR 13667 EN, 1991.

Ebert, W.L. and Gattu, V.K. “Production and Initial Testing of RAW-6 Materials,” FCRD-MRWFD-2016-000350, 2016.

Ebert, W.L., Gattu, V.K., and Indacochea, J.E. “A Degradation Model and Testing Protocol for Metallic Waste Forms,” NTRD-MRWFD-2017-000189, 2017. (in preparation).

Energy Solutions, “Generic Design for Small Standardized Transportation, Aging and Disposal Canister Systems,” DOE Advisory and Assistance Services Contract Task Order 18, UPDATED FINAL REPORT, May 14, 2015, 317 p.

Fillmore, D.L., “Parameter Selection for Department of Energy Spent Nuclear Fuel to be Used in the Yucca Mountain License Application, Idaho National Engineering and Environmental Laboratory Report,” INEEL/EXT-03-01032 Revision 1, October 2003

Gattu, V.K., Private Communication. February 18, 2017

Grambow, B., Bruno, J., Duro, L., Merino, J., Tamayo, A., Martin, C., Pepin, G., Schumacher, S., Smidt, O., Ferry, C., Jegou, C., Quiñones, J., Iglesias, E., Rodriguez Villagra, N., Nieto, J., Martínez-Esparza, A., Loida, A., Metz, V., Kienzler, B., Bracke, G., Pellegrini, D., Mathieu, Wasselin-Trupin, G., Serres, C., Wegen, D., Jonsson, M., Johnson, L., Lemmens, K., Liu, J., Spahiu, K., Ekeroth, E., Casas, I., de Pablo, J., Watson, C., Robinson, P., Hodgkinson, D., “Model Uncertainty for the Mechanism of Dissolution of Spent Fuel in Nuclear Waste Repository,” European Commission, Final Report for MICADO Project, EUR 24597, 2010.

JNC “Project to establish the scientific and technical basis for HLW disposal in Japan,” Japan Nuclear Cycle Development Institute, Supporting Report 2, Repository Design and Engineering Technology, 2000.

Jerden, J., Frey, K., Ebert, W., “Spent Fuel Matrix Degradation and Canister Corrosion: Quantifying the Effect of Hydrogen”, Report for Spent Fuel and Waste Science and Technology Project, Report #: SFWD-SFWST-2017-000039, February 28, 2017

Jerden J. Copple J., Frey K. Ebert W., “Prototype Fortran Version of the Mixed Potential Process Model for Used Fuel Degradation,” M4FT-15AN0806012, October 15, 2014

Jerden J., Hammond, G., Copple J., Cruse, T., Ebert W., “Fuel Matrix Degradation Model: Integration with Performance Assessment and Canister Corrosion Model Development,” FCRD-UFD-2015-000550, July 21, 2015

Jerden J. Frey K. Ebert W., “A Multiphase Interfacial Model for the Dissolution of Spent Nuclear Fuel, *Journal of Nuclear Materials*, vol. 462, pp. 135–146, 2015.

Johnson J, Anderson F, Parkhurst DL. Database thermo.com.V8.R6.230, Rev 1.11. Lawrence Livermore National Laboratory, Livermore, California; 2000

Johnson, L.H. and F. King, “Canister options for the disposal of spent fuel,” Nagra Technical Report 02-11, 2003.

Carter, J., Luptak, A., Gastelum, J., Stockman, C., Miller, A., “Fuel Cycle Potential Waste Inventory for Disposition,” FCR&D-USED-2010-000031 Rev 5, July 2012

Kaesche, H., “Metallic Corrosion,” National Association of Corrosion Engineers International, Houston, TX, 1985.

King F. and Kolar M., “An Improved C-Steel Corrosion Model For the Mixed-Potential Model for Used Fuel Dissolution (MPM Version 1.4),” Ontario Hydro, Nuclear Waste Management Division Report No: 06619-REP-01300-l0027-R00, 2001.

King F. and Kolar M., “The Mixed-Potential Model for UO_2 Dissolution MPM Versions V1.3 and V1.4,” Ontario Hydro, Nuclear Waste Management Division Report No. 06819-REP-01200-10104 R00, 2003.

King, F., “Overview of a Carbon Steel Container Corrosion Model for a Deep Geological Repository in Sedimentary Rock,” Nuclear Waste Management Organization Report TR-2007-01, March 2007, 71 p.

Kleykamp, H., “Constitution and Thermodynamics of the Mo-Ru, Mo-Pd, Ru-Pd and Mo-Ru-Pd Systems,” *Journal of Nuclear Materials*, vol. 167, pp. 49-63, 1989.

Laaksoharju M., Smellie, J., Tullborg, E-L., Gimeno, M., Hallbek, L., Molinero, J., Waber, N., “Bedrock hydrogeochemistry Forsmark site descriptive modeling SDM-Site Forsmark,” SKB R-Report (R-08-47), SKB, Stockholm, Sweden, 2008.

Lanza, F. and C. Ronsecco, “Corrosion of low-carbon steel in clay and sea sediments,” Commission of the European Communities Report EUR 10522 EN, 1986.

Mariner, P., Gardner, P., Hammond, G, Sevougian, D, Stein E., “Application of Generic Disposal System Models,” FCRD-UFD-2015-000126, SAND2015-10037, September 22, 2015, 209 p.

Marsh, G.P. and K.J. Taylor, “An assessment of carbon steel containers for radioactive waste disposal,” Corrosion Science vol. 28, pp. 289-320, 1988

Marsh, G.P., K.J. Taylor, S.M. Sharland, and P.W. Tasker, “An approach for evaluating the general and localized corrosion of carbon-steel containers for nuclear waste disposal,” Mat. Res. Soc. Symp. Proc. Vol. 84, Materials Research Society, Pittsburgh, PA, p. 227-238, 1987.

Marsh, G.P., A.H. Harker, and K.J. Taylor, “Corrosion of carbon steel nuclear waste containers in marine sediment,” Corrosion vol. 45, pp. 579-589, 1989.

Metz V., Loida A., Bohnert E., Schild D., Dardenne K., “Effects of Hydrogen and Bromide on the Corrosion of Spent Nuclear Fuel and γ-irradiated UO_2(s) in NaCl Brine,” *Radiochim. Acta* 96, 637–648, 2008.

Miller, W.M., W.R. Alexander, N.A. Chapman, I.G. McKinley, and J.A.T. Smellie, “Natural analogue studies in the geological disposal of radioactive wastes,” Studies in Environmental Sciences 57, Elsevier, Amsterdam (also Nagra Technical Report NTB 93-03), 1994.

Ollila, K., “Dissolution of Unirradiated UO_2 and UO_2 Doped with ^{233}U in Low- and High-Ionic-Strength NaCl Under Anoxic and Reducing Conditions,” Posiva Working Report 2008-50, 2008.

Pastina B., and LaVerne, J. A. "Effect of Molecular Hydrogen on Hydrogen Peroxide in Water Radiolysis", Journal of Physical Chemistry A 105, 9316-9322, 2001.

Peat, R. S. Brabon, P.A.H. Fennell, A.P. Rance, and N.R. Smart, “Investigation of Eh, pH and corrosion potential of steel in anoxic groundwater,” SKB Technical Report TR-01-01, 2001.

Posiva, “Safety case for the disposal of spent nuclear fuel at Olkiluoto – Design Basis 2012,” Eurajoki, Finland: Posiva Oy. POSIVA 2012-03. ISBN 978-951-652-184-1, 2012.

Radulescu, G., “Repository Science/Criticality Analysis,” Oak Ridge National Laboratory, Reactor and Nuclear Systems Division, FTOR11UF0334, ORNL/LTR-2011, Oak Ridge National Laboratory, Oak Ridge, TN., 2011.

Röllin S., Spahiu K., Eklunda U., “Determination of Dissolution Rates of Spent Fuel in Carbonate Solutions Under Different Redox Conditions with a Flow-through Experiment,” *Journal of Nuclear Materials*, vol. 297, pp. 231–243, 2001.

Shoesmith, D., “The Role of Dissolved Hydrogen on the Corrosion/Dissolution of Spent Nuclear Fuel,” Nuclear Waste Management Organization, Toronto, Ontario, Canada, TR-2008-19, November 2008.

Simpson, J.P. and P.-H. Valloton, “Experiments on container materials for Swiss high-level waste disposal projects, Part III,” Nagra Technical Report 86-25, 1986.

Simpson, J.P. 1989, “Experiments on canister materials for Swiss high- level waste disposal projects, Part IV. National Cooperative for the Storage of Radioactive Waste Technical Report,” NAGRA-NTB-89-19, 1989.

Smart, N.R., D.J. Blackwood, and L.O. Werme, “The anaerobic corrosion of carbon steel and cast iron in artificial groundwaters,” SKB Technical Report TR-01-22, 2001.

Smart, N.R., D.J. Blackwood, and L.O. Werme, “Anaerobic corrosion of carbon steel and cast iron in artificial groundwaters: Part 1 – electrochemical aspects,” Corrosion vol. 58, pp.547-559, 2002.

Wang Y. et al., “Used Fuel Disposal in Crystalline Rocks: Status and FY14 Progress,” FCRD-UFD-2014-000060, SAND2014, Sandia National Laboratories, Albuquerque, NM., 2014.

Wu, L., Qina, Z., Shoesmith, D.W., “An improved model for the corrosion of used nuclear fuel inside a failed waste container under permanent disposal conditions,” Corrosion Science vol. 84, pp.85–95, 2014.

3. NONLINEAR DYNAMICS AND INSTABILITY OF AQUEOUS DISSOLUTION OF SILICATE GLASSES AND MINERALS

3.1 Introduction

Chemical weathering of silicate glasses and minerals plays a critical role in global biogeochemical cycles and climate evolution (Berner and Kothavala, 2001; Brady, 1991). Silicate materials have also been used for numerous industrial, biomedical and environmental applications (Cailleteau et al., 2008; Gin, 2014). Borosilicate glasses have been proposed as a waste form for nuclear waste disposal, and the durability of these materials is a key physical property that needs to be evaluated for waste isolation (Gin, 2014). Despite decades of intensive research, the mechanism controlling aqueous dissolution of these materials still remains controversial (Gin, 2014; Dran et al., 1986; Gin et al., 2015; Putnis, 2015). The debate has centered on the possible formation of a leached surface layer and its role in material dissolution. A silica-rich surface layer has been detected on both manufactured and natural silicate materials (Dran et al., 1986; Doremus, 1975; Petit et al.; 1990). Alkali and alkaline cations in this layer are partially leached out and replaced by hydrogen ions during dissolution through a coupled diffusion-ion exchange process. The outer part of the leached layer may continuously be subjected to *in-situ* silicate network repolymerization and reorganization, leading to the formation of a dense silica gel layer that may passivate a dissolving solid surface and result in a dramatic drop in the dissolution rate (Cailleteau et al., 2008; Gin, 2015). However, this long-held view has recently been challenged by observations of extremely sharp interfaces between altered rims and pristine material domains (Putnis, 2015; Hellmann et al., 2015; Ruiz-Agudo et al., 2012), suggesting that material corrosion may undergo a direct dissolution-precipitation process (Putnis, 2015; Hellmann et al., 2015). This argument is supported by isotope studies. Isotopes such as ^{18}O and ^{26}Mg artificially introduced into the contacted solution tend to enrich in the altered rim of a silicate sample with no observable sigmoid-shape diffusion profile toward the unaltered core (Geisler et al., 2010). Furthermore, oscillatory zonings are often observed in the altered rim of a silicate sample (Figure 3-1A) (Putnis, 2015; Geisler et al., 2010; Dohmen et al., 2013; Jeong and Sohn, 2011). Such oscillatory behaviors are difficult to reconcile with the traditional leached layer concept (Putnis, 2015).

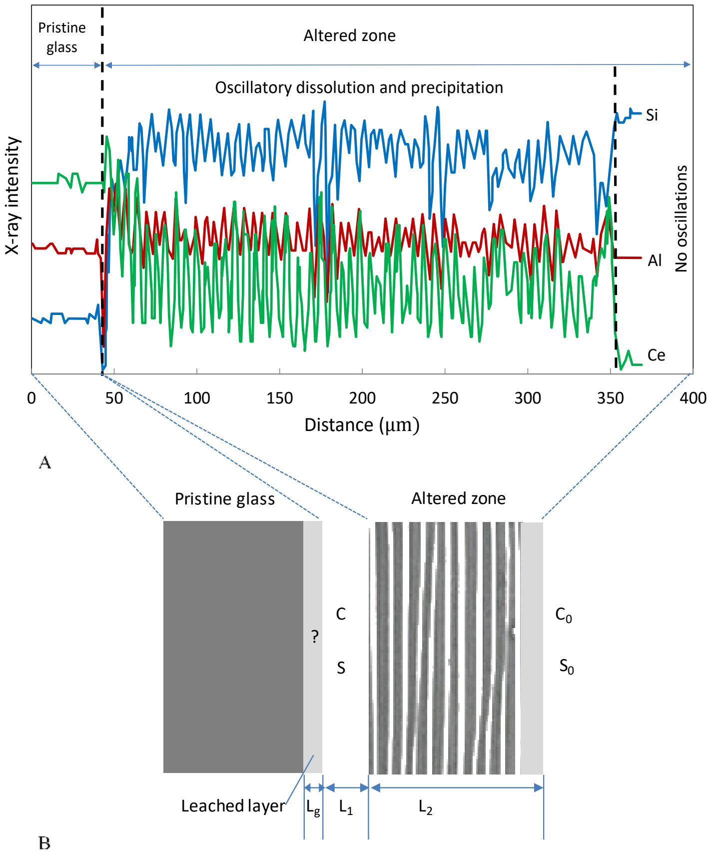

Figure 3-1. Oscillatory borosilicate glass dissolution and mineral precipitation as indicated by compositional zoning in an alteration zone (A) and schematic representation of modeling system (B). The actual Al and Ce contents are in the ranges of 0 – 0.4 wt% and 0 – 2.4 wt%, respectively. Data in (A) were taken from Geisler et al. (2010).

The contradicting observations clearly indicate the complexity of silicate material dissolution and call for a new theory to account for such complexity. The new theory must also be able to explain the multiple stages of a glass dissolution process (Figure 3-2A). As a silicate glass corrodes, the corrosion rate generally decreases, due to the reduction in chemical affinity for silicate network dissolution and the formation of a passivating layer on glass surfaces (Cailleteau et al., 2008; Gin, 2014; Gin et al., 2015). Interestingly, a sharp increase in corrosion rate after a long period of rate drop has been observed in silicate glass dissolution experiments (Neeway et al., 2014; Fournier et al., 2014), posing a serious concern about our ability to predict the long-term performance of borosilicate glasses as a durable waste form for nuclear waste disposal. The underlying mechanism for this rate resumption remains unknown (Gin, 2015).

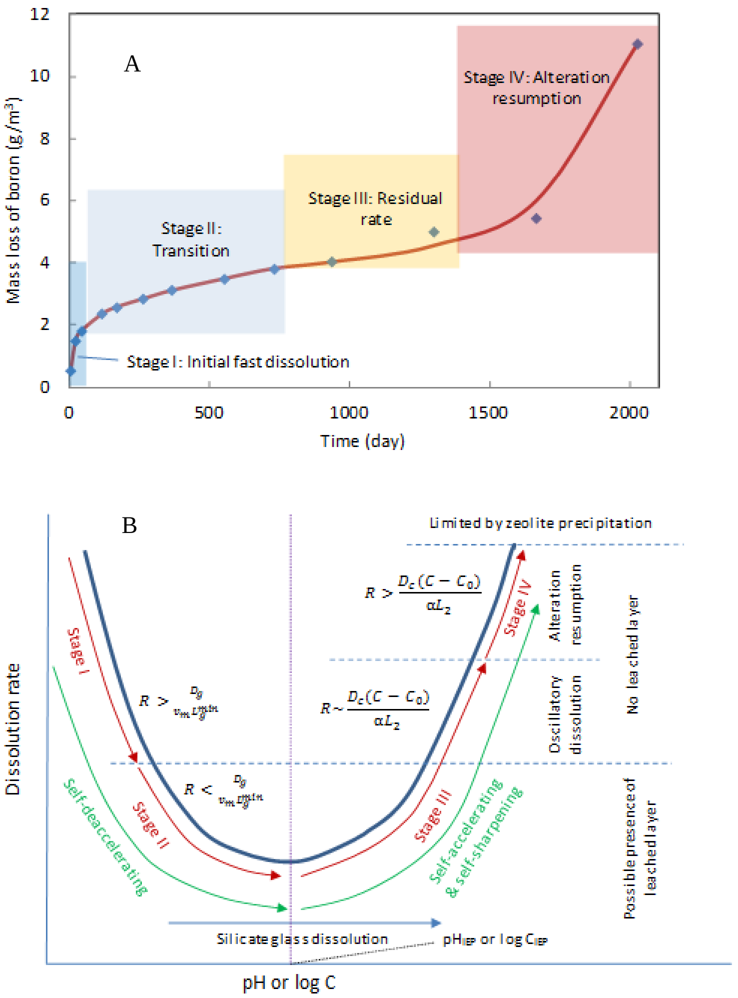

Figure 3-2. Evolution of silicate glass dissolution (A) and its nonlinear dynamics (B). A positive feedback between glass dissolution and solution chemistry may lead to oscillatory glass dissolution, interface sharpening and alteration resumption at the late stage of glass corrosion. Note that this feedback becomes effective only for the base leg of the dissolution curve (B). IEP: Isoelectric point. L_g^{min} is the minimum spatial resolution for a microanalysis and imaging technique for characterizing the sharpness of a reaction front (≤ 1nm). The data points in (A) were taken from Neeway et al. (2014).

3.2 Results

Our research started with addressing the issue of oscillatory zonings. Oscillatory zonings on archeologic glass samples have been attributed to seasonal fluctuations in temperature or hydrologic conditions (Brill and Hood, 1961). But this explanation is apparently not applicable to the oscillatory zonings produced in laboratory experiments, which are usually conducted under static conditions with no externally imposed periodic changes on experimental conditions (Geislaer et al.; 2010; Dohmen et al., 2013). Interestingly, temporal oscillations in silicate dissolution have been observed directly in laboratory experiments Falmon, 1996; Barkatt et a., 1993; Leturcq et al., 1999). Thus, the observed oscillatory dissolution behaviors must be self-organizational (Dohmen et al, 2013), i.e., they must originate from the internal dynamics of solid-water interactions. Self-organization requires a positive feedback among physical and chemical processes involved in a system (Nicolis and Prigogine, 1977; Wang and Merino, 1995). In silicate dissolution, the following positive feedback may operate: As a silicate material corrodes, cations (notably Na^+) in the material are released into the solution, resulting in a high cation concentration and pH at the reaction front ($\Delta[OH^-] \approx \Delta[\text{cation}]$ for charge balance). Under alkaline conditions, silicate dissolution is catalyzed by both hydroxyl groups and cations (Stumm, 1992; Wolery et al., 1996; Icenhower and Dove, 2000). The resultant high pH and cation concentration enhance silicate material dissolution, which in turn accelerates cation release. A silicate dissolution rate usually has a V-shape dependence on pH (Stumm, 1992). The proposed self-accelerating mechanism operates only under alkaline conditions, that is, on the right branch of the rate curve in Figure 3-2B.

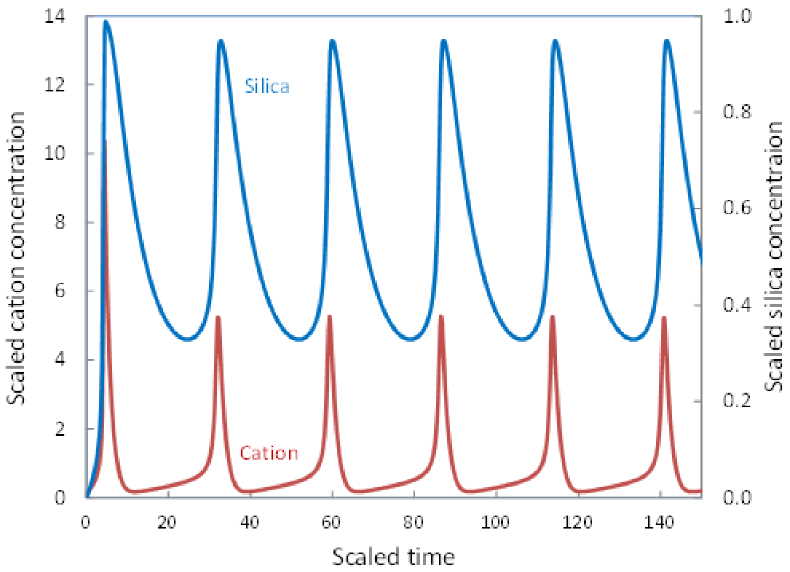

Figure 3. Predicted concentration oscillations at the glass dissolution interface. Parameter values used in the simulation**:** $\alpha = 0.4$, $\gamma = 0.9$, $n = 2.0$, $\beta = 5.0$, $\theta = 40$, $\eta = 2$, $\kappa = 2.0$, $c_0 = s_0 = s_p^e = 0.001$ (see Methods for parameter definitions). Silica precipitation rate and therefore the Si content in the altered zone oscillates in phase with the dissolved silica concentration [Equation (3-5)]. The amounts of impurities incorporated into the precipitated silica are expected to be proportional to both the concentrations of the impurities (roughly mimicked by the cation concentration shown in the figure) and the silica precipitation rate (Wang and Merino, 1995). The proposed model thus predicts that impurity contents in an altered zone of a silicate material oscillate precisely in phase with each other but slightly out of phase with silica content, as observed (Geisler et al., 2010) (Figure 3-1A).

To test the concept, we formulated a nonlinear dynamic model for glass dissolution (see equations and nomenclatures in Section 3.4 Methods). Numerical simulations of the model show that the proposed mechanism generates oscillatory dissolution within a reasonable parameter space (Figure 3-3). The equilibrium silica concentration for glass dissolution is estimated to be ~ 10^{-3} to 10^{-2} M (Gin et al., 2012). The cation concentration at the isoelectric point (IEP) (C_{IEP}) (Figure 3-2B) can vary widely depending on experimental or environmental conditions; a range of 10^{-4} to 10^{-2} M could be a reasonable choice Falmon, 1996). Accordingly, the concentration ratio between silica and cation (θ) in Fig. 3A varies from 1 to 100. Oscillatory dissolution occurs over a wide range of θ but only within a narrow range (0.8 to 3.0) of γ. The narrow γ range implies that self-organization requires the dissolution rate and the mass exchange rate to be on the same order of magnitude so that the two processes can interplay with each other. At the beginning of the dissolution, no altered zone is developed and the dissolution process is overwhelmed by mass exchange. Thus, γ always starts from a low value, and then increases as the alteration product builds up, leading to a transition from a plain altered zone to an oscillatory zone (Figure 3-4A), as observed in leaching experiments (Geisler et al., 2010; Dohmen et al, 2013). Oscillatory zoning thus tends to emerge at a late stage of a dissolution process. Self-organization also requires the order of the dissolution reaction with respect to cation to be higher than 1.4 (Figure 3-4B). The dissolution rate is known to be proportional to $[\equiv OH^-]^2$ (Wieland et al., 1988; Wirth and Gieskes, 1979), where $\equiv OH^-$ is the adsorbed hydroxyls. At a low surface coverage, $[\equiv OH^-] \propto [OH^-]$. Considering the additional catalytic effect of cations through ionic strength (Icenhower and Dove, 2000), the reaction order n is estimated to be ~ 1.0 to 2.5. Parameter α is constrained between 0.3 and 0.6 from glass compositions (Petit et al., 1990; Geisler et al., 2010; Barkatt et al., 1993). Oscillatory dissolution is thus expected to be relatively common in silicate material corrosion (Figure 3-4).

The time scale for each oscillation (T_b) is estimated to be (See Section 3.4 methods):

$$T_b \approx \tau_b T = \tau_b \frac{L_1 L_2}{D_c} \tag{3-1}$$

where τ_b is the scaled time for each oscillation, estimated to be 10 – 50 from the numerical simulations (Figure 3-3). A gap of micrometers has been observed between the pristine glass surface and the altered rim (Dohmen et al, 2013). If we take this gap as the boundary layer, the thicknesses of the boundary layer (L_1) would be on the order of ~ 1 to 10 μm. The thickness of the altered zone (L_2) is estimated to be on the order of ~10 to 100 μm, based on microstructural analyses of leached silicate samples (Geisler et al., 2010; Dohmen et al., 2013). The altered zone thickness is expected to be bounded by the thickness of the plain altered zone formed prior to oscillatory dissolution and the thickness of the overall altered zone. The diffusion coefficient (D_c) for a mobile species in the altered zone in a reorganized dense silica gel could be as low as 6×10^{-15} cm^2/s (Gin et al., 2015). As discussed below, such a dense layer is unlikely to form under the conditions for oscillatory dissolution. The actual altered zone could be porous (Dohmen et al., 2013) with a much higher diffusion coefficient. D_c is thus chosen to be 10^{-13} to 10^{-11} cm^2/s. From Equation (3-1), the time scale for each oscillation is estimated to range from hours to years, consistent with observations (Geisler et al., 2010; Dohmen et al., 2013; Brill and Hood, 1961). It is interesting to note that an archeologic study of ancient Roman glass artifacts show that each oscillatory layer might have formed over a time scale of a year (Brill and Hood, 1961). Similarly, the thickness of each band (L_b) can be estimated by (see Section 3.4 Methods):

$$L_b \approx \gamma v_m C_{\mathrm{IEP}}(1 + \beta \bar{c}^n) L_1 \tag{3-2}$$

where $\bar{c}$ is a typical scaled cation concentration chosen to be ~ 10 based on the numerical simulations; and v_m is the volume of pristine solid containing 1 mole of SiO$_2$, estimated to be ~30 cm^3/mole (Robie et al., 1978). For $\gamma \approx 1.0$, $\beta \approx 5$ (Figures 3-3 and 3-4) and $C_{IEP} = 10^{-4}$ to 10^{-2} M (see the discussion above), L_b is estimated to range from $0.1L_1$ to a few L_1 units, that is, sub-micrometers to tens of micrometers, consistent with observations (Hellmann et al., 2015; Dohmen et al., 2013).

The proposed mechanism provides a logical explanation for the occurrence of leached layers. The evolution of the leached layer thickness (L_g) is governed by (see Section 3-4 Methods for nomenclatures):

$$\frac{dL_g}{dt} \approx \frac{D_g}{L_g} - R v_m = \frac{D_g}{L_g} - v_m k_d C_{\mathrm{IEP}}(S_d^e - S)\left[1 + \beta\left(\frac{D_g L_2}{C_{\mathrm{IEP}} L_g}\right)^n\right] \tag{3-3}$$

where D_g is the cation diffusion coefficient in the leached layer. As material dissolution pushes the chemistry of the boundary layer toward the right branch of the dissolution curve in Fig. 2B and the reaction product builds up (increasing L_2), the second term in the far right-hand side would eventually overtake the first term. For reaction order $n > 1$, the leached layer then becomes progressively thinner (i.e., a smaller L_g makes the L_g decrease even faster) – a self-sharpening mechanism for the formation of an extremely sharp interface between a pristine silicate material and the surrounding altered rim (Hellmann et al., 2015;

Dohmen et al., 2013). Leached layers are thus transient and tend to form at an early stage of a dissolution process under mildly acid to neutral conditions (Figure 3-2B).

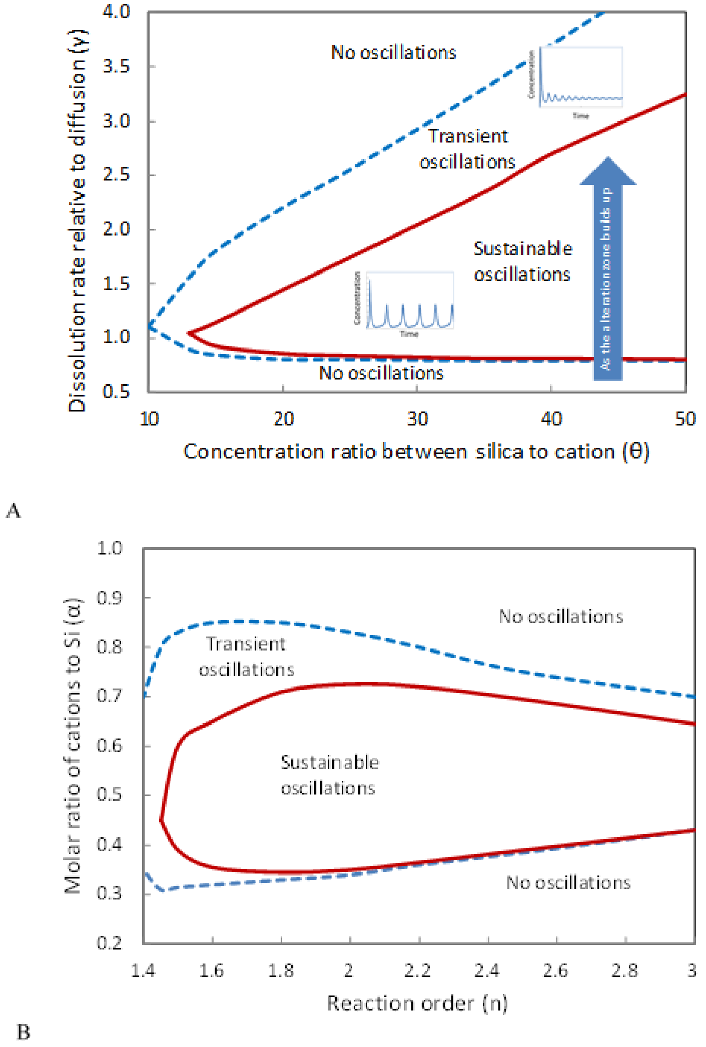

Figure 3-4. Behavior diagrams for silicate glass dissolution. As the alteration zone builds up, the dissolution transits from a no-oscillation state to an oscillation state as observed[9]. Parameter values used in the calculation: (A) $\alpha = 0.4$, $n = 2.0$, $\beta = 0.9$, $\eta = 2$, $\kappa = 2.0$, $c_0 = s_0 = s_p^e = 0.001$; (B) $\gamma = 1.0$, $n = 2.0$, $\beta = 1.0$, $\theta = 40$, $\kappa = 2.0$, $c_0 = s_0 = s_p^e = 0.001$ (see Section 3-4 Methods for parameter definitions).

The stage of alteration resumption is also a natural consequence of the self-accelerating mechanism. Assume that glass dissolution starts on the lower part of the dissolution curve in Figure 3-2B. Due to a low dissolution rate, a leached layer forms. As the dissolution proceeds, the dissolution rate increases as more cations accumulate in the boundary layer, leading to disappearance of the leached layer. When the dissolution rate becomes on the same order of magnitude as the mass exchange rate with the bulk solution, oscillatory dissolution may emerge. Eventually, the dissolution rate overtakes the mass exchange rate, leading to a "runaway" situation with a sharp increase in the cation concentration at the interface and therefore the dissolution rate. The sharp increase in both cation concentration and pH inevitably causes zeolite precipitation (Figure 3-5). Contradicting the existing view that the zeolite precipitation causes alteration resumption (Gin et al., 2012), our work suggests that zeolite formation is a consequence of the alteration resumption process, consistent with experimental observations that adding initial amount of zeolite (analcime) had no effect on glass alteration (Furnier et al., 2013). The precipitation of zeolite would eventually limit further increase in the reaction rate by removing cations from the boundary layer (Figure 3-5). Thus, the resumption rate may represent a long-term rate for silicate glass dissolution. Whether or how soon the alteration resumption occurs apparently depends on glass composition as well as the chemistry of the contacted solution. Thus, the durability of a glass can be improved by choosing an appropriate glass composition such that a proper alteration product will form which will limit the dissolution to the lower part of the dissolution curve (Figure 3-2B). Therefore, in principle, it is possible to formulate a glass composition that can adapt to a specific environmental condition to achieve optimal performance in terms of glass durability.

3.3 Discussion

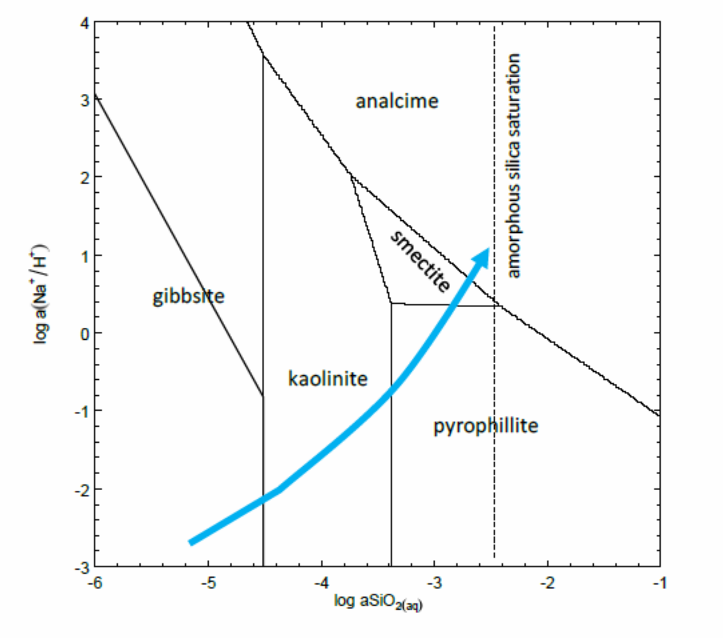

Figure 3-5. Evolution of water chemistry and mineral precipitation at a reaction front of silicate material dissolution.

One aspect to be considered in glass formulation is the content of dissolvable anionic components such as boron in a borosilicate glass. The release of boric acid from glass dissolution tends to compensate the aforementioned positive feedback between cation release and cation-enhanced dissolution kinetics. This effect can be factored into our model through an effective cation concentration [effective cation], defined as [total dissolved cations] – [total dissolved anions] with proper charge corrections. In this case, $\Delta[OH^-] \approx \Delta[\text{effective cation}]$. The release of dissolved anionic species would thus push the dissolution curve in Fig. 2B toward the right and therefore delay the transition of dissolution stages. In this sense, the inclusion of boron component in a glass formulation may enhance the durability of the glass. Similarly, any component from the contacted solution that can change the pH at the dissolution front through a reaction should also be taken into account. For instance, in glass alteration in seawater, Mg^{2+} from seawater can react with glass components to form Mg-smectite (Verney-Carron et al., 2010):

$$0.33Al^{3+} + 3.65Mg^{2+} + 3.67SiO_2(aq) + 4.66H_2O \rightarrow Mg_{3.65}Al_{0.33}Si_{3.67}O_{10}(OH)_2 + 7.32H^+ \quad (3\text{-}4)$$

The H^+ produced from this reaction tends to counter the pH rise caused by cation release from glass dissolution. Smectite precipitation may thus play the same role as zeolite precipitation in limiting the dissolution rate "runaway" at the alteration resumption stage (Figure 3-2B). It should be pointed out that the model presented here is only a first-order approximation to an actual complex dissolution process. A detailed evaluation of the potential impacts of material composition and water chemistry on dissolution kinetics requires an explicit consideration of chemical speciation and secondary mineral formation, which is beyond the scope of this paper but certainly an interesting topic for future research.

Temperature can play an important role in controlling the transition from one dissolution mode to another. The activation energy for aqueous ion diffusion typically ranges from 15 to 20 kJ/mole (Toryanik and Kisel'nik, 1969) whereas the activation energy for glass dissolution is ~ 86 kJ/mole (Verney-Carron et al., 2010). Assume that glass dissolution starts at the lower part of the dissolution curve in Figure 3-2B. As the temperature increases, the dissolution rate accelerates faster than the diffusion rate and eventually overtakes the latter, leading to oscillatory dissolution and possibly alteration rate resumption (Figure 3-2B). Thus, increasing temperature may enhance the chance for oscillatory zoning and alteration resumption. This may be a reason why the most extensive set of oscillatory zoning was observed in the experiment conducted at an elevated temperature (150 °C) (Geisler et al., 2010). Interestingly, alteration resumption has not been observed for borosilicate glasses in laboratory experiments at pH < 10 and temperature < 90 °C (Fournier et al., 2013). In general, based on our model, a low temperature, high dissolvable anion content, or low solution pH tends to delay or inhibit the occurrence of oscillatory zoning and alteration rate resumption.

This proposed self-accelerating mechanism may cause the instability of a dissolution front: A higher dissolution rate at one surface location would lead to a higher accumulation of cations and therefore a higher dissolution rate at that location, which would in turn promote the local dissolution. This positive feedback may lead to the formation of a wavy dissolution front (Wang and Merino, 1995). Interestingly, such wavy fronts are observed in silicate glass corrosion (Dohmen et al., 2013). The development of a wavy alteration front coupled with the oscillatory zoning may be responsible for the formation of growth rings on the surface of corroded Roman glasses (Dal Bianco et al., 2004). Growth rings are concentric banding patterns with a typical size of ~ 1 mm; the patterns are roughly equally spaced with each consisting of ~ 190 concentric rings in average; and those patterns seem to have grown simultaneously since the interface between two neighboring patterns is a straight line (Dal Bianco et al., 2004). Based on the concept proposed here, growth rings are thus the geometric intercepts of wavy repetitive alteration zones with a view plane.

Finally, the proposed mechanism provides a new perspective for predicting silicate mineral weathering rates in natural systems. The pH and cation concentration of water at a dissolution interface could be much higher than those in the bulk solution (e.g. extractable pore water). Using bulk pore water chemistry for prediction, as done currently, may significantly underestimate mineral reaction rates. Similarly, silicate mineral weathering in environments with limited water availability, for example, in semiarid to arid regions, may be more dynamic than previously thought. The proposed mechanism can create local high pH microenvironments in rocks and thus enhance CO_2 dissolution and mineralization, a mechanism probably responsible for continuous large CO_2 uptake by desert soils (Wohlfahrt et al., 2002).

3.4 Methods

The modeling system for oscillatory silicate glass dissolution is shown in Figure 3-1B. It consists of three physical domains: a pristine glass domain, a boundary layer, and an alteration zone. The leached layer in the figure is not included, because it is likely to be absent in oscillatory dissolution due to the self-sharpening effect of a reaction front as discussed above. The dynamics of aqueous silicate material dissolution can be described by:

$$L_1 \frac{dC'}{dt} = \alpha k_d C_{\mathrm{IEP}} \left[1 + \beta \left(\frac{C'}{C_{\mathrm{IEP}}}\right)^n\right] (S_d^e - S') - \frac{D_c}{L_2}(C' - C_0) \tag{3-4}$$

$$L_1 \frac{dS'}{dt} = \alpha k_d C_{\mathrm{IEP}} \left[1 + \beta \left(\frac{C'}{C_{\mathrm{IEP}}}\right)^n\right] (S_d^e - S') - \frac{D_s}{L_2}(S' - S_0) - k_p(S' - S_p^e) \tag{3-5}$$

where

C' – Cation concentration within the boundary layer
C_0 – Cation concentration in the bulk solution (outside the altered zone)
D_c – Diffusion coefficient of cations in the altered zone
D_s – Diffusion coefficient of dissolved silica in the altered zone
L_1 – Thickness of the boundary layer at the dissolution interface
L_2 – Thickness of the altered zone
k_d – Reaction rate constant for silicate material dissolution
k_p – Reaction rate constant for silica mineral precipitation
n – Order of silicate dissolution reaction with respect to cation
S' – Silica concentration within the boundary layer
S_0 – Silica concentration in the bulk solution

S_d^e – Equilibrium silica concentration for material dissolution
S_p^e – Equilibrium silica concentration for silica precipitation
t – Time
α – Molar ratio of cations (mainly Na^+) to Si^{4+} in the pristine silicate material
β – Positive constant characterizing the catalytic effect of cations on silicate material dissolution

The first terms on the right-hand side of Equations (3-4) and (3-5) represent the mass accumulation due to silicate material dissolution. The factor $\left[1+\beta\left(\frac{C\prime}{C_{IEP}}\right)^n\right]$ is introduced to capture the catalytic effect of cations on the dissolution of silicate network in the materials. We here only consider silicate material dissolution under alkaline conditions, that is, on the right branch of the dissolution curve in Figure 3-2B. The dissolution reaction is assumed to be first order with respect to the dissolved silica concentration (Gin et al., 2012). The other terms on the right-hand side of the equations represent the mass exchange between the boundary layer and the bulk solution or the mass consumption by silica mineral precipitation.

Equations (3-4) and (3-5) can then be cast into the following dimensionless equations:

$$\frac{dc}{d\tau} = \alpha\gamma(1+\beta c^n)(1-s) - (c - c_0) \qquad (3\text{-}6)$$

$$\theta\frac{ds}{d\tau} = \gamma(1+\beta c^n)(1-s) - \eta(s - s_0) - \kappa(s - s_p) \qquad (3\text{-}7)$$

with the following scaling factors:

$$\begin{array}{lll} c = \dfrac{C'}{C_{\mathrm{IEP}}} & s = \dfrac{S'}{S_d^e} & \tau = \dfrac{t}{T} \\ T = \dfrac{L_1 L_2}{D_c} & \gamma = \dfrac{k_d S_d^e L_2}{D_c} & \theta = \dfrac{S_d^e}{C_{\mathrm{IEP}}} \\ \eta = \dfrac{D_s S_d^e}{D_c C_{\mathrm{IEP}}} & \kappa = \dfrac{k_p S_d^e L_2}{D_c C_{\mathrm{IEP}}} & \end{array} \qquad (3\text{-}8)$$

where

c - Scaled silica concentration
s – Scaled silica concentrations
T – Characteristic time scale of the system
γ – Scaled glass dissolution rate relative to the rate of diffusional mass exchange between the boundary layer and the bulk solution
η – Scaled diffusivity ratio between silica and cation
θ – Characteristic concentration ratio between silica and cation
κ – Scaled rate constant for silica mineral precipitation
τ – Scaled time

Equations (3-6) and (3-7) were solved using an arbitrary-precision ordinary differential equation solver from python package mpmath (http://mpmath.org/) and Mathematica (Wolfram Research Inc. 2015). The behavior diagrams in Figure 4 were constructed by numerical simulations.

3.5 References

Barkatt, A., Sang, J. C. & Jakubik, R. F. Oscillations in the dissolution kinetics of silicate glass in tri-buffered aqueous media. *J. Non-Crystalline Solids* **155**, 141-148 (1993).

Berner, R. A. & Kothavala, Z. GEOCARB III: A revised model of atmospheric CO_2 over Phanerozoic time. *Am. J. Sci.* **301**, 182-204 (2001).

Brady, P. V. The effect of silicate weathering on global temperature and atmospheric CO_2. *J. Geophysical Lett.* **96**, 18101-18106 (1991).

Brill, R. H. & Hood, H. P. A new method for dating ancient glass. *Nature* **189**, 12-14 (1961).

Cailleteau, C. et al. Insight into silicate-glass corrosion mechanisms. *Nature Materials* **7**, 978-983 (2008).

Dal Bianco, B. et al. Glasses on the seabed: surface study of chemical corrosion in sunken Roman glasses. *J. Non-Crystalline Solids* **343**, 91-100 (2004).

Dohmen, L. et al. Pattern formation in silicate glass corrosion zones. *Int. J. Appl. Glass Sci.* **4**, 357-370 (2013).

Doremus, R. H. Interdiffusion of hydrogen and alkali ions in a glass surface. *J. Non-Crystalline Solids* **19**, 137-144 (1975).

Dran, J.-C., Petit, J.-C., Brousse, C. Mechanism of aqueous dissolution of silicate glasses yield by fission tracks. *Nature* **319**, 485-487 (1986).

Falmon, J. Oscillatory silicon and aluminum aqueous concentrations during experimental aluminosilicate weathering. *Geochim. Cosmochim. Acta* **60**, 2901-2907 (1996).

Fournier, M., Frugier, P. & Gin, S. Effect of zeolite formation on borosilicate glass dissolution kinetics. *Procedia Earth Planet. Sci.* **7**, 264-267 (2013).

Fournier, M., Frugier, P. & Gin, S. Resumption of alteration at high temperature and pH: rates measurements and comparison with initial rates. *Procedia Materials Sci.* **7**, 202-208 (2014).

Geisler, T. et al. Aqueous corrosion of borosilicate glass under acidic conditions: A new corrosion mechanism. *J. Non-Crystalline Solids* **356**, 1458-1465 (2010).

Gin, S. Open scientific questions about nuclear glass corrosion. *Procedia Materials Sci.* **7**, 163-171 (2014).

Gin, S. et al. Effect of composition on the short-term dissolution rates of ten borosilicate glasses of increasing complexity from 3 to 30 oxides. *J. Non-Crystalline Solids* **358**, 2559-2570 (2012).

Gin, S. et al. Origin and consequences of silicate glass passivation by surface layers. *Nature Communications* **6**, 6360 doi: 10.1038/ncomms7360 (2015).

Hellmann, R. et al. Nanometre-scale evidence for interfacial dissolution-reprecipitation control of silicate glass corrosion. *Nature Materials* **14**, 307-311 (2015).

Icenhower, J. P. & Dove, P. M. The dissolution kinetics of amorphous silica into sodium chlorite solutions: Effects of temperature and ionic strength. *Geochim. Cosmochim. Acta* **64**, 4193-4203 (2000).

Jeong, G. Y. & Sohn, Y. K. Mineralogy and microtextures of basaltic glass alteration in hyaloastite, Jeju Island, Korea. *J. Analytical Sci. Tech.* **2**, 12-22 (2011).

Leturcq, G., Berger, G., Advocat, T. & Vernaz, E. Initial and long-term dissolution rates of aluminosilicate glasses enriched with Ti, Zr and Nd. *Chemical Geology* **160**, 39-62 (1999).

Neeway J. J. et al. *A Strategy to Conduct an Analysis of the Long-Term Performance of Low-Activity Waste Glass in a Shallow Subsurface Disposal System at Hanford*. Pacific Northwest National Laboratory, Richland, Washington, PNNL-23503 (2014).

Nicolis, G. & Prigogine, I. *Self-organization in Non-Equilibrium Systems* (Wiley, New York, 1977).

Petit, J.-C. et al. Hydrated-layer formation during dissolution of complex silicate glasses and minerals. *Geochim. Cosmochim. Acta* **54**, 1941-1955 (1990).

Putnis, A. Sharpened interface. *Nature Materials* **14**, 261-261 (2015).

Robie, R. A., Hemingway, B. S. & Fisher, J. R. *Thermodynamic Properties of Minerals and Related Substances at 298.15 K and 1 Bar (10^5 Pascals) Pressure and at Higher Temperatures* (US Geological Survey, 1978).

Ruiz-Agudo, E. et al. Mechanism of leached layer formation during chemical weathering of silicate minerals. *Geology* **40**, 947-950 (2012).

Stumm, W. *Chemistry of the Solid-Water Interface: Processes at the Mineral-Water and Particle-Water Interface in Natural Systems* (Wiley, New York, 1992).

Toryanik, A. I. & Kisel'nik, V. V. Concentration and temperature dependence of the activation energy of self-diffusion in aqueous electrolyte solutions. *Theoretical Experimental Chem.* 5, 411-415 (1969).

Verney-Carron, A., Gin, S., Frugier, P. & Libourel, G. Long-term modeling of alteration-transport coupling: Application to a fractured Roman glass. *Geochim. Cosmochim. Acta* 74, 2291-2315 (2010).

Wang, Y. & Merino, E. Origin of fibrosity and banding in agates from flood basalts. *Am. J. Sci.* **295**, 49-77 (1995).

Wieland, R., Wehrli, B. & Stumm, W. The coordination chemistry of weathering: III. A generalization on the dissolution rates of minerals. *Geochim. Cosmochim. Acta* **52**, 1969-1981 (1988).

Wirth, G. S. & Gieskes, J. M. The initial kinetics of the dissolution of vitreous silica in aqueous media. *J. Colloid Interface Sci.* **68**, 492-500 (1979).

Wohlfahrt, G., Fenstermaker, L. F. & Arone III, J. A. Large annual net ecosystem CO_2 uptake of a Mojave Desert ecosystem. *Global Change Biology* **14**, 1475-1487 (2002).

Wolery, W. G., Tester, J. W. & Grigsby, C. O. Quartz dissolution kinetics from 100-200 ^{o}C as a function of pH and ionic strength. *AIChE J.* **42**, 3442-3457 (1996).

4. EXPERIEMNTAL STUDY OF URANIUM SORPTION ON BENTONITE SAMPLES FROM FEBEX

4.1 Introduction

Uranium (U) contamination in the subsurface is a part of the legacy of nuclear weapons and energy production, resulting from mining and milling activities, processing of nuclear materials, and nuclear waste disposal. The U.S. Department of Energy (DOE) is tasked with cleaning up U-contaminated aquifers at a number of sites, including the Uranium Mill Tailings Remedial Action (UMTRA) sites and the Savannah River, Oak Ridge, and Hanford sites where a variety of different radionuclides are present. In order for nuclear energy to be viable, a long-term nuclear waste disposal repository capable of isolating high-level (HLW) and low-level radioactive waste (LLW) over the time scales necessary for decay of long-lived radioactive isotopes ($> 10^6$ years) must be created. Most nuclear waste repositories currently under investigation use clay media (*i.e.*, bentonite or shale) as engineered barriers or as the host rock for geologic storage (Altmann, 2008; Altmann et al., 2012; Delay et al., 2007; Guyonnet et al., 2009; SKB, 2011; Tournassat et al., 2015). Clays are good barriers for HLW due to their low hydraulic conductivity, which restricts contaminants to diffusion-based transport, and their high adsorption capacity for contaminants, which slows transport even further. Montmorillonite, a smectite mineral, is the dominant clay mineral found in bentonite. It has a 2:1 layer-type phyllosilicate structure, with a large specific surface area ($\sim 750\ m^2/g$) and cation exchange capacity ($\sim 1\ mol_c/kg$).

Uranium can exist in both the tetravalent and hexavalent oxidation state. However, due to the limited solubility of U(IV), U(VI) is the most common oxidation state found in the dissolved phase. U(VI) adsorption varies as a function of pH, bicarbonate, and Ca concentrations due to changes in U(VI) aqueous speciation. At moderate bicarbonate concentrations (> 1 mM) above pH 7, U(VI) speciation is dominated by uranyl-carbonato complexes [$UO_2CO_3(aq)$, $UO_2(CO_3)_2^{2-}$, $UO_2(CO_3)_3^{4-}$] in the absence of Ca, and calcium-uranyl-carbonato ternary complexes [$Ca_2UO_2(CO_3)_3(aq)$, $CaUO_2(CO_3)_3^{2-}$] in the presence of typical groundwater Ca concentrations (> 1 mM) (Dong and Brooks, 2006; Fox et al., 2006; Guillaumont et al., 2003). These calcium-uranyl-carbonato complexes adsorb weakly or not at all to mineral surfaces, and thus changes in U(VI) speciation have a large impact on its sorption behavior and transport (Fox et al., 2012; Fox et al., 2006; Stewart et al., 2010). While U(VI) adsorption to purified Na-montmorillonite has been studied extensively over a range of chemical conditions (Marques Fernandes et al., 2012; Pabalan and Turner, 1996; Tournassat et al., 2017; Turner et al., 1996), the presence of mineral impurities and non-sodium forms of montmorillonite complicates U(VI) adsorption behavior and warrants further study.

Storage of HLW can result in high temperatures near the waste canisters resulting from radioactive decay. The effects of elevated temperature on the engineered barrier must be taken into account when designing a nuclear waste repository. Such effects may include changes in the hydrological and mechanical properties of clay, changes in pore water chemical compositions, and changes in the clay and accessory mineral composition (Cuadros and Linares, 1996; Wersin et al., 2007; Zheng et al., 2015). The conversion of montmorillonite to illite, known as illitization, is one of the primary mineralogical changes expected to occur during long-term exposure to high temperatures. Zheng et al. (2015) predicted the extent of illitization over a 1000-year simulation to be 1-8% (volume fraction) at 100 °C, and 1-27% at 200 °C in a modeling study. Concentrations of pore water potassium (K) and the abundance and dissolution rate of K-feldspar were the primary chemical factors controlling the extent of illitization in their study (Zheng et al., 2015). Intrusion of groundwater from the surrounding host rock may also have an effect on the clay properties. In order to investigate these combined effects on an engineered barrier, the FEBEX (Full-Scale Engineered Barriers Experiment) *in situ* heater test was conducted by Empresa Nacional de Residuos Radiactivos (ENRESA) under the auspices of the European Union at the Grimsel Test Site from 1997 to 2015. Highly compacted bentonite blocks, serving as the engineered test barrier, were placed in a radial arrangement around two underground heaters and heated to a maximum of 100 °C in a crystalline host rock. Detailed information on the test can be found elsewhere (ENRESA, 2000). The clay selected for the FEBEX experiment was a bentonite from the Cortijo de Archidona deposit (Almería, SE Spain), which is primarily made up of smectite (93%), with minor amounts of quartz (2%), plagioclase (3%), cristobalite (2%), potassium feldspar, calcite, and trydimite as accessory minerals (Fernández et al., 2004).

The primary goal of this work was to study the effect of bentonite heating under realistic field conditions on U(VI) adsorption behavior. Furthermore, we aimed to provide mechanistic insight into observed differences in U(VI) adsorption as a result of heat treatment. Bentonite samples from the FEBEX *in situ* experiment, which experienced varying temperature and water saturation conditions, were tested for U(VI) adsorption. In this section, we first present results from an experiment comparing U(VI) adsorption kinetics at a single condition of temperature, pressure, and water composition onto FEBEX bentonite samples, which experienced a range of temperature and water saturation conditions. Following that, we present results from equilibrium U(VI) adsorption experiments conducted over a wider range of chemical conditions on both unpurified ("bulk") and purified FEBEX bentonite. A comparison of the U(VI) adsorption behavior on unpurified and purified bentonite can be used to determine whether the observed differences in U(VI) adsorption as a result of heating are due to (1) changes in the pore water chemistry and accessory mineral components, or (2) structural changes in the smectite clay structure. Lastly, we present a brief discussion of planned future work.

4.2 Kinetics of Uranium(VI) Adsorption onto Heat-treated and Cold-zone FEBEX Bentonite

4.2.1 Materials and Methods

Bentonite samples were obtained from the second dismantling of the FEBEX (Full-Scale Engineered Barriers Experiment) *in situ* heater test in 2015, after 18 years of heating. The FEBEX heater test was conducted by ENRESA under the auspices of the European Union at the Grimsel Test Site. Detailed information on the test can be found elsewhere (ENRESA, 2000). Briefly, bentonite was compacted into blocks ("bentonite rock") at 1650 kg/m^3 dry density, placed in a radial arrangement around two underground heaters and heated to a maximum of 100 °C. The degree of water saturation and temperature varied with radial distance, with water saturation greatest and temperature lowest at the furthest distance from the heater (Table 4-1). For this study, we studied bentonite samples from four locations, two locations in the heater test zone (BD-48) at radial distances of 50 and 108 cm from the center axis and two locations from a control non-heated zone (BD-59) at the same radial distances. The section layout during dismantling is described by Detzner and Kober (2015). Three replicate blocks were used from each location, with the exception of BD-59 at 108 cm, where only two blocks were used. The blocks were split open and approximately 200 g of bentonite was removed from the center of each block and dried in an oven at 60 °C for one week. The dried bentonite was then crushed by hand using a porcelain mortar and pestle, and sieved through a 0.063 mm sieve in order to remove sand particles and reduce sample heterogeneity. Equivalent weights of each replicate block were mixed together to form composite samples for the four locations. Average water contents and historical *in situ* temperatures are shown for each composite sample in Table 2-1. In addition to the heater test bentonite samples, a sample of the original untreated bentonite, which had not been compacted into bentonite rock or emplaced in the *in situ* experiment, was also obtained. This original bentonite was dried, crushed, and sieved in the same manner as the other bentonite samples. FEBEX bentonite contained primarily smectite (93%), with minor amounts of quartz (2%), plagioclase (3%), cristobalite (2%), potassium feldspar, calcite, and trydimite as accessory minerals (Fernández et al., 2004). Bentonite stock solutions were prepared at concentrations of 5 g/L for each sample and stored at 4 °C prior to starting experiments.

Table 4-1. Composite FEBEX heater test samples used for U(VI) adsorption experiments

Test Section	Distance to axis (cm)	Replicate Blocks	Water Content (g water/g dry clay)	Average Temperature[(b)] (°C)
BD-48	50	BD-48-3, BD-48-6, BD-48-9	0.14	95
BD-48	108	BD-48-1, BD-48-4, BD-48-7	0.26	45
BD-59	50	BD-59-10, BD-59-11, BD-59-12	0.22	20
BD-59	108	BD-59-2, BD-59-3	0.26	20
Original[(a)]	-	-	0.09	-

(a) Unheated and uncompacted
(b) Average temperatures from ENRESA (2000) and L. Zheng, personal communication

4.2.2 Kinetic Adsorption Experiments

Batch kinetic U(VI) adsorption experiments were conducted on the four composite bentonite samples and the original bentonite at a single water chemical composition, in equilibrium with air at room temperature (22-24 °C). Chemical conditions were as follows: total U(VI) concentration = 8.4 x 10^{-7} M, pH = 7.5, NaCl concentration = 50 mM, and bentonite concentration = 0.5 g/L. The dissolved inorganic carbon (DIC) concentrations imposed by atmospheric CO_2 partial pressure under these conditions ranged between 0.18 and 0.28 mM. Experiments were conducted in 250 mL plastic (high-density polyethylene) bottles and subsamples were collected at various time points (4.8, 8.1, 24, 49, 75, and 168 hours) for up to one week. Samples were prepared by weighing appropriate volumes of stock solutions (1 M NaCl, 5 g/L bentonite stock) and MilliQ water to reach a total volume of 200 mL, then adjusting pH to 7.5 using 0.1 or 0.01 M HCl or NaOH. Duplicates were prepared for each bentonite sample. Samples were maintained under these conditions on an orbital shaker for 92 hours, adjusting pH 1-2 times a day as necessary to equilibrate the solids with the chemical conditions prior to spiking with U(VI). Samples were then spiked with U(VI) stock solution (3.15 x 10^{-4} M), and the pH was re-adjusted. At each sampling time, the samples were shaken to ensure the bentonite was fully suspended, then 15 mL was removed by pipet and transferred to 40 mL polycarbonate (Oak Ridge) centrifuge tubes and centrifuged at 39,000-x *g* for 20 minutes. This centrifuge speed and time was sufficient to remove all particles > 24 nm, as calculated from Stokes Law. After centrifuging, the supernatant was removed and analyzed for DIC and U, and metal concentrations (Ca, Mg, and K) by inductively coupled plasma mass spectrometry (ICP-MS). DIC was measured on a Shimadzu TOC-V analyzer, and metals on a Perkin Elmer Elan DRC II ICP-MS. ICP-MS samples were diluted with 0.15 M ultrex grade nitric acid and an internal standard was added prior to analysis. Solid-free control samples were also prepared and sampled in the same manner as the bentonite samples. All data are presented as the average and standard deviation of the duplicate samples.

4.2.3 Results and Discussion

Comparison of U(VI) Adsorption Kinetics across Bentonite Samples: Figure 4-1 shows U(VI) adsorption to FEBEX bentonite composite samples as a function of time. U(VI) adsorption was slightly higher for the first time point (4.8 hours) for all samples, with no clear kinetic trend after that, suggesting that U(VI) adsorption reached equilibrium very quickly. The magnitude of U(VI) adsorption was the same (61-62%) for all bentonite samples, except BD-48, 50 cm, which adsorbed 52%. The BD-48, 50 cm sample was located closest to the FEBEX heater, experiencing temperatures of approximately 95 °C for 18 years. The BD-48, 108 cm sample experienced temperatures closer to 45 °C, while the BD-59 samples and original bentonite samples served as *in situ* cold-zone (~20 °C) and un-heated controls, respectively. The water content also varied as a function of temperature and distance from the heater (Table 4-1). The fact that U(VI) adsorption was not significantly different across all other bentonite samples provides evidence that neither the mineralogical constituents nor the porewater chemical composition changed significantly enough to effect U(VI) sorption during the experiment for samples subjected to lower temperatures (≤ 45 °C) over this time scale.

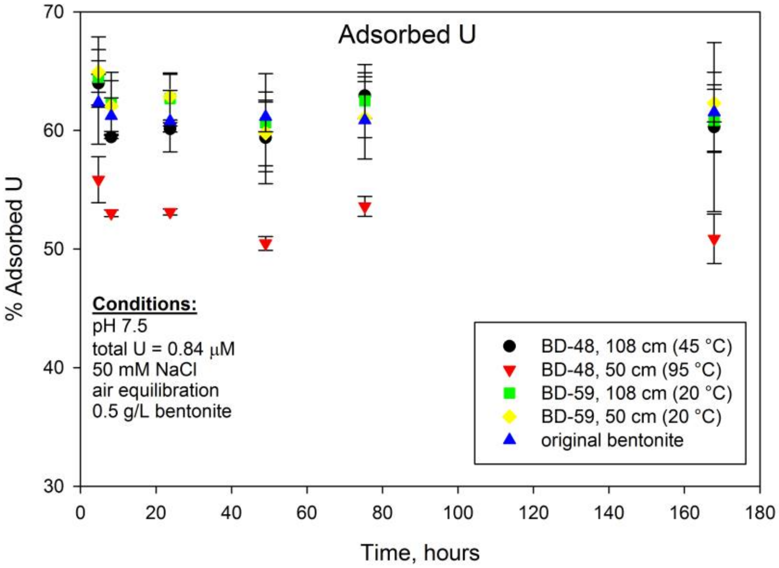

Figure 4-1. Kinetics of U(VI) adsorption onto FEBEX bentonite composite samples. Average historical temperatures experienced by each bentonite sample are shown in parentheses. Error bars represent standard deviations of replicate sorption experiments.

Chemical Composition during Kinetic U(VI) Adsorption Experiments: The chemical composition of the water in equilibrium with the bentonite samples was monitored throughout the experiment. Figure 4-2 shows measured pH, DIC, Mg, and Ca concentrations. These four parameters have a large effect on aqueous U(VI) speciation and consequently on U(VI) adsorption (Dong and Brooks, 2006; 2008; Fox et al., 2006; Guillaumont et al., 2003; Stewart et al., 2010) and thus are critical components of any U(VI) transport model. The pH was continuously adjusted throughout the experiment in order to maintain values close to the target pH (7.5). For the first two time points, pH values ranged from 7.30-7.42 then increased somewhat to values between 7.38-7.51 for the remainder of the experiment. The slightly lower initial pH is most likely due to the fact that the samples were initially spiked with an acidic (pH 2) U(VI) stock solution. DIC concentrations increased slightly over the first 48 hours of the experiment, seemingly reaching equilibrium after that. Ca and Mg concentrations decreased slightly over the first 48 hours, then either stayed the same (Ca) or increased slightly (Mg) for the duration of the experiment. Based on the observed small changes in U(VI) sorption and aqueous chemical conditions over time, it appears that 48-hour is sufficient time for U(VI) adsorption to reach equilibrium under these conditions and future experiments will be performed with a 48 hours reaction time.

All samples exhibited similar pH values, and DIC and Ca concentrations. However, the Mg concentrations for the BD-48, 108 cm sample were slightly lower than the other samples. The cause of this difference is unknown. Given the similarity in aqueous chemical conditions across bentonite samples, it is unlikely that the observed lower U(VI) adsorption for the BD-48, 50 cm sample was due to differences in aqueous U(VI) speciation. Instead, we hypothesize that the lower U(VI) adsorption resulted from either (1) structural changes in the clay mineralogy (*e.g.*, illitization of montmorillonite), or (2) changes in the amount or type of accessory minerals. Montmorillonite is the dominant clay mineral in FEBEX bentonite (Fernández et al., 2004), and illitization reactions (conversion of montmorillonite to illite) have been observed upon heating to temperatures of 100-200 °C (Cuadros and Linares, 1996; Wersin et al., 2007). Illitization may lead to a decrease in the specific surface area of bentonite (Macht et al., 2011) and consequently to a decrease in U(VI) adsorption capacity. Changes to the accessory mineral fraction may also occur because of heating, including dissolution of minerals (*e.g.*, calcite, K-feldspar) and precipitation of new mineral phases. Because montmorillonite is the most abundant and sorptive phase, any changes in the mass fraction of montmorillonite (*i.e.*, dissolution or precipitation of accessory minerals) will result in changes in the bulk U(VI) adsorption when expressed in terms of mass of solid.

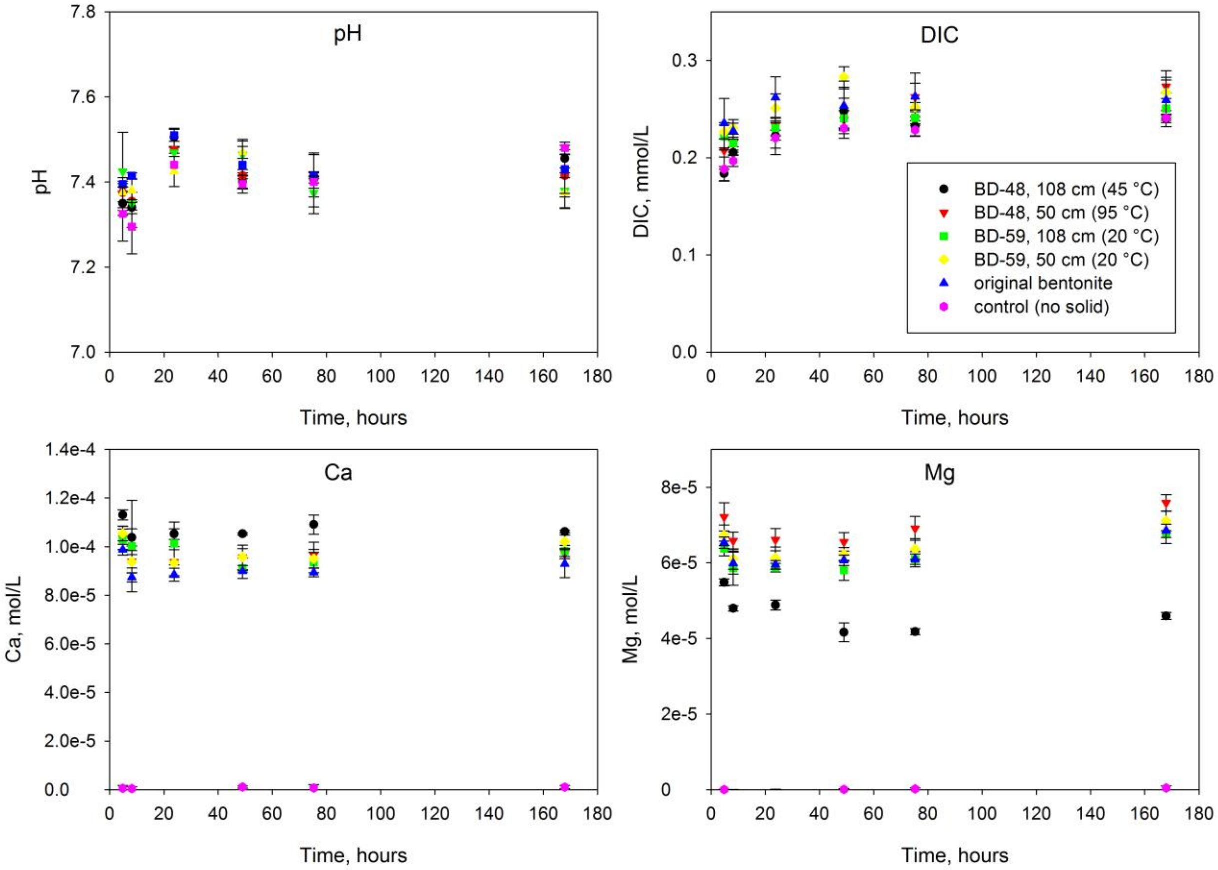

Figure 4-2. Aqueous chemical compositions over time for FEBEX bentonite U(VI) adsorption experiments. Average historical temperatures experienced by each bentonite sample are shown in parentheses. Error bars represent standard deviations of replicate sorption experiments.

4.3 Equilibrium Uranium(VI) Adsorption onto Purified and Un-Purified FEBEX Bentonite: Effect of Heat-Treatment

4.3.1 Materials and Methods

Bentonite Samples: Based on the similarity in U(VI) adsorption among all samples which were exposed to temperatures ≤ 45 °C in the kinetic experiments (Section 2), we chose to focus further experiments over a wider range of chemical conditions on two contrasting composite FEBEX bentonite samples: BD-48, 50 cm (sample heated to ~95 °C) and BD-59, 50 cm (cold zone sample experiencing ~20 °C). Experiments were performed with "bulk" composite samples (described in Section 4.2.1) and purified composite samples (described below). The comparison of U(VI) adsorption on purified and unpurified bentonite was then used to determine whether the observed difference in U(VI) adsorption on the heated sample was due to changes in the accessory mineral fraction or changes in the clay structure.

Bentonite Extraction and Purification: Composite FEBEX bentonite samples (BD-48, 50 cm and BD-59, 50 cm) were extracted and purified in order to compare extractable metal concentrations between the two samples and produce a purified clay sample for U(VI) adsorption experiments. The extraction and purification procedure was adapted from Tinnacher et al. (2016), allowing for the characterization of extracted metals. The procedure included the following major steps: (1) leaching of clay samples with water, (2) leaching with, and dialysis against, sodium acetate at pH 5 for carbonate mineral removal, (3) dialysis against NaCl to remove acetate and complete Na-saturation, (4) dialysis against water to remove excess salts, and (5) centrifugation to remove particles greater than 2 µm. Triplicate samples were extracted and purified for each composite sample, and extraction data are presented as the average and standard deviation of the replicates. Composite clay (2.5 g) was weighed into 40-mL polycarbonate centrifuge tubes and 25-mL of MilliQ water was added. Samples were placed on an end-over-end sample rotator and allowed to react for 5 hours, then centrifuged at 39,000-x *g* for 20 minutes. The supernatant was filtered through a 0.2 µm syringe filter polyvinylidene fluoride (PVDF) and retained for analysis of water soluble metals, dissolved inorganic carbon (DIC), dissolved organic carbon (DOC), and pH. Centrifuge tubes containing clay were weighed to determine the volume of entrained solution, then 25-mL of 1 M sodium acetate solution buffered at pH 5 with acetic acid was added. Samples were placed on the sample rotator and allowed to react for six days, then centrifuged, filtered, and retained for analysis of metals as described above. Clay samples were re-suspended in 15 mL of acetate buffer, transferred to pre-rinsed dialysis tubing (SpectraPor7, 8 kDa), and dialyzed against 900 mL of acetate buffer in a 1-L glass beaker for three days, changing dialysis solution daily. The acetate buffer dialysis solution was then exchanged with 1 M NaCl (dialyzed for one week), then with MilliQ water (dialyzed for two weeks), again changing dialysis solution daily. The purified clay suspensions were then transferred into plastic bottles and diluted and dispersed in MilliQ water to reach a clay concentration of approximately 15 g/L, and centrifuged at 1000-x *g* for 7 minutes. This centrifugation speed and time was deemed sufficient to remove all particles > 2 µm as calculated from Stoke's Law. The replicate < 2 µm clay fractions were then combined into a single bottle and diluted to reach a final clay stock concentration of 10 g/L. The exact clay stock concentration was determined by drying a subsample in a porcelain crucible at 85 °C. Clay stock solutions were stored at 4 °C prior to starting experiments.

1.1.1 **Batch Adsorption Experiments:** Equilibrium batch U(VI) adsorption experiments were conducted on purified and un-purified ("bulk") FEBEX bentonite composite samples at two Ca concentrations over the pH range 7 to 8 at an ionic strength of 0.1 M, using NaCl as the background electrolyte. Clay concentrations were 0.5 g/L and total initial U(VI) concentrations were 9.4×10^{-7} M. For purified bentonite samples, two separate experiments were conducted with Ca added to yield concentrations of 0.1 and 2.0 mM in solution, respectively. The 0.1 mM

Ca concentration was chosen based on the concentrations of Ca released during kinetic batch experiments (

Figure **4-2**). In unpurified bentonite samples, some Ca was present in the clay, so two samples were prepared, one without added Ca, and another spiked with 2.0 mM Ca, achieving final dissolved Ca concentrations of approximately 0.14 and 2.17 mM, respectively.

Adsorption experiments were conducted in 40-mL polycarbonate centrifuge tubes. Clay samples were suspended in water and aliquots of 1 M NaCl, 0.1 M $CaCl_2$, and 0.1 M $NaHCO_3$ stock solutions were added to reach the desired final concentrations of Ca and HCO_3^- (to facilitate equilibration with atmospheric CO_2), and an ionic strength of 0.1 M. The pH was then adjusted to the desired pH using 0.1 M HCl or NaOH and samples were allowed to equilibrate for 24 hours on an end-over-end sample rotator. After equilibration, samples were spiked with U(VI), the pH was re-adjusted, and samples were placed on an end-over-end rotator for 48 hours to allow for U(VI) adsorption. Samples were then centrifuged at 39,000 x *g* for 20 minutes and the supernatant was removed for analysis by ICP-MS (U, Ca, and other metals), DIC, and pH. Adsorbed U(VI) was calculated by subtracting the final dissolved U(VI) concentration from the initial (total) U(VI) concentration. U(VI)-free control samples were prepared in the same manner as samples at pH 8, but without the addition of U(VI) to verify that samples were not contaminated with U(VI). No contamination was observed.

Analytical Techniques: DIC, DOC, and total carbon (on solid samples) were measured on a Shimadzu TOC-V analyzer. DOC was measured by non-purgeable organic carbon by acidifying with HCl and purging with N_2 in order to remove inorganic carbon prior to analysis. Total carbon was measured by catalytically aided combustion oxidation at 900 °C and a Nondispersive Infrared Detector (NDIR) on a Shimadzu TOC-V analyzer equipped with a solids module (SSM). Samples were analyzed for metal concentrations by ICP-MS (Perkin-Elmer Elan DRC II) after acidification and dilution with ultrapure (ultrex grade) 0.15 M nitric acid and internal standard addition.

4.3.2 Results and Discussion

Bentonite Characterization Results: Water extractions of unpurified FEBEX bentonite released greater concentrations of metals (Na, K, Ca, and Mg) and organic carbon (OC) for the heated sample (BD-48, 50 cm) compared to the unheated sample (BD-59, 50 cm), as shown Table 4-2. The heated sample water leachates yielded lower inorganic carbon (IC) and pH values. It is possible that the soluble ion concentrations in both *in situ* samples have been altered compared to the original material due to intrusion of groundwater (cold-zone sample) and/or heat-caused alterations. For example, the lower concentrations of soluble metals and OC in the cold-zone sample may represent a loss due to groundwater leaching in this sample or an increase in the heated sample. While we did not perform extractions on the original bentonite sample, Fernández et al. (2004) reported concentrations of soluble salts during leaching experiments with the original FEBEX bentonite, although at a slightly higher solid to liquid ratio (0.15 kg/L compared to 0.1 kg/L in our study). In general, salt concentrations observed in the leachates of the original bentonite were in between the values observed in our study for the two samples (Na = 10.3 mM, K = 0.10, Mg = 0.12 mM, Ca = 0.10 mM), while pH (8.76) was closer to the pH in our cold-zone sample (Fernández et al., 2004). Because of the slightly higher solid to liquid ratio used in their study, it is very likely that the differences observed between the heated and cold-zone sample primarily represent a change in the heated sample. The change in pH and IC in particularly is noteworthy; suggesting that carbonate minerals may have been depleted from or altered in the heated sample. For example, a fraction of the calcite may have been converted to a lower-solubility carbonate mineral as a result of heating. Total carbon was measured in the unpurified clay solids, yielding slightly lower concentrations in the heated sample (0.12 ± 0.01% by mass) compared to the unheated sample (0.15 ± 0.002%). However, we were unable to quantify total inorganic carbon concentrations in the clay solids due to methodological constraints, so it is unknown if differences in total carbon are due to differences in IC or OC. The pH 5 acetate extractions released very similar concentrations of K and Ca for the two samples, but slightly higher Mg concentrations in the heated sample. The acetate extractions are designed to dissolve carbonate minerals, but can also release adsorbed cations.

Table 4-2. Concentrations of extracted metals, inorganic carbon (IC), organic carbon (OC) and pH values for water extractions of unpurified FEBEX bentonite samples. Extracted metals only are shown for acetate (1 M acetate, pH 5) extracts. Concentrations of extracted constituents are expressed as the average and standard deviation of replicate extracts in mM.

	Water Extractions		Acetate Extractions	
	BD-48, 50cm (heated, 95 °C)	BD-59, 50cm (cold-zone, 20 °C)	BD-48, 50cm (heated, 95 °C)	BD-59, 50cm (cold-zone, 20 °C)
pH	7.96 ± 0.02	8.63 ± 0.12	--	--
IC (mM)	1.02 ± 0.04	2.07 ± 0.04	--	--
OC (mM)	0.786 ± 0.072	0.164 ± 0.007	--	--
Na (mM)	11.3 ± 0.1	7.69 ± 0.20	--	--
K (mM)	0.192 ± 0.008	0.077 ± 0.000	1.37 ± 0.03	1.34 ± 0.05
Ca (mM)	0.370 ± 0.004	0.069 ± 0.001	25.0 ± 0.6	24.2 ± 0.2
Mg (mM)	0.356 ± 0.002	0.088 ± 0.002	16.8 ± 0.1	15.3 ± 0.1

Comparison of Uranium(VI) Adsorption on Heated and Cold-Zone FEBEX Bentonite: U(VI) adsorption to purified and unpurified FEBEX bentonite was studied over a range of chemical conditions, which are considered relevant for waste disposal scenarios, including the pH range 7 to 8 and Ca concentrations of approximately 0.1 and 2.0 mM. We did not test pH values greater than 8 due to supersaturation with respect to calcite (at 2 mM Ca) and low U(VI) adsorption at alkaline pH. Results from these experiments are shown in Figure 4-3.

The pH measurements were performed on samples open to the atmosphere and it took a very long time for pH to stabilize. This effect was observed on both purified and unpurified bentonite; however, with unpurified bentonite, the pH was particularly unstable, continuing to drift upwards for over 15 minutes. This pH drift made it difficult to obtain reliable pH measurements, particularly for the unpurified bentonite. We have plotted U(VI) adsorption as a function of both measured pH and measured DIC concentration; however, the plots with DIC may be more informative. As expected, U(VI) adsorption decreased with increasing pH and DIC concentration. U(VI) adsorption was also lower in the presence of high Ca (~2 mM) compared to low Ca (~0.1 mM), especially at higher pH and DIC values.

U(VI) adsorption onto unpurified (bulk) bentonite was higher on the cold zone sample (BD-59, 50 cm) compared to the heated sample (BD-49, 50 cm) over the entire DIC range at both low and high Ca. This is consistent with our observations in the U(VI) kinetic adsorption experiment (Section 4.2), which was performed at a single chemical condition (pH 7.5, low Ca, 0.05 M ionic strength).

U(VI) adsorption onto purified bentonite was also higher on the cold zone sample compared to heated sample over the entire range of DIC concentrations at both low and high Ca. This suggests that the difference in U(VI) adsorption between heated and cold zone samples is due to structural alteration of the smectite (montmorillonite) clay mineral, and not due simply to differences in pore water chemistry or the types and relative masses of accessory minerals. Further characterization, including cation exchange capacity, surface area, and x-ray diffraction, of the purified bentonite sample is needed to probe these structural changes.

In all cases, U(VI) adsorption was higher on purified bentonite compared to unpurified bentonite. This is expected and likely due to a ‘dilution’ effect from accessory minerals that have a much lower adsorption capacity compared to montmorillonite in the unpurified bentonite. These minerals may include silica and feldspar minerals as well as carbonate minerals (*e.g.*, calcite).

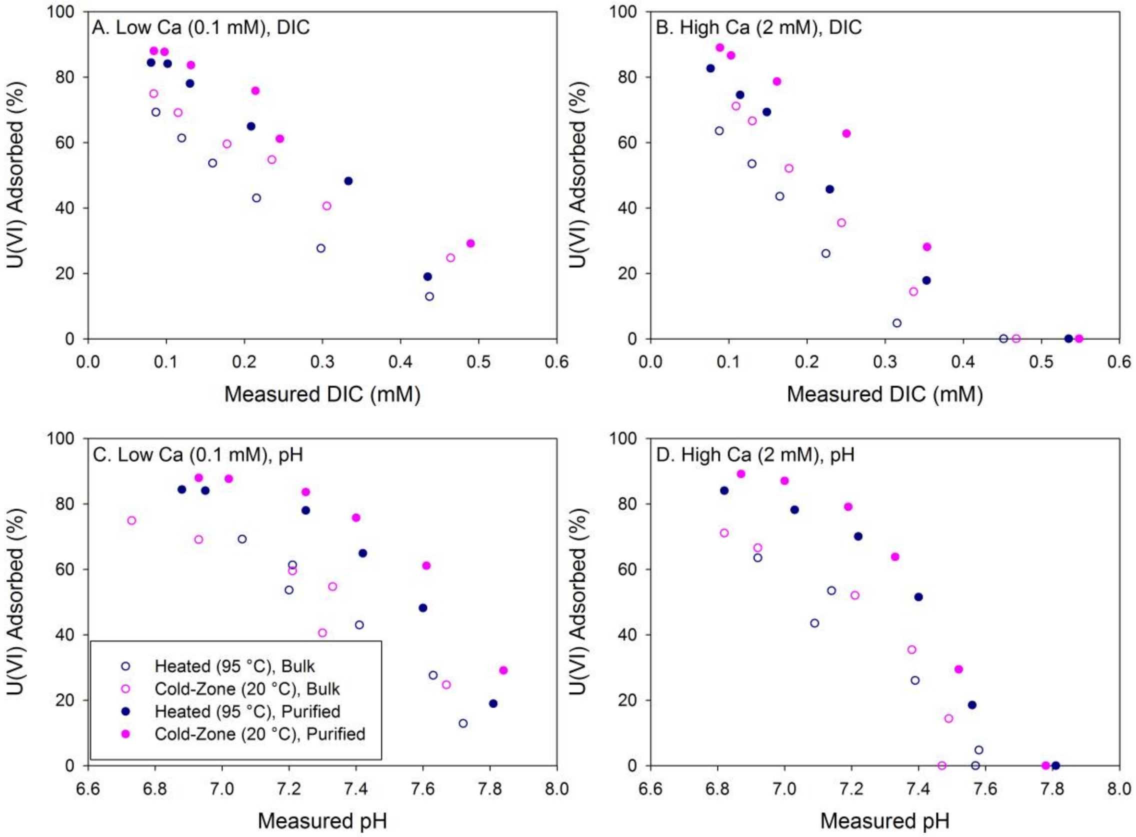

Figure 4-3. U(VI) adsorption as a function of DIC (A, B) and pH (C, D) onto bulk (unpurified) and purified FEBEX bentonite samples from the heated zone (BD-48, 50 cm, 95 °C) and cold zone (BD-59, 50 cm, 20 °C). A) and C) show experiments conducted at low Ca concentrations (approximately 0.1-0.14 mM); B) and D) show experiments conducted at high Ca concentrations (2.0-2.2 mM). All experiments were conducted at an ionic strength of 0.1 M using NaCl as the background electrolyte, with total U(VI) = 9.4×10^{-7} M and 0.5 g/L bentonite, and under open atmosphere at room temperature (22-24 °C).

4.4 Conclusions

This section detailed the results from a series of experiments conducted in FY17 designed to test the effect of bentonite heating on U(VI) adsorption. U(VI) adsorption onto bentonite samples from the FEBEX *in situ* experiment, which were subjected to 18 years of heating at temperatures of 45-100 °C, was compared to adsorption onto original FEBEX bentonite and cold-zone FEBEX bentonite from the *in situ* experiment. The major conclusions to date are as follows:

1) Kinetics of U(VI) adsorption appear to be very fast, reaching equilibrium in less than 8 hours, while DIC concentrations reach equilibrium in 48 hours. Small fluctuations in pH and DIC concentrations

over the 1-week experiment seem to coincide with small fluctuations in U(VI) adsorption observed over this period.

2) Although water and acetate extractions revealed small differences in the leachate compositions of heated and cold-zone FEBEX bentonite, the measured DIC, Ca, and Mg concentrations in solution during U(VI) adsorption kinetic experiments were similar for all FEBEX bentonite samples. This suggested that differences in aqueous U(VI) speciation were not responsible for differences in U(VI) adsorption.
3) U(VI) adsorption onto unpurified FEBEX bentonite samples which experienced sustained temperatures of approximately 95 °C was lower than adsorption onto original unheated and cold-zone (20 °C) FEBEX bentonite over a range of chemical conditions (pH 7-8, Ca = 0.1 and 2.0 mM) relevant to nuclear waste disposal.
4) U(VI) adsorption onto unpurified FEBEX bentonite which experienced more moderate temperatures (approximately 45 °C) was *not* lower than unheated FEBEX bentonite for the single chemical condition tested (0.05 M NaCl, pH 7.5, 0.1 mM Ca).
5) The difference in U(VI) adsorption between heated (95 °C) and cold-zone (20 °C) FEBEX bentonite persisted over the range of chemical conditions tested when the bentonite samples were purified to remove mineral impurities such as calcite, quartz, and feldspars. This suggests that the decrease in U(VI) adsorption was due to alteration of the clay mineral structure, and *not* due to a change in the pore water chemistry or amount and type of accessory minerals. This may reflect illitization of the montomorillonite; however, further clay characterization is needed to verify this hypothesis.

These results provide key information necessary for performance assessment of HLW disposal scenarios. The decreased adsorption observed in this study as a result of bentonite heating may impact the diffusion of U(VI) through engineered clay barriers. Because the decreased U(VI) adsorption was due to changes in the clay mineral structure and *not* to aqueous U(VI) speciation, other radionuclides may be similarly affected. Further investigation is needed to probe the structural changes, which occurred as a result of heating and to better understand the mechanisms underpinning this behavior.

For the upcoming fiscal year (FY18), we plan to:

1) Characterize purified bentonite clay, including measurements of specific surface area, cation exchange capacity, x-ray diffraction (XRD) analysis, and other analyses as necessary. This information is necessary not only to gain a better understanding of the structural changes occurring in the bentonite as a result of heat treatment, but also to provide a basis for surface complexation modeling.

2) Model U(VI) adsorption behavior onto purified and unpurified bentonite. This work will build upon the U(VI) adsorption model developed for Na-montmorillonite in previous years (Tournassat et al., 2017).

3) Conduct U(VI) adsorption experiments with FEBEX bentonite samples exposed to ‘intermediate’ heat (~60 °C) to explore the threshold temperature necessary to affect U(VI) adsorption.

4) Begin U(VI) diffusion experiments with compacted, purified FEBEX bentonite. This will provide information on U(VI) transport under physical conditions relevant for waste disposal scenarios.

4.5 References

Altmann, S., 2008. ‘Geo’chemical research: A key building block for nuclear waste disposal safety cases. *Journal of Contaminant Hydrology* 102, 174-179.

Altmann, S., Tournassat, C., Goutelard, F., Parneix, J.-C., Gimmi, T., Maes, N., 2012. Diffusion-driven transport in clayrock formations. *Applied Geochemistry* 27, 463-478.

Cuadros, J., Linares, J., 1996. Experimental kinetic study of the smectite-to-illite transformation. *Geochimica et Cosmochimica Acta* 60, 439-453.

Delay, J., Vinsot, A., Krieguer, J.-M., Rebours, H., Armand, G., 2007. Making of the underground scientific experimental programme at the meuse/haute-marne underground research laboratory, north eastern France. *Physics and Chemistry of the Earth*, Parts A/B/C 32, 2-18.

Detzner, K., Kober, F., 2015. FEBEX-DP drilling and sampling report sections 32-34, Internal Report. NAGRA.

Dong, W., Brooks, S.C., 2006. Determination of the formation constants of ternary complexes of uranyl and carbonate with alkaline earth metals (Mg^{2+}, Ca^{2+}, Sr^{2+}, and Ba^{2+}) using anion exchange method. *Environmental Science & Technology* 40, 4689-4695.

Dong, W., Brooks, S.C., 2008. Formation of Aqueous MgUO2(CO3)32− Complex and uranium anion exchange mechanism onto an exchange resin. *Environmental Science & Technology* 42, 1979-1983.

ENRESA, 2000. FEBEX Project: Full-Scale Engineered Barriers Experiment for a Deep Geological Repository for High Level Radioactive Waste in Crystalline Host Rock. Final Report. ENRESA.

Fernández, A.M., Baeyens, B., Bradbury, M., Rivas, P., 2004. Analysis of the porewater chemical composition of a spanish compacted bentonite used in an engineered barrier. Physics and *Chemistry of the Earth*, Parts A/B/C 29, 105-118.

Fox, P.M., Davis, J.A., Hay, M.B., Conrad, M.E., Campbell, K.M., Williams, K.H., Long, P.E., 2012. Rate-limited U(VI) desorption during a small-scale tracer test in a heterogeneous uranium-contaminated aquifer. *Water Resour*. Res. 48, W05512.

Fox, P.M., Davis, J.A., Zachara, J.M., 2006. The effect of calcium on aqueous uranium(vi) speciation and adsorption to ferrihydrite and quartz. *Geochimica et Cosmochimica Acta* 70, 1379-1387.

Guillaumont, R., Fanghanel, T., Neck, V., Fuger, J., Palmer, D.A., Grenthe, I., Rand, M.H., 2003. Update on the chemical thermodynamics of uranium, neptunium, plutonium, americium, and technetium. Elsevier, Amsterdam.

Guyonnet, D., Touze-Foltz, N., Norotte, V., Pothier, C., Didier, G., Gailhanou, H., Blanc, P., Warmont, F., 2009. Performance-based indicators for controlling geosynthetic clay liners in landfill applications. *Geotextiles and Geomembranes* 27, 321-331.

Macht, F., Eusterhues, K., Pronk, G.J., Totsche, K.U., 2011. Specific surface area of clay minerals: Comparison between atomic force microscopy measurements and bulk-gas (N_2) and -liquid (EGME) adsorption methods. *Applied Clay Science* 53, 20-26.

Marques Fernandes, M., Baeyens, B., Dähn, R., Scheinost, A.C., Bradbury, M.H., 2012. U(VI) sorption on montmorillonite in the absence and presence of carbonate: A macroscopic and microscopic study. *Geochimica et Cosmochimica Acta* 93, 262-277.

Pabalan, R.T., and Turner, D.R., 1996. Uranium(6+) sorption on montmorillonite: experimental and surface complexation modeling study. *Aquatic Geochemistry* 2, 203-226.

SKB, 2011. Long-Term Safety for the Final Repository for Spent Nuclear Fuel at Forsmark. Main report of the SR-Site project. Swedish Nuclear Fuel and Waste Management Co.

Stewart, B.D., Mayes, M.A., Fendorf, S., 2010. Impact of uranyl−calcium−carbonato complexes on uranium(vi) adsorption to synthetic and natural sediments. *Environ. Sci. Technol*. 44, 928-934.

Tinnacher, R.M., Holmboe, M., Tournassat, C., Bourg, I.C., Davis, J.A., 2016. Ion adsorption and diffusion in smectite: Molecular, pore, and continuum scale views. *Geochimica et Cosmochimica Acta* 177, 130-149.

Tournassat, C., Steefel, C.I., Bourg, I.C., Bergaya, F., 2015. Natural and Engineered Clay Barriers. Elsevier.

Tournassat, C., Tinnacher, R.M., Grangeon, S., Davis, J.A., 2017. Modeling uranium(vi) adsorption onto montmorillonite under varying carbonate concentrations: A surface complexation model accounting for the spillover effect on surface potential. *Geochim. Cosmochim. Acta* in review.

Turner, G.D., Zachara, J.M., McKinley, J.P., Smith, S.C., 1996. Surface-charge properties and UO_2^{2+} adsorption of a subsurface smectite. *Geochimica et Cosmochimica Acta* 60, 3399-3414.

Wersin, P., Johnson, L.H., McKinley, I.G., 2007. Performance of the bentonite barrier at temperatures beyond 100°c: A critical review. *Physics and Chemistry of the Earth*, Parts A/B/C 32, 780-788.

Zheng, L., Rutqvist, J., Birkholzer, J.T., Liu, H. H., 2015. On the impact of temperatures up to 200 °C in clay repositories with bentonite engineer barrier systems: A study with coupled thermal, hydrological, chemical, and mechanical modeling. *Engineering Geology* 197, 278-295.

5. THE ROLES OF DIFFUSION AND CORROSION IN RADIONUCLIDE RETARDATION

5.1 Introduction

This section summarizes research conducted at Lawrence Livermore National Laboratory (LLNL) within the Crystalline Disposal R&D Activity Number M4SF-17LL01030207 and Crystalline International Collaborations Activity Number M4SF-17LL01030208. The focus of this research is the interaction of radionuclides with Engineered Barrier System (EBS) and host rock materials at various physico-chemical conditions relevant to subsurface repository environments. They include both chemical and physical processes such as solubility, sorption, and diffusion.

LLNL is supporting the overall objectives of the Crystalline Disposal R&D control account. The objective of this control account is to advance our understanding of long-term disposal of spent fuel in crystalline rocks (including both granitic and metamorphic rocks) and to develop necessary experimental and computational capabilities to evaluate various disposal concepts in such media. The objectives of this work package are to conduct experimental and modeling studies to quantify radionuclide diffusion through bentonite under repository-relevant (reducing) conditions and to quantify radionuclide sequestration as a result of canister breaching and near field corrosion processes. Quantification of these processes will be included in the Generic Disposal System Analysis (GDSA) model. A basic ‘minimal’ process model for radionuclide diffusion and corrosion-enhanced radionuclide sequestration processes will be provided to GDSA to support a 2020 repository performance assessment schedule.

In FY17, LLNL continued their efforts in data collection and model development in support of the Spent Fuel Waste Science & Technology (SFWST) program. In particular, our research focused on identification, quantification, and parameterization of processes relevant for the evaluation of the performance of various repository scenarios under investigation by the SFWST program.

Our specific FY17 goals for the crystalline work package were the following:

- Completion of the Np(IV) diffusion experiments and quantification of the diffusion rates in bentonite backfill material.
- Evaluation of the radionuclide sequestration potential of corrosion products produced during canister breaching and radionuclide release

Our interest in radionuclide sequestration by corrosion products stems from (1) the potential for this process to significant inhibit radionuclide release during canister breaching and (2) from the absence of such processes in most repository performance assessments. Discussions with James Jerden (Argonne National Laboratory) suggest that a model of radionuclide incorporation can be added to the waste package cell of the GDSA model and may lead to a reduction in the source term of mobile radionuclides. Steel corrosion rates have been implemented within the spent fuel matrix degradation process model but have not yet been implemented into GDSA. Results from an experimental and modeling study of radionuclide partitioning into steel corrosion products will facilitate the incorporation of this process into the GDSA as the steel corrosion model is implemented.

LLNL evaluated this process from both an experimental and modeling perspective. Experimentally, LLNL has been in the process of developing methodologies to grow various iron oxides phases (goethite, hematite, magnetite) in the presence of radionuclides. We performed a small number of binary (RN-mineral) coprecipitation experiments to test radionuclide (Pu, Am, Np, and U) partitioning. Experiments are attempting to quantify coprecipitation partitioning and also examine the effects of aging and the potential iron oxide recrystallization effects associated with the presence of aqueous phase Fe(II).

LLNL is also supporting the overall objectives of the Crystalline International R&D control account. The Crystalline International work package is focused on identifying beneficial international partner programs that can facilitate the development of US GDSA models and ensure that repository development is performed using internationally recognized state of the art methodologies. Therefore, this work contributes to the GDSA model activities by providing parameter feeds and support requirements for the capability for a robust repository performance assessment model by 2020.

LLNL's contribution with this control account is summarized, in part, in the Crystalline and Argillite work packages. Specifically, LLNL efforts will be focused on the following:

- Continued engagement with the NEA TDB project through the support of Dr. Atkins-Duffin as the SFWST representative for international thermodynamic database development effort. This effort ensures that US GDSA model efforts are aligned with internationally accepted practices for repository performance assessment calculations.
- Continued collaboration with HZDR thermodynamic and sorption database development groups in support of the database needs of the SFWST program
- Completion of a state of the art manuscript regarding colloid facilitated transport in the context of nuclear waste repositories. A report was prepared in FY16. This report will provide the basis for 1) preparing a manuscript and 2) development of a colloid facilitated transport model for use in GDSA.

In this section, we summarize the results of two specific activities that fall under this level 4 Milestone: A summary of LLNL's engagement with NEA-TDB activities and a description of experiments performed as part of the canister corrosion and radionuclide sequestration study.

5.2 Engagement with NEA-TDB activities

On April 11, 2017, the NEA-TDB Executive Group presided over a Workshop on the Future of the Thermochemical Database (TDB) Project – Phase 6. The workshop was intended to discuss the interest of the international community in continuing the TDB effort into a Phase 6 (Phase 5 was intended to be complete in FY17). As part of the workshop, the executive committee invited international participation in the workshop. Mavrik Zavarin, Carlos Jove-Colon, and Cindy Atkins-Duffin all participated in the workshop discussions.

Prior to the workshop, Mavrik Zavarin and Carlos Jove-Colon prepared answers to a questionnaire that was distributed by the executive committee to the international community. The questionnaire was intended to help identify the need for a Phase 6 activity and the priority research areas associated with the Phase 6 activity. A summary of the responses and the associate workshop discussion is included in this report as Appendix A. There was overwhelming consensus that the NEA-TDB project remains an important asset to the international nuclear waste research community. The answers to the questionnaire revealed a widely shared acknowledgement of benefit from the TDB project. This was attributed "to (*i*) the high-quality core of values provided, that are used as a basis for the organizations to complete and use according to their individual needs, (*ii*) the detailed guidelines, and (*iii*) the study of common topics of interest.

The importance of centralizing thermodynamic datasets to a common point of reference was also pointed out as a benefit from the Project and as means to lower the cost of more numerous separate studies." The workshop also revealed some potential for improvements in the project, particularly from the standpoint of scheduling, timely electronic access to data, and responsiveness to specific needs of the NEA-TDB member states.

The workshop and associated questionnaire revealed the interest by the member states for the NEA-TDB's highest priority to remain the critical review of thermodynamic data relevant to the international nuclear waste repository research needs.

On April 12, 2017, The NEA-TDB Executive Group held its Eighth Meeting of the NEA TDB-5 Project. At the meeting, the status of the Blue Book critical reviews and State of the Art Reports was discussed. In addition, a new NEA-TDB electronic database for thermodynamic data was described; the electronic database feature will become available later in the year.

5.3 Plutonium Interaction with Iron Oxides

For the long-term performance assessment of nuclear waste repositories, knowledge about the interactions of actinide ions with mineral surfaces is imperative. Iron (oxy)hydroxides are common soil minerals and are present in intermediate level radioactive waste (Marshall et al., 2014). They also form as corrosion products of steel which is a primary structural component of a nuclear repository and of waste canister materials (Music et al., 1993). Studies have shown that Pu(IV) has high sorption affinity for goethite and hematite surfaces at circumneutral pH (Romanchuk et al., 2011; Sanchez et al., 1985; Zhao et al., 2016). At higher concentration, Pu(IV) colloids formed on goethite may undergo a lattice distortion, due to epitaxial growth, which leads to a stronger surface binding compared to other mineral phases, such as quartz (Powell et al., 2011). Gaining a detailed understanding of the interactions between iron oxide and plutonium is key in predicting the long-term stability and mobility of plutonium in the near field of nuclear waste repositories.

The hydrous ferric oxide, ferrihydrite (FH), is a common, poorly crystalline, metastable early product of both biotic and abiotic precipitation of iron, and is a precursor to other more crystalline iron oxides such as hematite (Fe_2O_3) and goethite (FeOOH). Ferrihydrite crystallizes to hematite or goethite depending upon solution conditions, pH, ionic strength and temperature (Schwertmann and Cornell, 2000). The hematite and goethite formation process begins with ferrihydrite particle aggregation (Fischer and Schwertmann, 1975), followed by recrystallization within the aggregate via dissolution and reprecipitation processes that occur at the nanoscale (Combes et al., 1990). During these processes, adsorbed plutonium has the potential to become incorporated into the structure of hematite or goethite.

The goal of this project was to:

- Study sorption of Pu(IV) to ferrihydrite;
- Determine the extent and mechanisms of structural incorporation (co-precipitation) of Pu into synthetic hematite and goethite synthesized from a ferrihydrite precursor.

5.3.1 Plutonium (IV) Sorption to Ferrihydrite

For this work, 2-line ferrihydrite was produced following the synthetic method proposed by Schwertmann and Cornell (2000). Briefly 10 g of $Fe(NO_3)_3.9H_2O$ is added to 125 mL of 18MΩ H_2O. While stirring, approximately 110 mL of 1M KOH is added slowly until the solution pH reaches a stable value between 7 and 8. The solution is centrifuged, the supernatant removed and the solid re-suspended with 18MΩ H_2O. This process is repeated at least twice before transferring the solid to a 3500 MWCO SnakeSkin pleated dialysis tubing, which is left in dialysis against 18MΩ H_2O water for 48 hours. The solid is then removed and suspended in a 0.1M ionic strength solution to form a 1g/L suspension. Sorption experiments were performed over the pH range of 2.5 and 9, with a Pu(IV) concentration of 10^{-10} M. A desired aliquot of plutonium was added to each specimen to obtain the desired Pu(IV) concentration and pH was adjusted using NaOH and HCl at 0.1, 0.5, and 1M. After known time intervals, the pH was measured and an aliquot of the sample removed, centrifuged with a 3 KDa filter and analyzed by liquid scintillation counting. Samples were open to the air and no effort was made to exclude carbonate.

Our preliminary results are reported in

Figure 5-3. 76% of Pu(IV) is sorbed onto the ferrihydrite surface at pH 2.5 within two hours of the start of the sorption experiment. At pH 6 and above the sorption (after 2 hours) is between 90-96% and equilibrium is reached within 24 hours at pH of 7 and higher. For samples equilibrated in the pH range of 2.6 and 4.4, the amount of plutonium sorbed onto ferrihydrite apparently decreases with time (

Figure 5-3). Two factors could be contributing to this apparent desorption trend: i) oxidation of Pu(IV) to Pu(V) or Pu(VI); ii) dissolution of ferrihydrite surface at low pH. To determine if the plutonium in solution oxidizes at these pHs, an oxidation state analysis was performed. The lanthanum fluoride precipitation method was used as it allows to discriminate between reduced (III/IV) and oxidized (V/VI) plutonium. Our results (

Figure 5-4) indicate that after 30 minutes, 40% of the plutonium left in solution at pH 2.5, and ~80-90% at pH 3 and 4, is oxidized; similar results are obtained for the same samples after one week sorption time.

This preliminary work has shown a strong affinity of Pu(IV) for the ferrihydrite surface. The sorption of Pu(IV) to ferrihydrite is fast at all pH values, however pH appears to influence sorption behavior. Whereas at pH>7, sorption reaches equilibrium in 24 hours, in the pH range of 2.5-5, some plutonium desorption occurs within a few hours from the start of the sorption experiment.

Additional experiments are needed to complete our study of Pu sorption. These include:

- Determining ferrihydrite dissolution at low pH to understand plutonium desorption behavior;
- Understanding Pu(IV) sorption to ferrihydrite in an oxygen free atmosphere.

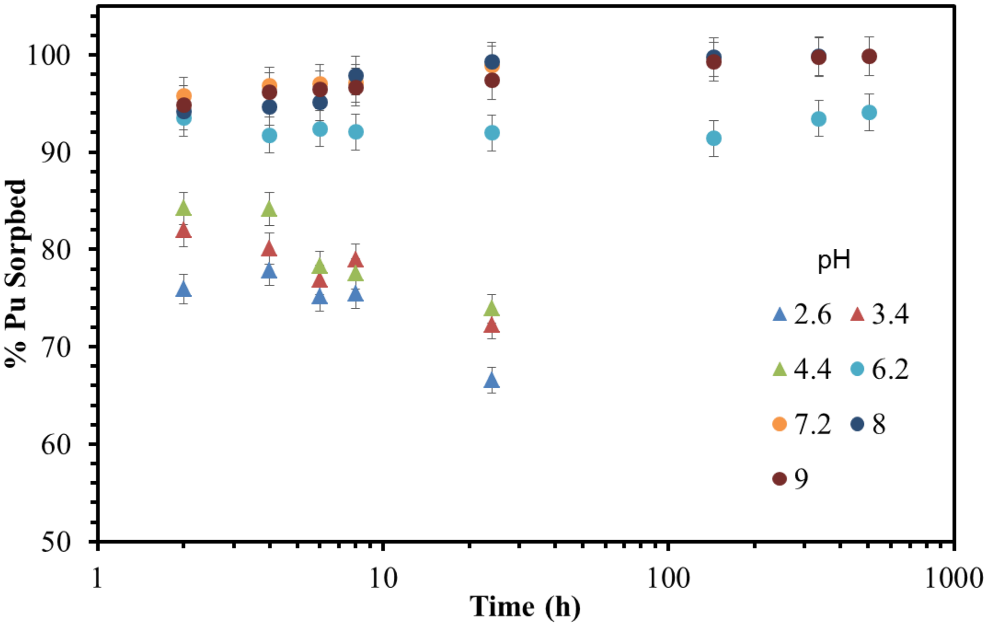

Figure 5-3. Sorption curve for suspended nano-particulate ferrihydrite with 10^{-10}M Pu(IV)

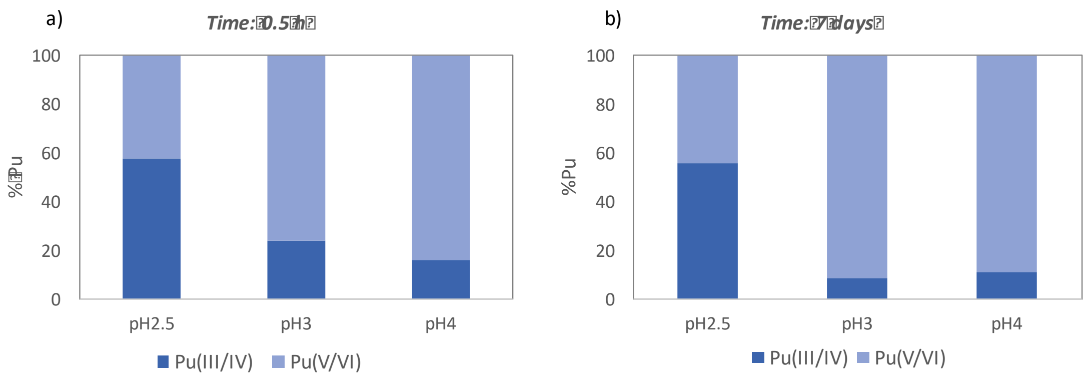

Figure 5-4. Oxidation state analysis of plutonium in the supernatant solution of plutonium sorption experiment on colloidal ferrihydrite a) after 30 minutes of sorption time; b) after 7 days

5.3.2 Plutonium Coprecipitation Studies with Hematite and Goethite

Co-precipitation (or structural incorporation) of co-contaminants into mineral structures most likely involves substitution of the cation site in the mineral or perhaps interstitial incorporation. Crystal chemical constraints that affect incorporation include: i) the cation coordination environment, ii) the cation charge and, iii) a charge balancing mechanism. It has been shown that goethite and hematite are able to accommodate various impurities into their structure including Si, Ti, Mn, Ni and U(VI) (Liu et al., 2012; Marshall et al., 2014). Coprecipitation of plutonium into stable mineral phases, such as iron (oxy)hydroxides, offers a pathway for sequestration with the potential for long term immobilization.

The aim of the work was to understand:

- the difference in plutonium uptake between hematite and goethite;
- how the timing of Pu addition during goethite and hematite synthesis affect the final form of plutonium associated with these minerals.

We investigated these topics by carefully designing synthetic methodologies for both goethite and hematite and by characterizing solutions and solids of the synthesized products by a variety of analytical techniques, including liquid scintillation counting (LSC), transmission electron microscopy (TEM), powder X-ray diffraction (P-XRD), and X-ray absorption spectroscopy (XAS).

Goethite and hematite were synthesized with varying amount of plutonium (300, 1000 and 3000 ppm) from a poorly crystalline ferrihydrite (FH) precursor. The initial FH material was obtained according to the following methodologies – note that the main difference within the two synthetic pathways is the timing of plutonium addition.

- *Method A* or *coprecipitation into FH*: 1 M $FeNO_3 \cdot 9H_2O$ solution was mixed with Pu(IV), ferrihydrite was then formed by slow addition of 5 M KOH (for goethite) or 1 M KOH (for hematite);
- *Method B* or *sorption to FH method*: a KOH (5M or 1M) was slowly added to a 1M $FeNO_3.9H_2O$ solution to form ferrihydrite, Pu(IV) was then sorbed onto the ferrihydrite precipitate.

The use of either 1M KOH or 5M KOH allowed us to obtain the desired iron oxide, goethite (5M KOH) or hematite (1M KOH). The initial ferrihydrite obtained following synthetic routes “Method A” or “Method B” was aged at 80°C for 72 hours. A total of 12 samples were synthesized (Table 5-1).

Table 5-2. List of goethite and hematite samples synthesized.

	3000 ppm Pu	1000 ppm Pu	300 ppm Pu
Goethite			
Method A	GA-3000	GA-1000	GA-300
Method B	GB-3000	GB-1000	GB-300
Hematite			
Method A	HeA-3000	HeA-1000	HeA-300
Method B	HeB-3000	HeB-1000	HeB-300

Powder X-ray diffraction patterns of all 12 goethite and hematite samples (Table 5-2) aged from plutonium sorbed-on or coprecipitated into FH were collected (Figure 5-3). No additional peaks beyond those characteristic of the two mineral phases were identified.

Figure 5-6 presents TEM images of samples GA-3000 and HeA-3000. Images show that goethite crystals are present as 100’s of nm long and 10’s of nm wide needles, banded together (Figure 5-6a); hematite crystals are uniform in size (50 to 60 nm) with a diamond shape (Figure 5-6b). These crystal morphologies are consistent with goethite and hematite crystals synthesized without plutonium as a co-contaminant. P-XRD and TEM results suggest that the addition of plutonium does not affect the final yield of the synthesis.

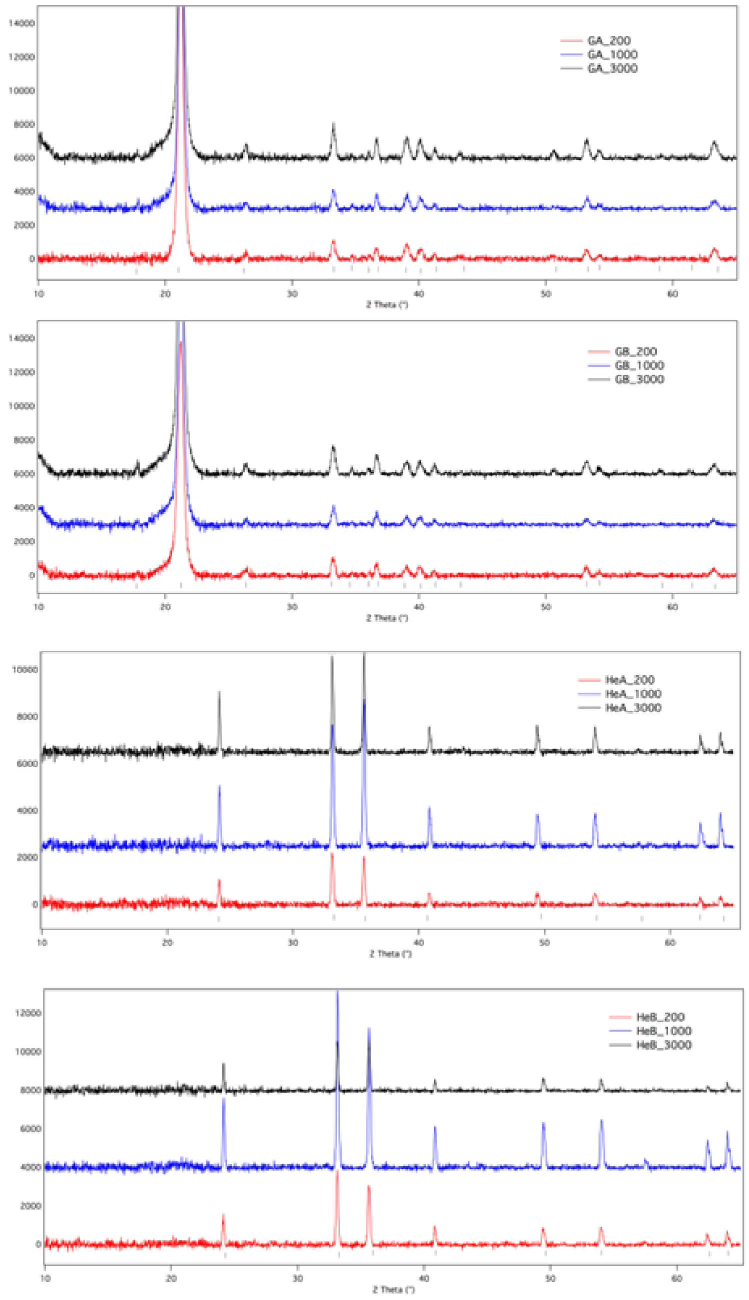

Figure 5-5. Powder XRD patterns of synthetic goethite (GA, GB) and hematite (HeA, HeB). PDF files to which powder XRD patterns were compared to are 00-001-0401 (goethite) and 00-002-0915 (hematite).

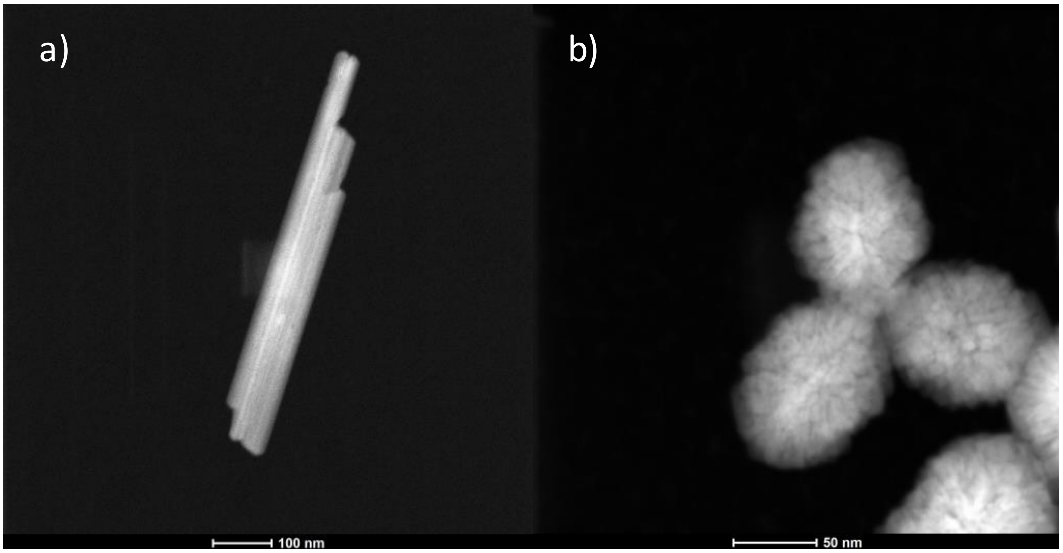

Figure 5-6. Scanning transmission electron microscope (STEM) image of a) goethite GA-3000 and b) hematite HeA-3000.

The fate of Pu(IV) during subsequent ferrihydrite alteration to goethite and hematite was monitored (Figure 5-7). For all samples, upon the completion of the synthesis (72 hours at 80°C) the plutonium concentration of the solution in contact with the mineral was measured. Solids were separated from solution by centrifugation and rinsed two times with 18MΩ H_2O. The plutonium concentration was measured for all rinse solutions. All plutonium concentrations were measured by liquid scintillation counting and samples were centrifuged with 3 kDa filters prior to analyses. Upon transformation of Pu(IV)–FH to goethite, 99% of the initial plutonium was associated with the solid for all samples (GA 300, 1000, 3000; GB 300, 1000, 3000 - Figure 5-7a). No plutonium was associated with hematite synthesized at lower plutonium concentrations (HeA 300, HeA 1000, HeB 300, HeB 1000). Only 10-20 % of plutonium was associated with the HeA 3000 and HeB 3000 samples. For all samples of goethite and hematite, the rinse solution contained < 0.01% of the initial Pu. These results suggest that Pu is strongly associated with the goethite solid, but not with hematite.

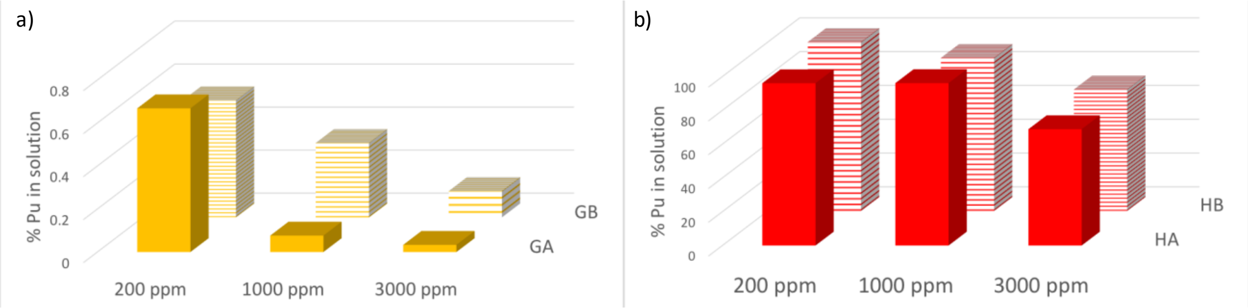

Figure 5-7. Plutonium measured in solution after the completion of the FH transformation to goethite (a) and hematite (b). Note y-axis on a) and b) are not to scale.

In this work, goethite and hematite were obtained using similar synthetic conditions such as chemicals used, pH and temperature and time of reaction. Differences in the extent of plutonium interaction with the two mineral phases (

Figure 5-7) may be explained by considering the crystal chemical constraints imposed by the goethite (FeOOH) and hematite (Fe_2O_3) structure (Figure 5-8). In both minerals, there is one symmetrically independent iron site in octahedral coordination. In hematite, each Fe octahedron shares one face, two edges and three vertices with adjacent polyhedra. The edge sharing of the octahedra (Figure 5-8b) creates a dense (5.3 g/cm^3) and compact structure. In goethite, each polyhedron shares three edges and three vertices with adjacent polyhedral (Figure 5-8c). These features together with the presence of hydroxo-groups results in a more open, less dense structure (4.2 g/cm^3), that may be more likely to accommodate plutonium.

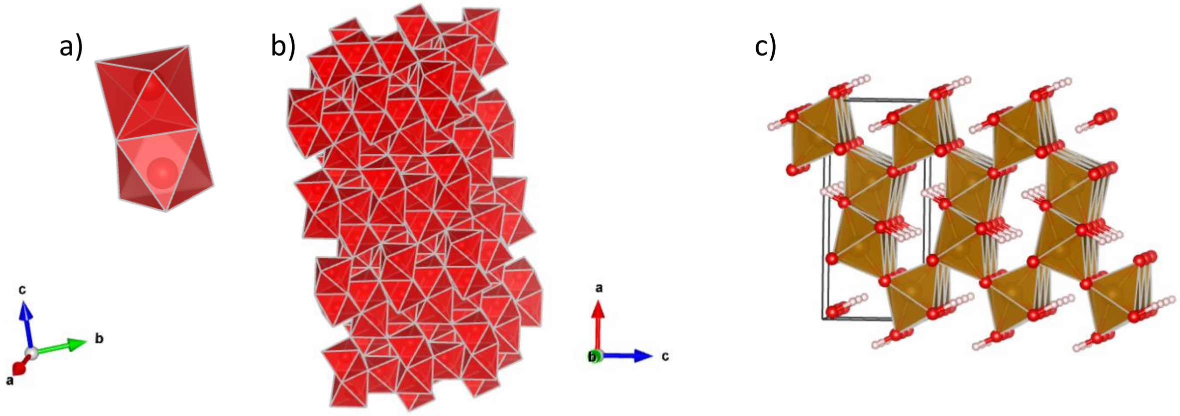

Figure 5-8. Polyhedral representation of the framework structure of hematite (a and b) and goethite (c). The iron coordination polyhedral are colored in red for hematite and brown for goethite.

Samples GA-3000 and GB-3000 were selected for x-ray adsorption spectroscopy (XAS) analysis at the Stanford Synchrotron Radiation Light Source (SSRL). In general, the XANES (X-ray absorption near edge structure) region of the XAS spectra provides information on oxidation state changes in the samples based on comparisons to standard reference materials. The EXAFS (extended X-ray absorption fine structure) region is fit to determine the nearby neighbors and their distances from the plutonium site.

The XANES region of the spectra confirmed that in samples GA-3000 and GB-3000 plutonium is present in the tetravalent oxidation state. However, the EXAFS spectra of samples GA-3000 and GB 3000 are different, suggesting that plutonium has different coordination environments in the two samples (Figure 5-
9,
Figure 5-10 and

Table 5-3). The GB-3000 EXAFS spectrum could be fit to the model structure of PuO_2, with four plutonium atoms at a distance of 3.82Å (

Table 5-3, Figure 5-9). This structural feature indicates that plutonium is likely present as a surface precipitate on sample GB-3000. Presence of surface bound plutonium oxides was confirmed by TEM imaging (Figure 5-9b). The GA-3000 spectrum could not be fit with a PuO_2 model. In GA-3000, plutonium is coordinated by eight oxygen atoms at 2.25(1)Å in the first coordination sphere. These bond distances are slightly shorter than the Pu-O bond distances of GB-3000, 2.31(1)Å (

Table 5-3). In GA-3000, only two plutonium atoms could be found at distances comparable to the structure of PuO_2. Furthermore, an additional peak in the Fourier transform suggests that the dominant structure surrounding Pu in GA-3000 is distinct from PuO_2. Additional data fitting is underway to determine if the EXAFS spectra are representative of Pu substitution for Fe in the goethite structure. Nevertheless, these results clearly indicate that the timing of Pu addition in the synthetic procedures (Method A or B) affects the final form of plutonium associated with goethite.

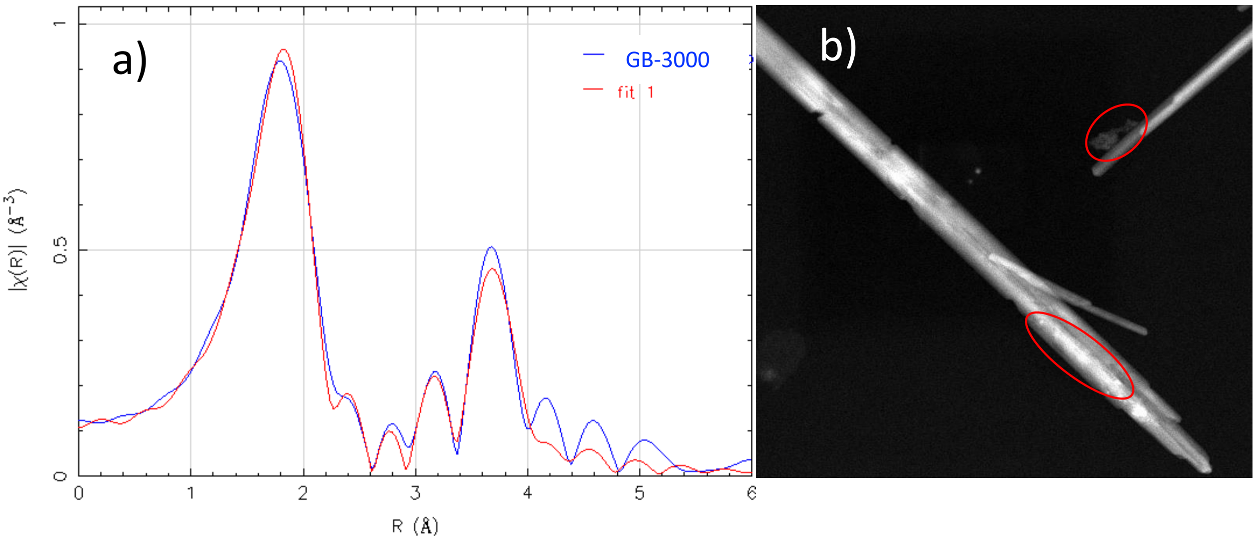

Figure 5-9. Fourier transforms in R (Å) of the calculated EXAFS spectra for sample GA-3000 (left) Blue line= experimental data; red line = model fit (a). STEM images of sample GB-3000, circled in red are areas of the samples where Pu surface precipitation was observed.

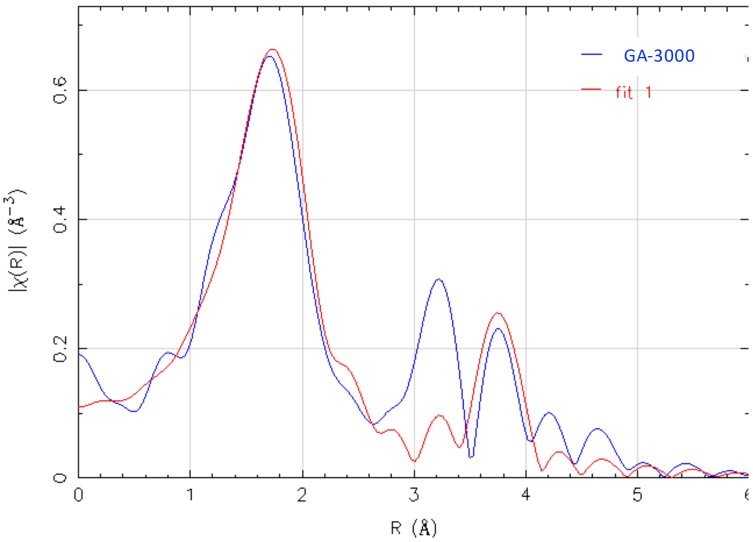

Figure 5-10. Fourier transforms in R (Å) of the calculated EXAFS spectra for sample GA-3000 (left) Blue line= experimental data; red line = model fit using Pu neighbors at ~3.8 Å.

Table 5-3. Ensemble averages of plutonium-oxygen distances and plutonium-plutonium distances in GA-3000 and GB-3000.

Sample	**1st contribution**	**2nd contribution**	**3rd contribution**
GA-3000	8 O at 2.25(1) Å S2 s^2 = 0.0084 Å^2		2.2 Pu at 3.82(1) Å s^2 = 0.003 Å^2
	s_o^2 = 1.0, e_o = 4.74 eV, e = 0.006, r(%) = 0.9		
GB-3000	6.8 O at 2.31(1) Å s^2 = 0.0084 Å^2	1.2 O at 3.26(1) Å s^2 = 0.0069 Å^2	4 Pu at 3.81(1) Å s^2 = 0.003 Å^2
	s_o^2 = 1.0, e_o = 4.74 eV, e = 0.004, r(%) = 0.9		

To date, our results reveal that:

- upon aging of a Pu-doped ferrihydrite precorsor into more crystalline phase, plutonium associates more strongly with goethite (FeOOH) than hematite (Fe_2O_3);
- the timing of Pu addition in the synthetic procedures affects the final form of plutonium associated with goethite.

5.4 Planned FY18 Efforts

In FY18, we plan to continue our efforts in data collection and model development in support of the SFWST program. Our specific FY18 goals for the crystalline and international work pages are the following:

- Completion of the Np(IV) diffusion experiments and quantification of the diffusion rates.
- Evaluation of the radionuclide sequestration potential of corrosion products produced during canister breaching and radionuclide release with an emphasis Pu incorporation into magnetite.
- Continued engagement with the NEA TDB project through the support of Dr. Atkins-Duffin as the NE representative for international thermodynamic database development effort.
- Continued collaboration with HZDR thermodynamic and sorption database development groups in support of the database needs of the UFD program

Our interest in radionuclide sequestration by corrosion products stems from (1) the potential for this process to significant inhibit radionuclide release during canister breaching and (2) from the absence of such processes in most repository performance assessments. Our FY17 experiments have revealed that Pu incorporation into iron oxides corrosion products will be controlled not only by the crystallographic form of the iron oxide but also by the timing of Pu release and iron oxide formation. A natural extension to our initial iron oxide studies is to expand into reduced forms of iron oxides that will likely predominate in a nuclear repository near field. In FY18, we will focus on synthesizing magnetite under reducing (glove box) conditions to examining the oxidation state and incorporation processes that may control Pu release under nuclear waste repository conditions.

5.5 References

Combes, J. M., Manceau, A., and Calas, G., 1990. FORMATION OF FERRIC OXIDES FROM AQUEOUS-SOLUTIONS - A POLYHEDRAL APPROACH BY X-RAY ABSORPTION-SPECTROSCOPY .2. HEMATITE FORMATION FROM FERRIC GELS. *Geochimica Et Cosmochimica Acta* **54**, 1083-1091.

Fischer, W. R. and Schwertmann, U., 1975. FORMATION OF HEMATITE FROM AMORPHOUS IRON(III)HYDROXIDE. *Clays and Clay Minerals* **23**, 33-&.

Liu, J., Liang, C., Zhang, H., Tian, Z., and Zhang, S., 2012. General Strategy for Doping Impurities (Ge, Si, Mn, Sn, Ti) in Hematite Nanocrystals. *Journal of Physical Chemistry C* **116**, 4986-4992.

Marshall, T. A., Morris, K., Law, G. T. W., Livens, F. R., Mosselmans, J. F. W., Bots, P., and Shaw, S., 2014. Incorporation of Uranium into Hematite during Crystallization from Ferrihydrite. *Environmental Science & Technology* **48**, 3724-3731.

Music, S., Gotic, M., and Popovic, S., 1993. X-RAY-DIFFRACTION AND FOURIER-TRANSFORM INFRARED-ANALYSIS OF THE RUST FORMED BY CORROSION OF STEEL IN AQUEOUS-SOLUTIONS. *Journal of Materials Science* **28**, 5744-5752.

Powell, B. A., Dai, Z., Zavarin, M., Zhao, P., and Kersting, A. B., 2011. Stabilization of Plutonium Nano-Colloids by Epitaxial Distortion on Mineral Surfaces. *Environmental Science & Technology* **45**, 2698-2703.

Romanchuk, A. Y., Kalmykov, S. N., and Aliev, R. A., 2011. Plutonium sorption onto hematite colloids at femto- and nanomolar concentrations. *Radiochimica Acta* **99**, 137-144.

Sanchez, A. L., Murray, J. W., and Sibley, T. H., 1985. THE ADSORPTION OF PLUTONIUM-IV AND PLUTONIUM-V ON GOETHITE. *Geochimica Et Cosmochimica Acta* **49**, 2297-2307.

Schwertmann, U. and Cornell, R. M., 2000. Iron oxides in the laboratory, *Iron Oxides in the Laboratory*. Wiley-VCH Verlag GmbH.

Zhao, P. H., Begg, J. D., Zavarin, M., Tumey, S. J., Williams, R., Dai, Z. R. R., Kips, R., and Kersting, A. B., 2016. Plutonium(IV) and (V) Sorption to Goethite at Sub-Femtomolar to Micromolar Concentrations: Redox Transformations and Surface Precipitation. *Environmental Science & Technology* **50**, 6948-6956.

6. INTERPRETATION OF COLLOID-FACILITATED RADIONUCLIDE TRANSPORT EXPERIMENTS IN A CRYSTALLINE ROCK AT THE GRIMSEL TEST SITE, SWITZERLAND

6.1 Introduction

^{137}Cs is considered an environmental health hazard even in trace concentrations because of its short half-life (30.17 years) and strong gamma emission (Zachara et al., 2002). High-level nuclear waste contains substantial amounts of ^{137}C and has leaked into soils and groundwaters in parts of the US and former Soviet Union, and excessive amounts have been released to the environment during nuclear accidents such as Chernobyl and most recently, Fukushima (Zachara et al., 2002; Chino et al., 2011; Takata et al., 2015). Once deposited in the environment, Cs may be remobilized from soils and be assimilated by plants and animals (Comans et al., 1989; Takata et a., 2015). Therefore, understanding the post-depositional fate of ^{137}C is critical in areas affected by nuclear waste.

Cs^+ concentrations are generally low because it strongly adsorbs via cation-exchange to particle surfaces, particularly clays, which have a negative surface charge (Cornell, 1993). Therefore, remediation and prevention efforts at waste repository sites have utilized clay liners to keep ^{137}Cs and other contaminants from entering groundwater systems. In particular, bentonite backfill is an ideal engineering barrier to line deep geological repositories owing to its low permeability, high sorption capacity, and swelling properties (Missana et al., 2004). However, competitive ions may displace ^{137}Cs from sorption sites on sediments, releasing the cation into aqueous solution. For example, ^{137}Cs that was released beneath storage tanks at the Hanford Site was only minimally retarded in some locations due to high concentration of hot Na+ brine that effectively competed with Cs for sorption sites (Zachara et al., 2002; Liu et al., 2003a,b). Perhaps more importantly, the backfill generates bentonite colloids that may have the capacity to transport adsorbed radionuclides (Missana et al., 1999, 2003; Iijima et al., 2010). Low-solubility and strongly adsorbing radionuclides (e.g., Pu, ^{137}Cs) were detected in the colloidal-fraction of groundwaters from the Hanford Site and from the BENHAM nuclear cavity at the Nevada Test Site, sparking numerous studies into the mechanism of colloid-facilitated radionuclide transport. (Buddemeier and Hunt; 1988; Zhuang et al., 2003; Kersting and Reimus, 2003; Huber et al., 2011).

Colloid-facilitated transport becomes a dominant transport mechanism when 1) the radionuclide is irreversibly or very slowly desorbed from the colloids and 2) the colloids to which the radionuclides are sorbed have very slow or irreversible filtration rates; or when 3) the colloids are present in substantial concentrations (Miller et al., 1994; Reimus, 2003). The relative amount of ^{137}Cs transported by a colloid also heavily depends the total ^{137}Cs concentration. Previous work has demonstrated that nonlinear isotherms and multiple partition coefficients (or K_d values) are required to model Cs sorption to colloidal clays (Cornell, 1993; Zhuang et al., 2003; Missana et al., 2004). Thus, a multi-site sorption model is typically employed whereby ^{137}Cs sorbs rapidly to more abundant planar sites on bentonite colloids and more slowly and irreversibly to less abundant but stronger frayed edge sites (Missana et al., 2004). More ^{137}Cs is therefore stripped from the colloids at higher ^{137}Cs concentrations (Zhuang et al., 2003). It follows then that ^{137}Cs transport on colloids is most effective at low concentrations of Cs.

The present study is designed to interrogate the properties of ^{137}Cs adsorption sites on colloids with respect to their potential to promote colloid-facilitated transport of the ^{137}Cs over the long time and distance scales associated with nuclear waste repository performance assessments. ^{137}Cs-bearing colloids in groundwater obtained from the Chancellor nuclear test cavity at the Nevada Nuclear Security Site (NNSS) were used in the experiments reported here. The methods used in this study build on the methods developed in a series of mini-column experiments conducted by Dittrich et al. (2015).

The interrogation of the properties of ^{137}Cs adsorption sites on colloids is dependent not only on the colloids and radionuclide, but also on the properties of the geologic media and the water chemistry in which the transport is occurring because these variables will dictate how strongly the media can compete with the colloids for adsorption of the radionuclide of interest. For this set of experiments, a granodiorite from the Grimsel Test Site and the Chancellor water chemistry were used. This system may not be of practical interest for nuclear waste repositories, but it was chosen for convenience and because previous work had been done with the water, colloids and granodiorite (Reimus and Boukhalfa, 2014). The goal was not to provide data relevant to any specific performance or risk assessment, but rather to demonstrate an interrogation method that could be applied to other systems of practical interest. However, the information obtained from the experiments has the potential to add to the understanding of field observations of colloid-facilitated ^{137}Cs transport at the Grimsel Test Site. Also, additional experiments are planned using ^{137}Cs-bearing bentonite colloids, which will be very relevant for performance assessments in crystalline rock repository systems.

One of the advantages of using the ^{137}Cs-bearing colloids from the Chancellor test cavity is that the nuclear test was conducted about 34 years ago, and the water was collected about 13 years ago, so any aging effects of ^{137}Cs association with the colloids should be well represented. Also, compared to most other nuclear test cavity waters, the Chancellor water has unusually high concentrations of both ^{137}Cs and colloids, which makes it ideal for colloid-facilitated ^{137}Cs transport experiments. It is possible that some of the ^{137}Cs may have become associated with the colloids as they were formed from alteration of glass or other refractory materials formed in the aftermath of the nuclear test. In this regard, there may be a greater potential for very strong associations that might not otherwise occur when ^{137}Cs is adsorbed onto groundwater colloids, and the situation might even be considered to be similar to what might occur in a nuclear waste repository during the formation of waste package or engineered system colloids. The greater possibility for strong associations of ^{137}Cs with the Chancellor water colloids also makes this water ideal for conducting studies in which the objective is to interrogate such strong associations.

It was concluded in previous column experiments with the Chancellor colloids (Reimus and Boukhalfa, 2014) that some of the ^{137}Cs associated with these colloids appeared to be very strongly bound to the colloid surfaces and some was more weakly bound. In a first pass through a column packed with crushed volcanic tuff from the vicinity of the Chancellor cavity, about 80% of the ^{137}Cs associated with the colloids desorbed onto the tuff. However, when the colloids that passed through the column were run through the column a second time, only about 40% of the remaining ^{137}Cs associated with the colloids desorbed, and in a third pass of the colloids through the column, hardly any of the ^{137}Cs that remained on the colloids after the second pass desorbed. This behavior suggests that after each pass through the column, the ^{137}Cs that remained adsorbed to the colloids was more strongly bound than the ^{137}Cs that was associated with the colloids prior to that pass. Each successive pass appeared to preferentially remove ^{137}Cs from weaker adsorption sites on the colloids and leave ^{137}Cs associated with stronger adsorption sites. The behavior of the strongest sorption sites are of greatest interest for colloid-facilitated transport over long time and distance scales because these are the sites that will contribute the most to dose/risk estimates over such scales.

The Grimsel granodiorite was expected to be a weaker adsorbent for ^{137}Cs than the NNSS volcanic tuff, although it was not known how much weaker. In the experiments of this study, a large volume of Chancellor groundwater containing both colloid-associated ^{137}Cs and solute ^{137}Cs was injected through a relatively small column packed with granodiorite, with the intent being to push the granodiorite to the limits of its ability to attenuate the transport of the ^{137}Cs. However, prior to reaching this limit, it was anticipated that there would be a noticeable decrease in the concentrations of both colloid-associated ^{137}Cs and solute

^{137}Cs, and that very little, if any, of the solute ^{137}Cs would transport through the column initially. The predominantly colloid-associated ^{137}Cs eluting through the column during the early portion of the column experiment would be collected and run through a second column packed with the granodiorite to determine whether the ^{137}Cs remaining on the colloids was more strongly associated with colloids than the ^{137}Cs associated with the starting colloids. Unlike the previous experiments with the NNSS volcanic tuffs, the second pass and any subsequent passes would not be through the same column as the first pass, but rather they would be run through columns packed with fresh granodiorite. Also, flow interruptions were planned during any subsequent passes to increase the residence time that the ^{137}Cs-bearing colloids remained in contact with the granodiorite, thus allowing interrogation of slower desorption rates.

6.2 Materials and Methods

6.2.1 Materials

The Grimsel Granodiorite was crushed and sieved to obtain particles between 75-500 µm. The crushed granodiorite material was then packed into mini-columns, as outlined by Dittrich et al. (2015). Mini-columns are ideal for radionuclide transport studies because they allow for quick evaluation of radionuclide and colloid transport, require small amounts of sediment material, and generate minimal radioactive waste (Dittrich et al., 2015). The columns were constructed from Teflon® tubes with a diameter of 0.9 cm and cut to ~ 11 cm length. Each column was tightly packed with ~11 g of the crushed granodiorite, which allowed for ~ 4 mL pore volumes (Table 6-1). The procedure(s) for the column experiments are discussed in Section 6.2.3.

Table 6-1. Column parameters. Porosity is calculated assuming a granodiorite density of 2.65 g/cm^3

	Length (cm)	Weight sediment (g)	Pore Volume (mL)	Porosity
1	11.3	10.7893	4.1098	0.50
2	11.2	10.7018	4.1350	0.51

Besides having high concentrations of colloids and ^{137}Cs, the Chancellor cavity water also has a high concentration of ^{3}HHO. The naturally high ^{3}HHO concentrations provide an ideal conservative tracer to determine breakthrough and transport parameters. Furthermore, the association of the ^{137}Cs with the colloids was already quite well known (Reimus and Boukhalfa, 2014; Reimus et al., 2006; Rose et al., 2011). Water from the top of an undisturbed 55-gallon drum of Chancellor water was pumped into Nalgene® bottles for use in the experiments using a peristaltic pump.

Synthetic water was prepared to match the composition of Chancellor cavity water without the presence of radionuclides or colloids. This water was used to saturate the columns prior to the experiments and as the background solution injected into all of the columns before and after injection of the Chancellor water. The composition was altered slightly to account for the lower temperature (and lower silica solubility) in the experiments relative to in the Chancellor cavity. The pH was also lowered (adjusted with HCl and KOH) to account for the lower atmospheric pressure in Los Alamos (Reimus and Boukhalfa, 2014). The composition of the synthetic water was verified by inductively coupled plasma – optical emission spectrometry (ICP-OES) measurements for cations and ion chromatography (IC) for anions (Table 6-2).

Table 6-2. Composition of the synthetic Chancellor Water

Ion	Measured (mg/L)	Recipe (mg/L)
SO_4^{2-}	69.2	63.4
Cl^-	35.8	26.9
SiO_2	19.1	25.0
Na^+	90.8	96.0
K^+	4.80	4.67
Ca^{++}	1.12	1.12
Mg^{++}	0.14	0.46
pH	8.7	8.7

6.2.2 Analytical Methods

^{3}HHO and ^{137}Cs were analyzed by liquid scintillation counting (LSC), with approximately 2 mL of a given sample pipetted into a plastic liquid scintillation vial, to which 18 mL of Ultima Gold AB scintillation cocktail was added. The samples were shaken and refrigerated until analysis. Samples were analyzed using a Perkin-Elmer Quantulus liquid scintillation counter. Each sample was counted 3 times for 60 min per iteration. The peaks for ^{3}HHO and ^{137}Cs are readily separated because of the much lower decay energy and higher abundance of ^{3}HHO compared to the ^{137}Cs. The long counting times were necessary to quantify the low ^{137}Cs concentrations.

Rose et al. (2011) previously determined that the dominant fission product in Chancellor water is ^{137}Cs. Therefore, no corrections were made to subtract other radionuclides from the spectra. The ^{3}HHO peak was readily distinguished from the edge of the ^{137}Cs peak at 280 keV. The channels between 1 and 280 keV were summed to determine the ^{3}HHO counts per minute per ml (CPM/ml), whereas those between 280 and 800 keV were summed to determine the ^{137}Cs CPM/ml. Figure 6-1 shows the raw spectra of the Chancellor water. The ^{137}Cs counts for the filtered Chancellor water were about half of the unfiltered Chancellor water, indicating that about half of the ^{137}Cs is in the dissolved phase and half in the colloidal phase. This partitioning is in good agreement with other measurements of Chancellor water (Reimus et al., 2006; Reimus and Boukhalfa, 2014).

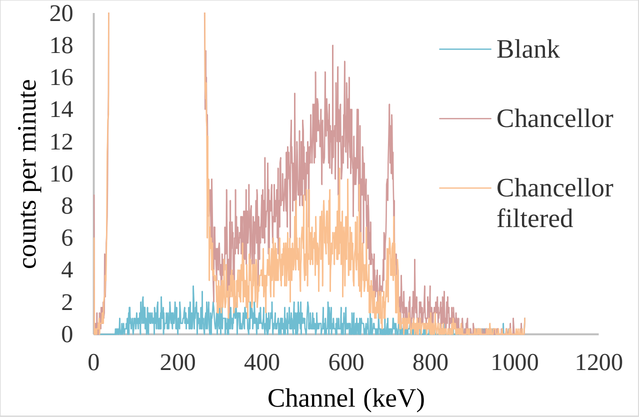

Figure 2-1. Raw spectra of the Chancellor water and filtered Chancellor water. The ^{3}HHO peak is truncated to emphasize the ^{137}Cs peak.

Colloid concentrations were determined by turbidity, which was measured using a Hach® 2100N turbidimeter. Turbidity measurements are known to be well correlated with colloid concentrations if the sizes and shapes of the colloids remain relatively stable in all samples, which was assumed to be the case here because the origin of the colloids was the same (i.e., the Chancellor water). The instrument was calibrated to obtain a relationship between nephelometric turbidity units (NTUs) and % Chancellor water, in "standards" prepared by diluting the Chancellor water with colloid-free deionized water that had zero measurable turbidity (Fig. 6-2). The calibration curve was then used to determine the colloid concentrations in unknown samples *relative to* the colloid concentration in the Chancellor water. The turbidity of the Chancellor water ranged from 7.89 to 8.08 NTU, and the practical lower detection limit was below 0.2 NTU, so the detection limit was effectively only 2-3 percent of the Chancellor water turbidity, and the calibration curve was essentially linear over the entire range. The absolute colloid concentration in the Chancellor water was not measured, but Reimus and Boukhalfa (2014) previously reported a value of 0.12 g/L for water that had been vigorously stirred before collection out of the 55-gallon drum of water. Thus, the unstirred water used in this study was assumed to have a slightly lower absolute colloid concentration of 0.1 g/L. This value was used as an assumption in the modeling calculations, and it has a minor effect on the reported model parameter values, but it otherwise has little bearing on the results of this study. The turbidity measurements were not destructive, so unlike the 2 ml that was used for LSC measurements, the water that was measured by turbidity could be poured back out of the vials and reused in another column.

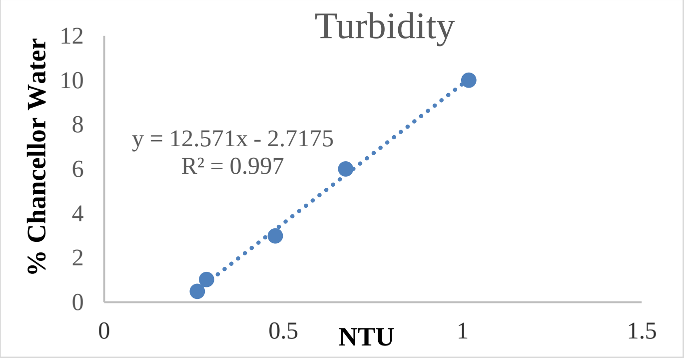

Figure 2-2. Calibration of the turbidity measurements as a function of NTU relative to Chancellor water

6.2.3 Column Experiments

The granodiorite-packed columns were saturated with the synthetic Chancellor water following the procedure of Reimus and Boukahalfa (2014). The saturation procedure ensures that no air pockets exist within the column that may impede the flow of colloids. Prior to saturation, the air in the void space of the columns was exchanged with CO_2, and then alternating treatments of vacuum and CO_2 flushing were applied, with the final step being a vacuum. Then, degassed synthetic water was introduced to the columns under vacuum. The columns were then aligned vertically and held in place with a C-clamp. The inlet of the column was attached to a syringe pump (KD Scientific 60 cc syringe) using PEEK tubing. The flow rate was set to 0.5 mL/hr, which established an 8-hour residence time of the solution in the column. The outlet of the column was attached with PEEK tubing to a Foxy Jr.® fraction collector. Collection times were set for 6 hours in order to collect the 3 mL of sample necessary for both turbidity and LSC analysis. The samples were collected in the fraction collector in glass vials, which were shown in separate tests to retain an insignificant amount of ^{137}Cs from the Chancellor water on their walls.

Small aliquots (1.5-2 mL) of the Chancellor water that was injected into the columns and also selected samples eluted from the columns were hand filtered (Whatman^{TM} 0.02 um) to obtain estimates of the "dissolved" or "solute" fraction of ^{137}Cs in the samples. Unfiltered samples were analyzed to determine the total ^{137}Cs, and the difference between the total and filtered ^{137}Cs was considered to be associated with the colloids.

~450 mL of degassed Chancellor water was injected into one of the columns after the column had been flushed with synthetic Chancellor solution until colloid concentrations eluting from it were stable and very low compared to the Chancellor water. The concentrations of ^{3}HHO, ^{137}Cs (both filtered and unfiltered), and colloids were measured in selected samples, but approximately every other sample was saved for injection into a second column. After the concentrations of all constituents reached their levels in the Chancellor water (indicating the granodiorite in the column was no longer adsorbing any ^{137}Cs or filtering colloids), the flow through the column was stopped for ~ 3 days. After 3 days, ~0.6 mL was slowly syringed back and forth through the column to liberate any colloids that may have stuck in the column during the flow interruption, and the 0.5 ml/hr flow rate was re-established. This procedure was done to determine whether there was either a net loss or a net gain of colloids resulting from the flow interruption and the back-and-forth swishing procedure. If there was little or no net loss or gain of colloids after the interruption, it would indicate that this procedure was effective in remobilizing colloids and not generating new colloids from the granodiorite. In this case, the procedure would be shown to be effective in increasing the residence time of the ^{137}Cs-bearing colloids in the column without resulting in irreversible loss of the colloids, which would complicate test interpretations. The flushing of the column was continued until the ^{3}HHO, ^{137}Cs, and colloid concentrations returned to that of the Chancellor water, and then the injection water was switched over to synthetic Chancellor water to elute the retained ^{137}Cs out of the column. The elution procedure was still in progress and ^{137}Cs concentrations exiting the column were still elevated over background at the time of writing this report. The elution will continue until background concentrations are reached so that a mass balance on the entire inventory of ^{137}Cs injected into the column can be calculated.

The granodiorite was expected to adsorb any dissolved ^{137}Cs or any ^{137}Cs weakly bound to the colloids until the adsorption capacity of the granodiorite was nearly exhausted. Over time, more and more solute ^{137}Cs and ^{137}Cs weakly bound to colloids was expected to break through the columns, and when all the adsorption capacity of the granodiorite was expended, the Chancellor water was expected to pass through the column unaffected by the granodiorite. The intent was to pool together many of the early samples eluting through the column, which were expected to predominantly contain ^{137}Cs that was strongly-bound to colloids, for injection into a second column. The samples to pool together were determined from the ^{137}Cs and colloid breakthrough curves from the column, and the pooled samples were then injected into a second column to determine whether the strongly colloid-bound ^{137}Cs would remain on the colloids or be stripped by the granodiorite. The colloid-associated ^{137}Cs concentrations remained relatively constant for approximately the first 108 ml, or approximately 26 pore volumes, that was eluted through the column, and then the concentrations began to sharply increase (see next section for results), suggesting that the granodiorite adsorption capacity was being reached. Of the first 108 ml, only about 45 mL was available for injection into the second column because of the solution volume that was expended by liquid scintillation counting. Most of this 45 ml was injected into a second column, and because of the relatively small volume of this injection, a flow interruption of nearly 3 days was introduced after only about 24 ml had passed through the column. The column flow was then re-established after employing a similar syringe swishing procedure as in the first column to remobilize any filtered colloids (see above), and samples were collected to determine the colloid and ^{137}Cs concentrations after the flow interruption. There was not enough volume remaining in the samples collected from the second column to consider an injection of the column effluent into a third column.

6.3 Results and Interpretation of Column Experiments

6.3.1 Results

To date, only the results from the first column injection of the Chancellor water through the granodiorite and preliminary results from the second pass, including the flow interruption during the second pass, are available. Figure 2-3 shows that essentially 100% of the colloids eluted through the first and second columns after the first pore volume, suggesting that none of the colloids were filtered by the granodiorite material. In the sample following the flow interruption in column 1, the turbidity slightly increased, but the increase was relatively minor and in only one sample, implying that the Chancellor colloids were remobilized (if they had ever become immobilized at all) and there were very few new colloids liberated from the granodiorite by the interruption and syringe swishing procedure. Synthetic Chancellor water devoid of colloids was then injected, and the colloid concentration dropped rapidly. In column 2, the turbidity reached a steady value that was about 1.2 times the value of unfiltered Chancellor water, but this value was in agreement with the injection solution consisting of pooled samples from the early portion of column 1, so the additional turbidity cannot be attributed to colloids generated in column 2. The reason for the increase in turbidity of the pooled samples is unknown, but it was not considered important because this additional turbidity passed through the second column without being affected, and thus it could be assumed that all of the ^{137}Cs-bearing colloids present in the pooled samples also passed through the column.

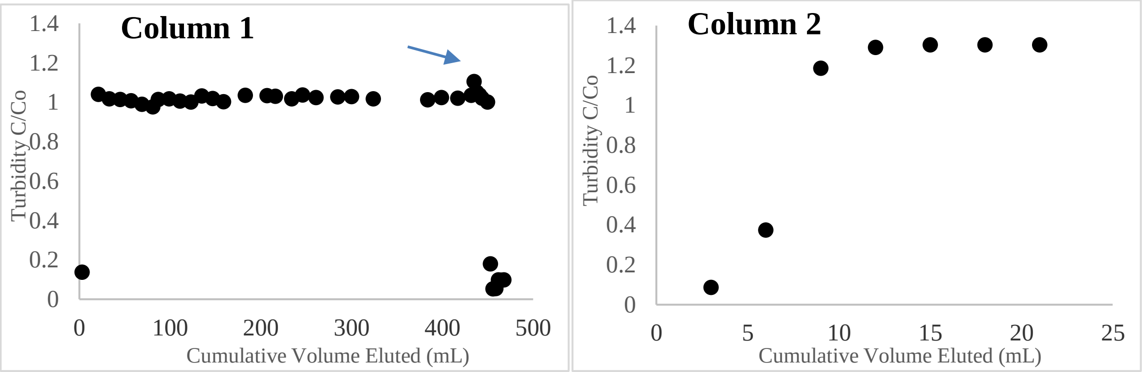

Figure 6-3. Turbidity (NTU) of the effluent from the first and second columns graphed as a function of Chancellor water turbidity. The flow interruption in column 1 is designated by the blue arrow.

Figure 6-4 shows the the solute and total ^{137}Cs breakthroughs from the first granodiorite column, along with the breakthrough of ^{3}HHO, which was conveniently present at high concentrations in the Chancellor water. Note the vastly different concentrations of ^{3}HHO and ^{137}Cs, plotted against the different vertical axes. The measurements of solute ^{137}Cs were obtained (by filtration) for only a few of the samples, and they were interpolated for the remaining samples for the modeling exercise discussed below. The colloid-associated ^{137}Cs concentrations in all cases were calculated as the difference between the total measured ^{137}Cs and the filtered ^{137}Cs concentrations (interpolated in most cases). The dashed lines show the approximate concentrations of the solute and total ^{137}Cs in the injected Chancellor water, with the difference being the colloidal ^{137}Cs.

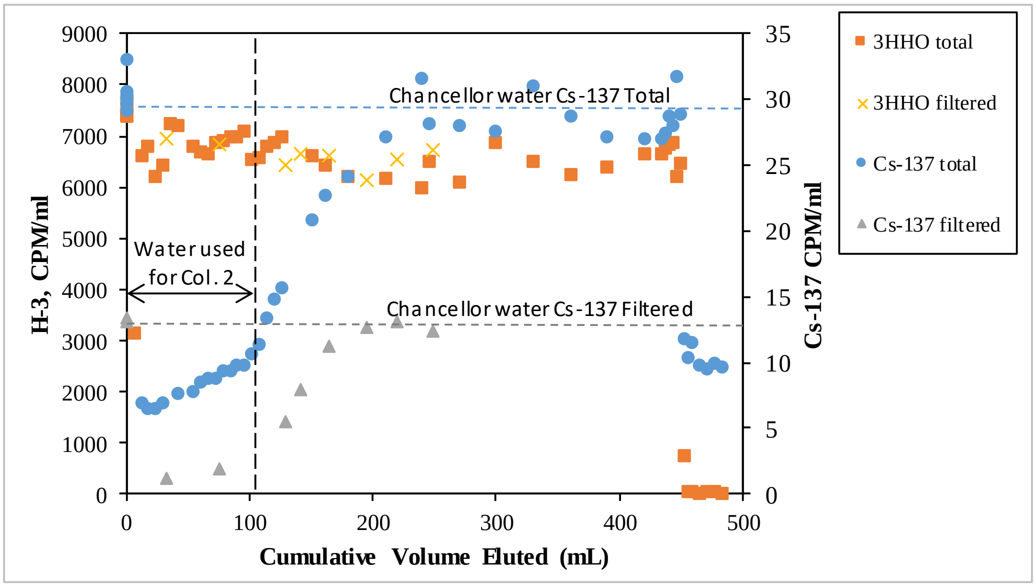

Figure 6-4. Measured breakthrough curves of ^{3}HHO and ^{137}Cs in Column 1. All points plotted at a cumulative volume of zero are measurements of the injected Chancellor water. The vertical dashed line indicates the samples that were pooled together for the injection into column 2. The horizontal dashed lines show the total and filtered ^{137}Cs concentrations in the injected Chancellor water.

It is apparent from Figure 6-4 that the initial breakthrough of ^{137}Cs occurred at the same time as ^{3}HHO, and the breakthrough was primarily ^{137}Cs associated with colloids. However, it is also apparent that more than half of the ^{137}Cs that was initially associated with the colloids desorbed from the colloids during the ~8-hr travel time through the column. As the experiment progressed, the solute ^{137}Cs concentrations slowly increased while the colloid-associated ^{137}Cs concentrations remained relatively steady for many pore volumes. The colloid-associated ^{137}Cs concentrations did not noticeably increase until about 26 pore volumes had passed through the column, but at that point, the rate of increase in concentrations of both solute and colloid-associated ^{137}Cs rose significantly, indicating that the granodiorite was approaching its adsorption capacity for ^{137}Cs. By the time 50 pore volumes had passed through the column, it was apparent that no more ^{137}Cs was being retained, as the total ^{137}Cs concentrations exiting the column were the same as those entering the column, with approximately the same ratio of colloidal and solute ^{137}Cs in both the entrance and exit as well.

All of the column effluent water that had not been expended by LSC analyses, up to the first 26 pore volumes (indicated by the dashed vertical line in Figure 6-4), was combined and injected into the second column packed with crushed granodiorite. Figure 6-5 shows the preliminary ^{137}Cs breakthrough curves from the second column, including the flow interruption that was implemented. The combined water was analyzed just prior to the injection, and the total and solute concentrations of ^{137}Cs are shown in Figure 6-5. It is apparent that the effluent ^{137}Cs concentrations in this column experiment reached a higher fraction of the injection concentration than in the first column, with a much higher percentage of the colloid-associated ^{137}Cs remaining associated with the colloids than in the first column. During the initial part of the first column experiment, only about 45% of the colloid-associated ^{137}Cs that was injected into the column remained associated with the colloids, but in the second experiment, nearly 90% of the colloid-associated ^{137}Cs remained associated with the colloids. It is also apparent that this association remained essentially unchanged after the 70-hr flow interruption, which occurred at a time in the experiment when there should have been plenty of available adsorption sites to compete for ^{137}Cs on the granodiorite (based on the results from the first column, which was packed with the same batch of crushed granodiorite). The apparent lack of desorption of ^{137}Cs from the colloids during the 70-hr flow interruption provides a good constraint for the rate constant for desorption of the ^{137}Cs remaining on the colloids at this time.

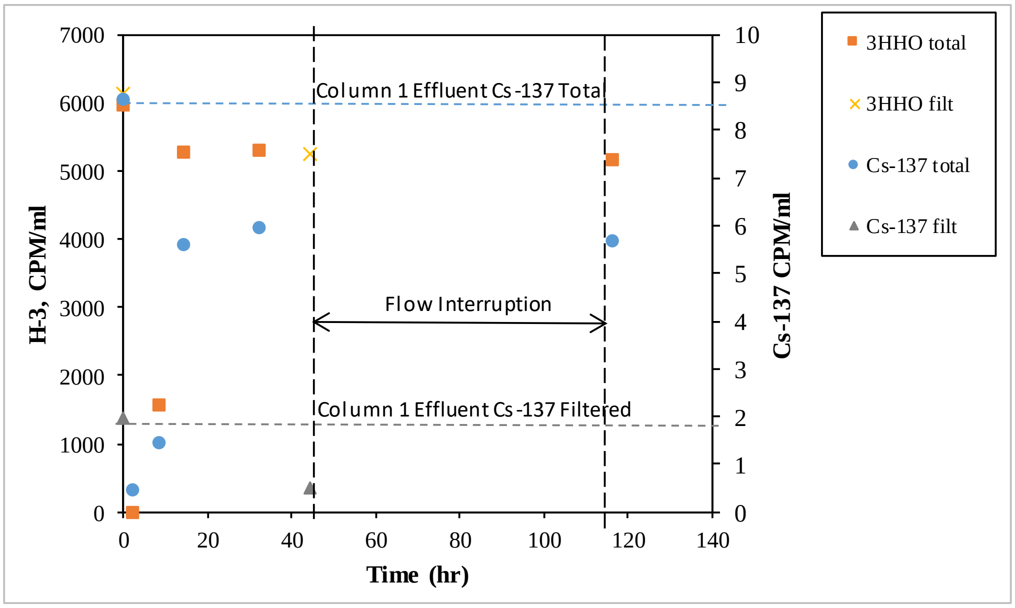

Figure 6-5. Measured breakthrough curves of ^{3}HHO and ^{137}Cs in Column 2 (plotted vs. time to illustrate the flow interruption). All points plotted at a cumulative volume of zero are measurements of the injected water from the pooled Column 1 samples. The horizontal dashed lines show the total and filtered ^{137}Cs concentrations in the injected Chancellor water.

6.3.2 Interpretations

The column transport experiments provided a unique opportunity to test the colloid-facilitated radionuclide transport capability described in Reimus et al. (2016) and Reimus (2017). In most previous cases in which this model had been run, including all of the benchmarking test cases documented in Reimus (2017), the adsorption site capacity on both the colloids and the immobile geologic media had been set to very high values. In such cases, these parameters do not come into play in the model predictions because the surfaces always behave as though there is an overabundance of sites, and sorption isotherms are therefore always linear. However, in the experiments conducted for this study, it became apparent that a limited sorption site capacity for a stronger sorption site on the colloids was necessary to explain the results.

The model, condensed to include only the terms needed to match the observed ^{137}Cs transport behavior in this study, is as follows:

Mobile Colloid Transport in Fractures (assumed to be conservative – no filtration):

$$\frac{\partial C_c}{\partial t} + div(v_c C_c - D_c \nabla C_c) = 0 \qquad (6\text{-}1)$$

Mobile Solute in Fractures:

Advective and Dispersive Transport: $\frac{\partial C_a}{\partial t} + div(v_a C_a - D_a \nabla C_a) =$ (6-2)

Reactions with Immobile Surfaces (1 sorption site): $-k_{as}\frac{\rho_B}{\emptyset}C_a\left(1-\frac{S_a}{S_{a,max}}\right)+k_{sa}\frac{\rho_B}{\emptyset}S_a+$

Reactions with Mobile Colloids (2 sites): $\sum_{i=1}^{2}\left[-k_{ac,i}C_aC_c\left(1-\frac{C_{ac,i}C_c}{C_{ac,max,i}C_c}\right)+k_{ca,i}C_{ac,i}C_c\right]$

<u>Solute Adsorbed onto Immobile Surfaces in Fractures</u>:

$$\frac{\partial S_a}{\partial t}=k_{as}C_a\left(1-\frac{S_a}{S_{a,max}}\right)-k_{sa}S_a \qquad (6\text{-}3)$$

<u>Solute Adsorbed onto Mobile Colloids in Fractures (2 equations; *i* = 1, 2)</u>:

$$\frac{\partial C_{ac,i}C_c}{\partial t}+div\left(v_aC_{ac,i}C_c-D_c\nabla C_{ac,i}C_c\right)=k_{ac,i}C_{ac,i}C_c\left(1-\frac{C_{ac,i}C_c}{C_{ac,max,i}C_c}\right)-k_{ca,i}C_{ac,i}C_c \qquad (6\text{-}4)$$

where, C_c = concentration of colloids in mobile phase, g/cm^3
C_a = solution concentration of solute in mobile phase, g/cm^3
S_a = adsorbed concentration of solute on granodiorite, g/g
$C_{ac,i}$ = concentration of solute sorbed to colloid site *i*, g/g colloid
$S_{a,max}$ = maximum adsorbed concentration of solute on granodiorite, g/g
$C_{ac,max,i}$ = maximum concentration of solute sorbed to colloid site *i*, g/g colloid
v_c = advective velocity of colloids in column, cm/hr
v_a = advective velocity of solutes in column, cm/hr
D_a = solute dispersion coefficient in column, cm^2/hr
D_c = colloid dispersion coefficient in column, cm^2/hr
ρ_B = effective bulk density within granodiorite, g/cm^3
$\emptyset$ = porosity within granodiorite
k_{as} = rate constant for sorption of solute onto granodiorite, cm^3/g-hr
k_{sa} = rate constant for desorption of solute from granodiorite, 1/hr
$k_{ac,i}$ = rate constant for sorption of solute onto colloid site *i*, cm^3/g-hr
$k_{ca,i}$ = rate constant for desorption of solute from colloid site *i*, 1/hr

When only the breakthrough curves for the injection of Chancellor water into the first granodiorite column were considered, it was found that the solute and colloid ^{137}Cs responses could be accounted for reasonably well with one adsorption site on the colloids. A comparison between the data and model is shown in Figure 6-6, and the model parameters corresponding to the model curves of Figure 6-6 are listed in Table 6-3. It is apparent that the colloid ^{137}Cs response was not matched as well as the solute ^{137}Cs response. Note that model was constrained to have a ratio of adsorption to desorption rates for ^{137}Cs on the colloids that yielded the observed ^{137}Cs partition coefficient in the Chancellor water. In this case, the adsorption site capacity on the colloids was assumed to be quite large relative to the amount of ^{137}Cs adsorbed to the colloids.

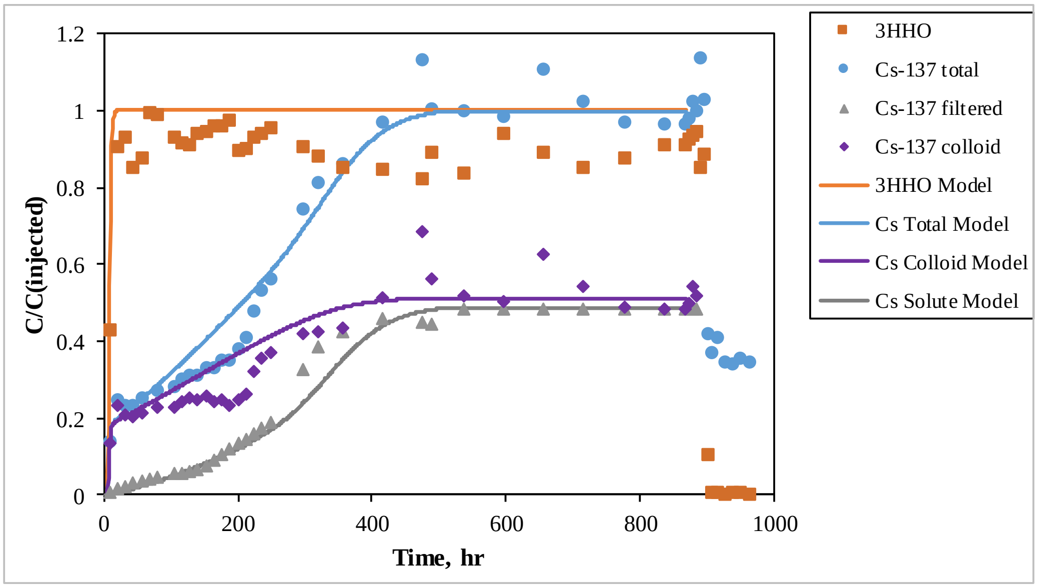

Figure 6-6. Matches of a single-adsorption-site model to the ^{3}HHO and ^{137}Cs breakthrough curves of Column 1 up to the time of the injection of synthetic Chancellor water. Filtered data points that appear here but not in Figure 2-4 are from interpolation of filtered ^{137}Cs data. Colloid data points were calculated as difference between total and filtered ^{137}Cs concentrations. All concentrations are normalized to the concentrations of either total ^{3}HHO or ^{137}Cs in unfiltered Chancellor water.

Table 6-3. Model parameters yielding the single-adsorption-site model curves of Figures 6-6 and 6-7

Parameter	**Value**
Column mean residence time, hr	9
Peclet number (*L*/dispersivity)	50
^{137}Cs $S_{a,max}$, g/g granodiorite	5 x 10^{-11}
^{137}Cs $C_{ac,max}$, g/g colloid	5 x 10^{-8}
^{137}Cs k_{as}, ml/g-hr	100
^{137}Cs k_{sa}, hr^{-1}	5
^{137}Cs k_{ac}, ml/g colloid-hr	1392
^{137}Cs k_{ca}, hr^{-1}	0.12

Notes: *L* = column length; Chancellor colloid concentrations assumed to be 0.1 g/L.

Figure 6-7 shows the match of the single-adsorption-site model to the breakthrough curves for the injection through the second granodiorite column. The model parameters from Table 2-3 were used for the second column, with the total ^{137}Cs activity from the pooled column 1 samples not redistributed between the colloids and the solution phase in the combined injection solution. Rather, the distribution between colloids and solute was left the same as in the samples exiting the column. By not redistributing the ^{137}Cs activity, the fraction of ^{137}Cs on the colloids was kept artificially high and the breakthrough of colloidal ^{137}Cs was thus artificially high in the model simulations. However, as Figure 6-7 shows, the model still significantly underpredicts the colloidal ^{137}Cs breakthrough in the second column. The model also dramatically overpredicts the amount of ^{137}Cs that desorbed from the colloids during the 70-hr flow interruption. It was concluded that at least one additional type of adsorption site on the colloids was needed to achieve a better simultaneous match to the breakthrough curves from both the first and second columns.

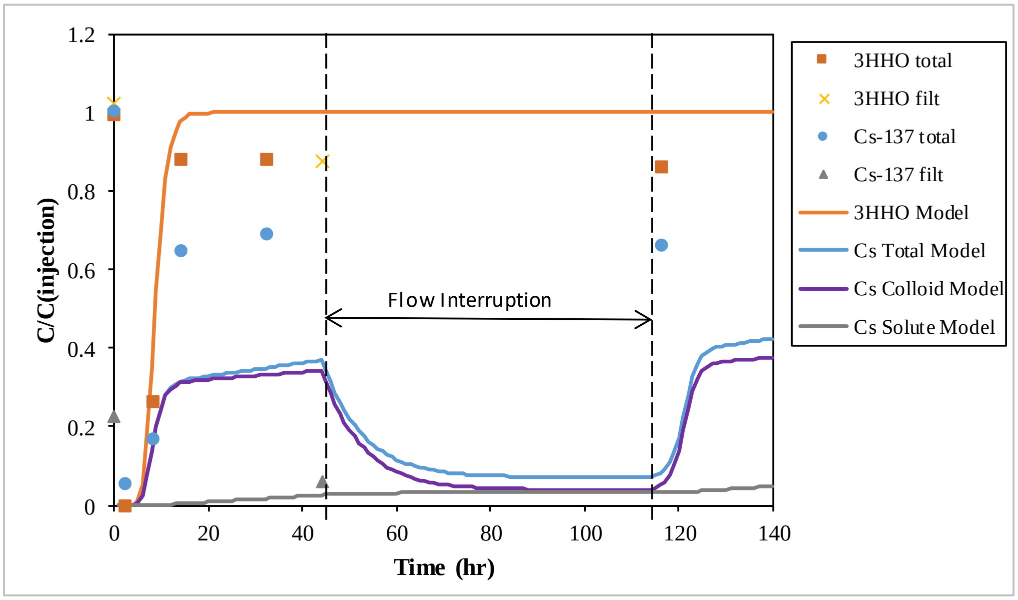

Figure 6-7. Matches of a single-adsorption-site model to the ^{3}HHO and ^{137}Cs breakthrough curves of Column 2. All concentrations are normalized to the concentrations of either total ^{3}HHO or ^{137}Cs in the pooled samples from Column 1 that were injected into column 2. Data points at time zero correspond to the concentrations measured in the pooled samples.

Figure 6-8 shows the results of matching a two-adsorption-site model to the ^{137}Cs solute and colloid breakthrough curves in the first column. The model parameters associated with this match to the data are listed in Table 6-4. Again, the model parameters were constrained to yield the partitioning of ^{137}Cs between the colloid and solution phases that is measured in the Chancellor water. The introduction of a second site that is relatively low in abundance but much stronger than the first site clearly improves the match to the data relative to that shown for a single-site model in Figure 6-7. The model predictions for the breakthrough curves in the second column, using the parameters listed in Table 6-4, are shown in Figure 6-9. In this case, the ^{137}Cs activity in the pooled samples from the first column was redistributed in the combined injection solution according to parameters of Table 6-4. This redistribution resulted in some of the ^{137}Cs on the colloids desorbing, and therefore the solute ^{137}Cs concentration in the injection solution was higher by about 40% relative to what the model predicted for the combined samples as they eluted from the first column. Essentially all of the ^{137}Cs that was predicted to have desorbed from the colloids came from the weaker, more abundant adsorption site on the colloids. We note that despite the redistribution of ^{137}Cs activity from the colloids to the solution phase, the predicted ^{137}Cs activity in solution was still less than what was measured in the actual injection solution. This discrepancy is caused by the fact that the model underpredicts the measured solute ^{137}Cs breakthrough and overpredicts the colloid ^{137}Cs breakthrough in the first column, resulting in an underprediction of solute ^{137}Cs injected into the second column. Even the redistribution of ^{137}Cs from the colloids to the solution phase in the model is not enough to match the measured solution phase ^{137}Cs in the injection solution.

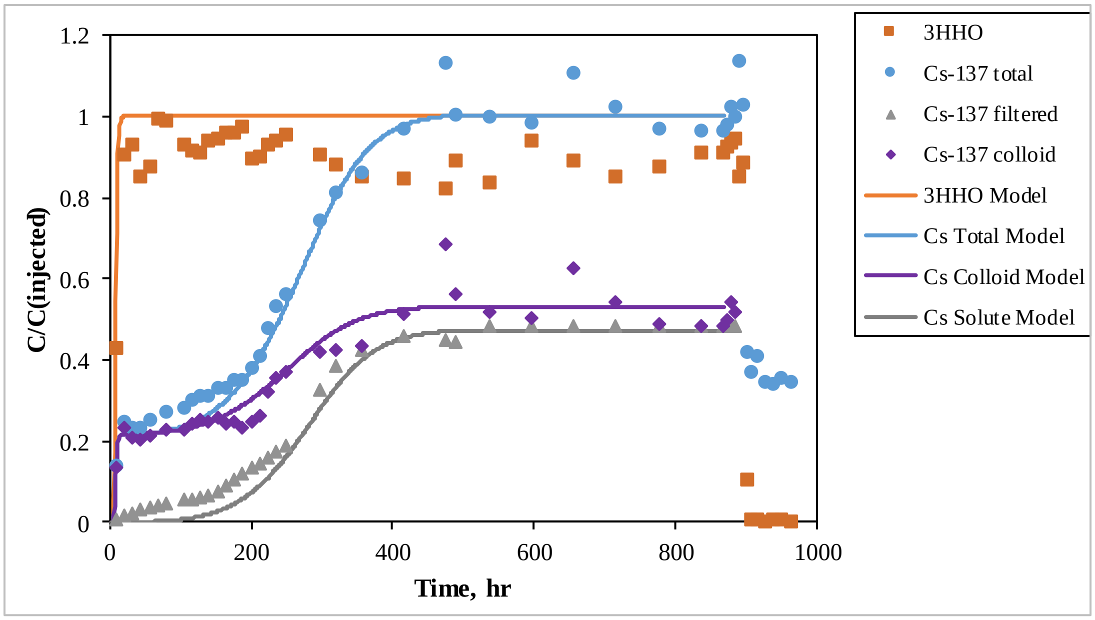

Figure 6-8. Matches of a two-adsorption-site model to the ^{3}HHO and ^{137}Cs breakthrough curves of Column 1 up to the time of the injection of synthetic Chancellor water. Filtered data points that appear here but not in Figure 6-4 are from interpolation of filtered ^{137}Cs data. Colloid data points were calculated as difference between total and filtered ^{137}Cs concentrations. All concentrations are normalized to the concentrations of either total ^{3}HHO or ^{137}Cs in unfiltered Chancellor water.

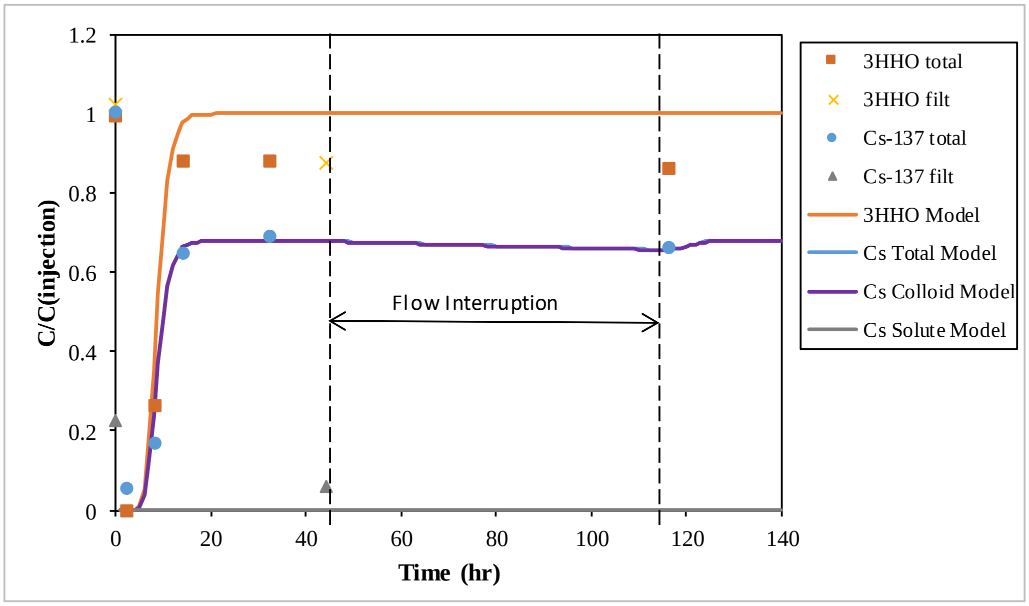

Figure 6-9. Matches of a two-adsorption-site model to the ^{3}HHO and ^{137}Cs breakthrough curves of Column 2. All concentrations are normalized to the concentrations of either total ^{3}HHO or ^{137}Cs in the pooled samples from Column 1 that were injected into column 2. Data points at time zero correspond to the concentrations measured in the pooled samples.

Table 6-4. Model parameters yielding the two-adsorption-site model curves of Figures 6-8 and 6-9

Parameter	Value
Column mean residence time, hr	9
Peclet number (*L*/dispersivity)	50
^{137}Cs $S_{a,max}$, g/g granodiorite	5 x 10^{-11}
^{137}Cs $C_{ac,max.1}$, g/g colloid	5 x 10^{-8}
^{137}Cs $C_{ac,max.2}$, g/g colloid	2.29 x 10^{-9}
Fraction of colloidal ^{137}Cs initially on colloid site 1	0.586
^{137}Cs k_{as}, ml/g-hr	110
^{137}Cs k_{sa}, hr^{-1}	5
^{137}Cs $k_{ac,1}$, ml/g colloid-hr	7127
^{137}Cs $k_{ca,1}$, hr^{-1}	1
^{137}Cs $k_{ac,2}$, ml/g colloid-hr	300.
^{137}Cs $k_{ca,2}$, hr^{-1}	0.0005

Note: *L* = column length; Chancellor colloid concentrations assumed to be 0.1 g/L.

It is apparent from Figure 2-9 that the modeled ^{137}Cs transport behavior in the second column is much better with the two-site model than with the single-site model (Figure 6-7). In particular, the fraction of ^{137}Cs that desorbs from the colloids during the initial part of the test, as well as during the flow interruption are both matched quite well. The flow interruption provides a good constraint on the desorption rate constant for the stronger adsorption site, although in retrospect, a better constraint would have been provided if the duration of the flow interruption had been increased because it is apparent that very little (if any) ^{137}Cs desorbed from the colloids during the flow interruption. Figure 6-10 shows the results of a model simulation in which the desorption rate constant of ^{137}Cs from the stronger adsorption site on the colloids was increased by a factor of four over that in Figure 6-9. It is apparent that the larger desorption rate is a little too fast to be consistent with the data, although it is not too fast to be consistent with the data prior to the flow interruption. This clearly illustrates how the flow interruption provides additional constraints on the lower bound for the desorption rate constant. There was some concern that the flow interruption might result in filtration of some of the colloids and thus a decrease in ^{137}Cs concentrations that was not necessarily associated with ^{137}Cs desorption from the colloids. However, the turbidity values in samples collected after the interruption were similar to those before the interruption (and both were slightly higher than the original Chancellor water), which suggests that the interruption did not result in significant colloid filtration. The pushing and pulling of a small amount of water (less than 1 ml) back and forth through the column prior to resuming the flow presumably helped remobilize any colloids that had settled onto granodiorite surfaces in the column. The results of Figures 6-8 and 6-9 suggest that a two-adsorption-site model on the colloids is adequate for representing the ^{137}Cs transport behavior, so a model with three adsorption sites was not attempted. Note that only one type of adsorption site was assumed to be present on the granodiorite in all cases, and this site was considerably weaker than the colloid adsorption sites.

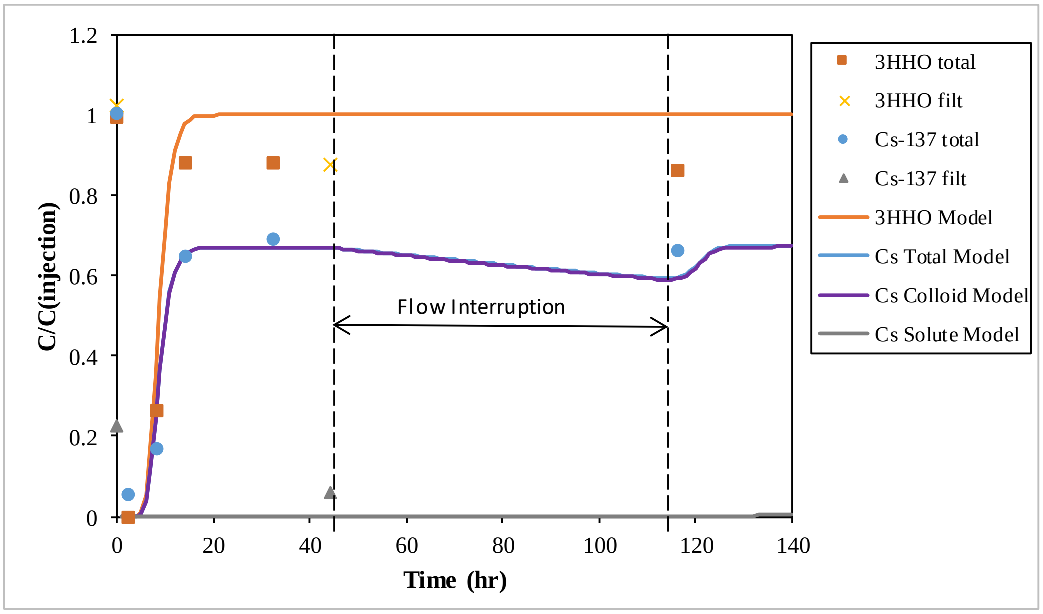

Figure 6-10. Matches of a two-adsorption-site model to the ^{3}HHO and ^{137}Cs breakthrough curves of Column 2 but with the desorption rate constant of the stronger adsorption site on colloids set to 4 times the value used in Figure 2-9 and listed in Table 2-4. All concentrations are normalized to the concentrations of either total ^{3}HHO or ^{137}Cs in the pooled samples from Column 1 that were injected into column 2. Data points at time zero correspond to the concentrations measured in the pooled samples.

6.4 Discussion

The interpretations discussed above clearly show how the injection of a solution from a first column into a second column can provide definitive discrimination between a single-adsorption-site model and a multiple-adsorption-site model on colloids, and they also show how a flow interruption can be used to better constrain the estimate of the all-important slowest desorption rate constant from the colloids. Although there were some discrepancies with modeling the solute ^{137}Cs transport behavior, the colloid ^{137}Cs breakthrough curves in both columns were modeled quite well with a single set of model parameters applied to both column experiments (at least in the case of the two-adsorption-site model). We note that some the of the discrepancies in explaining the solute ^{137}Cs behavior might be the result of some very small colloids passing through the 0.02-μm filters that were used to make the operational distinction between solute ^{137}Cs and colloidal ^{137}Cs. Thus, a portion of the “solute” ^{137}Cs might have actually been associated with very small colloids. This might also explain why the solute fraction of ^{137}Cs was higher than predicted in the injection solution for the second column. However, these discrepancies in predicting the solute transport behavior are of little concern for addressing colloid-facilitated transport of ^{137}Cs over long time and distance scales. The most important parameter for predicting colloid-facilitated transport over such scales is the desorption rate constant of the strongest adsorption site on the colloids because this parameter will dictate how far ^{137}Cs can move with the colloids before desorbing and becoming available for adsorption onto immobile surfaces in the system. The solute transport behavior does not have a significant effect on the estimation of this rate constant, and in fact the most constrained estimate of this parameter comes after the flow interruption in the second column, when solute concentrations were effectively at background levels. The deduced two-adsorption-site behavior of the ^{137}Cs on the Chancellor colloids is similar in many respects to the adsorption behavior of ^{137}Cs that has been reported for other colloids. For example, the nonlinearity of Cs sorption to colloids has been reported Zhuang et al. (2003), de Koning and Comans (2004), and Missana et al. (2004). Cesium is rapidly scavenged from aqueous solution onto planar sites of colloid surfaces, followed by a slower and stronger uptake onto the highly reactive sites that exist at much lower surface coverages (Missana et al., 2004). Therefore, it is not surprising that a small amount of ^{137}Cs is strongly adsorbed to the Chancellor colloids. This is reflected in the differences in the fractions of colloid-bound ^{137}Cs eluted from columns 1 and 2 relative to the colloid-bound fractions injected into each column. In the experiments conducted for this study, the granodiorite used in the columns had a very weak affinity for ^{137}Cs. This affinity was much weaker than in the case of the fracture fill material that was isolated from Grimsel granodiorite for earlier colloid-facilitated ^{137}Cs experiments that were previously reported (Wang et al. 2015, Chapter 8). This weak affinity resulted in a relatively early breakthrough of solute ^{137}Cs and consequently an early transition to having the column effluent look exactly like the injection solution into the column (i.e., unreacted Chancellor water). The original intent was to collect a significant volume of column effluent that contained mainly colloidal ^{137}Cs, with a minimal amount of solute ^{137}Cs, for injection into the second column, but the early transition greatly limited the volume of effluent that was suitable for injection into the second column. Thus, the results shown for the second column in the Section 2.3.1 represent almost the entire amount of water that was available to inject into the second column (after significant volume loss for radionuclide measurements by LSC). It was considered counterproductive to be injecting any solution into the second column that had relatively high solute ^{137}Cs concentrations or a relatively large fraction of colloidal ^{137}Cs adsorbed to weaker adsorption sites on colloids because this effectively dilutes the information obtained from the second column. Thus, the injection into the second column was limited to the remaining volume from the first 26 pore volumes from the first column, which was when relatively steady colloidal ^{137}Cs concentrations were observed that were presumably associated with the stronger adsorption sites on the colloids.

While the early transition of the effluent from the first column to the ^{137}Cs concentrations and solute-colloid distributions in the Chancellor water was a disadvantage from the standpoint of interrogating stronger adsorption sites in a second column injection, it offered the opportunity to interrogate the adsorption properties of the granodiorite with respect to ^{137}Cs. The difference between the injected and eluted masses of ^{137}Cs after the effluent concentrations were the same as the injection concentration can be attributed to ^{137}Cs adsorbed to the granodiorite, and the timing of the transition to the injection concentration provides a good constraint on the partition coefficient for the ^{137}Cs onto the granodiorite. However, it should be noted that the ^{137}Cs partition coefficient and the maximum adsorption site capacity on the granodiorite are two parameters that cannot be uniquely determined from the column experiment because these parameters have an inverse correlation once the site capacity drops below a certain value. Running a first column until the effluent reaches the injection concentration of a radionuclide may not always be practical if the material packed into the column has a strong affinity for the radionuclide, but it clearly offers additional information on the reactive transport behavior of the combined system. In the experiments of Reimus and Boukhalfa (2014), solute ^{137}Cs never broke through the columns, so no information was obtained on the adsorption properties of the immobile media other than a lower bound on the ^{137}Cs partition coefficient onto the volcanic tuff used in the columns.

If additional solution that did not contain solute ^{137}Cs had been available from the first column, the injection volume into the second column would have been greater, and if enough have been injected through the second column, an injection would have been conducted into a third column. Had it been known that the granodiorite was going to have so much less affinity for ^{137}Cs than the previously-used fracture fill material, we would have used a larger first column to increase the volume of effluent suitable for a second column injection. We recognize that if longer flow interruptions and a third column had been employed, it might have become necessary to introduce a third adsorption site on the colloids to explain all the data simultaneously. We had hoped to evaluate whether a third site was necessary, but the early breakthrough of solute ^{137}Cs prevented this. Nevertheless, we believe that the utility of the multiple sequential column injection method for interrogation of colloid-facilitated transport model parameters was adequately demonstrated.

In future testing, we plan to use the Chancellor water/colloids in a set of columns that are packed with crushed analcime, a zeolite that should have a very strong affinity for ^{137}Cs. The analcime should also remain relatively intact and not generate colloids/fines that could confound test interpretations and potentially jeopardize column permeability, as many other zeolites or clays with strong affinity for ^{137}Cs might. These experiments should allow us to obtain much larger volumes of solutions containing only colloidal ^{137}Cs for subsequent column injections, and they should also maximize the desorption of ^{137}Cs from the colloids because of the much greater ability of the analcime to compete with the colloids for ^{137}Cs. Thus, we should be able to obtain a much better interrogation of the ability of the Chancellor colloids to facilitate the transport of ^{137}Cs over long time and distance scales. The flow interruption technique will be used to increase the time scales of interrogation for desorption rate constants associated with the stronger adsorption sites on the colloids.

Additionally, we are already in the process of preparing sodium-exchanged FEBEX bentonite colloids similar to what we have used in past colloid-facilitated transport experiments (Wang et al., 2014, Chapter 6; Wang et al., 2015, Chapter 8) for use in future experiments. These colloids are similar to what has been used in field colloid-facilitated transport experiments at the Grimsel Test Site in Switzerland. The bentonite colloids will have carrier-free ^{137}Cs adsorbed onto them before being injected through analcime-packed columns. The carrier-free ^{137}Cs should keep total Cs concentrations to much lower levels than in previous colloid-facilitated transport tests at LANL (Wang et al., 2015, Chapter 8), which should increase the fraction of ^{137}Cs that is adsorbed to stronger adsorption sites on colloids. These tests are being planned to offer practical information on the potential for bentonite colloids (generated from erosion of backfill in a crystalline repository) to facilitate the transport of ^{137}Cs over long time and distance scales. While the use of analcime in column experiments does not necessarily have practical applications to repository scenarios, it should present a “best-case” scenario with respect to inhibiting colloid-facilitated transport of ^{137}Cs, and in that sense it should have value for repository performance assessments.

6.5 References

Buddemeier, R. W., Hunt, J. R., 1988. Transport of colloidal contaminants in groundwater: radionuclide migration at the Nevada Test Site. Applied geochemistry, *3*(5): 535-548.

Chino, M., Nakayama, H., Nagai, H., Terada, H., Katata, G., & Yamazawa, H., 2011. Preliminary estimation of release amounts of 131I and 137Cs accidentally discharged from the Fukushima Daiichi nuclear power plant into the atmosphere. Journal of nuclear science and technology, 48(7): 1129-1134.

Comans, R. N. J., Middelburg, J. J., Zonderhuis, J., Woittiez, J. R. W., De Lange, G. J., Das, H. A., Van Der Weijden, C. H., 1989. Mobilization of radiocaesium in pore water of lake sediments. Nature, 339(1): 367-369.

Cornell, R. M., 1993. Adsorption of cesium on minerals: a review. Journal of Radioanalytical and Nuclear Chemistry, 171(2): 483-500.

Dittrich, T. M., Reimus, P. W., Ware, S. D., 2015. Mini-columns for Conducting Breakthrough Experiments. Design and Construction (No. LA-UR-15-24392). Los Alamos National Lab.(LANL), Los Alamos, NM.

Huber, F., Kunze, P., Gekeis, H., Schäfer, T., 2011. Sorption reversibility kinetics in the ternary system radionuclide-bentonite colloids/nanoparticles-granite fracture filling material. Applied Geochemistry, 26: 2226-2237.

Iijima, K., Tomura, T., Shoji, Y., 2010. Reversibility and modeling of adsorption behavior of cesium ions on colloidal montmorillonite particles. Applied Clay Science, 49: 262-268.

Kersting, A. B., Reimus, P. W. (eds), 2003. Colloid-Facilitated Transport of Low-Solubility Radionuclides: A Field, Experimental, and Modeling Investigation. UCRL-ID-149688 Lawrence Livermore National Laboratory, Livermore, CA.

Liu, C., Zachara, J. M., Smith, S. C., McKinley, J. P., Ainsworth, C. C., 2003a. Desorption kinetics of radiocesium from subsurface sediments at Hanford Site, U.S.A.

Liu, C., Zachara, J. M., Qafoku, O., Smith, S. C., 2003b. Effect of temperature on Cs+ sorption and desorption in subsurface sediments at the Hanford Site, U.S.A.

Miller, W., Alexander, W. R., Chapman, N., McKinley, J., Smellie, J., 1994. Natural Analogue Studies in the Geological Disposal of Radioactive Waste. Elsevier, Amsterdam.

Missana, T., Turrero, M. J., Melón, A., 1999. Generation and characterization of colloids of the bentonite/granite interface. Mater. Res. Soc. Symp. Proc. 556, 647-654.

Missana, T., Alonso, Ú., Turrero, M. J., 2003. Generation and stability of bentonite colloids at the bentonite/granite interface of a deep geological radioactive waste repository. Journal of Contaminant Hydrology 61, 17-31.

Missana, T., García-Gutieérrez, M., Alonso, Ú, 2004. Kinetics and irreversibility of cesium and uranium sorption onto bentonite colloids in a deep granitic environment. Applied Clay Science 26, 137-150.

Reimus, P. W., 2003. Implications of Experimental Results/Interpretations and Previous Studies for CAU-Scale Colloid-Facilitated Radionuclide Transport. in Kersting, A. B., Reimus, P. W. (eds), Colloid-Facilitated Transport of Low-Solubility Radionuclides: A Field, Experimental, and Modeling Investigation. UCRL-ID-149688 Lawrence Livermore National Laboratory, Livermore, CA.

Reimus, P. W., Murrell, M., Abdel-Fattah, A. I., Garcia, E., Norman, D., Goldstein, S., Nunn, A., Gritzo, R., Martinez, B., 2006 Colloid characteristics and radionuclide associations with colloids in source-term waters at the Nevada Test Site (FY 2005 Progress Report) (LA-UR-05-8612), Los Alamos National Laboratory, Los Alamos, NM.

Reimus, P. W., Boukhalfa, H., 2014. Chancellor Water Colloids: Characterization and Radionuclide Associated Transport (No. LA-UR-14-27538). Los Alamos National Laboratory (LANL), Los Alamos, NM.

Reimus, P.W., Zavarin, M., and Wang, Y. 2016. Colloid-Facilitated Radionuclide Transport: Current State of Knowledge from a Nuclear Waste Repository Risk Assessment Perspective, FCRD-UFD-2016-000446 and LA-UR-16-26638, Los Alamos National Laboratory, Los Alamos, NM.

Reimus, P.W. 2017. Mathematical Basis and Test Cases for Colloid-Facilitated Radionuclide Transport: Modeling in GDSA-PFLOTRAN, SFWD-SFWST-2017-000117 and LA-UR-17-26560, Los Alamos National Laboratory, Los Alamos, NM.

Rose, T. P., Hu, Q., Zhao, P., Conrado, C. L., Dickerson, R., Eaton, G. F., Kersting, A. B., Moran, J. E., Nimz, G., Powell, B. A., Ramon, E. C., Ryerson, F. J., Williams, R. W., Wooddy, P. T., Zavarin, M., 20011. Radionuclide Partitioning in an Underground Nuclear Test Cavity (No. LLNL-TR-409817). Lawrence Livermore National Laboratory (LLNL), Livermore, CA.

Takata, H., Hasegawa, K., Oikawa, S., Kudo, N., Ikenoue, T., Isono, R. S., Kusakabe, M., 2015. Remobilization of radiocesium on riverine particles in seawater: The contribution of desorption to the export flux to the marine environment. Marine Chemistry, 176: 51-63.

Wang, Y., et al. 2014a. Used Fuel Disposal in Crystalline Rocks: Status and FY14 Progress, Used Fuel Disposition Campaign Milestone Report - Chapter 6, Laboratory Investigation of Colloid Facilitated Transport of Americium by Bentonite Colloids in a Granodiorite System. FCRD-UFD-2014-000060.

Wang, Y., et al. 2015. Used Fuel Disposal in Crystalline Rocks: FY15 Progress Report, Used Fuel Disposition Campaign Milestone Report - Chapter 8, Laboratory Investigation of Colloid Facilitated Transport of Cesium by Bentonite Colloids in a Crystalline Rock System. FCRD-UFD-2015-000125.

Zachara, J. M., Smith, S. C., Liu, C., McKinley, J. P., Serne, R. J., Gassman, P. L., 2002. Sorption of Cs+ to micaceous subsurface sediments from the Hanford Site, USA. Geochimica et Cosmochimica Acta, 66(2): 193-211.

Zhuang, J., Flury, M., Jin, Y., 2003. Colloid-facilitate Cs transport through water-saturated Hanford sediment and Ottawa Sand. Environmental Science and Technology, 37: 4905-4911.

7. COMPARATIVE STUDY OF DISCRETE FRACTURE NETWORK AND EQUIVALENT CONTINUUM MODELS FOR SIMULATING FLOW AND TRANSPORT IN FRACTURED MEDIA

7.1 Introduction

Disposal of high-level radioactive waste in a geological repository in crystalline host rock is one of the potential options under study in the United States by the Department of Energy. The disposal concept has also been studied in other countries such as Canada, Switzerland, Japan, Sweden and Finland to various degrees. Finland and Sweden currently have advanced repository implementation. A detailed review of international disposal concepts in crystalline rock is given by Rechard et al. (2011). The disposal concepts include an engineered barrier system at a nominal depth of 500 m and a natural barrier system consisting of variously fractured crystalline rock. Although the matrix rock has low permeability, the presence of fractures and faults has the potential to affect the hydrogeology of the host rock, and could result in the potential migration of radionuclides to the accessible environment. For this reason, the design of a disposal system in a crystalline rock requires a robust characterization of the fractured host rock.

Various fracture modeling approaches have been employed to represent the fractured rock. The approaches can be broadly divided into Discrete Fracture Network (DFN) and Equivalent Continuum Model (ECM) (Zhang and Sanderson, 2002). Various techniques are also used within the broad categories to characterize fractured rock.

The DFN approach is widely used in various applications, including nuclear waste disposal (e.g. Uchida et al., 1994; Dershowitz et al., 1998, 1999). In DFN approach interconnected networks for fractures are explicitly represented. Most DFN models (conventional DFN) assume that flow and transport only occur through the network with no participation of the rock matrix. In the model each fracture is a two-dimensional planar object with specific shape and size and object-specific hydraulic properties such as transmissivity and aperture. If the location of a fracture is known, then the fracture can be deterministically included in the model. Otherwise, fractures are generated stochastically based on the probability distributions of fracture orientation and size derived from field observations. The fracture generation also requires the knowledge of the fracture intensity expressed either in terms of fracture area per unit volume or number of fractures in the modeling domain. Small fractures, whose radius is smaller than a cutoff value, are usually excluded from the fracture network. The fracture transmissivity and aperture are often assumed to be positively correlated with the fracture size – larger fractures generally have higher transmissivity and aperture (Dershowitz et al., 1999). Recently, discrete fracture matrix models where fractures and matrix are coupled directly have been developed (Ahmed et al. 2015a, Ahmed et al., 2015b). However, this formulation is complex and computationally intense. Therefore, simplified matrix representations (e.g. Hao et al., 2013, Karra et al., 2015) are usually used instead.

In ECM individual fracture properties are translated into the properties of an equivalent porous medium. Different techniques have been proposed, but the main goal remains the same – reproduce the behavior (e.g. flow and transport) of the corresponding fracture network. The ECM is commonly used when the number of fractures in the model domain is large and/or the interaction between the matrix and fractures is an important factor. Examples of the ECM approach are found in Hsieh et al., (1985), Neuman and Depner (1988), Carrera et al. (1990), Tsang et al. (1996), and Altman et al. (1996) Jackson et al. (2000), and Hartley and Joice (2013). One of the main challenges with the ECM approach is that anisotropic permeability needs to be adequately represented to capture the preferential flow pathways in fractures. Jackson et al. (2000) provided a method of self-consistency that checks whether the ECM adequately represents the actual fracture system represented by a DFN method. They utilized the self-consistency method to demonstrate that the effective permeability of the ECM represents the fracture network.

Both DFN and ECM are useful tools for fracture modeling and for predictions of flow and transport. A number of studies compared DFN and ECM approaches, e.g. Selroos et al. (2002) and Leung et al. (2012). The common approach used in these studies is to specify the test/experiment conditions and let DFN and ECM modelers to develop their corresponding models. The modeling results are compared in terms of key upscaled observables, e.g., effective permeability and solute transport. However, details of the conceptual models and corresponding parameters were seldom provided. As a result, it is not possible to separate differences related to the interpretation of the test conditions and parameters from the differences between the DFN and ECM approaches.

This paper addresses this problem by developing an ECM approach that matches as closely as possible the DFN model in the conceptual representation and parameters. The same numerical code PFLOTRAN is used to simulate flow and transport to ensure that a fair comparison is possible. Under this formulation we can determine the advantages and disadvantages of the two approaches with regard to simulating flow and transport in fractured crystalline rock. The goals of this study are:
(1) To identify the differences between the predictions of flow and transport with DFN and ECM approaches in the far field of a hypothetical nuclear waste repository located in crystalline host rocks.
(2) To separate the differences related to the discrete versus continuum approach from the differences in the conceptual representation.
(3) To provide robust fracture characterization tools for use in flow and transport modeling of generic deep geologic disposal of nuclear waste in crystalline rocks. The tools would also be utilized in other simulation processes such as thermal analysis.

An outline of DFN and ECM approaches is provided in Section 7.2. The benchmark problem used for the comparison is described in Section 3. Section 4 describes modeling of flow and transport together with effective permeability estimation and observation of breakthrough curves for the different fracture network realizations. The major findings of this analysis are described in Section 5.

7.2 Modeling Approach

The DFN and ECM approaches used in this study are described in Sections 2.1 and 2.2, respectively. Both models use the same numerical solver for flow, PFLOTRAN. PFLOTRAN (Lichtner et al., 2015) is an open source, state-of-the-art massively parallel subsurface flow and reactive transport code that solves mass balance with Darcy’s law invoked for flow. The advection-diffusion equation (ADE) in PFLOTRAN is used for transport simulations in both models. Transport within the DFN is also simulated using a Lagrangian particle tracking code (Makedonska et al., 2015). Breakthrough curves from all transport models, ADE-ECM; ADE-DFN; and particle tracking-DFN, are compared.

7.2.1 The DFN Approach

Using DFN to model flow and transport through fractured media is an alternative to traditional continuum approaches where effective parameters are used to include the influence of the fractures on the transport properties through a porous medium. In the DFN approach, networks of fractures are created where the geometry and properties of individual fractures are explicitly represented. These networks are meshed for computation and the governing equations are numerically integrated to simulate flow. The choice to include the detailed geometry of the fractures and the connectivity of the fracture network allows for a more accurate representation of physical phenomenon and robust predictive simulation of flow and transport through fractured rocks compared to continuum approaches (Painter and Cvetkovic 2005).

In this study, we use the computational suite dfnWorks (Hyman et al., 2015a) to generate a discrete fracture network representation of the fracture network and to solve the flow equations therein. dfnWorks combines the feature rejection algorithm for meshing (FRAM) (Hyman et al., 2014), the LaGriT meshing toolbox (LaGriT, 2013), the parallelized subsurface flow and reactive transport code PFLOTRAN (Lichtner et al., 2015), and a Lagrangian particle tracking method (Makedonska et al., 2015; Painter et al., 2012). FRAM is used to generate three-dimensional fracture networks and LaGriT is used to create a computational mesh representation of the network for computation. PFLOTRAN is used to numerically integrate the governing flow equations. dfnWorks has been used in a variety of studies including hydraulic fracturing (O'Malley et al., 2015; Hyman et al., 2016a; Karra et al., 2015) and parameter assessment for subsurface flow and transport in large fracture networks (Hyman et al., 2015b; Makedonska et al., 2016; Hyman et al., 2016b). Details of the suite, its abilities, applications, and references are provided in Hyman et al. (2015a).

Figure 7-1 outlines the dfnWorks Workflow. Network generation is performed using DFNGEN (top row). The feature rejection algorithm for meshing (FRAM) is used to construct the network of fractures and the LAGRIT meshing toolbox is used to create a conforming Delaunay triangulation of the network. Next, DFNFLOW uses PFLOTRAN to resolve the steady-state pressure solution in the DFN. Lagrangian transport simulations are performed using DFNTRANS, which determines particles pathlines through the network. dfnWorks has capability to output the orientation and aperture of each fracture (if any) in every grid block of a user specified regular orthogonal grid based on the generated fracture network.

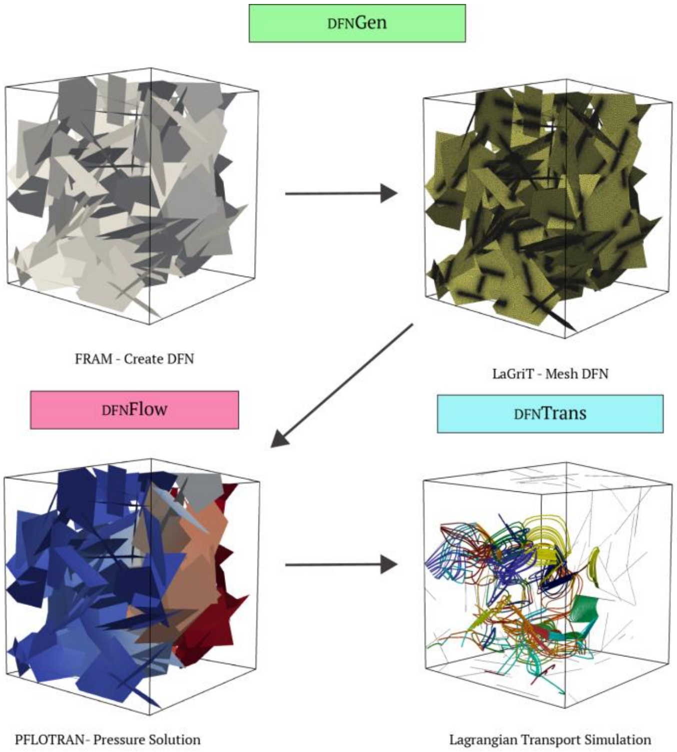

Figure 7-1 dfnWorks Workflow. The input for dfnWorks is a fractured site characterization that provides distributions of fracture orientations, radius, and spatial locations. DFNGEN: 1) FRAM - Create DFN: Using the fractured site characterization networks are constructed using the feature rejection algorithm for meshing. 2) LaGriT - Mesh DFN: The LaGriT meshing toolbox is used to create a conforming Delaunay triangulation of the network. 3) DFNFLOW PFLOTRAN- Compute Pressure Solution: The steady-state pressure solution in the DFN is obtained using PFLOTRAN. DFNTRANS: 4) Lagrangian Transport SimulationA Lagrangian particle tracking method is used to determine pathlines through the network and simulate transport.

7.2.2 The ECM Approach

The ECM approach used in this study was developed at Sandia National Laboratories. The software, called the Fracture Continuum Model, generates stochastic fractured continuum representation of the fracture network. It was originally developed for geothermal applications (specifically Enhanced Geothermal Systems) in which the matrix has to be included to properly simulate heat transport. The formulation and applications of this original approach are described in Kalinina et al. (2014) and Hadgu et al. (2016). Additional capabilities were added as a part of this study as described below to match the conceptual representations implemented using a DFN approach.

A number of different techniques have been proposed to translate individual fracture properties into a continuum model (Jackson et al. (2000), Botros, 2008; McKenna, 2005, Reeves, 2008). The approach implemented in this study is an extension of the method described in McKenna and Reeves (2005) and Reeves (2008). The approach is based on mapping fracture properties into a continuum model regular grid. The x-, y-, and z effective permeability values of a grid block are calculated from the tensor. (Chen, 1999):

$$k_{ij} = \frac{b^3}{12d} \begin{bmatrix} (n_2)^2 + (n_3)^2 & -n_1 n_2 & -n_3 n_1 \\ -n_1 n_2 & (n_3)^2 + (n_1)^2 & -n_2 n_3 \\ -n_3 n_1 & -n_2 n_3 & (n_1)^2 + (n_2)^2 \end{bmatrix} \qquad (7\text{-}1)$$

where k_{ij} is the permeability tensor in the $i = x, y, z$ and $j = x, y, z$ directions, b is fracture aperture, d is fracture spacing, and $n_{1,2,3}$ is the unit normal to the fracture plane in the x, y, and z direction, respectively. Eq. 7-1 evaluates permeability of all fractures intersecting a grid block, and representing the same fracture set. The number of fractures in the grid block is equivalent to L/d, where L is the grid block size and d is fracture spacing.

The unit normal components to the fracture plane are defined as:

$$n_1 = cos\left(\alpha \frac{\pi}{180}\right) sin(\omega \frac{\pi}{180}) \qquad (7\text{-}2a)$$

$$n_2 = cos\left(\alpha \frac{\pi}{180}\right) cos(\omega \frac{\pi}{180}) \qquad (7\text{-}2b)$$

$$n_3 = -sin\left(\alpha \frac{\pi}{180}\right) \qquad (7\text{-}2c)$$

where α is the fracture plunge (90^0 - dip) and ω is the fracture trend (strike - 90^0). If there are more than one fracture sets, the permeability tensor can be computed by adding the permeability tensors for individual fracture sets as shown below:

$$k_{ij}^* = \sum_{m=1}^{N} k_{ij}^m \qquad (7\text{-}3)$$

where N is the number of fracture sets and k_{ij}^m is defined by Eq. 1. The effective porosity of a grid block (n_i) is calculated as:

$$n_i = \frac{\Sigma V_f}{V_{gr}} \qquad (7\text{-}4)$$

and,

$$V_f = A_f \cdot b_f \qquad (7\text{-}5)$$

where $\sum V_f$ is the total volume of all the fractures in the grid block, V_{gr} is the volume of the grid block ($dx \cdot dy \cdot dz$), A_f is the fracture area, and b_f is the fracture aperture. The fracture area is calculated based on the fracture orientation in the grid block. Grid blocks without fractures are assigned matrix permeability and matrix porosity values. Consequently, the advective transport in the grid blocks with fracture is only within the fraction of the grid block representing the total fracture volume in this block. The transport in the grid block without fractures is within the pore volume defined by the matrix porosity.

Different assumptions and conceptual representations of fracture networks can be used to assign fracture aperture, spacing, strike, and dip values to each grid block. In the original implementation of the ECM approach (Kalinina et al. 2014, Hadgu et al. 2016), Sequential Gaussian Simulation (SGSIM) (Deutsch and Journel AG, 1998) was used to create correlated fields to represent fracture shape using anisotropic variograms which represent the shape of fracture zones. Fracture aperture, spacing, and orientation were drawn from probability distributions. This method does not provide the exact number of fractures.

For this study, the ECM was extended to use ellipsoids to better match the conceptual representation of individual fractures in DFN models. ELLIPSIM (Deutsch and Journel AG, 1998), a Boolean simulation method that produces fields with elliptical shapes, was used to generate fracture properties. The program generates ellipsoids of various sizes and anisotropies and places them at random until target proportion of the domain is filled with ellipsoids. ELLIPSIM was modified to generate a specified number of ellipses (fractures in the fracture set) and to draw the ellipse radius and orientation from specified probability distributions. The main conceptual difference between fracture networks generated using ELLIPSIM and dfnWorks is related to the fracture network connectivity. The ECM using ELLIPSIM does not guarantee the full connectivity of fracture network. This is because the ECM does not check the connectivity of the generated fracture network. If some realizations of the observed fracture properties result in not connected networks, these networks are not rejected, A capability to import the fracture network generated by dfnWorks (i.e. dfnWorks output containing the orientation and aperture of each fracture in every grid block of the user-defined regular orthogonal grid) into the ECM was developed to ensure that DFN and ECM models have the same connectivity. The ECM modeling case with the direct input from DFN is further referred to as ECM *Method 1,* while the ECM with ELLIPSIM is referred to as *Method 2*. Both methods use the same set of equations (Eqs. 7-1 to 7-5) to calculate the effective properties of the grid block. The methods are described in Section 7.3.2.

7.3 Benchmark Problem

The benchmark problem is constructed to represent the far field of a hypothetical repository in fractured crystalline rocks. A three-dimensional domain with dimensions of 1 km x 1 km x1 km is chosen. Groundwater flow is represented using a pressure gradient along the x-axis (west to east in the adopted coordinate system), with a constant pressure of 1.001 MPa on the west face (x = 0) and a constant pressure of 1.0 MPa pressure on the east face (x = 1 km). This represents a pressure gradient of 1.0 Pa/m. The other faces are assigned no flow boundary conditions. For simplicity (density and temperature are constant) gravity is not included and the pressures are applied to the entire faces. A pulse tracer source is assumed to be located along entire west face of the domain. The boundary conditions for transport are outlet (zero gradient) on east face and no flux on all the other boundaries. This conceptual representation assumes that the hypothetical repository is located outside the modeling domain and the transport boundary condition at the west face is defined based on the near field model (release to the accessible environment). These flow and boundary conditions have been implemented in both the DFN and ECM.

We do note that the west face transport boundary condition (injection position and mode) could influence transport properties. However, without the systemic quantification of these effects for the selected models it is not possible to know the influence of these properties. The study of these effects is beyond the scope of this section.

The fracture networks considered in this study are generic with some generation parameters modified from an existing site in crystalline rock (SKB, 2010, table 6-75). The network consists of stochastic fractures, whose positions cannot be uniquely determined. The parameters used to generate stochastic realizations of this network are provided in Table 7-1. The network is made up of three circular sets The fracture radius is defined with a truncated power law distribution as follows:

$$R = R_0 \cdot \left[1 - u + u \cdot \left(\frac{R_0}{R_u}\right)^{\alpha}\right]^{-1/\alpha} \qquad (7\text{-}6)$$

Here u is a random number sampled from the continuous uniform distribution on the open interval (0,1), R_0 is the minimum cutoff radius, R_u the maximum cutoff radius, and □ is a scaling factor, with the parameter values shown in Table 1. We set the upper cut off for the fracture networks to 500 meters and selected a lower cut off value of 15 meters. The number of fractures in the three sets was set to ensure that each generated network connects through the domain. The P32 target values were computed according to the methods in Hedin 2008 and are provided in Table 1. Fracture orientations follow Fisher distribution:

$$f(\theta) = \frac{\kappa \cdot sin\theta \cdot e^{\kappa \cdot cos\theta}}{e^{\kappa} - e^{-\kappa}}, \qquad (7\text{-}7)$$

where θ is the deviation of the fracture pole orientation from the mean orientation and the parameter $\kappa > 0$ is the concentration parameter also given in Table 7-1. Fracture transmissivity, T, is estimated using a power law relationship of a correlated transmissivity model (SKB, 2011):

$$\mathrm{T} = \gamma \cdot R^{\omega}, \qquad (7\text{-}8)$$

with parameters $\gamma = 1.6 \times 10^{-9}$, $\omega = 0.8$. Transmissivity depends on fracture size through Eq. 7-8. The fracture aperture, *b*, is correlated to transmissivity using the cubic law relationship (e.g. Witherspoon et al., 1980, Adler, 2012) as shown in Eq. 7-9.

$$T = \frac{b^3}{12} \frac{\rho g}{\mu} \qquad (7\text{-}9)$$

In Eq. 7-9, ρ is water density, g is acceleration due to gravity and μ is water viscosity.

Table 7-1. Fracture set statistics used in the DFN-ECM comparison. Note that the fracture statistics of NE in the SKB report are now being used for EW. (SKB, 2010, Table 6-75)

Fracture Set	Mean trend (degree)	Mean plunge (degree)	κ	a	R_u (m)	R_0 (m)	Number of fractures in 1 km^3	P_{32}
NS	90	0	22	2.5	500	15	2100	0.0061
EW	0	0	22	2.7	500	15	2000	0.0049
HZ	360	90	10	2.4	500	15	2300	0.0073

For the model comparison ECM simulations used the PFLOTRAN code for both flow and transport (advection-diffusion). DFN simulations used PFLOTRAN for flow. DFN simulations used both particle tracking and the ADE for transport. The particle tracking method integrates the trajectory equation using a first order (in space and time) predictor correct method. Velocities within each mesh element are determined using barycentric interpolation. The particle tracking is purely advective, no diffusion along pathlines is considered. A comprehensive description of the particle tracking method is in Makedonska (2015). The models were compared using: 1) effective permeability of the simulated fractured domain, and 2) breakthrough curves (BTCs) of nonreactive solute transport at the opposite to release (east) face.

7.3.1 Fracture Network Generation for DFN

dfnWorks was used to generate 25 independent realizations of the fracture network defined in Table 7-1. Figure 7-2 shows one DFN realization where fractures are colored by their permeability. This realization consists of 6,531 fractures, 6,092,806 control volume cells and 12,421,385 triangular elements.

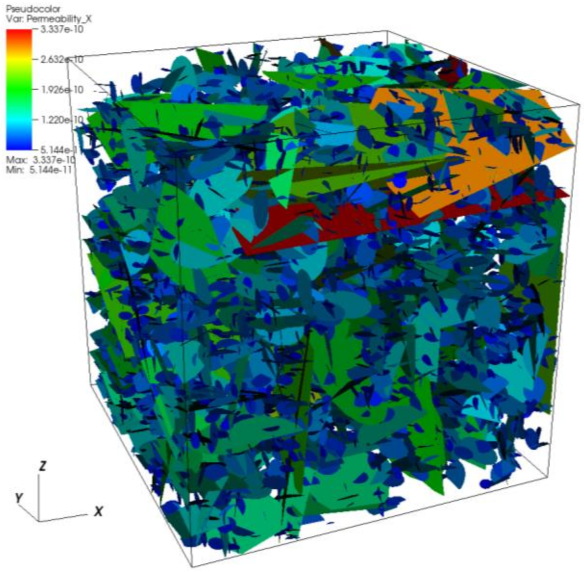

Figure 7-2 DFN realization where fractures are colored by their permeability. Fracture permeability is positively correlated to the fracture radius, i.e., larger fractures have higher permeability values.

7.3.2 Fracture Network Generation for ECM

Two methods were used to generate the fracture networks for ECM. In ECM *Method 1*, the network of interconnected fractures generated by dfnWorks is converted into the inputs for ECM. In this case fracture data processed by dfnWorks is mapped into a uniformly discretized hexahedral grid for use in ECM. If a fracture in the DFN intersects a grid cell in the uniform continuum mesh, then that element of the hex mesh is tagged as a fracture element; otherwise the element is a matrix element. The properties of the fractures in this element (orientation and aperture) are written in the output file that is then used as an input into ECM. ECM uses this input to calculates the effective permeability and porosity of each grid block (Eqs. 7-1 through 7-5). Matrix cells, those that do not intersect a fracture, are assigned a uniform low value of permeability (10^{-22} m^2). Five realizations of the fracture network are produced using this method. An example of the permeability and porosity fields is provided in Fig. 3 for one realization. *Method 1* preserves the fracture network connectivity created in DFN. The remaining conceptual difference between the models is in discrete (DFN) versus effective continuum (ECM) representation. For this case comparison of the DFN and ECM output is based on calculated effective permeability and breakthrough curves of individual realizations.

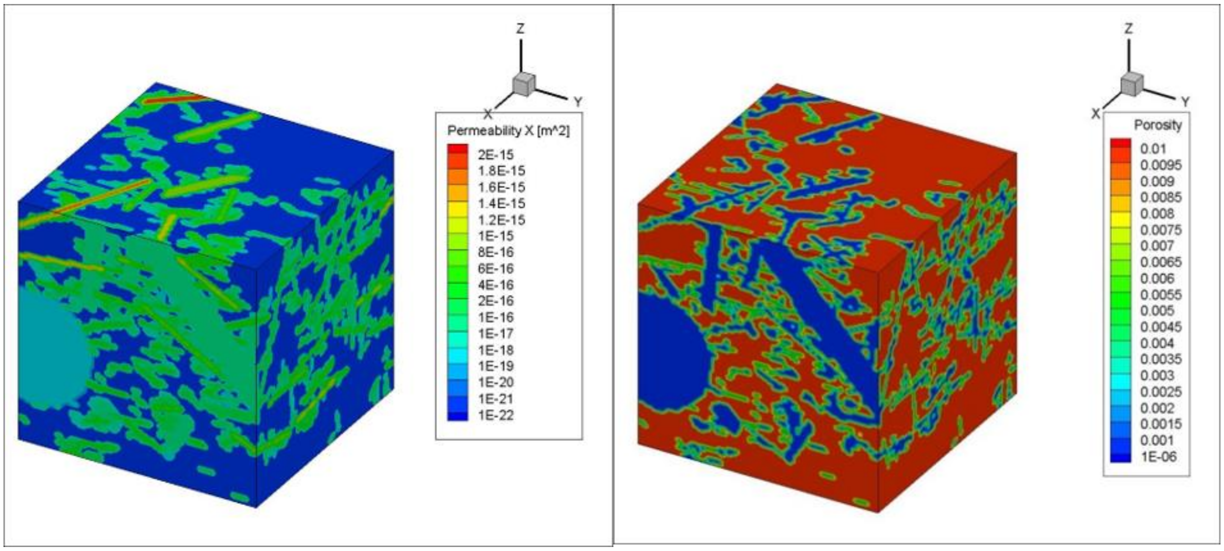

Figure 7-3. ECM *Method 1* permeability and porosity fields obtained from DFN outputs.

ECM *Method 2*, is designed to make an indirect comparison between DFN and ECM. In this ECM method ELLIPSIM was used to generate 25 realizations of the fracture network, independent of the DFN. This method does not guarantee the same fracture network connectivity as the DFN model, which is a major difference between these DFN and ECM methods. The fracture set parameters were defined in accordance with Table 7-1, with the exception that fracture radius distributions were defined to match the radius distribution sampled by DFN. The sampled fracture radius probability distributions generated with DFN slightly deviate from the power law distribution. Also, they have larger percent of long fractures than the distributions in Table 1 to create connectivity. ELLIPSIM generates each fracture set separately and then combines all fracture sets as shown in Figure 7-4. For this case comparison of the DFN and ECM is based on statistical output of effective permeability and breakthrough curves.

NS Fracture Set **EW Fracture Set**

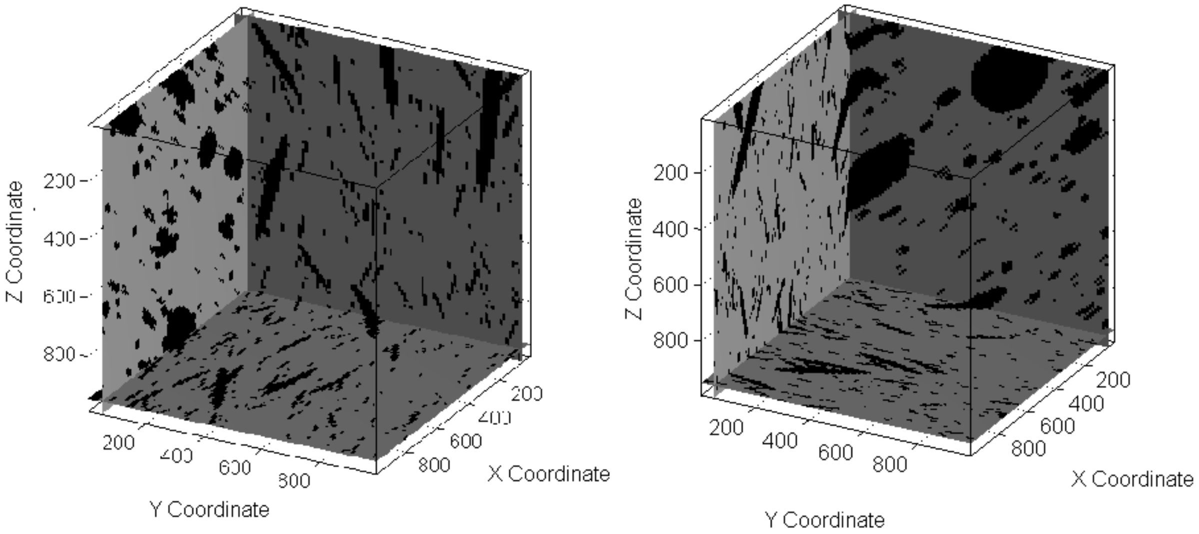

HZ Fracture Set **NS-EW-HZ Fracture Set**

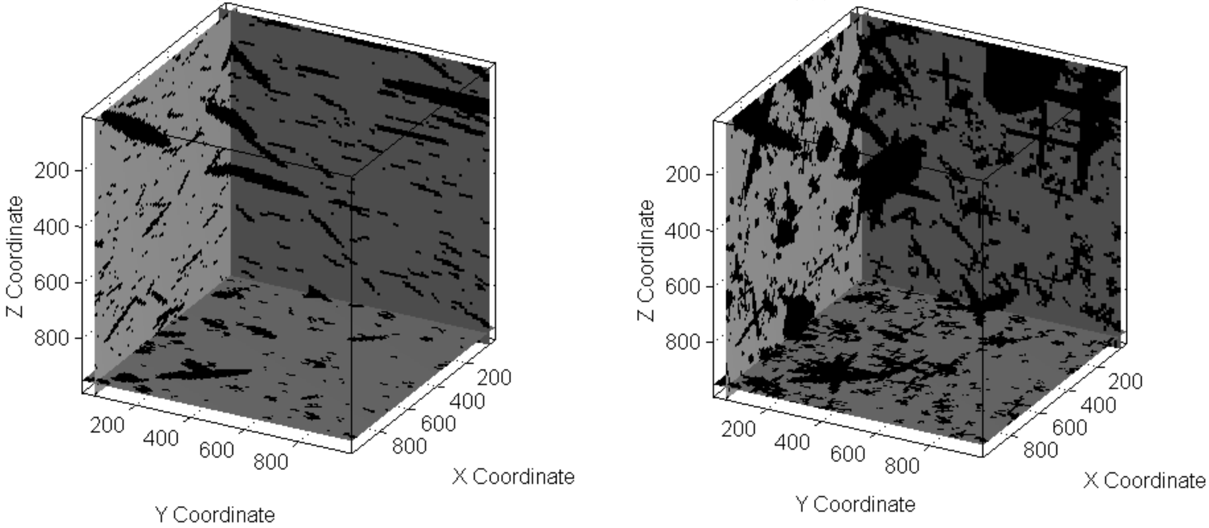

Figure 7-4. Example of ECM *Method 2* single (top and bottom left) and combined (bottom right) fracture sets.

7.4 Flow and Transport Modeling

7.4.1 Fluid Flow Simulations

For the DFN and ECM methods, steady state PFLOTRAN simulations were run. The DFN steady-state pressure solution is shown in Figure 7-5.

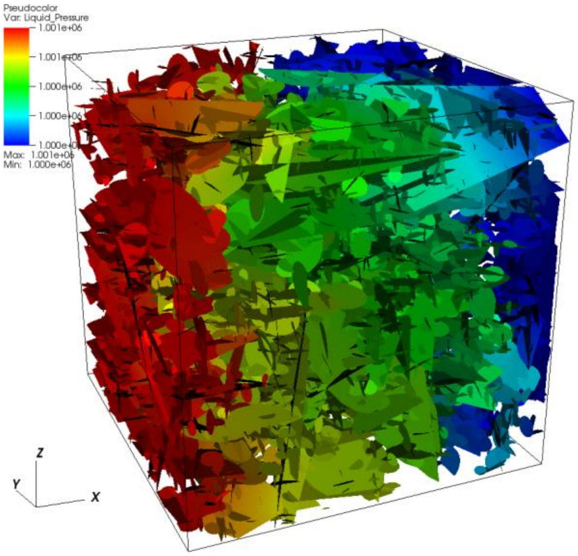

Figure 7-5. Steady state pressure solution, where flow direction is from west (x=0 face) to east (x=1km face).

For both DFN and ECM approaches the steady state flow field is used to evaluate effective permeability for each realization. The effective permeability is calculated using Darcy's law from the east face flux. Table 2 compares the effective permeability values calculated for 5 DFN realizations and 5 corresponding ECM *Method 1* realization. The effective permeability values are in good agreement (the average difference is 4%) indicating that the ECM reproduced the same flow through the fracture network as the DFN. The slight differences are due to the process of conversion of dfnWorks output to ECM continuum representation. These differences reflect the differences between explicit (DFN) and effective (ECM) representation of fracture network. Note that the flow through the matrix in the ECM approach was negligible because the matrix rock permeability was set equal to 10^{-22} m^2.

Table 7-2. Effective Permeability Values for 5 DFN and ECM *Method 1* Realizations.

Realization	DFN Effective Permeability m^2	ECM Effective Permeability m^2
0	3.77E-17	4.60e-17
1	4.24E-17	3.91e-17
2	4.28E-17	4.18e-17
3	3.81E-17	3.62e-17
4	3.35E-17	3.81e-17

The effective permeability values are also calculated for 25 DFN realizations and 25 ECM *Method 2* realizations. This is an indirect comparison case where the ECM fracture characterization is using ELLIPSIM, and is independent of the DFN (Section 7.2.2). For this case comparison of DFN and ECM is based on statistical output. The DFN effective permeability values have a mean and standard deviation of, 4.14E-17 m^2 and 2.34E-17 m^2, respectively. Thus, the mean values are within the standard errors of one another. The corresponding values for the ECM method were 3.66E-17 m^2 and 1.55e-17 m^2, respectively. The differences in the mean values are similar to the differences observed for *Method 1*. Fig. 6 compares the calculated effective permeability values using statistical representation. The mode of the distributions of the DFN and ECM approaches is the same. The difference is on the high end of the distribution tails. This could be related to deviations of the sampled radius distributions in DFN (as described above) from the power-law distributions.

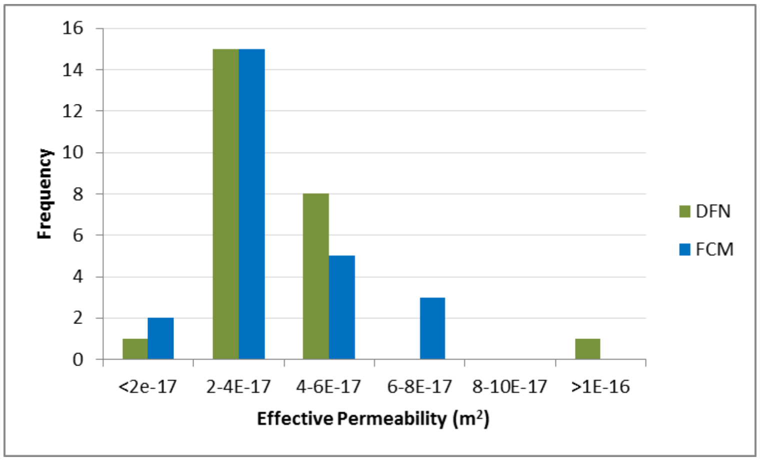

Figure 6. Comparison of the effective permeability values calculated with DFN and ECM (*Method 2*).

7.4.2 Transport Simulations

The fluxes from the steady state flows are used to simulate transport of a dissolved, nonreactive tracer through the system. The output from the transport simulations is used to calculate normalized breakthrough curve (concentration at east face divided by concentration at west face at each time) for each DFN and ECM realization. Fig. 7-7 shows the normalized breakthrough curves (BTCs) obtained with particle tracking for 25 realizations of DFN, where particles are released from fracture edges at west face of the domain and followed to the east out-flow face. The mass of each particle is equal, i.e. resident injection is considered [Frampton and Cvetkovic 2009, Hyman et al. 2015]. The total travel time is captured when particles leave the domain. 2.5×10^5 particles participated in every BTC for each DFN realization. Fig. 7-8 shows BTCs obtained with advection-diffusion equation (ADE) in PFLOTRAN for the same 25 realizations of DFN.

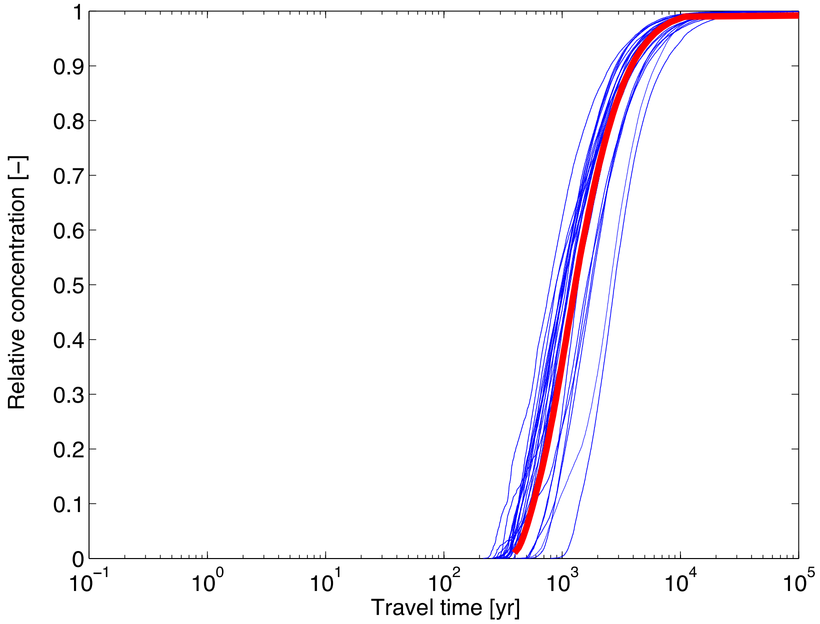

Figure 7-7. BTCs obtained with particle tracking for 25 realizations of DFN. Bold red line represents a mean curve over 25 DFN realizations.

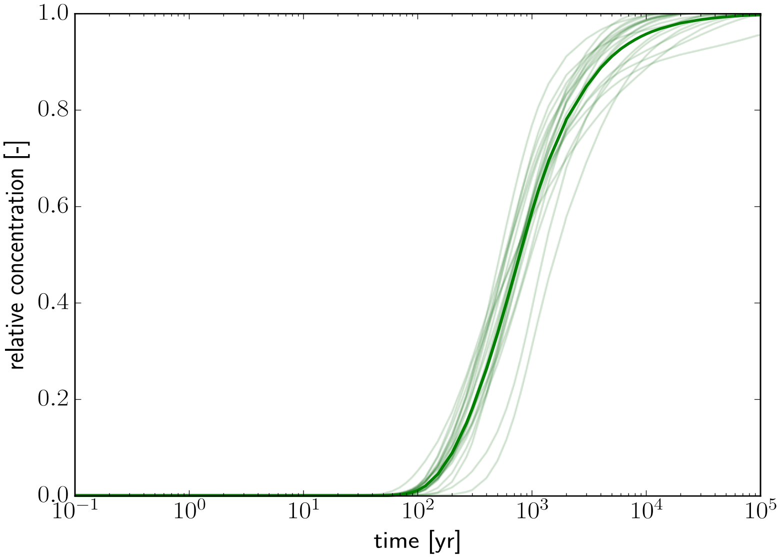

Figure 7-8. BTCs obtained with PFLOTRAN (Advection-Diffusion for 25 realizations of DFN. Bold line is a mean curve over 25 DFN realizations.

The fracture network generated with ECM has both, fractures and matrix. To make an adequate comparison between the DFN and ECM (exclude the potential impacts from matrix diffusion) the matrix was deactivated.

Figure 7-9 shows tracer distributions at the different simulation times for a single realization using ECM *Method 1* (direct output from DFN). Notice that transport occurs only in fractures, as a result of the deactivation of the matrix rock (i.e. no matrix diffusion).

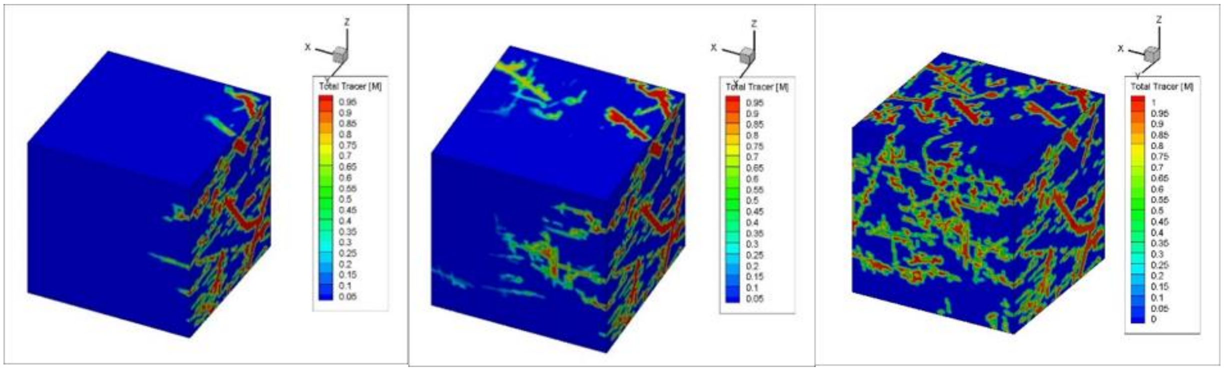

Figure 7-9. Tracer transport results for ECM *Method 1* realization 0 after 70 years, 400 years and 10^5 years of simulation time (from left to right).

Figure 7-10 compares BTCs of 4 ECM and 4 DFN realizations. These four realizations were selected out of many for illustration. The BTCs for the three methods show similar trends, although there are differences in arrival times. The differences reflect the effects due to grid discretization, fracture characterization techniques, and the mathematical representation of transport inherent in the methods. Note that the first arrival times for ECM and DFN with particle tracking curves are very similar in three of the four realizations. The late times in ECM are delayed and smeared compared to DFN with particle tracking. This could be a result of the fracture characterization techniques as well as numerical dispersion in the advection-diffusion solution. There are differences between the results of the DFN advection-diffusion and DFN with particle tracking methods, particularly at early time. Since both methods use the same fracture characterization, the differences could be due to numerical dispersion. However, a systematic comparison between Lagrangian and Eulerian transport algorithms on DFN that would identify the reason behind the discrepancy is beyond the scope of this paper. Tests with the use of very small time steps in the ECM simulations did not appreciably change the BTCs.

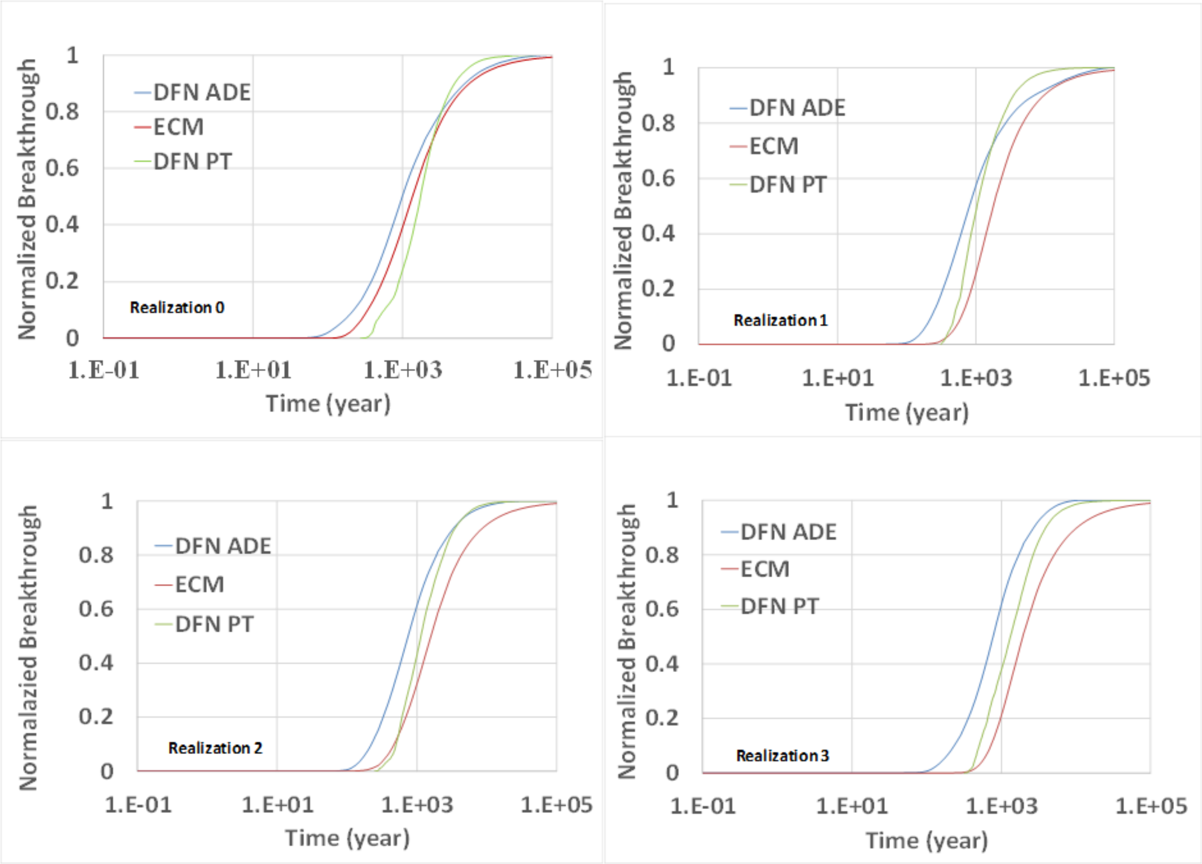

Figure 7-10. Comparison of DFN (Particle Tracking), DFN ADE (Advection-diffusion, PFLOTRAN) and ECM (Advection-diffusion, PFLOTRAN) BTCs for four realizations.

Figure 7-11 compares the following results: DFN (ADE, PFLOTRAN), DFN (Particle Tracking), ECM *Method 1* (5 realizations), and ECM *Method 2* (25 realizations). ECM *Method 1* and *Method 2* are described in Section 2.2. Comparison of the mean DFN (ADE, PLOTRAN) and ECM *Method 2* BTCs indicates that the ECM is delayed. The differences are due to the differences in effective permeability, as discussed in Section 4.1 (and Figure 7-6), affecting fluid flow. When compared to the mean breakthrough curve of DFN with particle tracking, the ECM *Method 2* has a better agreement at early time and the DFN (ADE, PFLOTRAN) has a better agreement at later times.

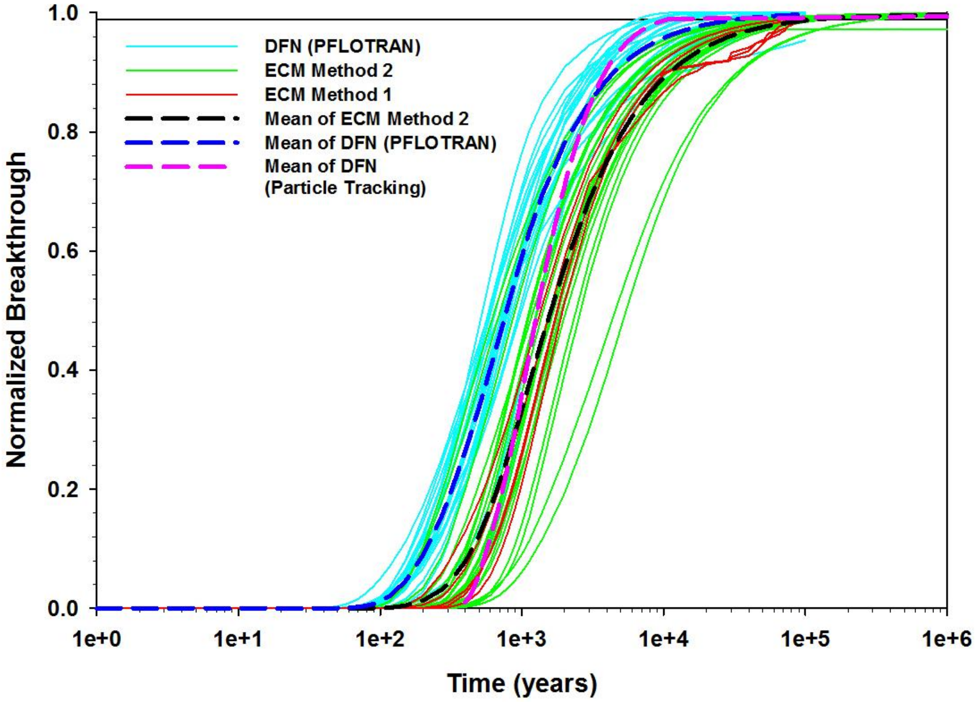

Figure 7-11. Comparison of BTCs for DFN (ADE, PFLOTRAN) (cyan), ECM *Method 2* (green), and ECM *Method 1* (red). ECM *Method1* and *Method 2* are described in Section 2.2.

Figure 7-12 demonstrates the effect of matrix diffusion for one of the ECM realizations. Matrix diffusion in this context refers to diffusion in the matrix rock within the specified domain. For each grid block the matrix rock occupies (1 – porosity) x grid block volume. The early time behavior of the BTCs is very similar because the transport is dominated by the transport through the fractures. At later times, the differences are significant, due to the slow release of the tracer from the matrix back into the fractures after the early time peak is gone.

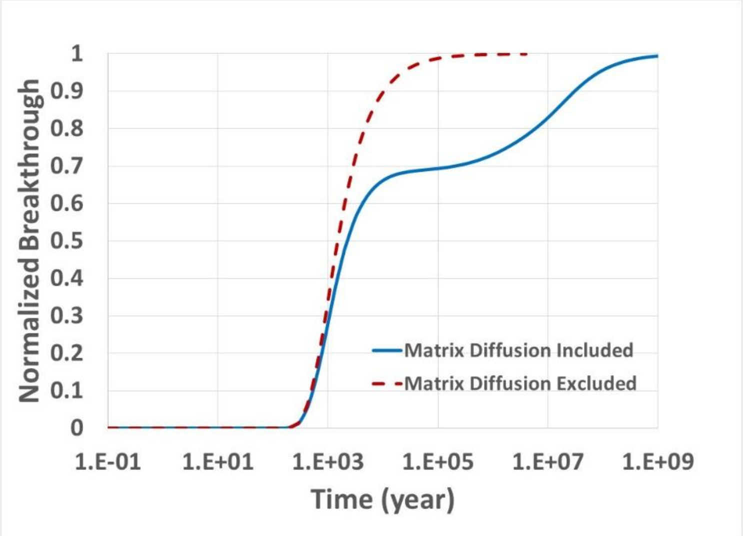

Figure 7-12. BTCs with and without matrix diffusion for one of the ECM realizations.

7.5 Conclusions

Fracture networks in crystalline rock are very complex systems. The fracture data are inherently spatially limited and extrapolating these properties over large volumes of rocks is a challenging problem. While the same fracture data are used as input, the resulting fracture networks reflect the differences in the underlying assumptions and are affected by the method-specific limitation. In this study, a hypothetical site in crystalline rocks with generic fracture properties was used as a test case to compare two different methods, DFN and ECM. The comparison was first done using as close DFN and ECM conceptual representations as possible. This comparison (DFN versus ECM *Method 1*) demonstrates the impacts of effective grid block properties (e.g. upscaling). The subsequent comparisons (DFN versus ECM *Method 2*) were done to evaluate the effects of connectivity and matrix diffusion. The focus of this study was on comparing the two different models. Some aspects, such as the effects due to grid discretization and boundary conditions were left for the future study.

The analysis in this work demonstrated that when ECM is constructed using direct upscaling of DFN (*Method 1*) it is capable of reproducing the flow and transport behavior predicted with the DFN. When the ECM (i.e. ECM *Method 2*) fracture network is generated independently of DFN, the differences between the BTCs are more pronounced. The ECM BTCs are delayed at later times. This effect can be attributed to the differences in the fracture network connectivity. The discrete fracture networks were designed to always contain at least one connected path between inflow and outflow boundary so that breakthrough curves could be obtained and compared with those obtained using ECM. The ECM paths may have included connected fracture grid blocks and connected fracture and matrix grid blocks. In the later conceptual representation, the matrix grid blocks can be viewed as the rock with small fractures not included in DFN, such as fractures smaller than 15 m in radius in the considered test case.

Finally, matrix diffusion can have a significant impact on transport even when the matrix permeability is very low. The early time behavior of the BTCs with and without matrix is similar because the transport is dominated by the transport through the fractures. At later times, the differences are significant, due to the slow release of the tracer from the matrix back into the fractures.

The following factors should be taken in consideration when selecting an approach most suitable for the site-specific conditions:

- An expected number of fractures in the modeling domain: if the number is large DFN may be computationally very challenging due to the explicit meshing on each fracture. For example, in this study the DFN model used 6,092,806 control volume cells and 12,421,385 triangular elements in one realization, while the ECM used 1,000,000 grid blocks.
- Fracture network data: when the fracture network is well mapped and its parameters are well characterized, DFN approach may be advantageous because of its ability to explicitly model the individual fractures.
- The properties of the permeability tensor: when the non-diagonal components of the tensor are significant, the effective continuum representation may not be accurate because it uses only the principal components in x, y, and z. This is due to the limitation of the conventional ground water flow solvers. The DFN approach allows for more accurate modeling of anisotropy due to explicit representation of fractures while the ECM model can introduce errors due to upscaling assumptions made in the analytic derivation.

- Diffusion and sorption: when the groundwater transport is affected by matrix diffusion and sorption, an effective continuum approach has an advantage because matrix is the part of the model while DFN requires adding matrix diffusion explicitly via other methods. This is also applicable to thermal analysis when heat transport through the matrix rock is of importance.

- Fracture connectivity: the DFN approach should be used if the small fractures are believed to have low importance on flow and transport. The effective continuum approach should be used if the small fractures (usually associated with the matrix) may provide additional connectivity.

Finally, a combination of the two approaches can be considered when wide scales of fractures are involved.

7.6 References

Adler, P. M., Thovert, J.F. and Mourzenko, V.V.: Fractured porous media. Oxford University Press. (2012)

Ahmed, R., Edwards, M.G., Lamine, S., Huisman, B., and Pal, M: Control-volume distributed multi-point flux approximation coupled with a lower-dimensional fracture model. J. Comput. Phys. 284, 462–489 (2015a)

Ahmed, R., Edwards, M.G., Lamine, S., Huisman, B., and Pal, M: Three-dimensional control-volume distributed multi-point flux approximation coupled with a lower-dimensional surface fracture model. J. Comput. Phys. 303, 470–497 (2015b)

Altman, S. J., Arnold, B.W., Barnard, R.W., Barr, G.E. Ho, C.K., McKenna, S.A., and Eaton, R.R.: Flow calculations for Yucca Mountain groundwater travel time (GWTT-95), SAND96-0819: Albuquerque, New Mexico, Sandia National Laboratories, 170 p. (1996)

Botros F.E., Hassan AE, Reeves D.M., and Pohll G: On mapping fracture networks onto continuum. Water Resour. Res., 44, W08435 (2008)

Carrera, J., Heredia, J., Vomvoris, S., and Hufschmied, P.: Modeling of flow on a small fractured monzonitic gneiss block: Selected paper in Hydrogeology of Low Permeability Environments. International Association of Hydrogeologists, Hydrogeology, 2, 115-167 (1990)

Chen M, Bai M, Roegiers J-C: Permeability tensors of anisotropic fracture networks. Mathematical Geology, 31, 4 (1999)

Dershowitz, B., LaPointe, P., Eiben, T., and Wei, L.: Integration of discrete fracture network methods with conventional simulator approaches: Society of Petroleum Engineers Annual Technical Conference and Exhibition, New Orleans, Louisiana (September 27–30), SPE Paper 49069, 9 p. (1998)

Dershowitz, W., Follin, S., Eiben, T., Andersson, J.: SR 97-alternative models project: discrete fracture network modelling for performance assessment of Aberg, SKB Report R-99-43. Swedish Nuclear Fuel and Waste Management Co., Stockholm, Sweden (1999)

Deutsch, C.V., and Journel, A.G.: GSLIB Geostatistical software library and user's guide. 2nd ed. Oxford Univ. Press, New York (1998)

Frampton, A. and Cvetkovic, V., 2009. Significance of injection modes and heterogeneity on spatial and temporal dispersion of advecting particles in two-dimensional discrete fracture networks. Advances in water resources, 32(5), pp.649-658.

Hadgu, T., Kalinina, E, and Lowry, T.S.: Modeling of Heat Extraction from Variably Fractured Porous Media in Enhanced Geothermal Systems, Geothermics. 61, 75-85 (2016)

Hao, Y., Fu, P., Carrigan, C.R.: Application of dual-continuum model for simulation of fluid flow and heat transfer in fractured geothermal reservoirs. Proceedings, 38-th Workshop on Geothermal Reservoir Engineering, Stanford University, Stanford, California, February 11–13, 2013, SGP-TR-198 (2013)

Hartley, L. and Joyce, S.: Approaches and algorithms for groundwater flow modeling in support of site investigations and safety assessment of the Forsmark site, Sweden: Journal of Hydrology, 500, 200-216 (2013)

Hedin, A.: Semi-analytic stereological analysis of waste package/fracture intersections in a granitic rock nuclear waste repository. Mathematical Geosciences, 40(6), 619-637 (2008).

Hsieh, P.A., Neuman, S.P., Stiles, G.K., and Simpson, E.S.: Field determination of the three dimensional hydraulic conductivity tensor of anisotropic media, 2, Methodology and application to fractured rocks: Water Resour. Res., 21 (11), 1667- 1676 (1985)

Hyman J.D., Gable C.W., Painter S.L., and Makedonska N.: Conforming Delaunay triangulation of stochastically generated three dimensional discrete fracture networks: A feature rejection algorithm for meshing strategy, SIAM Journal of Scientific Computing, 36(4), A1871–A1894 (2014)

Hyman, J.D., Karra, S., Makedonska, N., Gable, C.W., Painter, S.L. and Viswanathan, H.S.: "dfnWorks: A discrete fracture network framework for modeling subsurface flow and transport." Computers & Geosciences 84, 10-19 (2015a)

Hyman, J.D., S. L. Painter, H. Viswanathan, N. Makedonska, and S. Karra (2015b), "Influence of injection mode on transport properties in kilometer-scale three-dimensional discrete fracture networks." Water Resour. Res. 51, No. 9, 7289-7308, (2015b)

Hyman, J.D., Jiménez-Martínez, J., Viswanathan, H.S., Carey, J.W., Porter, M.L., Rougier, E., Karra, S., Kang, Q., Frash, L., Chen, L. and Lei, Z.: Understanding hydraulic fracturing: a multi-scale problem. Phil. Trans. R. Soc. A, 374(2078) (2016a)

Hyman, J.D., G. Aldrich, Viswanathan, H., Makedonska, N., and Karra, S.: Fracture size and transmissivity correlations: Implications for transport simulations in sparse three-dimensional discrete fracture networks following a truncated power law distribution of fracture size. Water Resour. Res. 52 (8), 6472-6489 (2016b)

Jackson, C. P., Hoch, A. R., and Todman, S.: Self-consistency of a heterogenous continuum porous medium representation of a fractured medium, Water Resour. Res. 36, No. 1, 189-202, (2000)

Kalinina, E., McKenna, S.A; Klise, K.A., Hadgu, T., Lowry, T.S.: Applications of Fractured Continuum Model to Enhanced Geothermal System Heat Extraction Problems, SpringerPlus, 3, 110 (2014)

Karra, S., Makedonska, N., Viswanathan, H. S., Painter, S. L., and Hyman, J. D.: Effect of advective flow in fractures and matrix diffusion on natural gas production. Water Resour. Res, 51(10), 8646-8657 (2015)

LaGriT: Los Alamos Grid Toolbox, (LaGriT), http://lagrit.lanl.gov, Los Alamos National Laboratory (2013)

Lichtner, P., Hammond, G., Lu, C., Karra, S., Bisht, S., Andre, B., Mills, R., and Kumar, J.: PFLOTRAN user manual: A massively parallel reactive flow and transport model for describing surface and subsurface processes, Technical report LA-UR-15-20403, Los Alamos Natl. Lab., Los Alamos, N. M. (2015)

Leung, C. T. O., Hoch, A. R., and Zimmerman, R.W.: Comparison of discrete fracture network and equivalent continuum simulations of fluid flow through two-dimensional fracture networks for the DECOVALEX – 2011 project, Mineralogical Magazine, Dec. 2012, 76(8), 3179-3190 (2012)

Makedonska, N., Painter, S.L., Bui, Q. M., Gable, C.W., and Karra, S.: Particle tracking approach for transport in three-dimensional discrete fracture networks. Computational Geosciences, 19(5), 1123-1137 (2015)

Makedonska, N., Hyman, J.D., Karra, S., Painter, S.L., Gable, C.W., and Viswanathan, H.S.: Evaluating the effect of internal aperture variability on transport in kilometer scale discrete fracture networks. Advan. in Water Resour. 94, 486-497 (2016)

McKenna S.A. and Reeves P.C.: Fractured continuum approach to stochastic permeability modeling in Coburn T.C., Yarus J.M., Chambers R.L., eds. Stochastic Modeling and Geostatistics: Principles, Methods, and Case Studies, II, 1–14 (2015)

Neuman, S.P. and Depner, J.S.: Use of variable-scale pressure test data to estimate the log hydraulic conductivity covariance and dispersivity of fractured granites near Oracle, Arizona: Journal of Hydro., 102, No. 1-4, 475-501 (1988)

O'Malley, D., Karra, S., Currier, R.P., Makedonska, N., Hyman, J.D., and Viswanathan, H.S.: Where does water go during hydraulic fracturing? *Groundwater* (2015)

Painter, S., and Cvetkovic, V.: Upscaling discrete fracture network simulations: An alternative to continuum transport models, Water Resour. Res, (2005). doi:10.1029-2004WR003682. 41, W02002.

Painter, S. L., Gable, C.W., and Kelkar, S.: Pathline tracing on fully unstructured control-volume grids. Computat. Geoscie. 16, no. 4, 1125-1134 (2012)

Rechard, R.P., Goldstein, B., Brush, L.H., Blink, J., Sutton, M., and Perry, F.V.: Basis for identification of disposal options for research and development for spent nuclear fuel and high-level waste. FCRD-USED-2011-000071 (2011)

Reeves D.M., Benson D.A., and Meerschaert M.M.: Transport of conservative solutes in simulated fracture networks: 1. Synthetic data generation, Water Resour. Res., 44, W05404 (2008)

Selroos, J-O, Walker, D.D., Strom, A., Gylling, B., and Follin, S.: Comparison of alternative modelling approaches for groundwater flow in fractured rock, J. of Hydrolog., 257, 174-188 (2002)

SKB: Data report for the safety assessment SR-Site, Technical Report SKB TR-10-52, Swedish Nuclear Fuel and Waste Management Co., Stockholm, Sweden (2010)

SKB: Long-term safety for the final repository for spent nuclear fuel at Forsmark. main report of the SR-site project, Technical Report SKB TR-11-01, Swedish Nuclear Fuel and Waste Management Co., Stockholm, Sweden (2011)

Snow D.T.: Rock fracture spacings, openings, and porosities. Journal of the Soil Mechanics and Foundations Division, Proceedings of American Society of Civil Engineers, 94, 73-91 (1968)

Snow D.T.: Anisotropic permeability of fractured media. Water Resour. Res., 5, 1273–1289 (1969)

Tsang, Y. W., Tsang, C. F., Hale, F. V., and Dverstop, B.: Tracer transport in a stochastic continuum model of fractured media: Water Resources Research, v. 32, p. 3077–3092 (1996)

Uchida, M., Doe, T., Dershowitz, W., Thomas, A., Wallmann, P., Sawada, A.: Discrete-fracture modeling of the Aspo LPT-2, large-scale pumping and tracer test, SKB International Cooperation report ICR 94-09. Swedish Nuclear Fuel and waste Management Co., Stockholm, Sweden (1994)

Wang, Y., Hadgu, T., Matteo, E., Kruichak, J.N., Mills, M.M., Tinnacher, R., Davis, J., Viswanathan, H., Chu, S., Dittrich, T., Hyman, J.D., Karra, S., Makedonska, N., Reimus, P., Zavarin, M., Zhao, P., Joseph, C., Begg, J., Dai, Z., Kersting, A.B., Jerden, J., Copple, J.M., Cruse, T., and Ebert, W.: Used Fuel Disposal in Crystalline Rocks: FY15 Progress Report, FCRD-UFD-2015-000125. U.S. Department of Energy, Used Fuel Disposition R&D Campaign (2015)

Witherspoon, P. A., Wang, J., Iwai, K., and Gale, J.: Validity of cubic law for fluid flow in a deformable rock fracture, Water Resour. Res., 16(6), 1016–1024 (1980)

Zhang, X. and Sanderson, D.J.: Numerical Modelling and Analysis of Fluid Flow and deformation of Fractured Rock Masses, Elsevier, London, 300 pp. (2002)

8. DISPERSION AND MIXING IN THREE-DIMENSIONAL FRACTURE NETWORKS

8.1 Introduction

Fractures and discontinuities are widespread in the subsurface, existing in all types of rocks and at different scales, ranging from micro to regional scale [Singhal and Gupta, 2010]. This implies a spatial scaling of hydraulic parameters including storage coefficient and hydraulic conductivity [Jiménez-Martínez et al., 2013]. In low permeable media, they are the primary regions for the movement of fluids, involving processes taking place at multiple length scales. Therefore, fractures and discontinuities are relevant for groundwater development [Roques et al., 2016], geothermal energy [Barbier, 2002], nuclear waste disposals [Cvetkovic et al., 2004], and unconventional gas production [Hyman et al., 2016a]. However, while in some regions one or several families of discontinuities are well identified (e.g., Äspö Hard Rock Laboratory, [Rhén, 1997]), in others, the coexistence of different type of discontinuities such as bedding planes, fractures, joints, faults and shear zones, foliation (including cleavage) or dykes makes difficult the definition of families. For this reason, fractured media are usually conceptualized and classified in the literature as regular (i.e., structured) or disordered (i.e., random) networks.

Discrete Fracture Network (DFN) models have been used from 80's [Long and Witherspoon, 1985] to conceptualize fractured media by representing each fracture individually within a network and resolve flow and transport at different scales [Cacas et al., 1990; de Dreuzy et al., 2004; Dreuzy et al., 2012; Dershowitz, 2014; Erhel et al., 2009; Hyman et al., 2015b; Ji et al., 2011; Mustapha and Mustapha, 2007; Makedonska et al., 2016; Pichot et al., 2010, 2012]. The interplay between features and scales can result in flow channeling within these networks. Both the structure of a network [Tsang and Neretnieks, 1998; Dreuzy et al., 2012] and the spatial variability of aperture within a single fracture [Moreno et al., 1988; Tsang and Tsang, 1989; Johnson et al., 2006] can create preferential flow regions. The topology of the network also results in variable flow field within fractures even when an assumption of uniform aperture is adopted [Hyman et al., 2015b; Makedonska et al., 2016]. de Dreuzy et al. [Dreuzy et al., 2012], using DFN, studied the combined effect of fracture scale heterogeneity (i.e., distribution of local apertures) and network topology (i.e., fracture length distribution and density) on the flow properties, showing there is a significant coupling between flow heterogeneities at the fracture scale and at the network scale. However, when the system size is sufficiently larger than the correlation length, this coupling is found to be weak. Therefore, fracture apertures, length and density distributions [Dreuzy et al., 2012], and local roughness [Tsang and Tsang, 1989], all control flow in fractured rocks, contributing substantially to the spreading of dissolved chemicals [Tsang et al., 1996].

The emergence of anomalous transport (i.e., dispersion), also called non-Fickian or non-Gaussian, i.e., non-linear scaling with time of the mean-square displacement of solute distributions, is a direct consequence of the highly heterogeneous velocity field in this type of systems [Berkowitz and Scher, 1997, 1998; Kang et al., 2015, 2017]. The dynamics of fluids or solute mixing -the process that increases the actual volume occupied by the solute by smoothing out concentration contrasts [Ottino, 1989; Kitanidis, 1994; Dentz et al., 2011] is also controlled by the structural and hydraulic heterogeneity of the network [Kang et al., 2015].

Transport processes have been studied in regular [Kang et al., 2015], commonly characterized by heterogeneity in hydraulic conductivity, and disordered [Berkowitz and Scher, 1997, 1998; Kang et al., 2017] fracture networks. The impact of interplay between the network heterogeneity and hydraulic conductivity heterogeneity on solute dispersion and mixing is still an open question that requires a three dimensional fracture network model capable of resolving the multiple length scales within a fracture network. The smallest scale in these networks is along fracture intersections/traces (quasi 1D elements, lines). In these regions, mixing models in 2D, e.g., streamline routing or complete mixing, have been proposed and their influence on upscaled transport behavior quantified [Kang et al., 2015]. However, in 3D the existence of a hydraulic head distribution along the intersection allows local fluid circulation [Park et al., 2003; Hyman et al., 2015a], with the subsequent impact on fluids and solute mixing. At a slightly larger scale there are the fractures themselves, (quasi 2D elements, planes), where variable aperture, boundary conditions (i.e., locations of inflow and outflow fractures), and stress [Kang et al., 2016], can lead to flow channelization that increases fluids and solute mixing [Johnson et al., 2006]. Then, there is the scale of the entire fracture network level (3D), where the fracture orientation [Rubin and Buddemeier, 1996], density [Huseby et al., 2001], and network connectivity are the principal controls on solute dispersion and mixing.

We focus on the two largest scales (network and fracture scale) within a structured and a disordered three dimensional fracture networks. We simulate flow and transport through these networks with varying degrees of hydraulic heterogeneity. The structured network is composed of square fractures drawn from three families whose mean orientations are orthogonal to one another and are aligned with the primary Cartesian directions. The disordered network is composed of the same sized square fractures whose orientations are uniformly random. The density and surface areas of the two networks are the same for a fair comparison. We introduce hydraulic heterogeneity by setting fracture permeabilities to be constant or drawn from log normally distributions with variance of 0.5 and 1.0, i.e., moderate degrees of heterogeneity. We compute a measure of disorder in fracture networks that integrates topological, geometric, and hydraulic properties, the Shannon entropy of the spectrum of the Laplacian of a weighted graph representation of the networks, and provide a first approach to the dispersion within fracture networks.

We represent the spreading of a nonreactive conservative solute by a cloud of passive tracer particles, i.e., using a Lagrangian approach. At uniformly spaced control planes we compute the longitudinal dispersion and the relative concentration of particles that cross a median plane, a proxy for transverse dispersion. The latter provides a first approach to the ’mixing capacity’, but also reactive capacity, i.e., for fluid-fluid mixing-driven chemical reactions (fast reactions), depending on the fracture network type (i.e., structured or disordered) and the hydraulic heterogeneity of it.

8.2 Flow and Transport within Fracture Networks

We use dfnWorks [Hyman et al., 2015a] to generate each DFN, solve the steady-state flow equations and simulate transport therein. dfnWorks combines the feature rejection algorithm for meshing (FRAM) [Hyman et al., 2014], the LaGriT meshing toolbox [LaGriT, 2013], the parallelized subsurface flow and reactive transport code PFLOTRAN [Lichtner et al., 2015], and an extension of the walkabout particle tracking method [Painter et al., 2012; Makedonska et al., 2015]. fram is used to generate three dimensional fracture networks and LaGriT is used to create a conforming Delaunay triangulation of the DFN in parallel. pflotran is used to numerically integrate the governing equations for pressure. A modification of the walkabout particle tracking method is used to determine pathlines through the DFN and simulate solute transport. Details of the suite, its abilities, applications, and references for detailed implementation are provided in Hyman et al. [2015a].

8.2.1 Discrete Fracture Networks

We consider two fracture networks both composed of square fractures with length λ in a cuboid domain of size 25λ × 10λ × 10λ. Fracture centers are uniformly distributed throughout the domain using a Poisson process. The first network is composed of three fracture families with the same target density, P32 = 3 (total fracture surface area over domain volume). Mean normal vectors of the families are aligned with the three principal axis of Cartesian space. We sample the fracture orientations from the three-dimensional Fisher distribution,

$$f(\mathbf{x};\boldsymbol{\mu},\kappa) = \frac{\kappa \exp(\kappa \boldsymbol{\mu}^T \mathbf{x})}{4\pi \sinh(\kappa)}. \tag{8-1}$$

where **μ** is the mean direction vector (T denotes transpose), which can be expressed in terms of spherical coordinates, θ and φ, and $\kappa \geq 0$ is the concentration parameter that determines the degree of clustering around the mean direction. Values of κ approaching zero result in a uniform distribution of points on the sphere while larger values create points with a small deviation from mean direction. The Fisher distribution is sampled using the algorithm provided by Wood [1994]. In the first network, we select a κ value of 20. We refer to this network as structured due to the lattice like network that is obtained. Orientations in the second network are determined by taking the parameters used for the structured network and setting $\kappa = 0.1$, which results in uniformly random orientations. We refer to this network as random. Figure 8-1 shows the normal vectors for fractures in the (a) structured network and (b) the random network. Fractures from the same families are the same color. Complete generation parameters for the networks are provided in Table 8-1.

Table 8-1. DFN generation parameters. Parameters of the Fisher distribution for fracture orientation, mean trend (θ), mean plunge (ϕ), and the concentration parameter (κ). Final values of P32 (total fracture surface area over domain volume) and number of fractures are also provided.

Network	Fisher distribution			Fracture density	
	θ	ϕ	κ	P_{32}	# of fractures
Structured				8.64102	12303
$\sigma^2_{\ln k} = 0.0$	0	0	20	2.88	4073
$\sigma^2_{\ln k} = 0.5$	$\pi/2$	0	20	2.81	4083
$\sigma^2_{\ln k} = 1.0$	$\pi/2$	$\pi/2$	20	2.95	4147
Random				8.79216	12956
$\sigma^2_{\ln k} = 0.0$	0	0	0	2.89	4268
$\sigma^2_{\ln k} = 0.5$	$\pi/2$	0	0	2.90	4256
$\sigma^2_{\ln k} = 1.0$	$\pi/2$	$\pi/2$	0	3.00	4432

Once the network is generated all isolated fractures are removed, which results in slight differences in final P32 values and final fracture counts between families. The structured network contains 12303 individual fractures that meshed with 37812181 triangles and the random network contains 12956 fractures that are meshed with 39120858 triangles. Meshing the networks takes ≈ 1 hour (wall clock) using 32 AMD Opteron(TM) Processors 6272 (1.4 GHz) and obtaining steady state pressure solution requires ≈ 1.5 hours (wall clock) using the same configurations. One hundred thousand particles are tracked through the domain using a single core and takes around 10 hours of wall clock time. On both networks we consider three different scenarios in terms of fracture permeabilties. In the baseline case the fracture permeabilties are constant and equal between fractures (k = 10−12 m2). We consider two additional cases with moderate levels of heterogeneity, in which permeabilties are sampled from a log normal distribution with log variance of $\sigma^2 = 0.5$ and $\sigma^2 = 1.0$. The mean value of the distributions are equal to the value used in the constant case. Fracture permeabilities are constant within each fracture plane, in-fracture variability is not considered. Apertures are determined using the cubic law and the fracture permeability. Because all fractures are the same size, there is no correlation between fracture-size and transmissivity, which is a common assumption in DFN models [Hyman et al., 2016b].

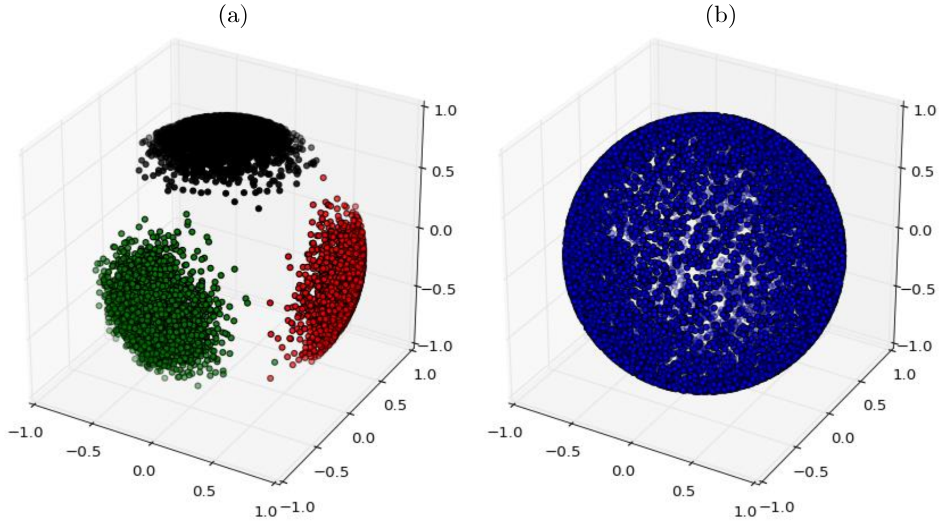

Figure 8-1. Normal vectors of the fractures in the structured network (a) and random network (b) projected onto the surface of the unit sphere. All fractures are the same size. Colors in the structured network indicate fracture family. There are three distinct families in the structured network, each with mean orientation aligned with one of the primary Cartesian axis. There is variability around the mean sampled using a Fisher distribution. The random network has uniformly random fracture orientation.

(a) Structured, $\sigma^2_{\ln k} = 0.0$ (b) Structured, $\sigma^2_{\ln k} = 0.5$ (c) Structured, $\sigma^2_{\ln k} = 1.0$

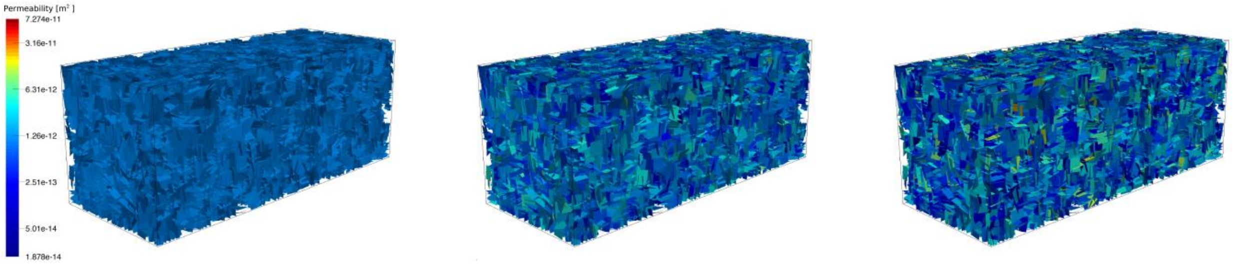

(d) Random, $\sigma^2_{\ln k} = 0.0$ (e) Random, $\sigma^2_{\ln k} = 0.5$ (f) Random, $\sigma^2_{\ln k} = 1.0$

Figure 8-2. Structured (a-c) and random (d-f) networks with fractures colored by permeability for permeability distributions with log variance σ2 = 0.0, σ2 = 0.5, and σ2 = 1.0 (left to right). Colors are shown on a logarithmic scale.

Figure 8-2 (a)-(c) shows the structured networks for the different permeability distribution: (a) constant network, (b) $\sigma^2 = 0.5$, and (c) $\sigma^2 = 1.0$. Fractures are colored by permeability plotted on a log scale. Figure 1-11 (d)-(f) shows the corresponding plots for the random networks.

8.2.2 Flow Equations

We assume that the matrix surrounding the fractures is impervious and there is interaction between flow within the fractures and the solid matrix. Within each fracture the flow of a Newtonian fluid, in our case water, at low Reynolds numbers is governed by the Darcy equation,

$$\mathbf{q} = -\frac{\mathbf{K}}{\nu}\nabla P \tag{8-2}$$

where q is the Darcy flow rate, ∇P is the pressure gradient, ν is the fluid viscosity, and K is the fracture permeability tensor, which we take to be a scalar in this study K = k. We drive flow through the domain by applying a pressure difference of 1 MPa across the domain. No flow boundary conditions are applied along lateral boundaries. The effects of gravity are not considered in these simulations. These boundary conditions along with mass conservation:

$$\nabla \cdot \mathbf{q} = 0 \tag{8-3}$$

and equation (8-3) are used to form an elliptic partial differential equation for steady-state distribution of pressure within the network:

$$\nabla \cdot (k(\mathbf{x})\nabla P) = 0. \tag{8-4}$$

Note that while k is uniform in each fracture plane, it does vary between fractures for cases with $\sigma_2 > 0.0$. This variability between fractures is another degree of heterogeneity in the system, in addition to the structural differences between the two networks, that effects the pressure solution. Figure 8-3 shows the steady-state pressure solution in the structured network (a) and the random network (b) for $\sigma_2 = 1.0$. The resulting pressure and volumetric flow rates are used to determine the velocity field u at every node in the conforming Delaunay triangulation throughout each domain using the methods of Painter et al. [2012] and Makedonska et al. [2015]. Complete mixing, where the probability of a particle exiting in a given direction is proportional to the outgoing flux in that direction, is adopted at fracture intersections [Makedonska et al., 2015].

8.2.3 Transport Simulations

We represent the spreading of a nonreactive conservative solute through each DFN by a cloud of indivisible passive tracer particles, i.e., using a Lagrangian approach. The use of particle tracking methods allows for the investigation direct links between transport properties and the network structure while mitigating issues of numerical dispersion that are associated with Eulerian transport simulations. Let Ω denote the set of particles with unique initial positions x0. Given a fixed mass M represented by Ω and total area of fractures along the inlet plane A, the mass associated with each particle, m(x0), is uniformly distributed across all the particles, M:

$$m(\mathbf{x_0}) = \frac{M}{A}. \tag{8-5}$$

This initial condition is referred to as uniform or resident injection, as opposed to flux-weighted injection [Kreft and Zuber, 1978]. These two initial conditions represent different physical scenarios and have been studied in both heterogeneous porous media and fracture networks [Vanderborght et al., 1998; Demmy et al., 1999; Gotovac et al., 2009; Frampton and Cvetkovic, 2009; Gotovac et al., 2010; Janković and Fiori, 2010; Hyman et al., 2015b; Kang et al., 2017]. We choose resident (uniform) injection, having the same mass (number of particles) per unit of fracture length at the inlet plane, so that variability in the concentration profile along the inlet plane depends solely on network structure, not flux profile. This initial condition allows us to study the impact of structural and hydraulic heterogeneity on the evolution of transport behavior as the plume of particles moves through each network.

8.3 Simulation Results

In this section we first report structural (topological and geometric) and hydrological attributes of the fracture networks. Then, we report observations of flow velocities and transport through them.

(a) (b)

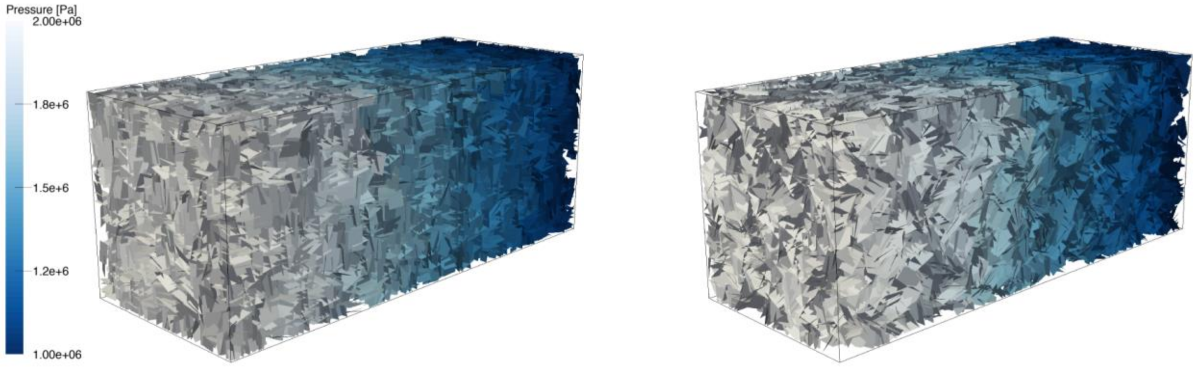

Figure 8-3. Steady-state pressure solution in the structured network (a) and the random network (b), both permeability distributions with log variance of $\sigma^2 = 1.0$.

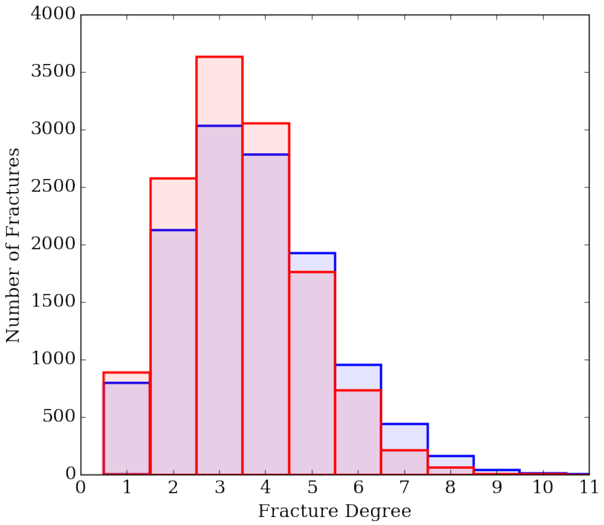

Figure 8-4. Distribution of fracture connectivity (fracture degree). Values for the structured network are shown in blue and values for the random network are shown in red.

8.3.1 Network Structure

The two fracture networks, structured and random, have different topological properties, which result from the different family structures. We quantify their differences by considering two topological properties, one local and one global. Topological characterization is done by constructing a graph representation of each network using the method described in Hyman et al. [2017]. For every fracture in the DFN, there is a unique node in a graph. If two fractures intersect, then there is an edge in the graph connecting the corresponding nodes. Edges are assigned unit weight to isolate topological attributes from other attributes that could be considered. All fractures that intersect the inflow plane are connected to a source node and all fractures that intersect the outflow plane are connected to a target node. Thus, the graphs are based solely on the topology (connectivity) of the networks. We use the NetworkX graph software package [Hagberg et al., 2008] to compute topological properties of interest of the graphs.

The local attribute we consider is the number of other fractures that each fracture intersects (i.e., local topological heterogeneity), which we refer to as the fracture degree. The distribution of these values for both type of networks (i.e., structured and random) is provided in Figure 8-4. The integer median of these distributions are 4 for the structured network and 3 for the random network. Thus, a typical fracture in the structure network connects to four other fractures while a typical fracture in the random network only connects to three other fractures. Moreover, the distribution of the structured network has higher variance (2.64) than the random one (2.02). These values indicate that the structured network is slightly more connected locally than the random network.

The global (i.e., network-scale heterogeneity) property considered is the node connectivity of the networks, which is the number of nodes (fractures) that need to be removed to disconnect the inflow and boundaries. This value indicates how well a network is connected with respect to the flow boundaries. The higher the value, the more difficult it is to disconnect the inflow and outflow boundaries. The node connectivity is 75 for the structured and 61 for the random network. These values indicate that the structured network is globally better connected than the random network.

Although each fracture is the same shape, a range of length scales exists within the fracture plane due to intersections with other fractures. A first order approximation of the transport distances within the fracture planes can be obtained by computing the distance between centers of intersections (traces) within fracture planes (l). Figure 8-5 (a) shows the distribution of these distances for the structured (blue) and the random network (red). The observed distribution of lengths is quite similar, having a mean[m]±variance[m^2] of 0.52 ± 0.049 and 0.49 ± 0.044 for the structured and random network, respectively.

Another length scale can be obtained by considering the ratio of the fracture permeability over these distances ($l' = k/l$). The importance of this length scale can be seen by a change of variables within Darcy's law,

$$\mathbf{q} = -\frac{k\Delta P}{\nu l} \rightarrow \mathbf{q} = -l'\frac{\Delta P}{\nu}. \tag{8-6}$$

The ratio ΔP /ν has the dimension of 1/time, so ν /ΔP is a characteristic time scale of the system. Therefore,

$$l' = -\mathbf{q}\frac{\nu}{\Delta P} \tag{8-7}$$

is the distance traveled within a fracture plane in a characteristic time step, at a given speed. Figure 8-5 (b) shows the distribution of l for the structured (blue) and the random network (red) for the three cases hydraulic variability we consider: $\sigma^2 = 0.0$ (solid), $\sigma^2 = 0.5$ (dashed), $\sigma^2 = 1.0$ (dotted). The distributions for larger values of σ^2 have wider variance, as expected. The distributions of these in-plane attributes are nearly indistinguishable. In all cases, the Kolmogorov-Smirnov test does not reject the null hypothesis that two samples are drawn from the same distribution. The similarity of these distributions indicates that at the scale of individual fractures the two networks are analogous.

We combine topological, geometric, and hydrological properties to examine the interplay between structural and hydraulic heterogeneity with respect to their influence on transport properties through the fracture networks. Specifically, we compute the Shannon entropy for each of the networks as a measure how easily particles can move about the networks. For this computation, we use a different graph representation of each DFN than the one used above. To better include more geometric and hydrological information into a graph representation of the networks, nodes in the graph represent intersections between two fractures and edges in the graph represent paths between traces along a fracture plane. This mapping allows for geometric and hydrological properties to be represented as edges weights in the graph. This mapping is similar to those used in pipe-network flow simulations within DFN, e.g., Dershowitz and Fidelibus [1999].

We consider four different edge weighting schemes. In the first, the weights are uniform and the graph is purely topological, no geometric or hydrological features are included. In the second, we include geometric information. Weights are based on the length between intersections and we use a exponential weighting scheme where $w = e^{-(\sqrt{2}\lambda/l)}$. The value $\sqrt{2\lambda}$ is the maximum distance trace centroids that can be from one to another on a square fracture plane with sides of length λ and acts as a normalization factor. In the third, we include hydrological properties by weighting edges based on the fracture permeability using the same exponential weighting scheme $w = e^{-(k_0/k)}$, where k_0 is the minimum permeability in all networks ($k_0 = 10^{-14}$ [m^2]). Finally, we consider weights that combine geometric and hydrological features, those based on $l' = k/l$, using the same exponential weighting scheme $w = e^{-(k_0/k)} e^{-(\sqrt{2}\lambda/l)}$ where k_0 and l are defined as above. Using each of these graph representations, we determine the spectrum of the normalized graph Laplacian, and then compute the Shannon entropy of it as: $E = -\sum_{i=1}^{n} p(c_i) \log p(c_i)$ where $p(c_i)$ is the eigenvalue probability distribution. Values of the Shannon entropy for all networks and weighting schemes are provided in Table 8-2.

8.3.2 Velocity Distributions

Figure 8-6 shows the distribution of velocity magnitudes in the structured network (blue) and the random network (red) for all three hydraulic cases. Log variance of permeability fields are distinguished by line type: $\sigma^2 = 0.0$ (solid), $\sigma^2 = 0.5$ (dashed), $\sigma^2 = 1.0$ (dotted). The distributions exhibit a peak at high velocities and then a rapid decay in lower velocities. The random networks have more low velocity regions than the structured networks. The amount of low velocity increases with higher values of σ^2 in both network structures.

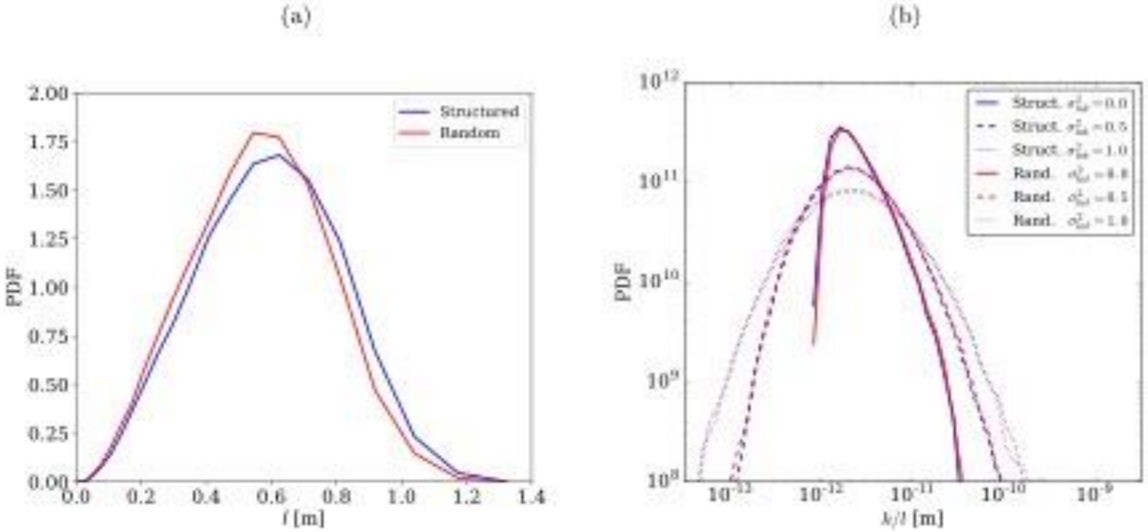

Figure 8-5. (a) In-fracture length [m] and (b) permeability / in-fracture length [m] distributions. Values for the structured (blue) and random (red) networks; log variance of hydraulic conductivity σ2 = 0.5 (solid line) and σ2 = 1.0 (dashed line).

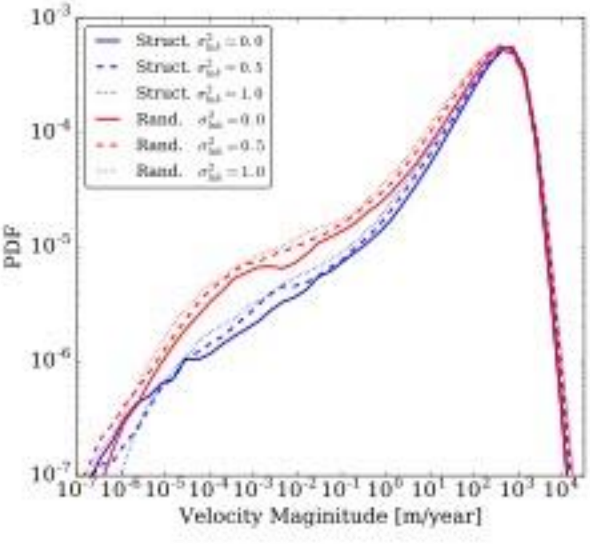

Figure 8-6. Distribution of velocity magnitudes in the structured (blue) and the random (red) network. Log variance of permeability fields are distinguished by line type: σ2 = 0.0 (solid), σ2 = 0.5 (dashed), σ2 (dotted).

Table 8-2. Shannon entropy for the fracture networks, structured and random, and three different permeability scenarios considered. Entropy is computed using the weighted graph Laplacian with uniform weights (1), weights based on distance between traces, l, fracture permeability, k, and their ratio k/l.

	Structured				Random			
Weights	1	l	k	k/l	1	l	k	k/l
$\sigma^2_{\ln k} = 0.0$	2.506	2.857	2.506	2.857	2.580	2.899	2.580	2.899
$\sigma^2_{\ln k} = 0.5$	2.506	2.857	2.507	2.857	2.580	2.899	2.580	2.899
$\sigma^2_{\ln k} = 1.0$	2.506	2.857	2.507	2.857	2.580	2.899	2.580	2.899

8.3.3 Particles Transport

The influence of these low velocity regions is borne witness in the breakthrough times at the outlet plane, $L = 25\lambda$ (Fig. 8-7). Figure 8-7 (a) shows the distributions of breakthrough times. Times have been non-dimensionalized by the median breakthrough time of particles through the structure network with constant permeability ($\sigma^2 = 0.0$). The peak breakthrough is lower and later for the random than the structured network for all three σ^2 cases. Figure 8-7(b) shows the complimentary cumulative distributions of breakthrough times. Later breakthrough times are observed in the random networks than their structured counterparts. As hydraulic heterogeneity increases, later breakthrough times are observed in both network structures.

The evolution of plume spreading in the primary direction of flow is quantified by computing the mean squared displacement σ_{τ}^{2} at equidistant control planes ($\Delta x = \lambda$). The best fits for the spatial evolution of σ_{τ}^{2} are provided in Table 8-3. In all cases, the R^2 value for the fits was greater than 0.99. These slopes are larger for the random than the structured networks, and increase with higher values of σ^2 . The derivative of σ^2 with respect to primary flow direction $\partial\sigma_{\tau}(x)/\partial x$ is shown in Figure 8-8, where colors and line style are the same as in Figure 8-7, to highlight plume growth rates. In all cases, the majority of plume spreading occurs prior to the first control plane. Beyond the first control plane, the values of $\partial\sigma_{\tau}^{2}(x')/\partial x$ are somewhat constant, i.e., σ_{τ}^{2} increases roughly linearly, as the plume moves through subsequent control planes for all cases. Note that the largest value of σ^2 for the random network shows more substantial fluctuations than the other samples and does not follow this trend. The random network has consistently higher values of $\partial\sigma_{\tau}^{2}(x')/\partial x$ than the structured one for the same value of σ^2 , indicating faster growth of the plume.

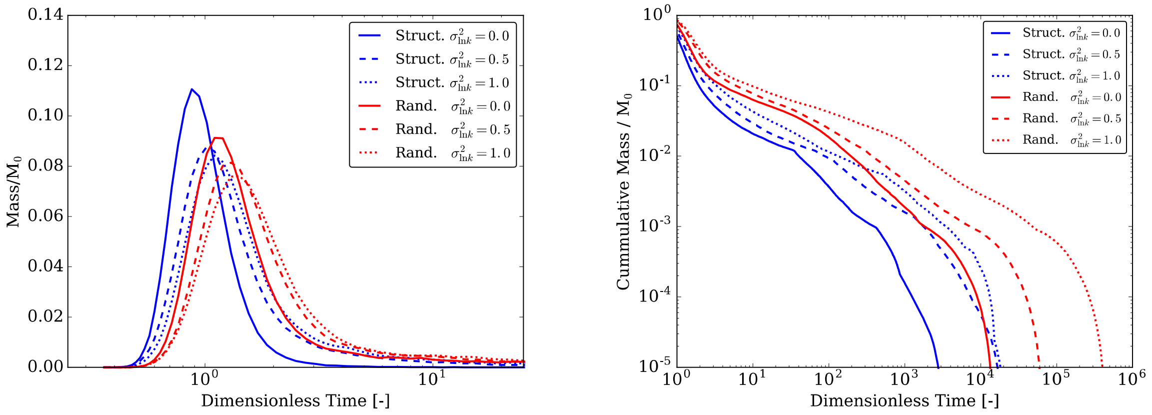

(a) (b)

Figure 8-7. Breakthrough times at the outlet plane (L = 25λ) for structured (blue) and random (red) networks. Log variance of permeability fields are distinguished by line type: σ2 = 0.0 (solid), σ2 = 0.5 (dashed), σ2 = 1.0 (dotted). Times are non-dimensionalized by the median breakthrough time of structure network with log variance σ2 = 0.0. (a) Distributions of breakthrough times. (b) Complimentary cumulative breakthrough.

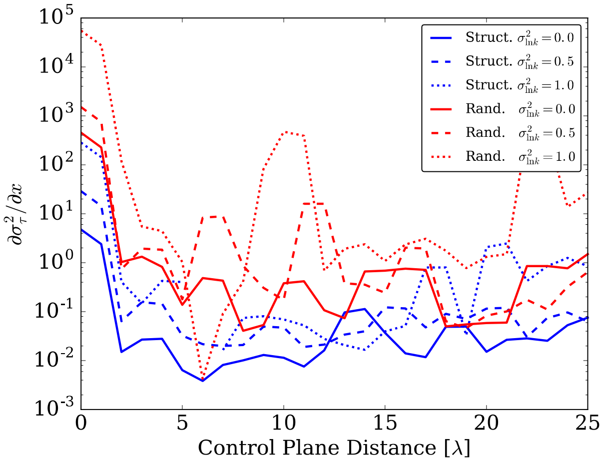

Figure 8-8. Derivative of mean squared displacement στ2 of breakthrough times respect to the primary direction of flow (plume growth rate). ∂ στ2 (x′)/∂ x plotted as a function of control plane distance for structured (blue) and random (red) network. Log variance of permeability fields are distinguished by line type: σ2 = 0.5 (dashed), σ2 = 1.0 (dotted), σ2 = 0.0 (solid).

Particles also disperse through the network in directions transverse to the primary direction of flow. Figure 8-9 shows 100 particle pathlines in the randomly oriented network with $\sigma^2 = 1.0$. The pathlines are colored according to particle initial positions. Particles starting on the left side of the domain are colored blue and those starting on the right are colored red. Along with the pathlines, uniformly spaced control planes normal to the main flow direction are also included. As particles move through the domain, they transition across this median plane, i.e., transverse movement within the network. The left side of the image shows snapshots of particle locations at the normal control planes. At the inlet plane, particles are divided but by the end of the domain they are mixed together. We measure how much of the mass has transitioned across the median plane with distance traveled.

Table 8-3. Slope of mean squared displacement (σ^2_τ) as a function of distance in the primary direction of flow (m) and exponent of power law fit to relative concentration (M*) as a function of distance (α).

	m			α		
	$\sigma^2_{\ln k} = 0.0$	$\sigma^2_{\ln k} = 0.5$	$\sigma^2_{\ln k} = 1.0$	$\sigma^2_{\ln k} = 0.0$	$\sigma^2_{\ln k} = 0.5$	$\sigma^2_{\ln k} = 1.0$
Structured	0.01	0.03	0.06	0.52	0.48	0.48
Random	0.05	0.1	0.23	0.61	0.64	0.67

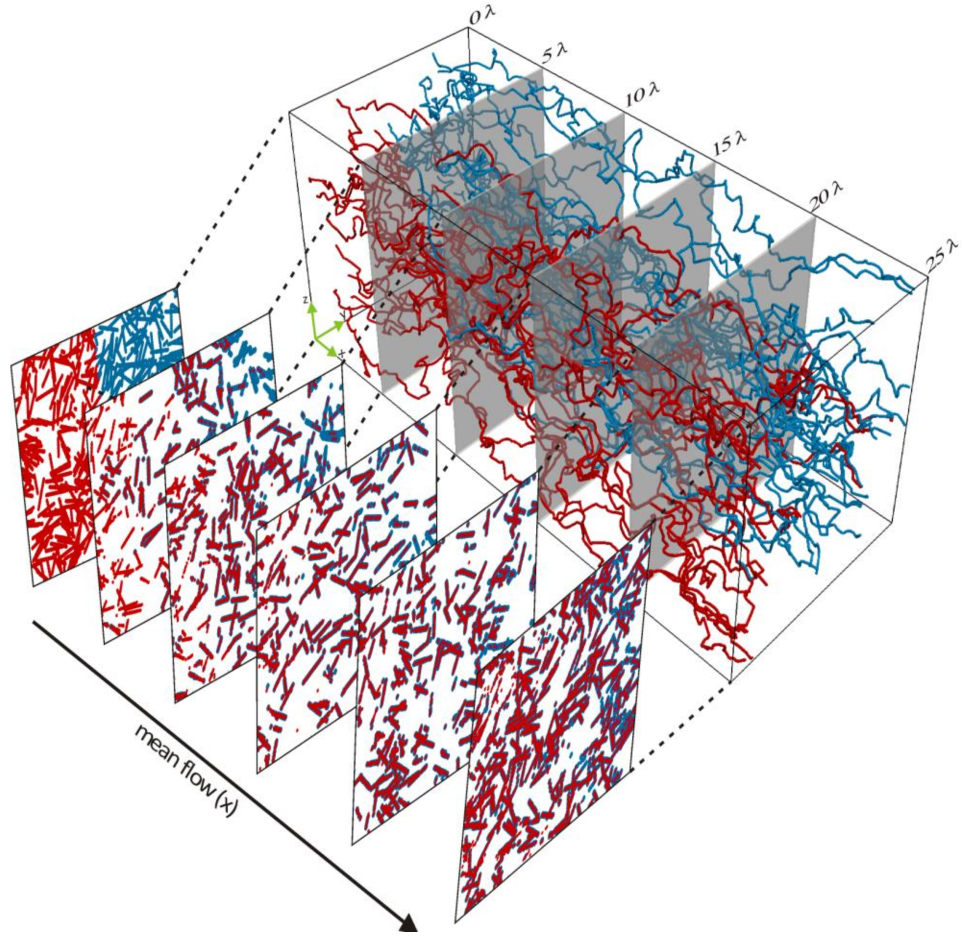

Figure 8-9. Pathlines of 100 particles in the random network and σ2 = 1.0. The pathlines are colored according to particle initial positions: left-blue and right-red. Uniformly spaced [0λ − 25λ] control planes (grey) normal to the main flow direction are also included. The left side of the image shows snapshots of particle locations at the normal control planes. As particles move through the domain, they transition across a median plane.

8.4 Discussion

By a number of measures, the two fracture networks studied, structured and random, are very similar. This, along with the same boundary and initial conditions, allows for a systematic and quantitative comparison between them, as well as address the impact of the interplay between structural and hydraulic heterogeneity on the solute dispersion and mixing.

8.4.1 Structural Control

Differences in transport behavior within the two networks for the same value of σ^2 are the result of differences in their network scale (i.e., macro-scale) structure. This conclusion is supported by the following observations. First, the networks were designed to be analogous at the scale of individual fractures. They are composed by equal sized fractures whose centroids are uniformly distributed throughout the domain and have similar values of total fracture surface area (over domain volume) and density. Second, their hydraulic properties are statistically indistinguishable, aving either the same permeabilities on every fracture or the fracture permeabilites are drawn from the same distribution. Distributions of distances between trace centroids are similar (Fig. 8-7 (a)) and the distributions of the length scale l' (ratio of permeability and distance between centers of fracture plane intersections), which we proposed to establish a relationship between structural and hydraulic properties, are also nearly indistinguishable for the same values of σ^2 between the networks (Fig. 8- (b)). The principal difference between the two networks is the orientation of fracture families. In the structured network, the mean orientations of the three fracture families are orthogonal to one another and are aligned with the primary Cartesian directions. Therefore, two of the three families in the structured network contain fractures that are aligned with the principal direction of flow and provide little resistance to flow and transport. In contrast, the disordered network is composed of the same sized square fractures whose orientations are uniformly random and provide no preferred direction or resistance to flow. This difference between orientations also resulted in networks with different connectivity properties. The two measures proposed for connectivity, fracture degree and node connectivity, indicate that structured network is better connected local and globally respectively than the random counterpart. Thus in addition to providing less resistance in the direction of flow, it is easier for transport to pass between fractures in the structured network.

The fracture degree (i.e., the number of fractures each fracture intersects) corresponds to the coordination value a global topological characteristic for the entire fractured network in percolation theory. Karrer et al. [2014] showed that percolation threshold ρ_c a critical probability below which the connections are too sparse to form a pathway through a sample leading to an interrupted macroscopic flow and transport is given by $\rho_c = 1/(\text{fracture degree} - 1)$. This definition of percolation threshold, originally proposed for sparse networks (treelike network), has been found to be accurate for denser networks (many short loops) as well [Jim´enez-Mart´ınez and Negre, 2017]. ρ_c was 0.333 and 0.500 for structured and random network, respectively; while the theoretical ρ_c for 3D systems is 0.312. The smaller average fracture degree of the random network, results in a percolation threshold that is similar to a well-connected 2D systems (0.590) [Berkowitz and Balberg, 1993]. Although the obtained percolation threshold is subject to uncertainty, it does confirm that structured network is better connected globally.

8.4.2 Spreading

The structured network shows a narrower distribution of velocities than the random network for all log variance values considered. In general, the random network displays wider variance in the velocity field distribution, in which low velocities regions coexist with connected preferential paths where velocities are high. This variance is also controlled by σ^2. In contrast to 2D DFN simulations, dead-end fractures, those with fracture degree of one, are not no-flow regions. Gradients can exist along the single intersection on a dead-end fracture and create low velocity flow cells within the dead-end fractures. Thus, recirculation regions exist within in dead-end fractures and these flow cells have been shown to contribute to delays in the particle transport, i.e., particle residence times are increased [Park et al., 2003]. This effect is less pronounced in the structured network due to the higher average fracture degree and wider variance of it, as well as the higher network-scale connectivity.

Higher values of σ^2 result in more longitudinal dispersion in both networks. However, the faster first arrival times in the structured network and a lower and later breakthrough peak in the random networks for all three σ^2 cases, indicate that the larger longitudinal dispersion in the particle plume is mainly structurally controlled. Similar conclusions have been recently reached in porous media, having higher variance of the solutes arrival times in spatially disordered than more orderly conductivity fields, while in the last case higher skewed distributions, as for higher σ^2 , have been reported [Bianchi and Pedretti, 2017]. Reported values of $\sigma_\tau{}^2$ increase rapidly through the first few control planes. This early spreading is related with the type of injection. For uniform injection, particles are uniformly injected across the injection section (lines that correspond to the intersection of the fractures with the control plane at $x = 0$ or 0λ) and a relative large number of particles are released at positions with low flux values. The result is an initially super-dispersive system in all cases (e.g., Kang et al. [2017]). Higher values of σ^2 result in higher values of σ_τ in both network structures. The systematically higher values of σ^2 for the random network, independent of σ^2 highlights that network structure controls macro-scale dispersion. However, as the plume moves through the domain the values of $\sigma_\tau{}^2$ increase at a lower rate. That rate is roughly the same for the structured network but varies with the σ^2 for the random network. This last observation indicates the more relevant role that hydraulic properties play in the random network than in the structured system, i.e., widening the velocity distribution and enhancing the creation of preferential paths and low velocity regions.

8.4.3 Transverse Dispersion: Mixing Capacity

Transverse dispersion provides a first approach to the mixing and reactive capacity of the system, i.e., for fluid-fluid mixing-driven chemical reactions (fast reactions). The relative concentration, M^*, or transverse movement within the network, i.e., particles crossing median plane, was systematically higher in the random network. This indicates that structural heterogeneity plays a major role in controlling transverse dispersion (e.g., Rubin and Buddemeier [1996]), and therefore on mixing. In general, the influence of hydraulic heterogeneity is less pronounced here than in the longitudinal direction. However, for the structured network, larger transverse dispersion above certain threshold in σ^2 (i.e., $\sigma^2 = 1.0$) is observed, being heterogeneity in hydraulic properties the main control on traverse dispersion. M^*, as for $\sigma_\tau{}^2$, increases with similar rate as the plume moves through the domain (i.e., with distance): slightly decreasing and increasing with σ^2 for the structured and random network, respectively. In 3D fracture networks, the combination of divergence-free flow fields and gradients along fracture intersections contribute to the redistribution of the solute particles. As in porous media (e.g., Willingham et al. [2010]), streamline convergence in flow focusing zones compresses transverse concentration, while streamline divergence after flow focusing zones expands it. This is an important mechanism for mixing diffusion limited reactions under laminar flow conditions as it increases the number of particles that cross the median plane, and thus the probability to interact with the other set of particles, i.e., mixing. Therefore, and for the similar, in statistical sense, networks studied, the ‘mixing capacity’, as well as the reactivity (i.e., the quality of being or the degree to it is reactive), are mainly structurally controlled, being higher for the random than for the structured network.

Different measures to describe and quantify solute mixing in topological complex environments, including porous and fractured media, have been proposed, between them: scalar dissipation rate, mixing degree or dilution index. Dilution index quantifies dilution as the distribution of solute mass over a media volume, i.e., volume of the media occupied by a solute cloud. This metric is expressed as the exponential of the Shannon entropy, computed from the solute concentration probability distribution. Entropy has been marginally used to measure spatial disorder of a permeability field and its control on the flow (e.g., Journel and Deutsch [1993]). The entropy computed from the eigenvalue probability distribution provide a measure of the 'mixing capacity' of the system (e.g, Jim´enez-Mart´ınez and Negre [2017]). The random network presents higher entropy values than structured one for all of weighting schemes considered (Table 8-2). Therefore, the random network has, a priori, a higher 'mixing capacity'. Compared to the structured network, particles experienced a larger number of heterogeneity transitions in the random network, which promote mixing (e.g., Bianchi and Pedretti [2017]). Interestingly, for a same network and different values of σ^2, weighting by the permeability (k) has little effect on the entropy (differences are observed at 4 significant figures), indicating that topology, i.e., macro structure, is the dominant control in the spectrum of the graph. This connection between higher values of network entropy with higher dispersion and mixing capacity underscores that the network structure is a dominant force controlling transport properties within fracture media.

8.5 Solute Transport Modeling for Swedish Long-Term Diffusion Experiments

LTDE (Long Term Sorption Diffusion Experiments) have been conducted in Sweden and focused on tracer transport in the stagnant pore water of the rock matrix. In the in situ experiment, a cocktail of both sorbing and non-sorbing tracers was allowed to contact a natural fracture surface, as well as the unaltered rock matrix, for a time period of 200 days. Analyzing the shape of the tracer penetration profiles observed in the experiment and comparing it to the predicted general shape of a 1D diffusion model, vastly different behavior was observed for the natural fracture surfaces and for the unaltered rock matrix. Figure 8-10 shows the measured experimental shapes of Cs penetration profile (symbols) and modeled penetration profile (dashed line). In order to understand the differences in the behavior, certain features of the samples and processes that are not included in the modeling should be considered.

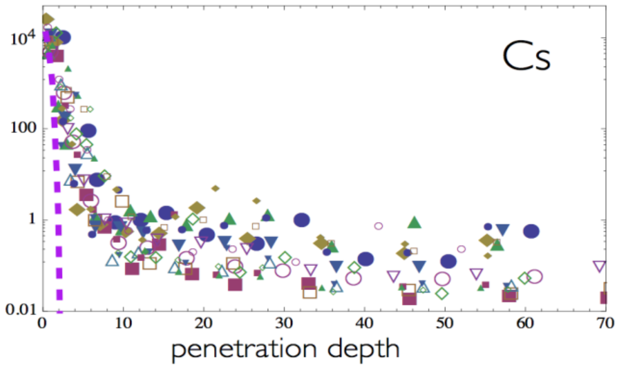

Figure 8-10. The measured experimental shapes of Cs penetration profile (symbols) do not satisfy modeled penetration profile (dashed line).

Our study focuses on understanding how micro fractures, which provide faster transport paths, affect the penetration profile. The micro fractures were observed in different slices of the sample core. Several slices of the individual cores had micro fractures that were fresh and consequently they were likely newly formed, i.e. induced by drilling or stress release. The surface of micro fractures forms an external damage layer of the sample, while the inner core (center of the sample) represents unaltered matrix rock. Porosity measurements indicate no major porosity variance within the unaltered matrix rock samples, and an increased porosity is found in fractured material samples. Moreover, a strongly heterogeneous porosity distribution is found in fracture mineralization and altered rock.

A Discrete Fracture Network (DFN) model is used to investigate, how the thickness of fractured layer affects the penetration profile of tracer driven by pure diffusion. The dfnWorks software, based on DFN model and recently developed at LANL, was successfully applied to subsurface flow and transport simulations in multiple tasks, such as underground contamination study, CO_2 sequestration, prediction of natural gas production in reservoir modeling (Hyman et al. 2015). Here, dfnWorks is applied to micro fracture modeling for the first time.

In the DFN modelling approach, the transport through fracture networks, where fractures are planar polygons that intersect each other in a 3D simulation domain, is usually used to simulate advection through fractured rock. Diffusion into the matrix is usually ignored in the DFN approach. In order to include diffusion into the rock matrix, a new method of mapping of DFN onto a high-resolution continuum mesh is developed. This new capability is used to study the effect of micro fractures on diffusive transport.

8.5.1 Methodology

Input DFN parameters

A DFN is generated according to Äspö characteristics for the fracture data, with slight modifications for micro-structure modeling:

- Domain size is 5cm × 5cm × 5cm; total volume 125cm^3.
- All fractures size follows a power law distribution, where smallest fracture length is 1 mm and longest fracture length is 1 cm.
- All fractures in the DFN are connected and provide a connected path through fractures for transport.

The DFN input parameters used are shown in Table 8-4.

Table 8-4. DFN input parameters

Set	Trend	Plunge	Kappa	R_{Min}	R_{Max}	Alpha	P_{32}
1	280	20	10	0.0005	0.005	2.6	750
2	20	10	15	0.0005	0.005	2.6	1000
3	120	50	10	0.0005	0.005	2.6	500

A DFN realization, generated based on parameters presented in Table 8-4 is shown on Figure 8-11. Every fracture is indicated by its own color. Fractures represented as two-dimensional polygons, are located in the three-dimensional domain and intersect each other forming one big cluster of the fracture network. Initially, fractures are generated and placed randomly into the domain, and then a connectivity check is performed and all the isolated fractures or isolated clusters are removed. This way, the remaining fracture network guarantees a connected path for transport from the in-flow boundary face to out-flow boundary face.

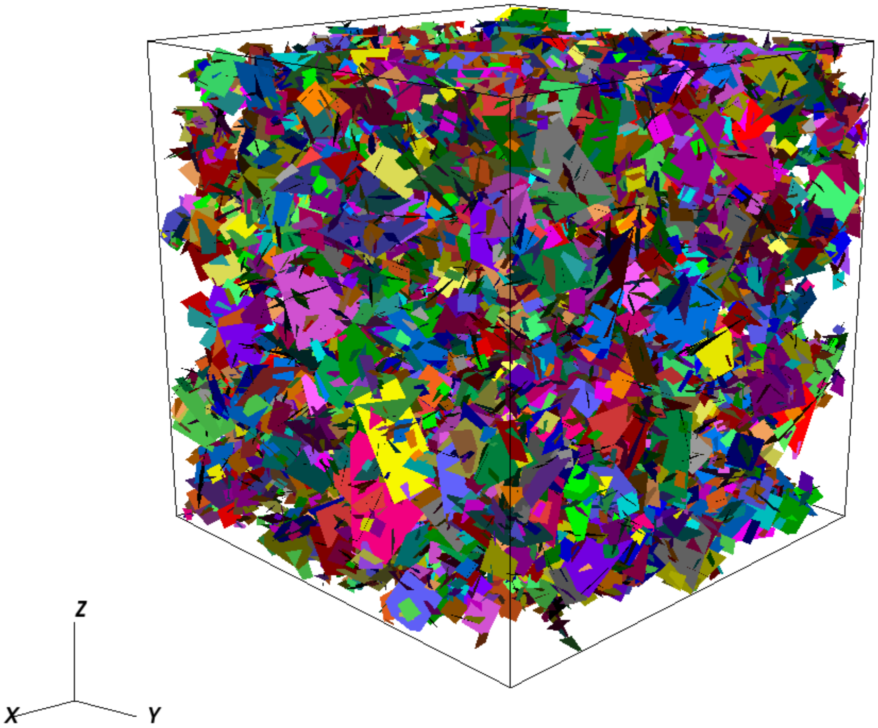

Figure 8-11. The example of DFN realization, generated according to micro fracture parameters (Table 1-6).

Conceptual approach of mapping a fracture network onto a continuum model

In the current model fractures represent porous paths between grains. In order to include the diffusion process between fracture surface and grains, the generated DFN (e.g., Figure 8-11) is mapped onto a continuum mesh (Figure 8-12). Each voxel has a dimension of 0.2 mm^3, which is 5 times smaller than the shortest fracture length. The obtained continuum mesh consists of 250 x 250 x 250 hexagonal units.

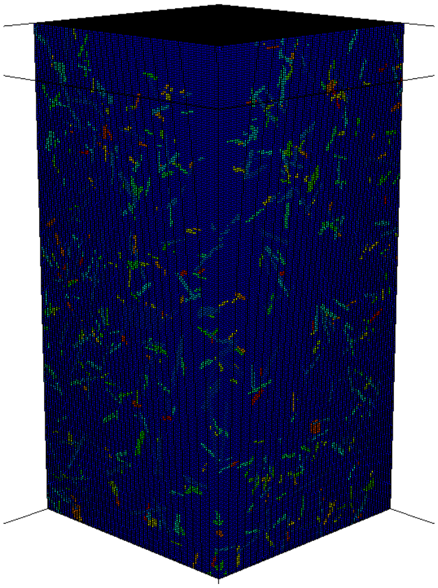

Figure 8-12. Slice of the obtained continuum mesh with mapped fracture network.

During the mapping process, the position of each voxel is matched to the fracture network. If the fracture crosses the voxel, then voxel is assigned fracture parameters. Otherwise, the matrix rock characteristics are given to the cell. The main parameter that is being translated from DFN to continuum is porosity. Porosity of fracture cells varies from 0.05 to 0.005 depending on fracture size, while rock matrix cell porosity is 0.003, as measured in the experiment. Figure 8-13 shows the example of mapped DFN into continuum, where colors represent the cell porosity.

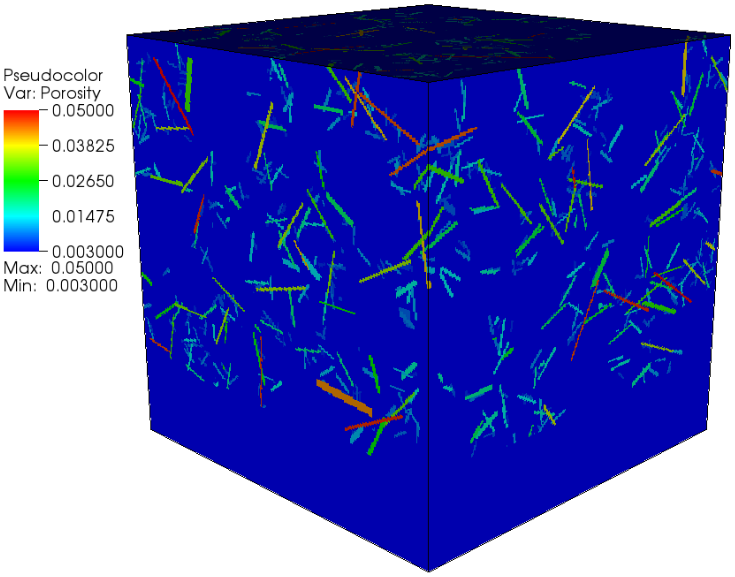

Figure 8-13. Example of a DFN mapped onto a continuum mesh. Colors represent cell's porosity. Fracture porosity vary from 0.05 to 0.005, rock matrix porosity is 0.003.

Model setup

The thickness of the fractured coating on the sample can be different and the damaged surface thickness can vary. In our model we consider 7 different variations in 50 mm intervals between the external surface and the sample center: from 10 mm to 40 mm with a step of 5 mm, moving from surface to the center. The center of the sample remains the unaltered rock with porosity 0.003. Figure 8-14schematically shows the setup of the model.

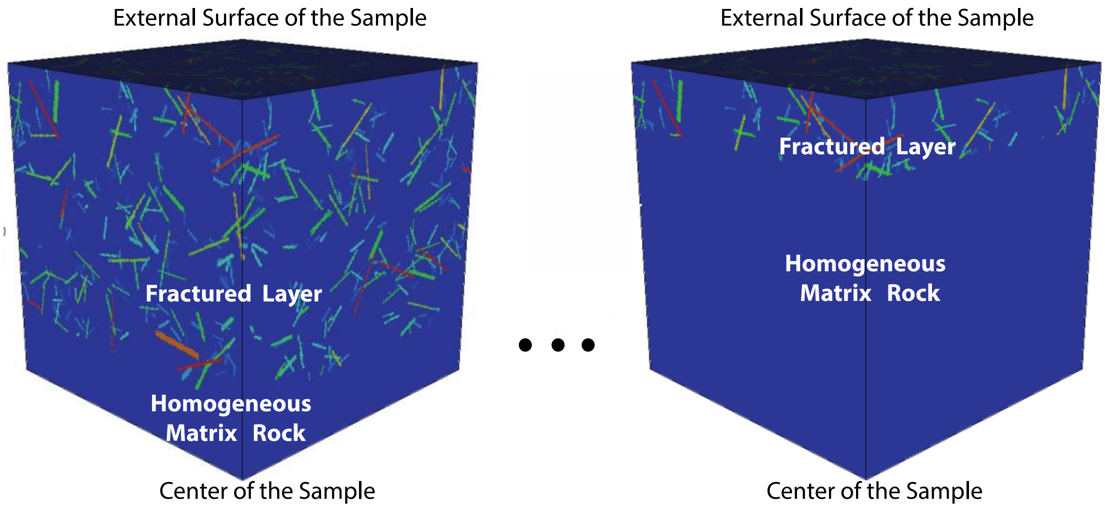

Figure 8-14. Schematic representation of the model with different variations of damage zone thickness.

Figure 8-15 shows an average porosity calculated at horizontal plane with a 2 mm step from fracture surface to sample center for each considered case. The average porosity at the fractured layer varies between 0.0045 and 0.0063, while rock matrix porosity remains 0.003.

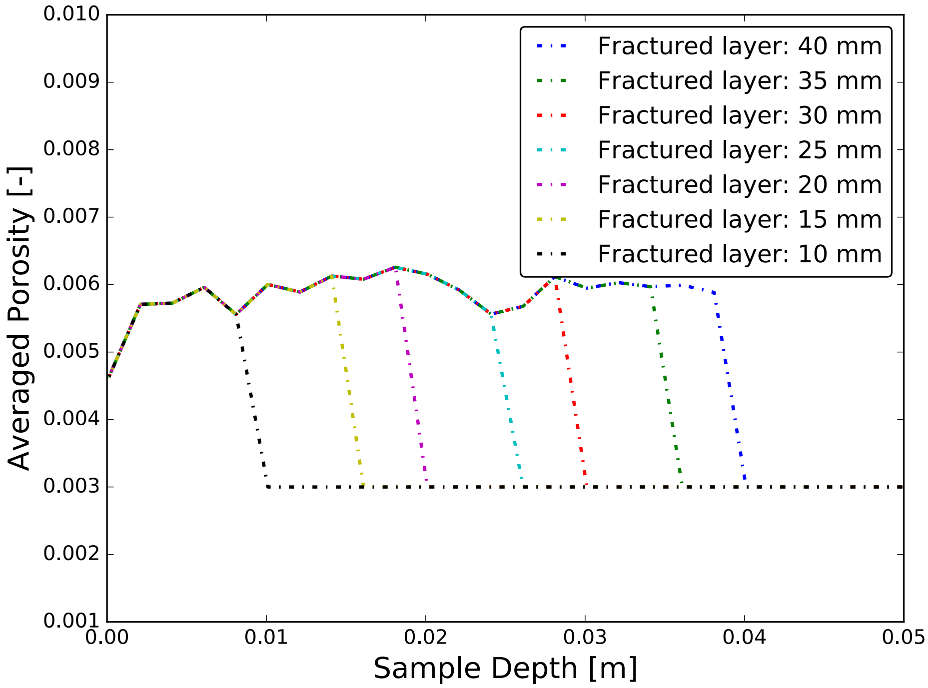

Figure 8-15. An average porosity calculated at horizontal planes from sample surface to sample center with 2 mm step for each considered case of damage zone thickness.

The massively parallel multi-physics code, PFLOTRAN (Lichtner et al. 2015), is used to simulate pure diffusion of tracer from top to bottom, from fractured surface to sample center. Dirichlet boundary conditions are applied to the top surface; we assume zero gradient boundary condition at the bottom in that the tracer cannot go through the bottom face, which is the sample center.

8.5.2 Results

Figures 8-16 and 8-17 show the tracer penetration at 200 days of diffusion simulations in case of 10 mm and 40 mm of fractured surface, respectively. The heterogeneity of tracer movement is clearly observed at fractured layers due the presence of micro fractures and the difference in porosities, even though only diffusion is considered in these simulations.

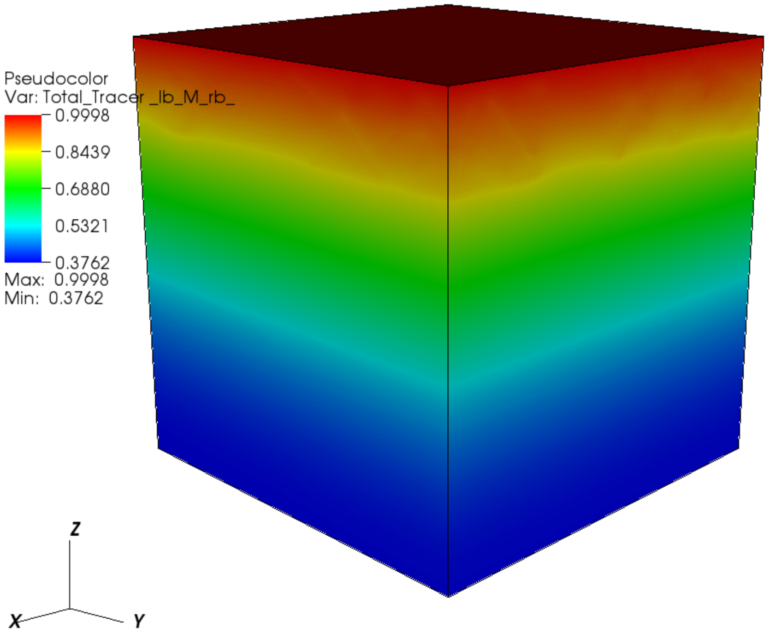

Figure 8-16. The tracer penetration at 200 days of diffusion simulation. Fractured surface thickness is 10mm.

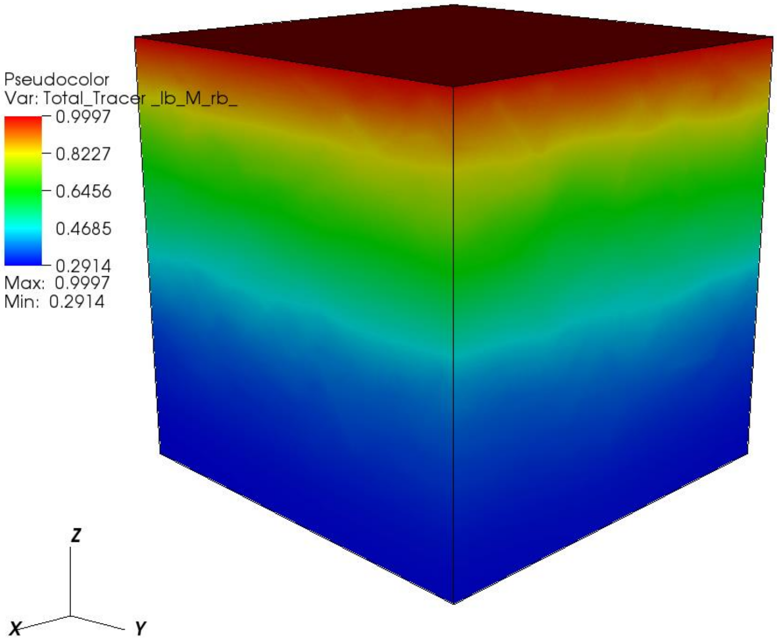

Figure 8-17. The tracer penetration at 200 days of diffusion simulation. Fractured surface thickness is 40mm.

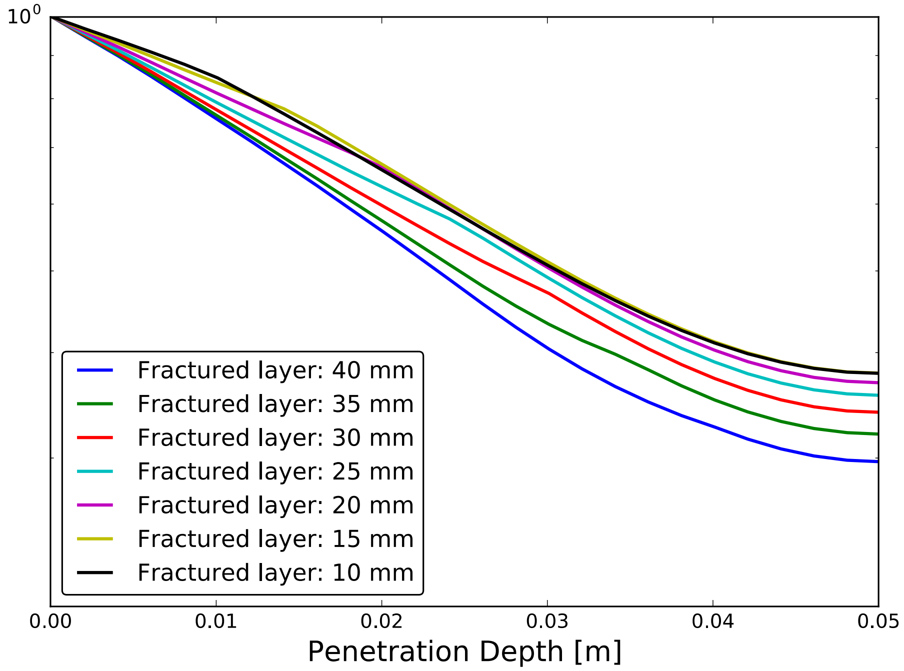

Figure 8-18. Penetration profile of tracer concentration in 200 days of diffusion simulations.

Figure 8-18 shows penetration profile of tracer driven by diffusion for 200 days. The combination of both, fractured layer and unaltered rock matrix, results in different behavior than was observed in the previous diffusion simulations. As fractured layer increases, the concentration is lower at the same depth due to porosity increase at the damage surface. The behavior of the system shows better qualitative agreement to the experiments compared to the 1D diffusion simulation where heterogeneity due to micro fractures was not considered.

The results emphasize the importance of including heterogeneity into the simulation process. Micro fractured surface contributes to initial fast decrease of concentration followed by a slower penetration as tracer gets into homogeneous medium.

8.6 Conclusions

Heterogeneity exists at many length scales within fractured media. We designed two synthetic networks to isolate the influence of structure and disorder at the macro-scale and then compare its importance relative to moderate levels of hydraulic heterogeneity. The networks were constructed to be analogous at the scale of individual fractures, most macro-scale properties, and hydraulic properties. The random network was designed to be a disordered network where fractures were not aligned with any direction. This construction resulted in lower values of connectivity compared to a structured network, which could be linked to more variation in transport behavior. We proposed and used the Shannon entropy of the fracture network, which can integrate topological, geometric, and hydraulic properties, to provide a qualitative idea of which system going to disperse or mix more even though it is not sufficient to characterize transport behavior.

The primary findings of our study are the following:

- For moderate levels of hydraulic heterogeneity, fracture network structure is the principal

control on transport times and dispersion within fracture networks.
- The less mechanical dispersion observed in the structured network appeared to be linked to the higher levels of connectivity than in the poorly connected random network.

As hydraulic heterogeneity increased, both longitudinal and traverse dispersion also increased.

- The influence of the interplay between structural and hydraulic heterogeneity is nonlinear; increased hydraulic heterogeneity for the random network resulted in more dispersion than for the structured network.
- The higher Shannon entropy of the spectrum of the normalized graph Laplacian, a measure of the disorder in the network, was linked to more disperse transport and higher mixing capacity.

Beyond the fact that heterogeneities at different scales imply a spatial scaling of hydraulic parameters (i.e., storage coefficient and hydraulic conductivity), the non-inclusion of some of heterogeneity families could suppose changing from a random to a structural network, with the subsequent implications for transport and mixing as shown in this work. Therefore, geological characterization (planes) at all scales (from foliation to large-scale fractures), including laboratory (e.g., cores) and field (e.g., well logs, cartography) work, are essential at the time to propose an equivalent system from DFN. Below the scale of individual fractures there are more levels of heterogeneity to consider, e.g., in-fracture aperture variability and mixing rules along intersects. The influence of these features will be the focus of subsequent studies.

8.7 References

Barbier, E., Geothermal energy technology and current status: an overview, Renew. Sust. Energ. Rev., 6, 3–65, 2002.

Berkowitz, B., and I. Balberg, Percolation theory and its application to groundwater hydrology, Water Resour. Res., 29(4), 775–794, 1993.

Berkowitz, B., and H. Scher, Anomalous transport in random fracture networks, Phys. Rev. Lett., 79(20), 4038, 1997.

Berkowitz, B., and H. Scher, Theory of anomalous chemical transport in random fracture networks, Phys. Rev. E, 57(5), 5858, 1998.

Bianchi, M., and D. Pedretti, Geological entropy and solute transport in heterogeneous porous media, Water Resour. Res., doi: 10.1029/2003WR002655, 2017.

Cacas, M. C., E. Ledoux, G. De Marsily, A. Barbreau, P. Calmels, B. Gaillard, and R. Margritta, Modeling fracture flow with a stochastic discrete fracture network: Calibration and validation: 2. The transport model, Water Resour. Res., 26(3), 491–500, 1990.

Cvetkovic, V., S. Painter, N. Outters, and J. Selroos, Stochastic simulation of radionuclide migration in discretely fractured rock near the A ̈sp ̈o hard rock laboratory, Water Resour. Res., 40(2), doi:10.1029/2003WR002655, 2004.

de Dreuzy, J.-R., C. Darcel, P. Davy, and O. Bour, Influence of spatial correlation of fracture centers on the permeability of two-dimensional fracture networks following a power law length distribution, Water Resour. Res., 40(1), 2004.

Demmy, G., S. Berglund, and W. Graham, Injection mode implications for solute transport in porous media: Analysis in a stochastic Lagrangian framework, Water Resour. Res., 35(7), 1965–1973, 1999.

Dershowitz, W., FracMan version 7.4-Interactive discrete feature data analysis, geometric modeling, and exploration simulation: User documentation, http://fracman.golder.com/, 2014.

Dershowitz, W., and C. Fidelibus, Derivation of equivalent pipe network analogues for three-dimensional discrete fracture networks by the boundary element method, Water Resour. Res., 35(9), 2685–2691, 1999.

Dreuzy,J.-R.,Y.M´eheust,andG.Pichot,Influenceoffracture scale heterogeneity on the flow properties of three-dimensional discrete fracture networks (dfn), J. Geophys. Res., 117(B11), 2012.

Erhel, J., J.-R. De Dreuzy, and B. Poirriez, Flow simulation in three-dimensional discrete fracture networks, SIAM J. Sci. Comput., 31(4), 2688–2705, 2009.

Frampton, A., and V. Cvetkovic, Significance of injection modes and heterogeneity on spatial and temporal dispersion of advecting particles in two-dimensional discrete fracture networks, Adv. Water Resour., 32(5), 649–658, 2009.

Gotovac, H., V. Cvetkovic, and R. Andricevic, Flow and travel time statistics in highly heterogeneous porous media, Water Resour. Res., 45(7), 2009.

Gotovac, H., V. Cvetkovic, and R. Andricevic, Significance of higher moments for complete characterization of the travel time probability density function in heterogeneous porous media using the maximum entropy principle, Water Resour. Res., 46(5), 2010.

Hagberg, A. A., D. A. Schult, and P. Swart, Exploring network structure, dynamics, and function using networkx, in Proceedings of the 7th Python in Science Conferences (SciPy 2008), vol. 2008, pp. 11–16, 2008.

Huseby, O., J. F. Thovert, and P. M. Adler, Dispersion in threedimensional fracture networks, Phys. Fluids, 13(3), 594–615, 2001.

Hyman, J., et al., Understanding hydraulic fracturing: a multiscale problem, Phil. Trans. R. Soc. A, 374(2078), 20150,426, 2016a.

Hyman, J. D., C. W. Gable, S. L. Painter, and N. Makedonska, Conforming Delaunay triangulation of stochastically generated three dimensional discrete fracture networks: A feature rejection algorithm for meshing strategy, SIAM J. Sci. Comput., 36(4), A1871–A1894, 2014.

Hyman, J. D., S. Karra, N. Makedonska, C. W. Gable, S. L. Painter, and H. S. Viswanathan, dfnWorks: A discrete fracture network framework for modeling subsurface flow and transport, Comput. Geosci., 84, 10–19, 2015a.

Hyman, J. D., S. L. Painter, H. Viswanathan, N. Makedonska, and S. Karra, Influence of injection mode on transport properties in kilometer-scale three-dimensional discrete fracture networks, Water Resour. Res., 51(9), 7289–7308, 2015b.

Hyman, J. D., G. Aldrich, H. Viswanathan, N. Makedonska, and S. Karra, Fracture size and transmissivity correlations: Implications for transport simulations in sparse three-dimensional discrete fracture networks following a truncated power law distribution of fracture size, Water Resour. Res., 52(8), 6472– 6489, doi:10.1002/2016WR018806, 2016b.

Hyman, J. D., A. Hagberg, G. Srinivasan, J. Mohd-Yusof, and H. S. Viswanathan, Predictions of first passage times in sparse discrete fracture networks using graph-based reductions, Phys. Rev. E (In Press), 2017.

Jankovi´c, I., and A. Fiori, Analysis of the impact of injection mode in transport through strongly heterogeneous aquifers, Adv. Water Resour., 33(10), 1199–1205, 2010.

Ji, S.-H., Y.-J. Park, and K.-K. Lee, Influence of fracture connectivity and characterization level on the uncertainty of the equivalent permeability in statistically conceptualized fracture networks, Transport Porous Med., 87(2), 385–395, 2011.

Jim´enez-Mart´ınez, J., and C. F. A. Negre, Eigenvector centrality for geometric and topological characterization of porous media, Phys. Rev. E (In Press), 2017.

Jim´enez-Mart´ınez, J., L. Longuevergne, T. Borgne, P. Davy, A. Russian, and O. Bour, Temporal and spatial scaling of hydraulic response to recharge in fractured aquifers: Insights from a frequency domain analysis, Water Resour. Res., 49 (5), 3007–3023, 2013.

Johnson, J., S. Brown, and H. Stockman, Fluid flow and mixing in rough-walled fracture intersections, J. Geophys. Res., 111(B12), 2006.

Journel, A. G., and C. V. Deutsch, Entropy and spatial disorder, Math. Geol., 25(3), 329–355, 1993.

Kang, P., S. Brown, and R. Juanes, Emergence of anomalous transport in stressed rough fractures, Earth Planet. Sci. Lett., 454, 46–54, 2016.

Kang, P. K., M. Dentz, T. Le Borgne, and R. Juanes, Anomalous transport on regular fracture networks:

Impact of conductivity heterogeneity and mixing at fracture intersections, Phys. Rev. E, 92(2), 022,148, 2015.

Kang, P. K., M. Dentz, T. Le Borgne, S. Lee, and R. Juanes, Anomalous transport in disordered fracture networks: spatial markov model for dispersion with variable injection modes, Adv. Water Resour., doi:10.1016/j.advwatres.2017.03.024, 2017.

Karrer, B., M. E. Newman, and L. Zdeborova ́, Percolation on sparse networks, Phys. Rev. Lett., 113(20), 208,702, 2014. Kitanidis, P. K., The concept of the Dilution Index, Water Resour. Res., 30(7), 2011–2026, 1994. Klint, K., P. Gravesen, A. Rosenbom, C. Laroche, L. Trenty,

Kreft, A., and A. Zuber, On the physical meaning of the dispersion equation and its solutions for different initial and boundary conditions, Chem. Eng. Sci., 33(11), 1471–1480, 1978.

LaGriT, Los Alamos Grid Toolbox, (LaGriT) Los Alamos National Laboratory, http://lagrit.lanl.gov, 2013.

Lichtner, P., G. Hammond, C. Lu, S. Karra, G. Bisht, B. Andre, R. Mills, and J. Kumar, PFLOTRAN user manual: A massively parallel reactive flow and transport model for describing surface and subsurface processes, Tech. rep., (Report No.: LAUR-15-20403) Los Alamos National Laboratory, 2015.

Long, J., and P. A. Witherspoon, The relationship of the degree of interconnection to permeability in fracture networks, J. Geophys. Res., 90(B4), 3087–3098, 1985.

Makedonska, N., S. L. Painter, Q. M. Bui, C. W. Gable, and S. Karra, Particle tracking approach for transport in threedimensional discrete fracture networks, Computat. Geosci., pp. 1–15, 2015.

Makedonska, N., J. D. Hyman, S. Karra, S. L. Painter, C. W. Gable, and H. S. Viswanathan, Evaluating the effect of internal aperture variability on transport in kilometer scale discrete fracture networks, Adv. Water Resour., 94, 486–497, 2016.

Moreno, L., Y. W. Tsang, C. F. Tsang, F. V. Hale, and I. Neretnieks, Flow and tracer transport in a single fracture, a stochastic model and its relation to some field observations, Water Resour. Res., 24, 2033–48, 1988.

Mustapha, H., and K. Mustapha, A new approach to simulating flow in discrete fracture networks with an optimized mesh, SIAM J. Sci. Comput., 29, 1439, 2007.

Painter, S. L., C. W. Gable, and S. Kelkar, Pathline tracing on fully unstructured control-volume grids, Computat. Geosci., 16(4), 1125–1134, 2012.

Park, Y.-J., K.-K. Lee, G. Kosakowski, and B. Berkowitz, Transport behavior in three-dimensional fracture intersections, Water Resour. Res., 39(8), 2003.

Pichot, G., J. Erhel, and J. De Dreuzy, A mixed hybrid mortar method for solving flow in discrete fracture networks, Appl. Anal., 89(10), 1629–1643, 2010.

Pichot, G., J. Erhel, and J. de Dreuzy, A generalized mixed hybrid mortar method for solving flow in stochastic discrete fracture networks, SIAM J. Sci. Comput., 34(1), B86–B105, 2012.

Rh ́en, I., A ̈spo ̈ HRL: geoscientific evaluation 1997/4: results from pre-investigations and detailed site characterization: comparison of predictions and observations: hydrology, groundwater chemistry and transport of solutes, Svensk k ̈arnbr ̈anslehantering AB/Swedish Nuclear Fuel and Waste Management, 1997.

Roques, C., O. Bour, L. Aquilina, and B. Dewandel, High-yielding aquifers in crystalline basement: insights about the role of fault zones, exemplified by armorican massif, france, Hydrogeol. J., 24(8), 2157–2170, 2016.

Rubin, H., and R. W. Buddemeier, Transverse dispersion of contaminants in fractured permeable formations, J. Hydrol., 176(1), 133–151, 1996.

Singhal, B. B. S., and R. P. Gupta, Applied hydrogeology of fractured rocks, Springer Science & Business Media, 2010.

Tsang, C. F., and I. Neretnieks, Flow channeling in heterogeneous fractured rocks, Rev. Geophys., 36(2), 275–298, 1998.

Tsang, Y. W., and C. F. Tsang, Flow channeling in a single fracture as a two-dimensional strongly heterogeneous permeable medium, Water Resour. Res, 25(9), 2076–2080, 1989.

Tsang, Y. W., C. F. Tsang, F. V. Hale, and B. Dverstorp, Tracer transport in a stochastic continuum model of fractured media, Water Resourc. Res., 32(10), 3077–3092, 1996.

Vanderborght, J., D. Mallants, and J. Feyen, Solute transport in a heterogeneous soil for boundary and initial conditions: Evaluation of first-order approximations, Water Resour. Res., 34(12), 3255–3270, 1998.

Willingham, T., C. Zhang, C. J. Werth, A. J. Valocchi, M. Oostrom, and T. W. Wietsma, Using dispersivity values to quantify the effects of pore-scale flow focusing on enhanced reaction along a transverse mixing zone, Adv. Water Resour., 33 (4), 525–535, 2010.

Wood, A. T., Simulation of the von Mises Fisher distribution, Commun. Stat. Simulat., 23(1), 157–164, 1994.

9. FRACTURE DATA ANALYSIS AND PRELIMINARY MODELING FOR MIZUNAMI SITE

Through the Development of Coupled Models and their Validation against Experiments (DECOVALEX-2019) project, we have obtained a comprehensive set of hydrologic and chemical data from a research tunnel at the Japan Atomic Energy Agency (JAEA) Mizunami Underground Research Laboratory (MIU). In this section, we show how to develop a general workflow or methodology to synthesize these data into a flow and transport model. This work was carried out for Task C of DECOVALEX 2019 - Groundwater Recovery Experiment in Tunnel (GREET). The data obtained from the experiments in a research tunnel located at 500 m depth, at the MIU. The main aim of GREET is to understand the hydrological-mechanical-chemical environment in the vicinity of the research laboratory. One of the objectives of Task C, Step 1, is to establish modeling methods and tools for analysis of excavation of the tunnel. Fracture data analysis and preliminary modeling analysis were carried out at Sandia National Laboratories as part of Task C, Step 1. The fracture data analysis utilized fracture data collected in the research tunnel and monitoring borehole 12MI33. A discrete fracture model was developed based on fracture orientation, size and intensity derived from the fracture data analysis. The discrete model was upscaled to an effective continuum model to be used in flow and transport simulations. Section 9.1 provides details of the fracture analysis. The preliminary modeling analysis also used project data to construct a simulation model to predict inflow into the inclined drift and the Closure Test Drift (CTD) during excavation. The modeling analysis also predicts pressure and chloride concentration histories at observation points. The modeling analysis is described in Section 9.2. For both fracture model development and modeling analysis data from JAEA were used.

9.1 Fracture Data Analysis and Fracture Model Development

9.1.1 Introduction

The major goal of this study was developing fracture model of the granite rocks for the area surrounding the MIU Research tunnel at 500 m depth. The fracture model is needed for simulation of hydrogeologic and geochemical conditions in the various experiments being conducted in the research tunnel as a part of GREET project.

The modeling domain is 100x150x100m with the main experimental part of the tunnel, Closure Test Drift (CTD), located approximately in the center. The majority of model is within the lower sparsely fractured domain (LSFD) of the Toki granite. Figure 9-1-1 shows the modeling domain, the research tunnel (CTD and Inclined Drift), the horizontal monitoring borehole 12MI33 (with 6 test intervals), and the vertical exploratory borehole MIZ-1 (only 2 test intervals are inside the modeling domain).

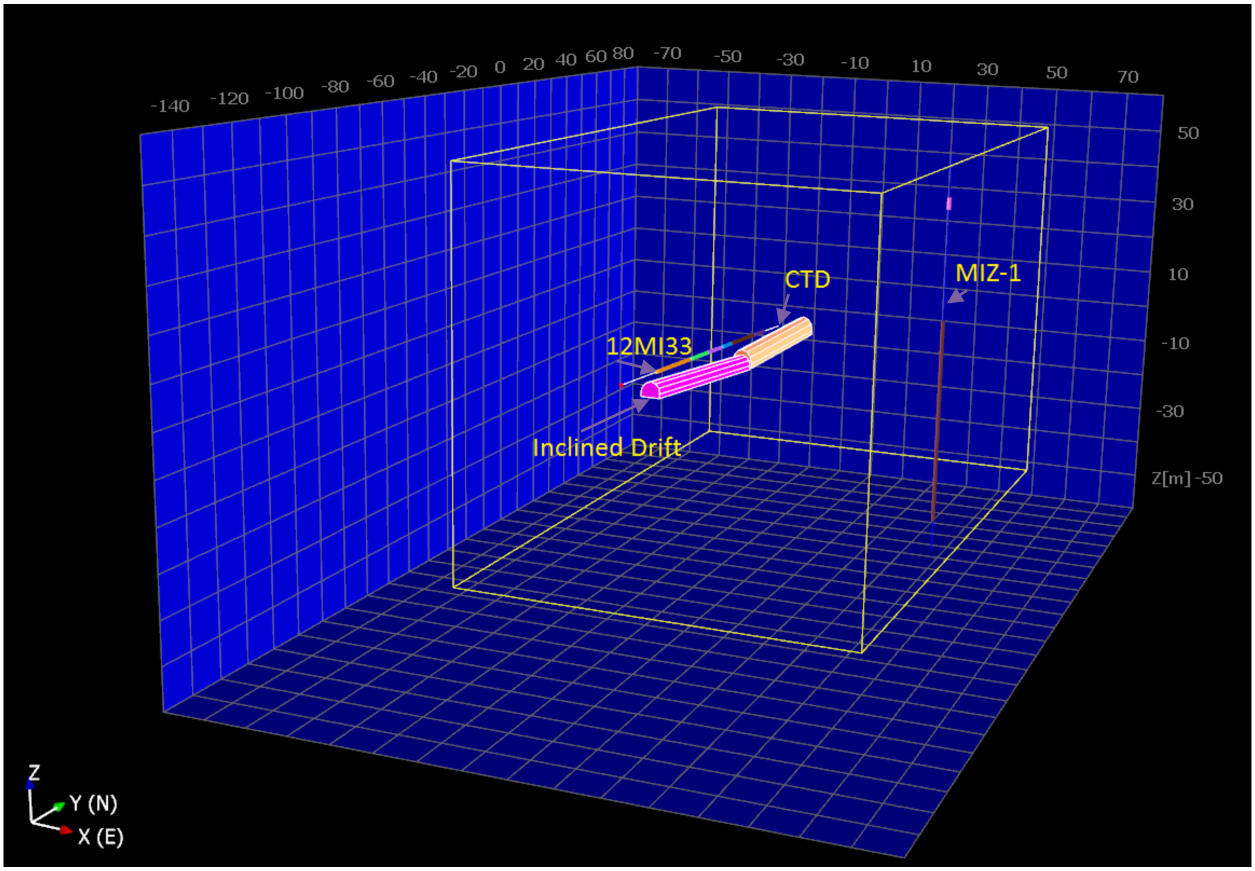

Figure 9-1-1. Modeling Domain and Location of Research Tunnel and Boreholes.

The following data were used in the fracture analysis:

- Fractures traces on the walls of CTD, Inclined Drift, and Access Drift. Note that Access drift fracture data were used in the analysis even though this drift is outside the modeling domain.
- Fractures observed in borehole 12MI33.
- Packer test data in 6 test intervals of 12MI33 and 2 test intervals of borehole MIZ-1.
- Measured inflow into the research drift.

The goal of the fracture analysis was to estimate fracture orientation, size and intensity and use these estimates to develop discrete fracture model (DFN). The DFN model is then converted to an equivalent continuum model with the grid cell size 1x1x1 m (1,500,000 grid blocks) using Oda's method (Golder, 2017). Multiple realizations of DFN and corresponding equivalent continuum model will be used to simulate groundwater flow and transport in vicinity of the research tunnel. The developing of DFN is demonstrated using one realization as an example. Fracman (Golder software, Golder, 2017) was used to develop the model.

9.1.2 Generating Fractures Using Research Tunnel Fracture Trace Data

2,023 fractures were observed on the wall of the research tunnel. Figure 9-1-2 shows the observed fracture traces and location of monitoring points in borehole 12MI33. The fracture trace data include trace segment coordinates, length, dip, strike, alteration (if any), and flow range (if any). If alteration was observed, the filling was described using the following categories: carbonate; chlorite and/or sericite; and unconsolidated clayey fillings including smectite.

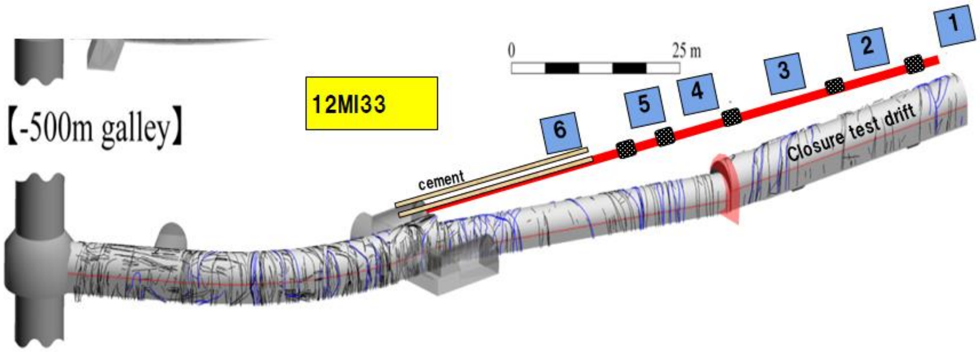

Figure 9-1-2. Observed Fracture Traces in the Research Tunnel and Location of Monitoring Points in Borehole 12MI33.

It was assumed that the fractures that did not exhibit any flow discharge are either closed fractures or small fractures not connected to the fracture network. There are 146 fractures (7.2%) with the observed flow discharge. They are characterized in the original data set based on the flow range as “flow” (F) fractures (>1L/min), “drop” (D) fractures (>0.1L/min), and “wet” (W) (<0.1L/min) fractures. These fractures were selected for the analysis and fracture model development (Table 9-1-1). The trace data were imported into the model and are shown in Figure 9-1-3.

Table 9-1-1. Research Tunnel Fractures Included in the Fracture Analysis.

Research Tunnel Area	**F-Fractures** (flow>1.0 L/min)	**D-Fractures** (flow>0.1 L/min)	**W-Fractures** (flow<0.1 L/min)	**All Fractures with Flow**
CTD	4	15	3	22
Inclined Drift	14	42	N/A	56
Access Drift	N/A	65	3	68
Total	**18**	**122**	**6**	**146**

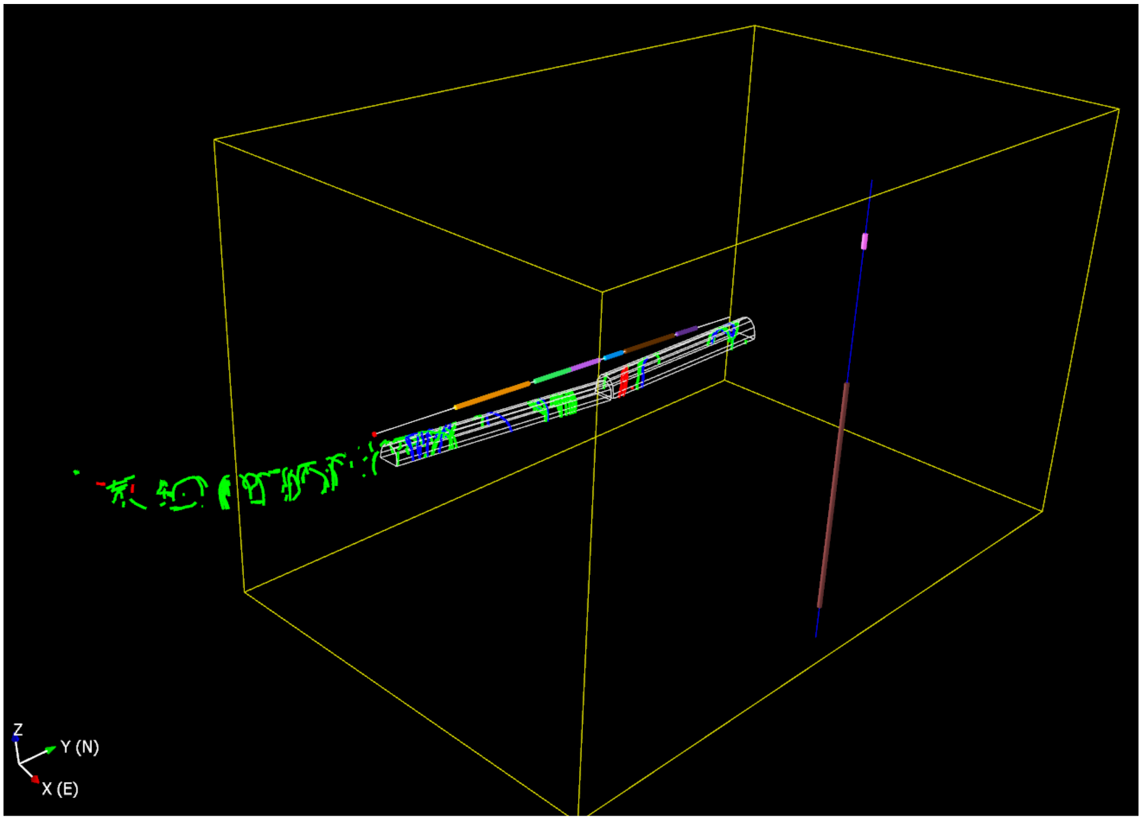

Note: F-fractures are shown in blue; D-fractures are shown in green; and W-fractures are shown in red color.

Figure 9-1-3. Traces of the Fractures Included in the Analysis on the Research Tunnel Walls.

The observed fracture traces can be used to generate each individual fracture. The dip direction and dip angle of the fracture are derived from the plane containing the fracture traces. Thus, the location of the fracture plane center and its orientation is fixed. However, the fracture size and shape are generally not known and need to be defined. This analysis assumes that the fractures have circular shape (aspect ratio 1:1), which is a common assumption of discrete fracture network (DFN) models.

The fracture size was derived from the trace length analysis. It was assumed that the fractures with different flow discharges may have different sizes. Consequently, the analysis was conducted separately for F-; D-; and W- fractures. Fracman uses algorithm described in Zhang (2002) and La Pointe (2002) to estimate fracture size (equivalent radius) from the trace length and offers different probability distributions for fitting the data. The power-law and lognormal distributions were considered in this analysis.

The results of the fracture size analysis are shown in Figure 9-1-4 for the power-low and in Figure 9-1-5 for the lognormal distribution. The distributions of W- and D- fractures are very similar and were combined in one. The F- fracture distribution is different from D- and W- fracture distributions. The trace length distributions of all sets are best described with the lognormal distribution. The power-law distribution, that is often assumed for fracture size, is not a good fit to these data.

The equivalent fracture radius distributions estimated from the trace length data are summarized in Table 9-1-2. The F- fractures with greater flow rates are also the ones with the larger size. This is consistent with the common concept according to which the fracture parameters that affect the flow (transmissivity and aperture) are positively correlated with the fracture radius.

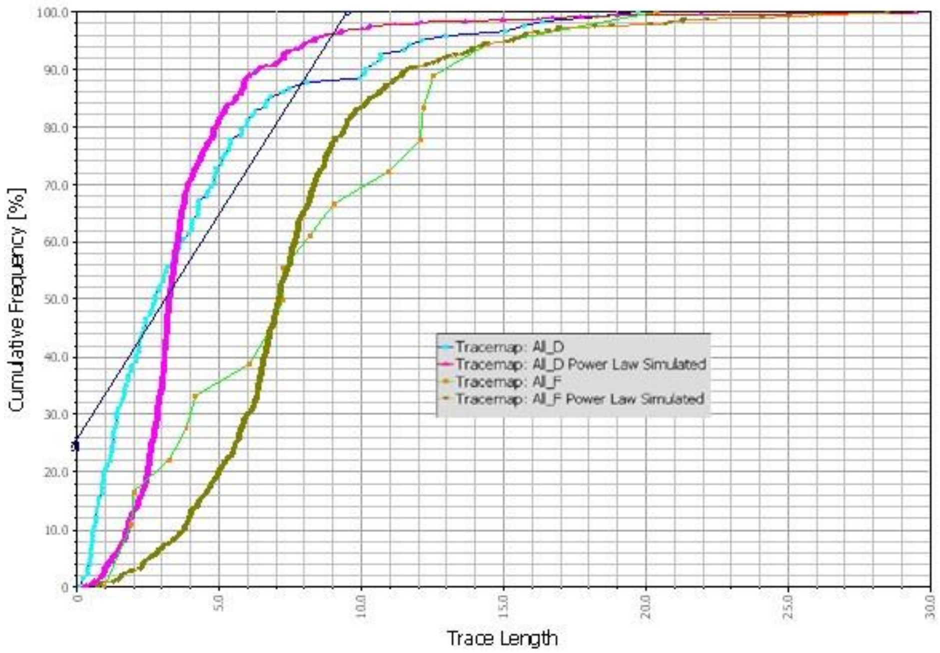

Figure 9-1-4. Power-Law Distribution Fit to the Fracture Trace Data.

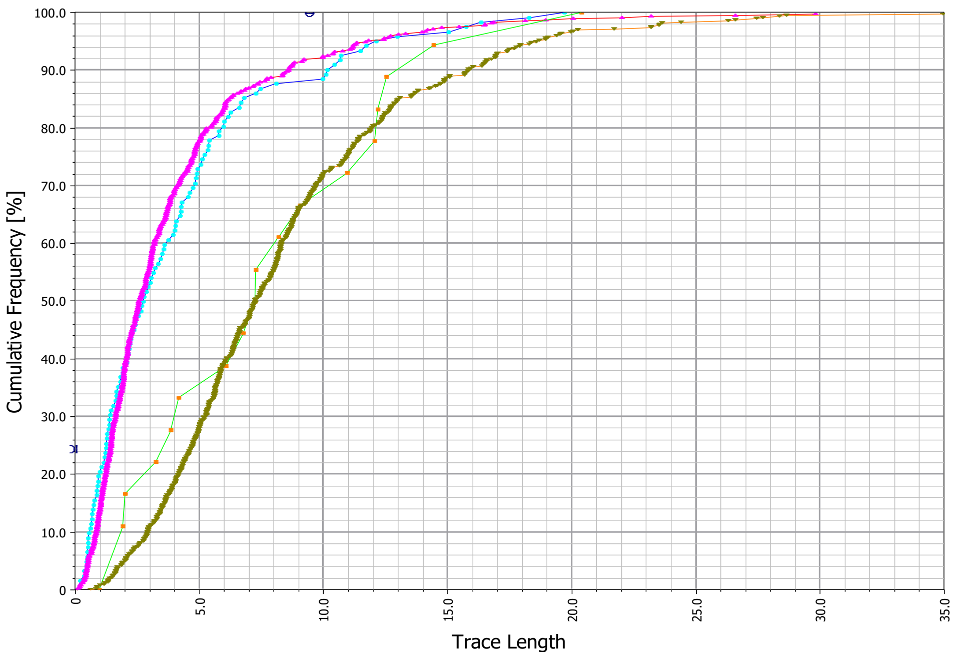

Figure 9-1-5. Lognormal Distribution Fit to the Fracture Trace Data.

Table 9-1-2. Equivalent Fracture Radius Distribution Parameters.

Fracture Set	Distribution Type	Mean/Minimum Radius (m)	Standard Deviation/Exponent
D- and W-Fractures	Lognormal	1.42	1.29
F-Fractures	Lognormal	3.88	2.15
D- and W-Fractures	Power-Law	1.5	3.4
F-Fractures	Power-Law	3.3	3.9

146 fractures were generated in the Research Tunnel using the lognormal distributions defined in Table 9.1.2 for the equivalent fracture radius (either F- or W- and D- depending on the fracture type). Note that the size of fractures will vary from realization to realization. Figure 9.1.6 shows the generated fractures for one realization.

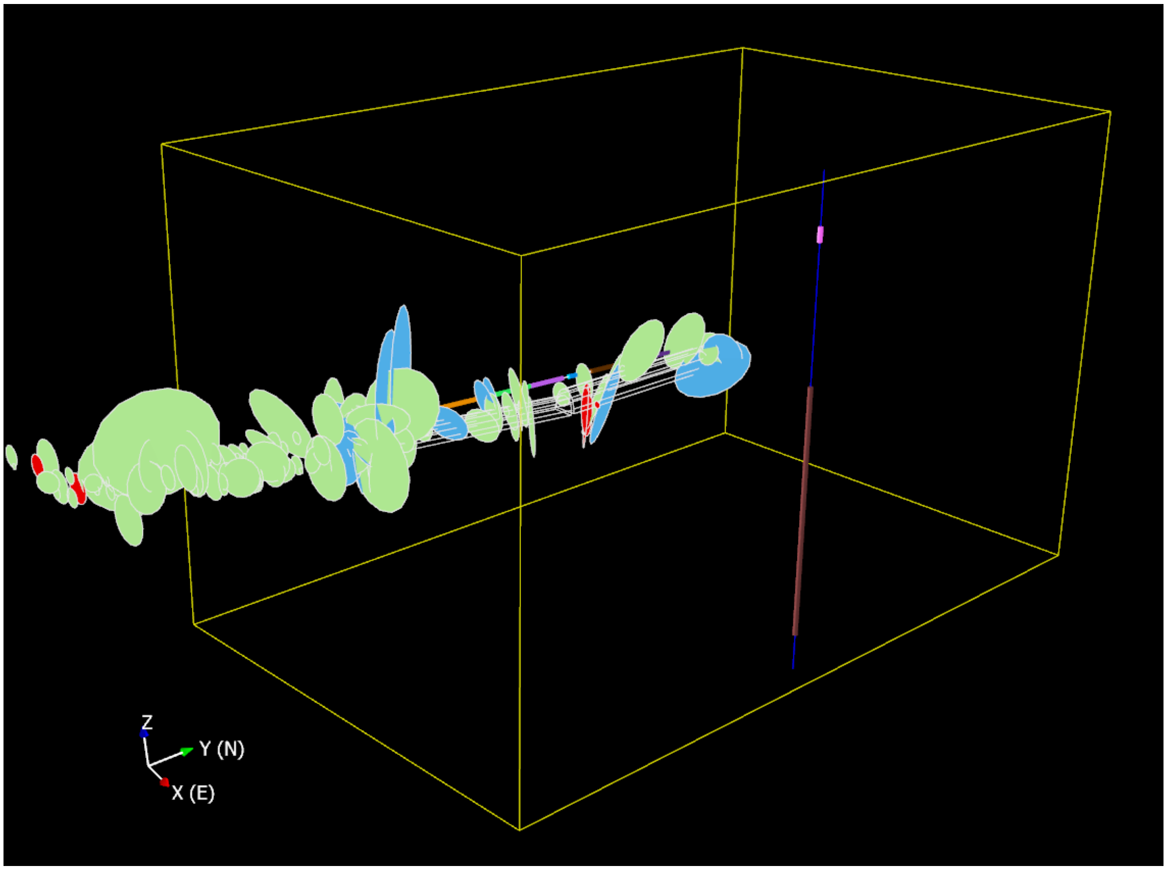

Note: F-fractures are shown in blue; D-fractures are shown in green; and -fractures are shown in red color.

Figure 9-1-6. Fracture Generated in the Research Tunnel.

The remaining fracture parameters that have to be defined for DFN are fracture hydraulic conductivity (or permeability) and fracture aperture. Very few data are available on fracture aperture. Even when fracture aperture is reported, it seems to apply only to the surface of the tunnel or borehole walls. The values are too large (1 mm or greater) to be representative of the conditions within the rock mass. The fracture aperture values typical for granite rocks are in the order of tenths to hundreds micron, with the exception of the large fractures in fault zones.

The hydraulic conductivity k_{int} was derived from the transmissivity evaluated in the packer tests T_{int} as:

$$k_{int} = \frac{T_{int}}{l_{int}} \qquad , \qquad (9.1.1)$$

where l_{int} is the length of the test interval.

T_{int} measured in these tests represents the transmissivity of the test interval. A test interval may intersect different types of fractures with different connections to the fracture network. These fractures may have different size, hydraulic conductivity, and aperture. Thus, the interval transmissivity and hydraulic conductivity values cannot be easily converted to fracture transmissivity and hydraulic conductivity. Same principle applies to the observed inflow into the tunnel.

This analysis uses all available data in combination with the discrete fractures generated in the tunnel and borehole 12MI33 to evaluate fracture transmissivity. The initial evaluation of fracture transmissivity is based on the observed range of flow through the different types of fracture. The analytical solution for the unit inflow (Q) into a circular tunnel with radius r located at depth h (Butscher, 2012) is:

$$Q = \frac{2\pi k(A+H)}{\ln(\frac{h}{r}+\sqrt{\frac{h^2}{r^2}-1}} \qquad , \qquad (9.1.2)$$

$A = h(1-\alpha^2)/(1+\alpha^2)$ and $= \frac{1}{r}(h - \sqrt{h^2 - r^2}$,

where k is the hydraulic conductivity.

The inflow through the fracture (Q_{fr}) with aperture b is:

$$Q_{fr} = Q \cdot b \; = \frac{2\pi T(A+H)}{\ln(\frac{h}{r}+\sqrt{\frac{h^2}{r^2}-1}} \qquad (9.1.3)$$

$$T = k \cdot b$$

where T is fracture transmissivity.

Fracture transmissivity T was calculated from Eq. 9.1.3 assuming r= 2.5 m and h=500m. The transmissivity of F- fractures (Q_{fr} > 1.0 L/min) is > $3.2 \ast 10^{-8}$ m^2/s, transmissivity of D- fractures (Q_{fr} > 0.1 L/min) is > $3.2 \ast 10^{-9}$ m^2/s, and the transmissivity of W- fractures (Q_{fr}< 0.1 L/min) *is* < $3.2 \ast 10^{-9}$ m^2/s.

It was assumed that the inflow into CTD (Q_{CTD}) and Inclined Drift (Q_{Incl}) can be approximated by the following equations:

$$Q_{CTD} = Q_{CTD\_F} + Q_{CTD\_D} + Q_{CTD\_W} \qquad (9.1.4)$$

$$Q_{CTD\_F} = 1.0\frac{L}{min} \cdot N_{F_{CTD}} \cdot c, \qquad Q_{CTD\_D} = 0.1\frac{L}{min} \cdot N_{D_{CTD}} \cdot c, \qquad Q_{CTD\_W} = 0.1\frac{L}{min} \cdot N_{W_{CTD}}$$

$$Q_{Incl} = Q_{Incl\_F} + Q_{Incl\_D} + Q_{Incl\_W} \qquad (9.1.5)$$

$$Q_{Incl\_F} = 1.0\frac{L}{min} \cdot N_{F_{Incl}} \cdot c, \qquad Q_{Incl\_D} = 0.1\frac{L}{min} \cdot N_{D_{Incl}} \cdot c, \qquad Q_{Incl\_W} = 0.1\frac{L}{min} \cdot N_{W_{Incl}}$$

where N_{F_CTD} and N_{F_Incl} is the number of F-fractures in CTD and Inclined Drift respectively, N_{D_CTD} and N_{D_Incl} is the number of D-fractures, N_{W_CTD} and N_{W_Incl} is the number of W-fractures, and c is a constant. Introducing c accounts for the fact that the flow through a fracture was express in terms of a value greater or smaller than specific limit. The value of c=2.3 was derived by matching the observed inflow into CTD and Inclined Drift with the inflow values calculated with Eq. 9.1.4 and 9.1.5.

The Access Drift was not considered because of two reasons: it is outside the modeling domain and it is affected by the proximity to the Main Shaft fault and HFUD.

The observed and calculated values are summarized in Table 9.1.3. The fracture transmissivity values that correspond to the calculated inflow values are: 7.3*10^{-8} m^2/s (F-fractures), 7.3*10^{-9} m^2/s (D- fractures), and 3.2*10^{-9} m^2/s (W- fractures).

Table 9-1-3. Comparison of Measured and Calculated Inflow into the Research Tunnel.

Research Tunnel Area	**Measured Tunnel Inflow (L/min)**	**Number of Fractures**			**Calculated Inflow (L/min)**			
		F	**D**	**W**	**F**	**D**	**W**	**Total**
CTD	13	4	15	3	9.2	3.45	0.3	12.95
Inclined Drift	43	14	42	N/A	32.2	9.66	0	41.86

The fracture aperture can be estimated from the cubic law relationship (Snow, 1969) between the transmissivity and aperture:

$$T = \frac{b^3}{12}\frac{\rho g}{\mu} \qquad (9\text{-}1\text{-}6)$$

where ρ is the water density, g is the gravity acceleration and μ is the water viscosity.

Assuming ρ=998 kg/m^3 and μ=0.001 N s/m^2 the calculated aperture values are: 45 micron (F-fractures), 21 micron (D-fractures), and 16 micron (W-fractures).

The fracture permeability (k) can be calculated as:

$$k = \frac{b^2}{12}\frac{\rho g}{\mu} \qquad (9.1.7)$$

The calculated fracture permeability values (approximation of mean) are: 1.7x10^{-10} m^2 (F-fractures), 3.6x10^{-11} m^2 (D-fractures). and 3.5x10^{-12} m^2 (W-fractures).

The following ranges were derived for the fracture parameters:

- Fracture transmissivity: $3.2 \times 10^{-9} – 7.3 \times 10^{-8}$ m^2/s.
- Fracture permeability: $3.5 \times 10^{-12} – 1.7 \times 10^{-10}$ m^2
- Fracture aperture: 16 – 45 micron

Note that these ranges apply to the average parameter values.

There is no enough data to develop probability distributions for permeability and aperture. Instead, this analysis assumes correlations between the lognormally distributed fracture equivalent radius (R) and fracture permeability (k) and aperture (b) in the following form:

$$k = \gamma_1 \cdot R^{\omega} \qquad (9.1.8)$$

$$b = \gamma_2 \cdot R \qquad (9.1.9)$$

where γ_1, γ_2, and ω are coefficients.

The coefficients were adjusted to match the calculated inflow into the tunnel with the observed inflow. Eq. 9.1.3 was used to calculate the inflow through each fracture shown in Figure 9-1-6. Each fracture has different radius and, thus, different permeability and aperture (Eq. 9.1.8 and 9.1.9) and different transmissivity (Eq. 9.1.6). A good match was obtained with the following coefficient values:

- $\gamma_1 = 1.55 \times 10^{-12}$
- $\gamma_2 = 1.16\text{xE}^{-5}$
- $\omega = 2.3$

The results of the calculations with these coefficients are summarized in Table 9-1-4. The average transmissivity of fracture is 2.5×10^{-8} m^2/s. This falls into the estimated transmissivity range 3.2×10^{-9} – 7.3×10^{-8} m2/s.

Table 9-1-4. Comparison of Calculated Inflow from Generated Fractures and Observed Inflow into Research Tunnel.

Generated Fractures		
Type	**∑ Transmissivity (m^2/s)**	**∑ Inflow (L/min)**
D	1.94E-06	61.03
F	1.58E-06	49.78
W	9.71E-08	3.06
Total	**3.62E-06**	**113.87**
Measured Inflow into the Research Tunnel (L/min): 104		

9.1.3 Generating Fractures Using Borehole 12MI33 Fracture Data

Borehole 12MI33 is a horizontal borehole that is parallel to the Research tunnel (Figure 9-1-1). The packer tests were conducted in 6 test intervals. The test intervals also serve as the monitoring points (Figure 9-1-2) for observation of temporal variations in pressure and geochemistry in vicinity of the Research tunnel.

297 fractures were recorded in the borehole. The fractures were classified as “crack”; “hair crack”; “discontinuity crack”; and “mineral vein”. The fractures described as cracks that had recorded aperture values were assumed to be permeable fractures, such as F-, D-, and W-fractures observed in the Research tunnel. 17 such fractures were identified. The fractures data were imported into the model. The fractures were generated in accordance with these data (depth and orientation) using F-fracture lognormal distribution for fracture radius. F-fracture radius distribution produced closer results to the packer test results as shown below.

The fractures generated in the borehole are shown in Figure 9-1-7 along with the Research tunnel fractures. Figure 9-1-7 also shows the transmissivity of the test intervals obtained in the packer tests. The high transmissivity intervals 1, 2’ and 6 coincide with the zones in which fractures generated in both, Research tunnel and borehole, are present. Intervals 2 and 3 intersect a few fractures and their transmissivity is lower. Intervals 4 and 5 do not intersect any of generated fractures and their transmissivity is significantly lower.

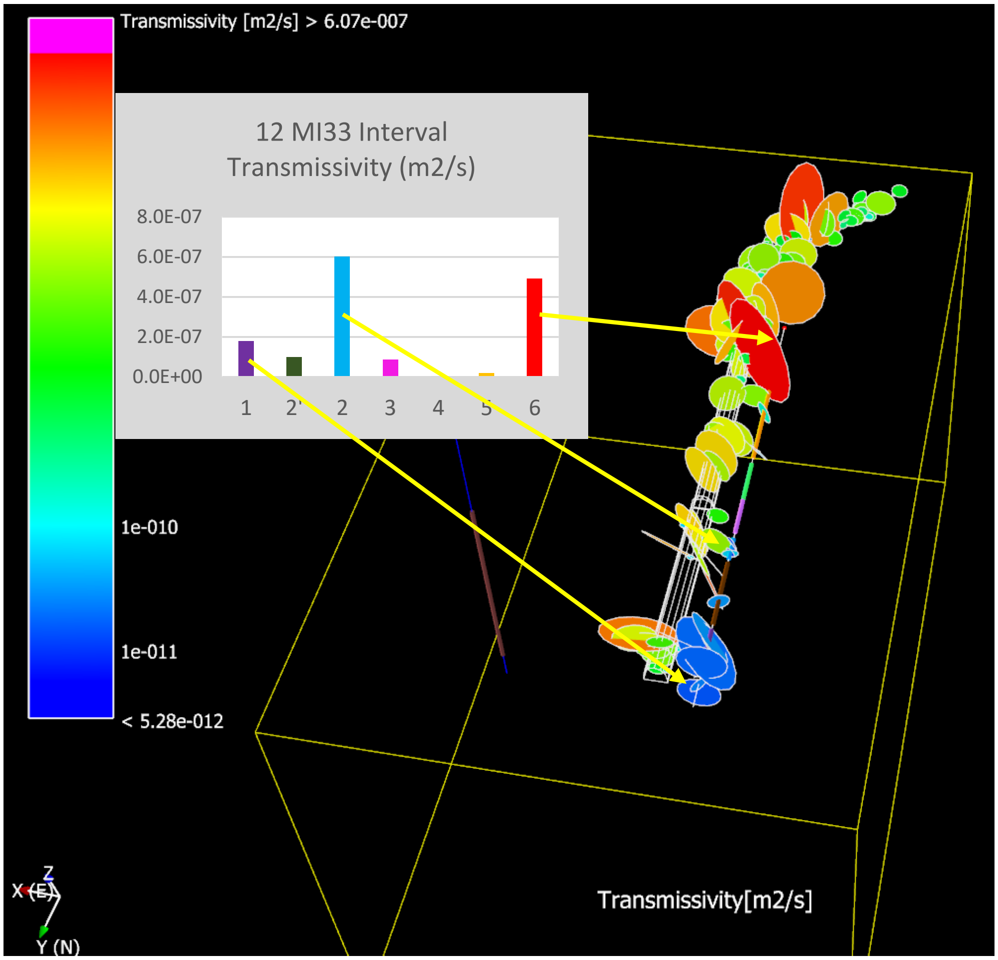

Figure 9-1-7. Transmissivity of Fractures in the Research Tunnel and Borehole 12MI33.

Tables 9-1-5 and 9-1-6 compare the transmissivity of the generated fractures in borehole 12MI33 and the transmissivity of the test intervals from the packer tests in this borehole. The total transmissivity of fractures generated in the borehole (7.6x10^{-7} m^2/s) is close to the total transmissivity of the test intervals (9.9x10^{-7} m^2/s).

The following can be concluded:

- The locations of 17 fractures generated in borehole 12MI33 are consistent with the locations of fractures in the Research tunnel.
- Fracture properties derived from the Research tunnel fracture trace analysis are consistent with the packer test data in borehole 12MI33.

Table 9-1-5. Transmissivity of the Generated fractures in Borehole 12MI33

Fracture	Transmissivity (m^2/s)	Fracture	Transmissivity (m^2/s)
1	1.14E-08	10	8.30E-09
2	2.71E-09	11	5.36E-09
3	1.74E-08	12	2.62E-09
4	7.26E-09	13	1.60E-08
5	1.39E-08	14	2.34E-08
6	2.94E-09	**15**	4.27E-07
7	6.28E-08	**16**	6.59E-08
8	5.01E-08	**17**	1.82E-08
9	2.30E-08	**Total**	**7.58E-07**

Table 9-1-6. Transmissivity of the Test Intervals from Borehole 12MI33 Packer Tests.

Interval	Transmissivity (m^2/s)
1	1.78E-07
2'	9.78E-08
2	6.01E-07
3	8.65E-08
4	4.96E-09
5	1.93E-08
6	4.91E-07
Total	**9.88E-07**

9.1.4 Generating Stochastic Fractures in the Modeling Domain

The Research tunnel fracture trace analysis considered in Section 9.1.2 provided estimates of the fracture size, permeability, and aperture. These estimates were corroborated by comparing the packer test results with the transmissivity of fractures generated in borehole 12MI33 in Section 9.1.3. The fractures with the deterministic locations and stochastic properties (radius and correlated with radius permeability and aperture) were generated in the Research tunnel and borehole 12MI33 (Figure 9-1-7).

The size and properties of the fractures outside the Research tunnel and borehole 12MI33 can be assumed in accordance with the above estimates. However, the locations of these fractures are not known. Thus, the stochastic approach is needed. The stochastic generation of fractures requires the following input parameters:

- Number of fracture sets
- Orientation distribution of each set
- Fracture intensity in each set

9.1.4.1 Number of Fracture Sets and Fracture Orientation

The number of fracture sets and their orientation was obtained from the analysis of the fractures generated from the tunnel traces using Fracman tool Interactive Set Identification System (ISIS). ISIS (Golder, 2017) defines fracture sets from field data using an adaptive probabilistic pattern recognition algorithm. ISIS calculates the distribution of orientations for the fractures assigned to each set, and then reassigns fractures to sets according to probabilistic weights proportional to their similarity to other fractures in the set. The orientations of the sets are then recalculated and the process is repeated until the set assignment is optimized. Figure 9-1-8 shows the ISIS set assignment results for the Research tunnel fractures. Even though 3 sets are defined, most of the fractures are in Set 2. The significance levels of the fitted Fischer distributions are low for all sets meaning there is no clear separation into the different sets.

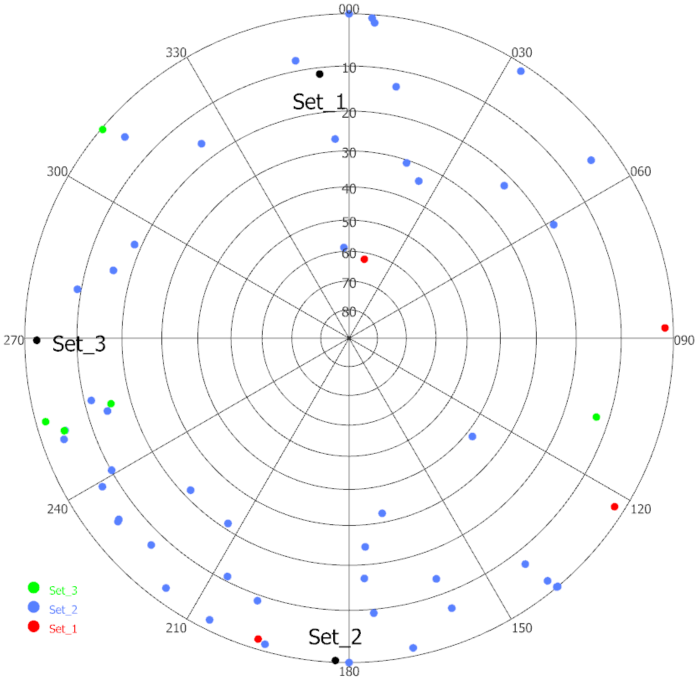

Figure 9-1-8. ISIS Set Assignment Results for the Research Tunnel Fractures.

In the next step, the fractures in the Access Drift were removed from the analysis because they may be affected by the Main Shaft fault. For example, set 3 in Figure 9-1-8 contains only the Access Drift fractures. The ISIS analysis of fractures in the Inclined Drift and CTD identified only one fracture set. The best distribution (Kolmogorov-Smirnov probability 87%) was Fisher distribution with the flowing parameters:

- mean trend 208^0
- mean plunge 8^0
- concentration parameter ķ equal to 7

Note that orientation is given in the local coordinate system. The actual coordinate system was rotated 10.2^0 clockwise in x-y plane to align the tunnel with the y axis. The calculated Fisher distribution is shown in Figure 9-1-9. The low ķ signifies large dispersion or wide range in fracture orientations.

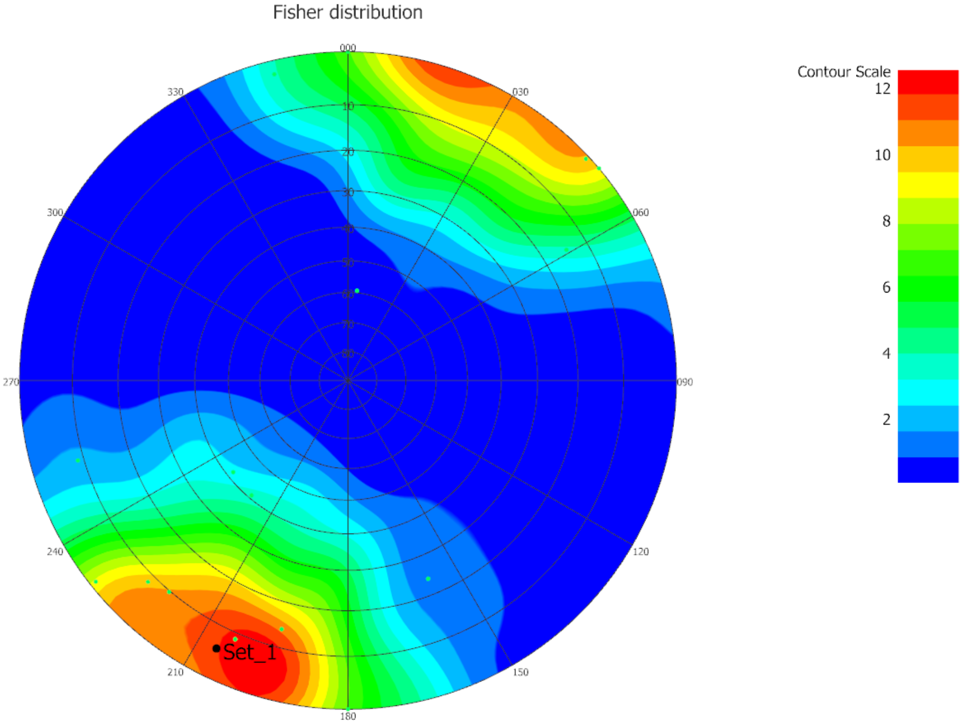

Figure 9-1-9. Calculated Fisher Distribution for Inclined Drift and CTD Fractures.

9.1.4.2 Fracture Intensity

Fracture intensity has direct impact on how many fractures will be generated in the modeling domain. Fracture intensity can be specified either as number of fractures in the set (not recommended because it is scale dependent) or as volumetric intensity of fractures in the set, also known as P_{32}. P_{32} [1/m] is scale independent (invariant with respect to the distribution of fracture size) and represents fracture area per unit volume of rock. Neither number of fractures or P_{32} can be directly measured.

This analysis uses the observed linear intensity P_{10} (number of fractures per unit length) of fractures in the Research tunnel (0.19 fractures/m) and in the borehole 12MI33 (0.17 fractures/m) to evaluate P_{32}. The stochastic fractures were generated using Fisher distribution (Section 9.1.4.1), fracture radius (Table 9-1-2), fracture permeability (Eq. 9.1.8), and fracture aperture (Eq. 9.1.9). The fracture P_{32} value is iteratively redefined until the P_{10} values in 2 arbitrary placed imaginary horizontal boreholes matched P_{10} of fractures observed in the Research tunnel and borehole 12MI33.

Figure 9-1-10 shows the stochastic fractures intersected by the two imaginary horizontal boreholes with P_{32}=0.22 1/m. P_{10} in both imaginary boreholes (0.19 fractures/m) matches the observed P_{10} in the Research tunnel and is very close to the observed P_{10} in borehole 12MI33.

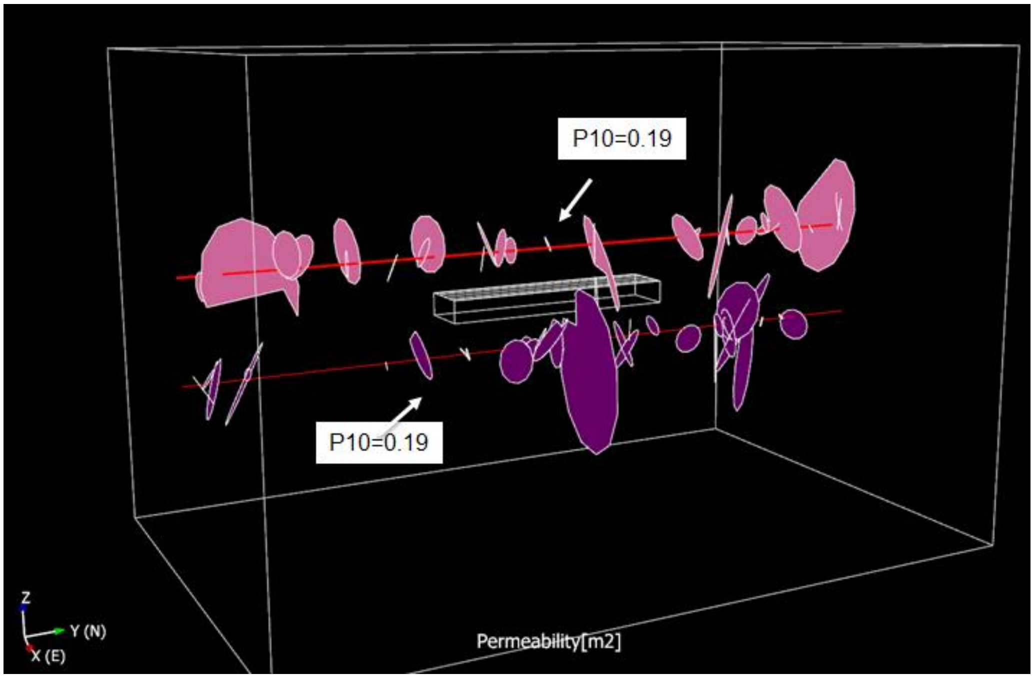

Figure 9-1-10. Stochastic Fractures Intersecting Two Imaginary Horizontal Boreholes.

The significantly lower P_{10} values (0.04) were calculated for two arbitrarily placed vertical boreholes (Figure 9-1-11). This is because vertical borehole has lower probability of intersecting sub-vertical fractures.

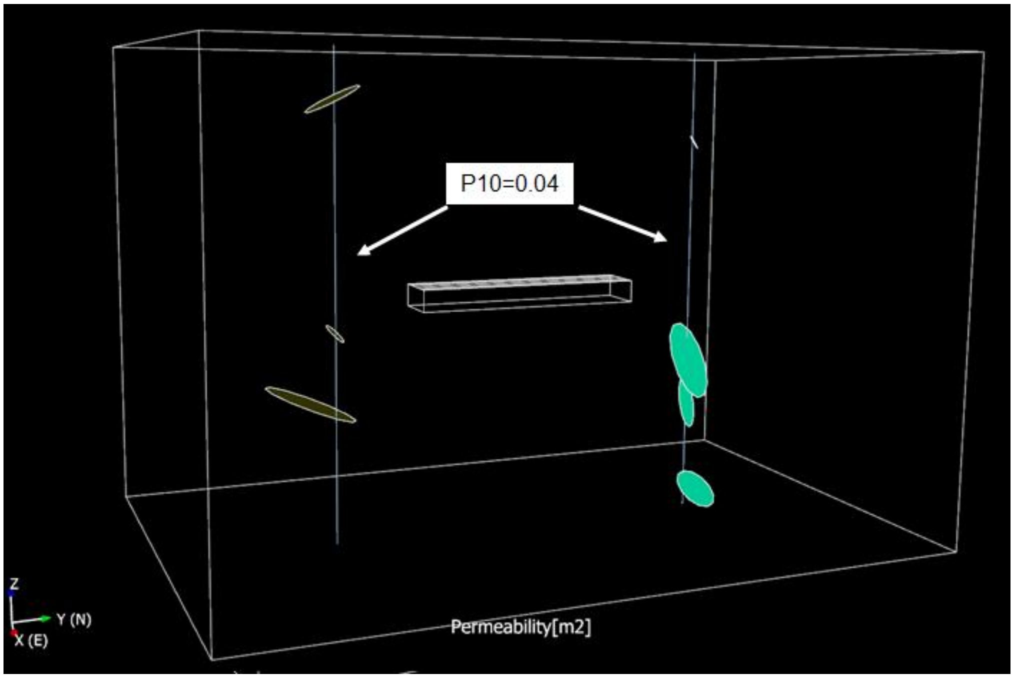

Figure 9-1-11. Stochastic Fractures Intersecting Two Imaginary Vertical Boreholes.

9.1.4.3 Comparison to the Packer Test Results in Borehole MIZ-1

Figure 9-1-12 shows the stochastic fractures that intersect upper and lower test intervals of the vertical borehole MIZ-1. The transmissivity of the generated fractures is provided in Table 9-1-7. The packer test results are summarized in Table 9.1.8. The total transmissivity of generated stochastic fractures ($2.1x10^{-7}$ m^2/s) is higher than the total transmissivity obtained in the packer tests ($4.2x10^{-8}$ m^2/s). The horizontal flow to the vertical borehole in the packer tests is affected by the horizontal permeability. The horizontal permeability is lower than vertical because the fractures are sub-vertical. This can explain some of the difference. Also, only one realization was used in this comparison.

Table 9-1-7. Transmissivity of Stochastic Fractures Intersected by Borehole MIZ-1.

Fracture	Transmissivity (m^2/s)
1	9.54E-08
2	3.54E-08
3	7.34E-09
4	2.52E-08
5	4.38E-08
Total	**2.07E-07**

Table 9-1-8. Packer Test Results in Borehole MIZ-1.

Interval		Transmissivity (m^2/s)
Top (m)	**Bottom, m**	
-260.4	-263.3	3.69E-08
-290.9	-342.4	5.16E-09
Total		**4.20E-08**

NOTE: Only the test intervals within the modeling domain are considered.

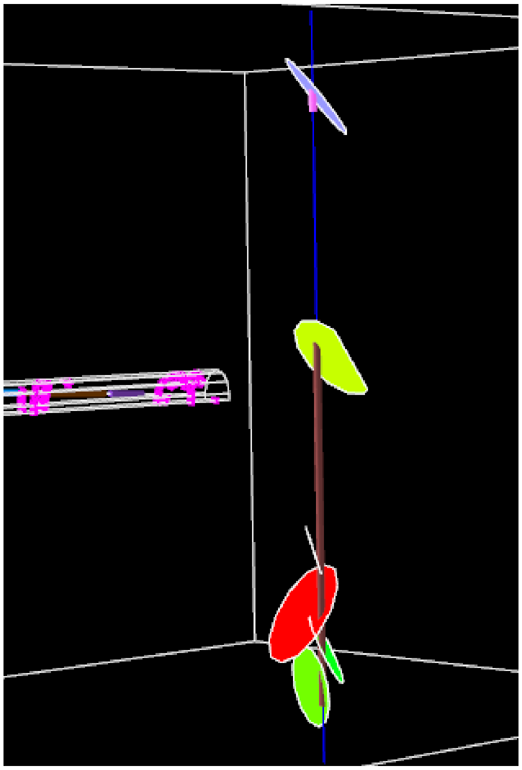

Figure 9-1-12. Stochastic Fractures Intersected by Borehole MIZ-1.

9.1.4.3 Stochastic Fracture Generation

The stochastic fractures were generated assuming one fracture set with the orientation defined in Section 9.1.4.1 and P_{32}=0.22 calculated in Section 9.1.4.2. The Enhanced Baecher model in Fracman was used. In the original Baecher model (Baecher et.al, 1978) the fracture centers are located uniformly in space, and, using a Poisson process, the fractures are generated as disks with a given radius and orientation. The Enhanced Baecher model extends the Baecher model by providing a provision for fracture terminations and more general fracture shapes.

Figure 9-1-13 shows one realization of the stochastic fractures generated in the modeling domain. The color scale is used to show fracture transmissivity. One realization of the fractures in the Research tunnel and borehole 12MI33 (Figure 9-1-7) is also included.

Figure 9-1-14 shows the stereonet of the generated stochastic fractures. Figures 9-1-15 and 9-1-16 show the sampled distribution of fracture permeability and aperture respectively. The median permeability is 2.3×10^{-11} m^2 and the median aperture is 27 micron.

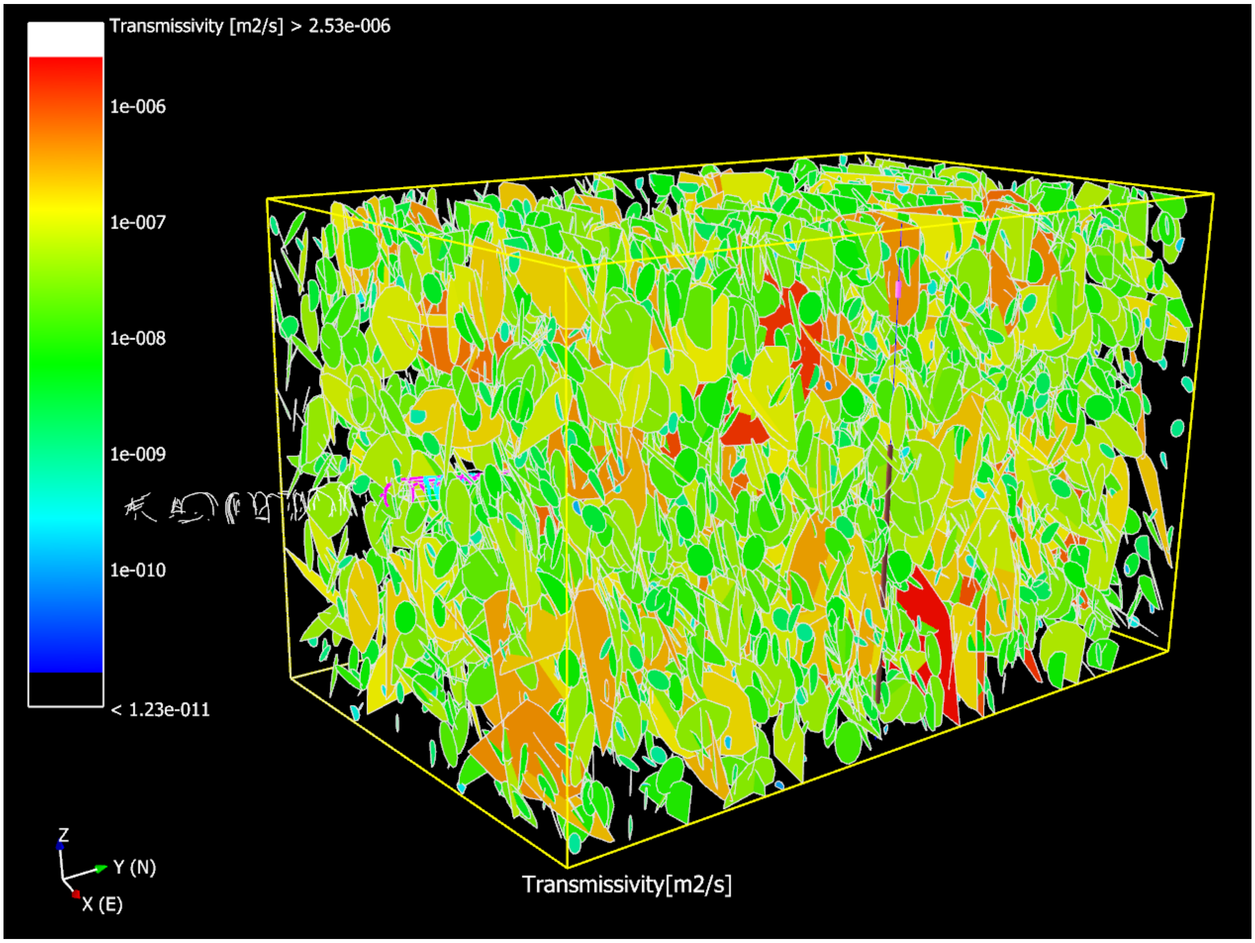

Figure 9-1-13. One Realization of the Stochastic Fractures Generated in the Modeling Domain.

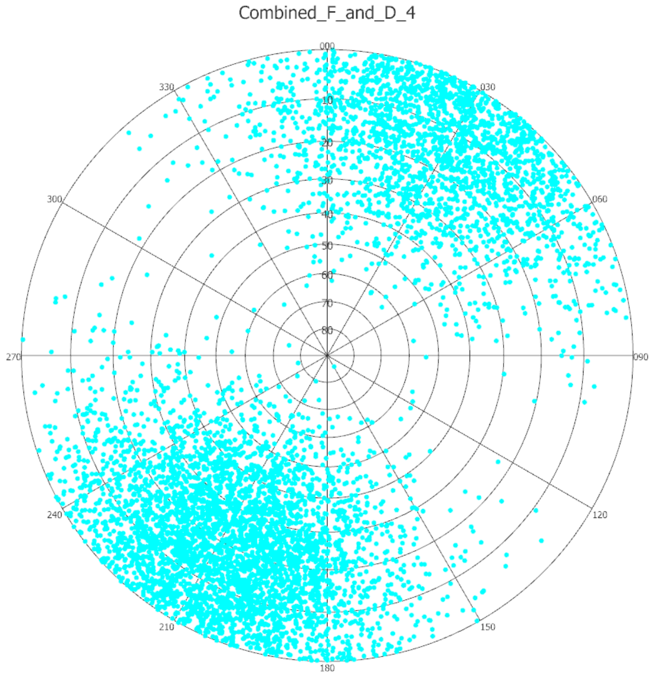

Figure 9-1-14. Sampled Stochastic Fracture Stereonet.

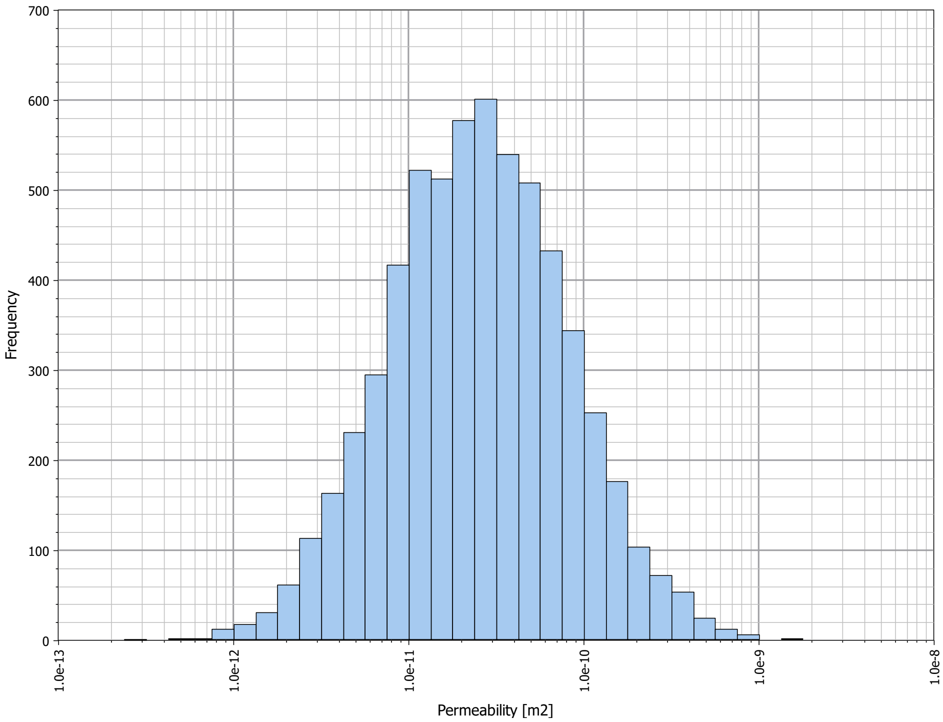

Figure 9-1-15. Sampled Stochastic Fracture Permeability.

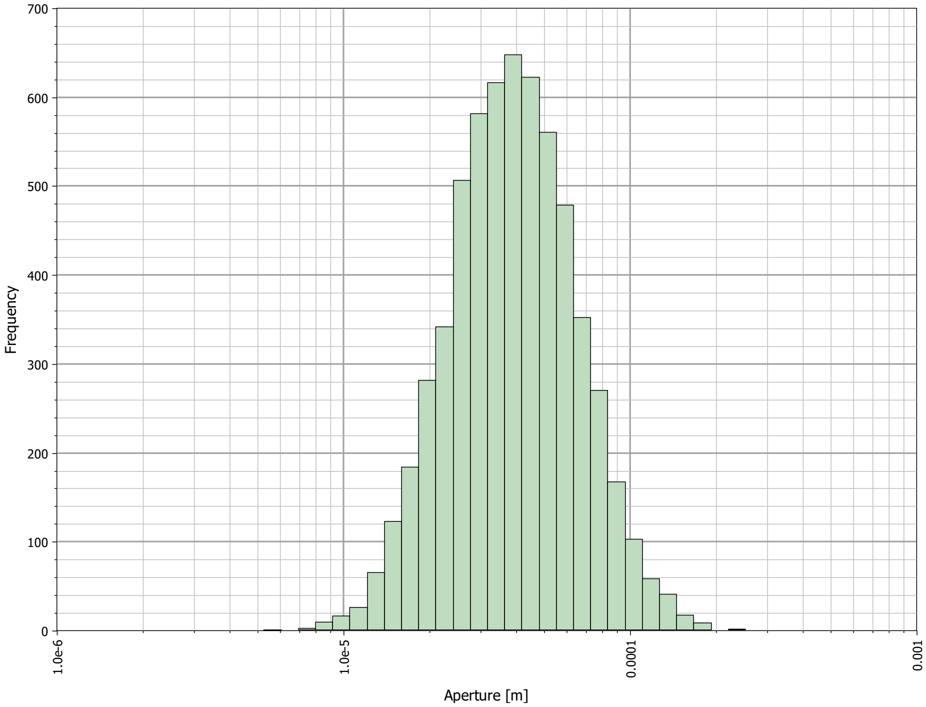

Figure 9-1-16. Sampled Stochastic Fracture Aperture.

9.1.5 Upscaling DFN to the Equivalent Continuum Model

After DFN is generated, it can be upscaled to an equivalent continuum model using Oda's method. Oda's method calculates permeability tensors in three dimensions for each cell. Oda tensor is a simplification of Darcy's Law for flow through an isotropic porous medium. The fracture permeability (*k*) is projected onto the plane of the fracture and scaled by the ratio between the fracture volume (porosity) and the volume of the grid cell. The method is implemented in Fracman in accordance with the following equation (Golder, 2017):

$$K_{i,j} = \frac{1}{12}(F_{k,k}\delta_{i,j} - F_{i,j}) \qquad (9.1.10)$$

$$F_{i,j} = \frac{1}{V}\sum_{k=1}^{N} A_k T_k n_{i,k} n_{j,k}$$

where $K_{i,j}$ is permeability tensor; $\delta_{i,j}$ is Kroenecker's delta; $F_{i,j}$ is fracture tensor; V is grid cell volume; N is total number of fractures in grid cell; A_k is area of fracture k; T_k is transmissivity of fracture k; and $n_{i,k}$, $n_{j,k}$ are the components of a unit normal to the fracture k. Note that only principle components of the permeability tensor (K_{xx}, K_{yy}, and K_{zz}) are the inputs into the flow and transport model.

Fracture porosity (ϵ) of the grid cell is calculated as:

$$\in = \frac{1}{V}\sum_{k=1}^{N} A_k b_k \qquad (9.1.11)$$

where b_k is the aperture of fracture k.

The permeability and porosity of the grid cells without fractures can be defined in accordance with the matrix permeability and porosity. Figure 9-1-17 shows the grid cell permeability (K_{xx}) of the DFN alization shown in Figure 9-1-13. Figure 9-1-18 shows the vertical slices through CTD and Inclined drift.

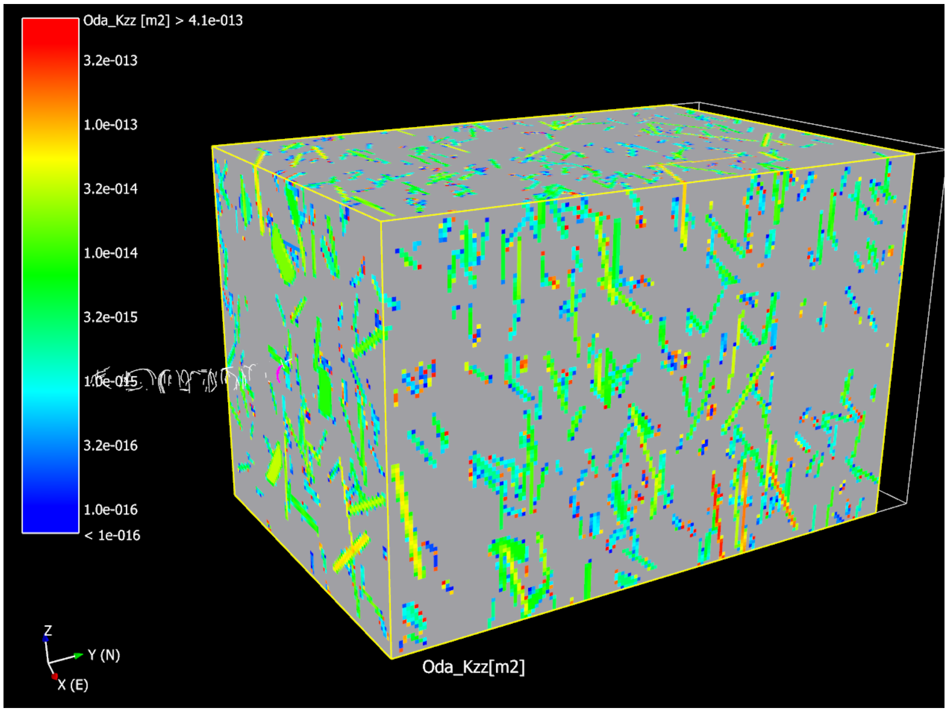

Figure 9-1-17. Vertical Grid Cell Permeability for DFN Realization Shown in Figure 9-1-13.

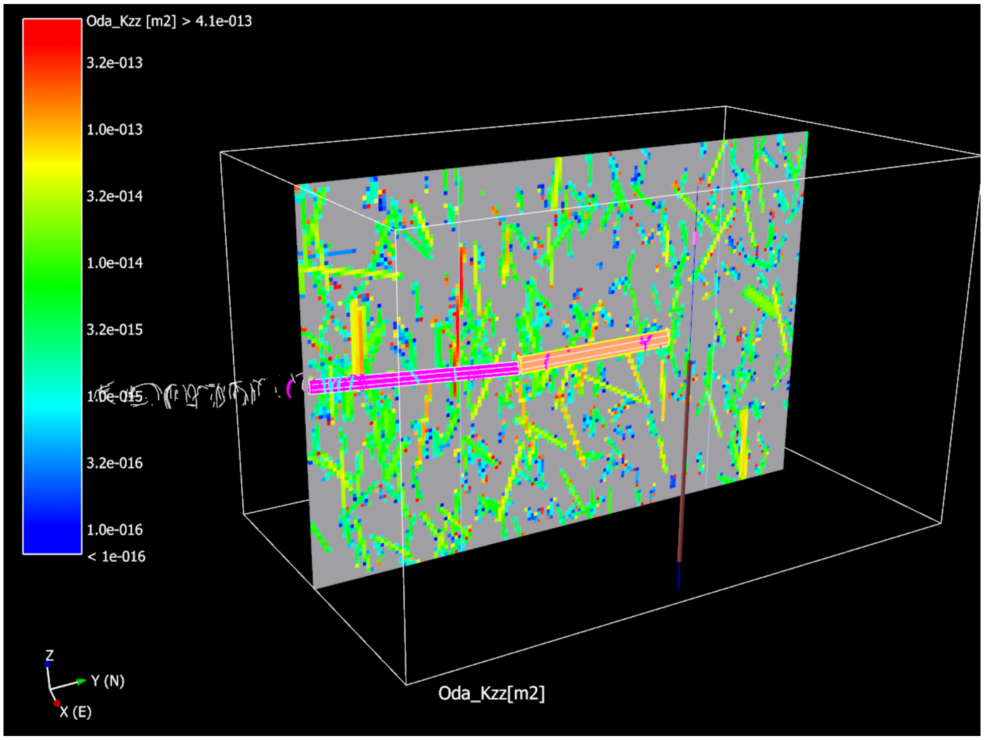

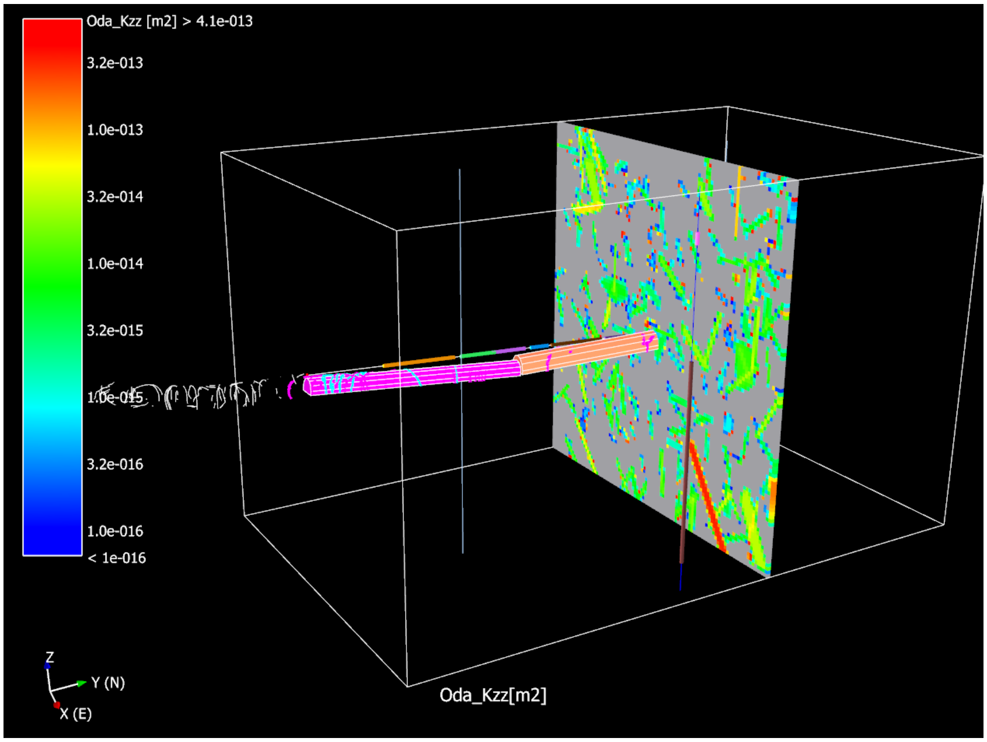

Figure 9-1-18. Vertical Slices of Vertical Grid Cell Permeability for DFN Realization Shown in Figure 9-1-13.

Table 9-1-9 summarizes the mean properties of the grid cells in the modeling domain. The calculated mean permeability values are close to suggested reference permeability (1E-15 m^2). However, the permeability is anisotropic and changes over a few orders of magnitudes.

Table 9-1-9. Effective Continuum Model Mean Grid Cell Properties.

Parameter	Notation	Mean Value
Permeability (m^2)	K_{xx}	3.04E-15
	K_{yy}	1.31E-15
	K_{zz}	3.5E-15
Anisotropy	K_{xx}/K_{zz}	0.87
	K_{yy}/K_{zz}	0.37
	K_{yy}/K_{xx}	0.43
Fracture Porosity	€	1.64E-05
Number of cells with fractures		40%

Note that the permeability and porosity values calculated with Eq. 9.1.10 and 9.1.11 will be very low if the total area of the fractures ($\sum A_k$) is very small. The proposed cutoffs for permeability and porosity values are 1x10^{-19} m^2 and 1x10^{-8}. The cells with the permeability lower than 1x10^{-19} m^2 or/and porosity lower than 1x10^{-8} were considered to be matrix cells. The number of cells that were below the cutoff values is 1.1% of the total number of cells with fractures in the considered example.

9.1.6 Corroboration with the Other Studies of the Tono Area

A large amount of fracture data was collected in Tono area. The fracture data analysis and development of the fracture models at the different scales is an ongoing effort. Bruines (2014) describes the development of the discrete fracture network models for 2 scales – local (9kmx9km) and site-scale (2kmx2km). Both models extend from the surface to the depth of 2 km and are based on the data from MIU Project Phase I and II investigations.

The characterization of the fractured crystalline rock at the depth of the MIU is based on the data from the boreholes DH-2, DH-15 and MIZ-1 (Phase I data) and 33 boreholes drilled from galleries (Phase II data). The data includes well log data and hydraulic test data. Hydraulic tests were conducted in different sections of the boreholes on the different scales. The models consider both, UHFD and LSFD. The DFN models were upscaled to the equivalent continuum models for transport simulations. Bruines (2014) provided a discussion of the methodology used to develop DFN and equivalent continuum models. However, the results of the analysis were provided only for UHFD. The authors noted that significantly less data is available for the LSFD. The fracture data for LSFD data can be found in JAEA report (Ando, 2012) for boreholes DH-2, DH-15 and MIZ-1.

The modeling domain considered in this study is within the LSFD. It occupies a very small volume of the site-scale model in Bruines (2014). The data used to develop the fracture model are primarily based on the Research tunnel fracture traces and fracture observations in borehole 12MI33. A portion of borehole MIZ-1 is within the modeling domain. The other boreholes are outside the modeling domain. The major goal of this section is to compare the parameters derived for the small-scale model to the parameters developed for the large-scale models.

The large-scale models use the following conceptual assumptions:

- The fractures are square shaped.
- The fracture size follows power-law distribution.
- The fracture transmissivity is lognormally distributed and independent of fracture size.

The large-scale DFN was upscaled to the equivalent continuum model using 3 different grid block sizes: 30 m, 70 m, and 100 m.

As it was previously discussed, the small-scale model assumes circular shape of fracture. The fracture size follows lognormal distribution (Section 9.1.2, Figures 9-1-4 and 9-1-5). The fracture permeability and aperture are correlated with fracture radius (the larger fractures have larger transmissivity). The small-scale DFN is upscaled to the equivalent continuum model with the grid block size of 1 m.

Both, large-scale and small-scale models assume that not all the fractures conduct flow. As it was shown in Ishibashi (2015), only a small portion of all observed fractures are open fractures. The large-scale model further assumes that only open fractures connected to the network conduct flow. These fractures are called the water conducting features (WCFs). The fractures used in developing small-scale model are the fractures in the Research tunnel that showed water discharge and the fracture in 12MI33 borehole with the recorded apertures (~10% of observed fractures).

9.1.6.1 Fracture Size

The fracture size defined in Ando (2012) for LSFD follows power-law distribution with minimum 2.5 m, maximum 3,000 m and slope 4.1 (Table 5.3.3-1 in Ando, 2012). The fracture size in the small-scale model is based on the analysis of the fracture traces in the tunnel. The power-law distributions derived from this analysis (Table 9-1-2) have minimum size of 1.5 m and 3.3 m and slopes 3.4 and 3.9. These values are close to the large-scale model size distribution. However, as it was shown in Section 9.1.2, the lognormal distributions provided better fit to the data. The comparison between the large-scale and small-scale models is shown in Figure 9-1-19. While there are some differences, the distributions are similar.

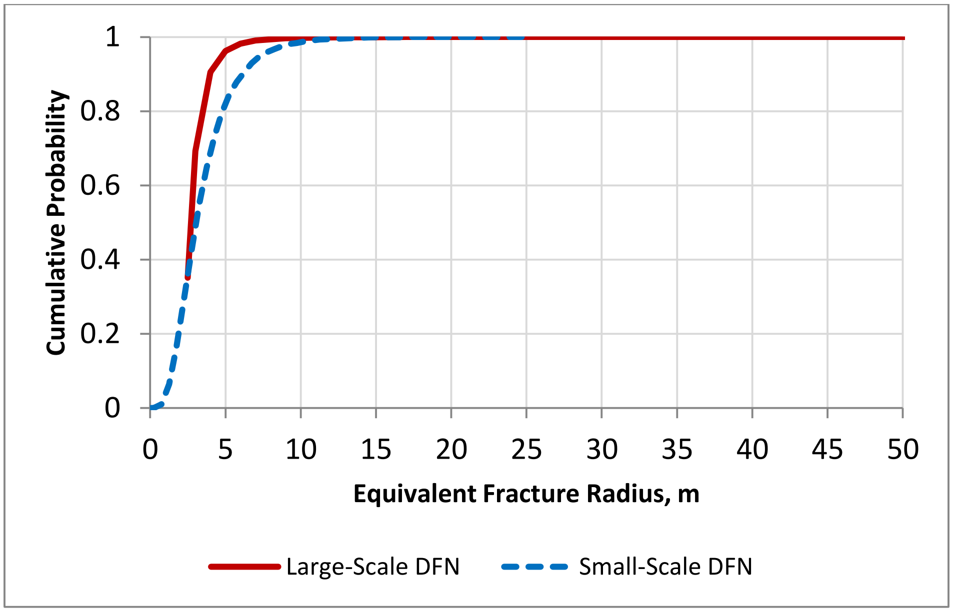

Figure 9-1-19. Equivalent Fracture Radius Distributions in Large-Scale and Small-Scale Models.

9.1.6.2 Fracture Orientation and Intensity

Ando (2012) described 4 sets of fractures in borehole MIZ-1 (Table 5.3.1-6). 3 of these sets consist of north trending sub-vertical fractures (total number of fractures in these sets is 12). The small number of fractures in each set and high values of Fisher dispersion coefficient (ķ is 80-147) suggests that 3 sets could, in fact, be one set with lower ķ (higher dispersion). Note that Golder (2017) recommends to use ķ in the range from 20 to 50 for the low orientation variability. The average plunge in 3 sub-vertical fracture sets is 8^0, which is the same as the plunge defined for the stochastic fractures in the small-scale model. The fractures in the small-scale model are north trending as well. The additional set of sub-horizontal fractures could have been in the depth interval that is outside the small-scale model domain.

The total liner intensity of the 3 sets of sub-vertical fractures in borehole MIZ-1 is 0.045 fractures/m (Table 5.3.1-6 in Ando, 2012). This is consistent with P_{10}=0.04 calculated for two arbitrarily placed imaginary vertical boreholes intersecting one realization of stochastic fractures (Figure 9.1.11).

The range in calculated (3 set total) volumetric intensity (P_{32}) is from 0.01 to 0.28 m^2/m^3 (Figure 5.3.1-20 in Ando, 2012). The calculated P_{32} of the stochastic fractures (0.22) is within this range.

9.1.6.3 Equivalent Continuum Model Hydraulic Conductivity

The hydraulic conductivity of the large-scale equivalent continuum model was calculated using dynamic upscaling of large-scale DFN. Figure 9.1.20 shows the cumulative probability distribution of the effective hydraulic conductivity (borehole MIZ-1) for 100-m, 70-m, and 30-m grid block resolution cases (Figure 6.2.2-1 in Ando, 2012). The effective value represents the mean of the hydraulic conductivity in 3 principal directions. The effective hydraulic conductivity of the small-scale equivalent continuum model (1-m grid block) was added to this figure for comparison.

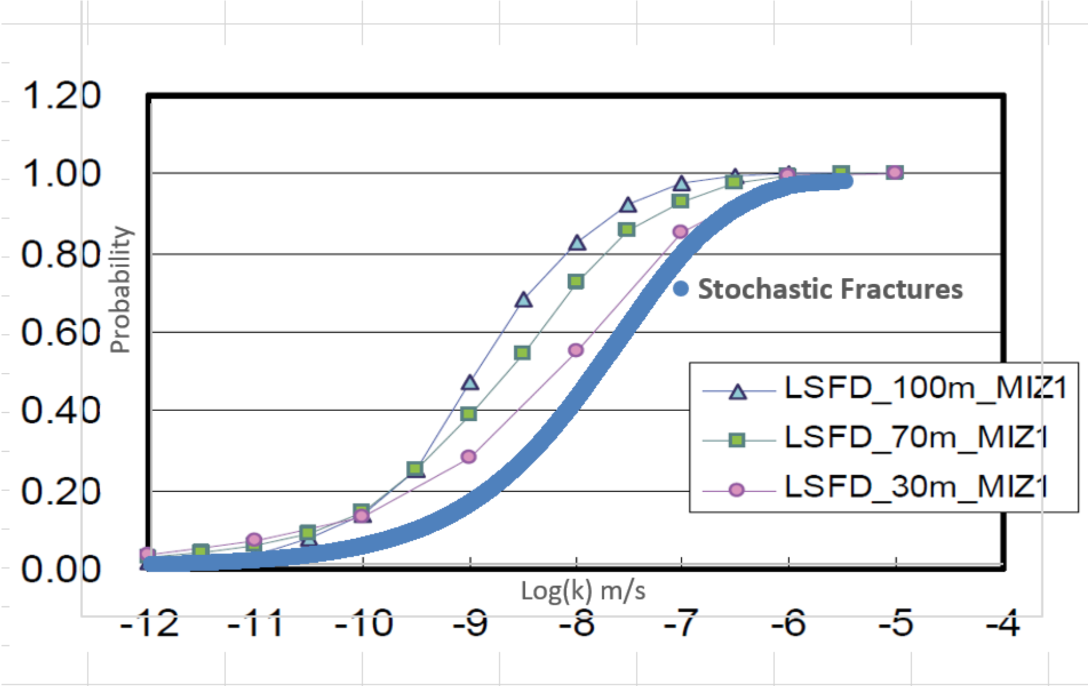

NOTE: This figure was copied from Figure 6.2.2-1 (a) in Ando, 2012. The distribution obtained from the small-scale equivalent continuum model (stochastic fractures) was added to this figure for comparison.

Figure 9-1-20. Cumulative Probability Distribution of Effective Hydraulic Conductivity in LSFD.

The hydraulic conductivity distribution of the small-scale equivalent continuum model is very similar to the hydraulic conductivity in the 30-m grid block large-scale model. Note that the distributions shift to the right when the grid block size decreases. Consequently, additional shift can be expected when the grid block size change to 1 m (small-scale model).

The large-scale equivalent continuum model cumulative probabilities of the hydraulic conductivity in 3 principal directions (borehole MIZ-1) are shown in Figure 9.1.21 for 30-m grid block case (Figure 6.2.2-1 b in Ando, 2012). The up-scaled permeability tensor has evident anisotropy consistent with the fracture orientation – the vertical hydraulic conductivity (K_{11}) is higher than horizontal (K_{22}) and the horizontal hydraulic conductivity is higher along the predominant fracture plane (K_{33}). The hydraulic conductivity in 3 principal direction of the small-scale equivalent continuum model was added to this figure for comparison. The anisotropy in hydraulic conductivity in the small-scale equivalent continuum model is similar to the one in the large-scale model - $K_{zz}>K_{xx}>K_{yy}$.

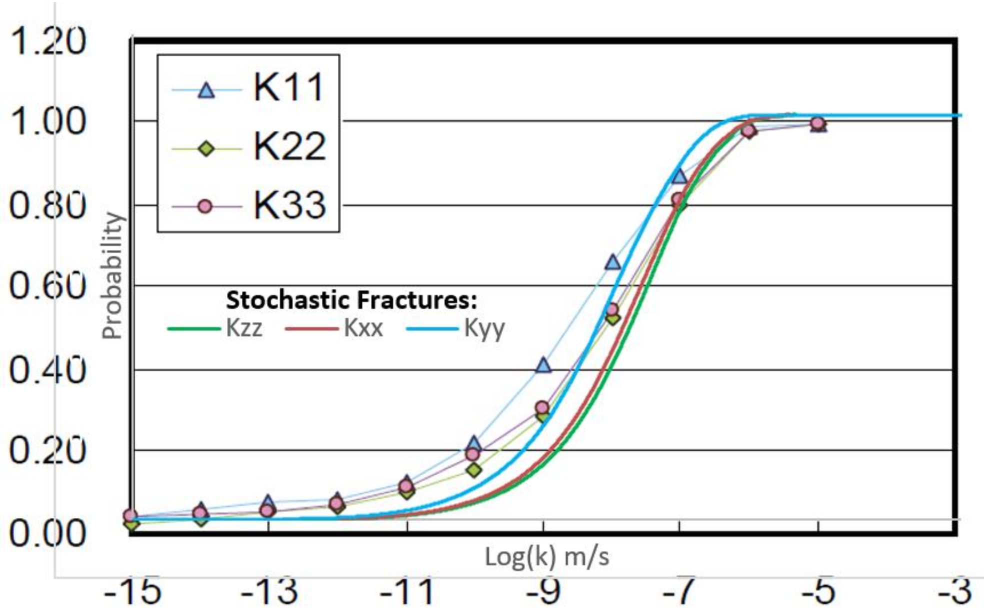

NOTE: This figure was copied from Figure 6.2.2-1 (b) in Ando, 2012. The distributions obtained from the small-scale equivalent continuum model (K_{xx}, K_{yy}, and K_{zz}) were added to this figure for comparison.

Figure 9-1-21. Cumulative Probability Distribution of Hydraulic Conductivity in 3 Principal Direction in LSFD in Large-Scale and Small-Scale Models.

9.1.7 Summary

The goal of this analysis was to develop the discrete fracture network model (DFN) for the small-scale area surrounding the MIU Research tunnel at 500 m depth. The DFN model was upscaled to an equivalent continuum model with the grid cell size 1x1x1 m using Oda's method for the flow and transport simulations (Section 9.2).

The DFN model includes:

(1) The fractures observed in the Research tunnel and borehole 12MI33. These fractures have deterministic location and stochastic (radius, permeability, and aperture) properties derived from the fracture analysis.
(2) Stochastic fractures (the location changes with each realization) generated based on the fracture size, orientation, intensity, and properties derived from the fracture analysis.

The major results of the fracture analysis are described below.

❑ Analysis of Fractures Traces on the Walls of CTD, Inclined Drift, and Access Drift

The analysis of the fracture traces in the Research tunnel considered 146 fractures that showed flow discharge. It concluded that the fracture size is best described with the lognormal distributions. The fractures with observed flow >1L/min (F-fractures) have the mean radius of 3.9 m (standard deviation 2.2). The fractures with the observed flow >0.1 L/min (D-fractures) have the mean radius of 1.4 m (standard deviation 1.3).

The analytical solution was used to calculate fracture transmissivity from the observed range of fracture discharge and the total discharge into the Research tunnel. The fracture aperture was calculated from the cubic law relationship between the transmissivity and aperture. The fracture permeability was calculated from transmissivity and aperture. The following ranges were derived for the fracture parameters:

- Fracture transmissivity: $3.2\text{x}10^{-9} – 7.3\text{x}10^{-8}$ m^2/s.
- Fracture permeability: $3.5\text{x}10^{-12} – 1.7\text{x}10^{-10}$ m^2
- Fracture aperture: 16 – 45 micron

It was assumed that fracture permeability (k) and aperture (b) are correlated with the equivalent radius (R). The following relationships were proposed:

$$k = 1.55 \cdot 10^{-12} \cdot R^{2.3} \quad \text{and} \quad b = 1.16 \cdot 10^{-5} \cdot R$$

❑ Analysis of Fractures Observed in Borehole 12MI33

17 fractures with the recorded aperture values were assumed to be permeable fractures in borehole 12MI33. These fractures were generated using the same parameters as in the Research tunnel. The following conclusions were made:

- The locations of 17 fractures generated in borehole 2MI33 are consistent with the locations of fractures in the Research tunnel.
- Fracture properties derived from the Research tunnel fracture trace analysis are consistent with the packer test data in borehole 12MI33.

❑ Analysis of Fracture Orientation and Intensity for Stochastic Fracture Generation

Analysis of fracture orientation concluded that there is one fracture set with the following Fisher distribution parameters:

- mean trend 208^0
- mean plunge 8^0
- concentration parameter ķ equal to 7

Note that orientation is given in the local coordinate system. The actual coordinate system was rotated 10.2^0 clockwise in x-y plane to align the tunnel with the y axis.

The observed linear intensity of the fractures in the Research tunnel and borehole 12MI33 P_{10} was used to calculate volumetric intensity P_{32}. The fracture P_{32} value was iteratively redefined until the P_{10} values in selected locations matched the observed P_{10}. The calculated P_{32} is 0.22.

- ☐ **Upscaling to Equivalent Continuum Model**

The DFN was upscaled to an equivalent continuum model using Oda's method. The following mean effective parameters were obtained (one realization):

K_{xx}	3.04E-15
K_{yy}	1.31E-15
K_{zz}	3.50E-15
Porosity	1.64E-05

The calculated mean permeability values are close to suggested reference permeability (1E-15 m^2). However, the permeability is anisotropic and changes over a few orders of magnitudes.

- ☐ **Corroboration with the Other Studies of the Tono Area**

The parameters developed for the small-scale model were compared to the parameters incorporated in the large-scale models. The discrete fracture network models were developed for 2 scales – local (9kmx9km) and site-scale (2kmx2km). Both models extend from the surface to the depth of 2 km and are based on the data from MIU Project Phase I and II investigations.

The comparison was done for fracture size, orientation, intensity, and effective permeability. It was concluded that the parameters of the small-scale model are consistent wth the parameters of the large-scale models.

9.2 Preliminary Flow and Transport Modeling Analysis

9.2.1 Introduction

A preliminary modeling analysis was developed using the GREET project data to predict inflow into the inclined drift and the Closure Test Drift (CTD) during excavation. The analysis is part of the activities of Task C, Step 1. This report summarizes current progress of the modeling work at Sandia National Laboratories.

The main aim of the current work is to predict inflow into the tunnel as excavation progresses, and provide pressure histories at selected monitoring locations. The project provided data of tunnel excavation progress as the inclined drift and the CTD were excavated. The original data was in the form of excavation progress in meters along the axis of the tunnel as a function of excavation dates. Figure 9-2-1 shows a modified version of the excavation progress obtained from the project in terms of days since excavation began. Time zero in Figure 9-2-1 refers to 4/6/2013 in the project data. Time 173 days refers to the completion of excavation of the CTD on or around 9/25/2013. The excavation data in Figure 9-2-1 have been used in simulations of inflow into the tunnel.

Simulations were conducted with PFLOTRAN, an open source, state-of-the-art massively parallel subsurface flow and reactive transport code (Hammond et al., 2014) in a high-performance computing environment. The excavation progress was modeled by progressively removing material assigned as the host rock. This is equivalent to increasing the grid blocks representing the tunnel. A schematic diagram of the process is shown in Figure 9.2.2. In order to get a better representation of the excavation progress a small portion of rock material was removed at a time. Thus, the material removal was in 1 m increments for a total of 103 m (i.e. 57 m of the Inclined Drift and 46 m of the CTD). This resulted in 103 PFLOTRAN runs applying the pressure and chloride concentration boundary conditions assigned for the excavated area. The modeling was carried out with output of each PFLOTRAN run used as input for the next run until the complete excavation of the tunnel parts. To automate the simulation process the Sandia developed optimization code DAKOTA (Adam, et al., 2017) was used as a driver to PFLOTRAN. A schematic diagram of the process in shown in Figure 9.2.3. DAKOTA also provides statistical analysis of the process, which will be used in future simulations.

Simulations were carried out for a homogenous representation using a Visualization Area domain, which is a CTD-scale domain recommended by the project, and a larger domain to test the boundary conditions. These simulations are detailed in Section 9.2.2. Simulations were also conducted for a fracture system developed based on the fracture analysis described in Section 9.1. The fracture modeling is described in Section 9.2.3. A summary of the simulation exercise is given in Section 9.2.4.

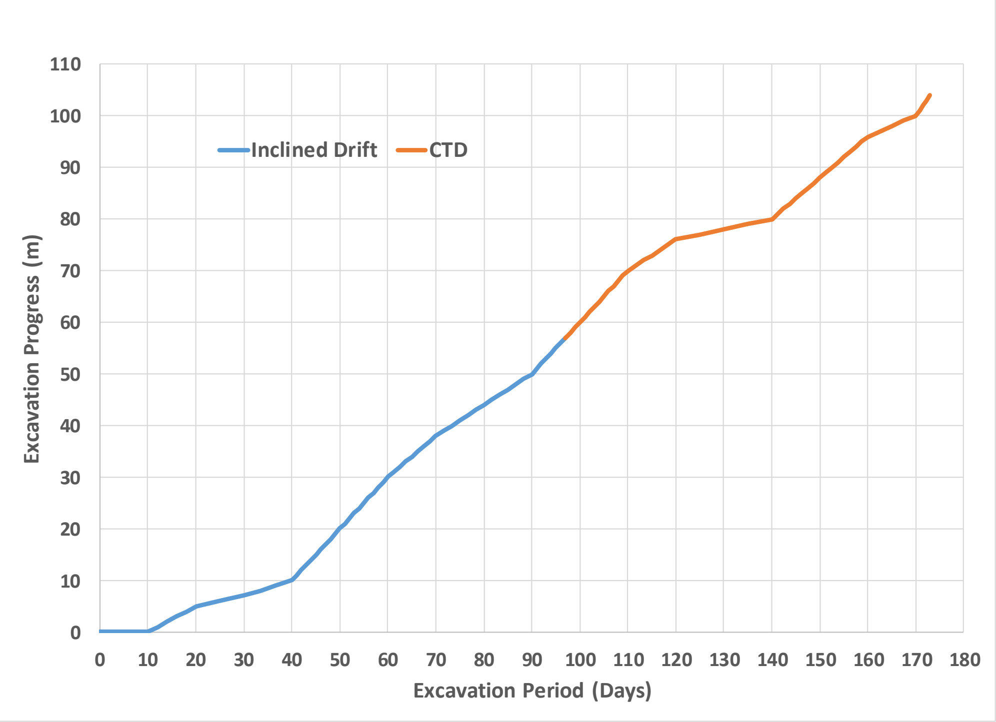

Figure 9-2-1. Data of excavation progress

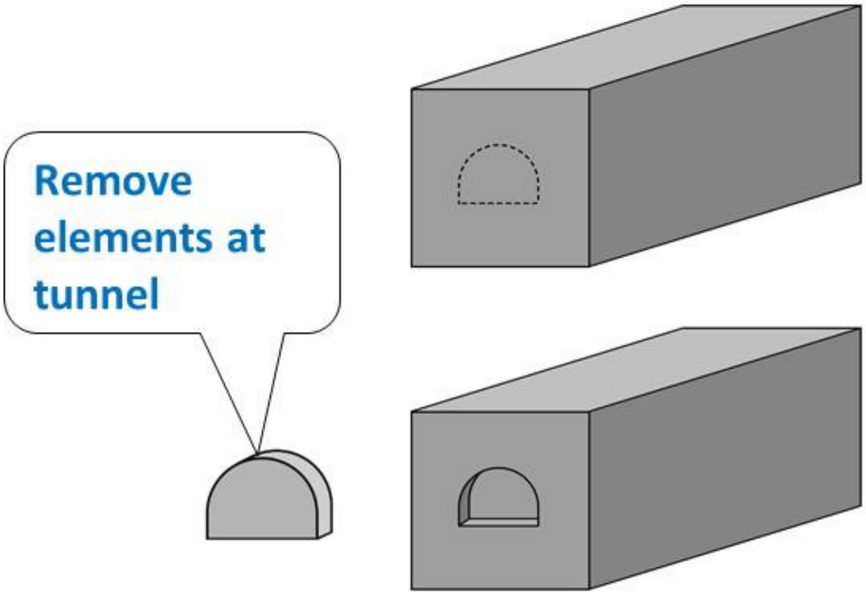

Figure 9-2-2. Schematic diagram showing simulation approach.

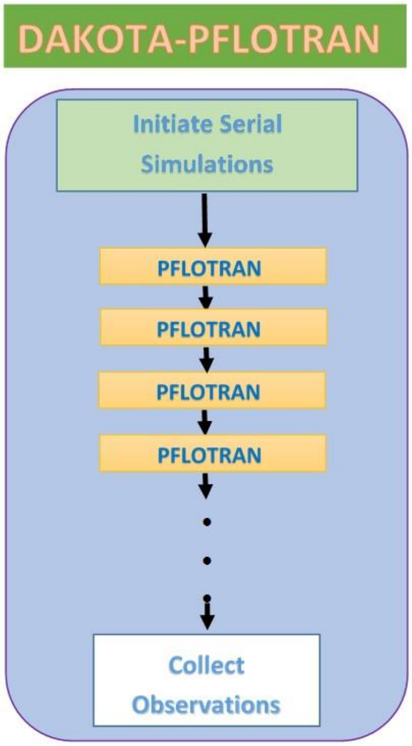

Figure 9-2-3. Schematic diagram for DAKOTA-PFLOTRAN coupling

9.2.2 Homogenous Model

9.2.2.1 Visualization Area Domain

Simulations were conducted for a homogenous model with reference hydraulic conductivity. As outlined by the Task C project, simulations were based on the visualization Area domain specified by the project. The model has a geometry of 100 m x 150 m x 100 m in the x, y and z directions. The modeling domain is a CTD-scale model and incorporates the inclined drift and the CTD. The physical coordinates of the simulation domain are given in Table 9-2-1. The simulation domain also incorporates the monitoring sections in Well 12MI33. The coordinates of the monitoring section are given Table 9-2-2. A schematic representation of the modeled part of the tunnel and the monitoring well is shown in Figure 9-2-4.

For the simulations a refined Uniform (structured) grid was selected, with grid block size of 1 m x 1m x 1m for a total of 1,500,000 grid blocks. The Inclined Drift is slightly inclined but was modeled as horizontal for ease of meshing. The dimensions of these two tunnel parts are given below.

Inclined Drift	**CTD**
Length = 57 m	Length = 46.5 m
Width = 4.5 m	Width = 5.0 m
Height = 3.5 m	Height = 4.5 m

For the simulations physical properties obtained from the monitoring well 12MI33 and other sources were used. Estimated hydraulic conductivity for Toki granite is in the range of log (-8 ± 1) m/s. The homogenous simulations used:

- Reference hydraulic conductivity 10^{-8} m/s (permeability 10^{-15} m^2)
- Porosity 0.001
- Effective diffusion coefficient 10^{-12} m^2/s

Initial and boundary conditions were based on those specified for Task C. Hydrostatic initial pressure conditions are represented by average head measurements of 110 EL m, based on data from monitoring wells. Top, bottom and side boundary conditions were also assigned head of 110 EL m. The excavated area was assigned a constant pressure boundary condition of 1.0 atmosphere. Head data were converted to pressure as shown below. For the conversion, the head of 110 EL m and elevation data in Table 9-2-1 were used.

Pressure at domain top = density x g x (head + elevation) = 3.6 MPa

Pressure at domain bottom = density x g x (head + elevation) = 4.6 MPa

Hydrostatic pressure boundary was assigned on the sides. In PFLOTRAN the bottom was assigned no flux condition. The initial and boundary conditions also include chloride concentrations based on data from monitoring wells. For the simulations, the top and bottom boundaries were assigned 332 mg/L and 428 mg/L chloride concentrations, respectively. The side boundaries were assigned a concentration gradient varying between the top and bottom boundary values. The excavated region was modeled as a free boundary.

Pressure monitoring points were setup using the coordinates in Table 9-2-2. The points were selected to be in the middle of the monitoring section. The chloride concentration units were converted to molarity (M) for use in PFLOTRAN. The conversion is shown below, using Cl molecular weight of 35.453 g/mol:

Concentration at top = 332 mg/L / (1000 x 35.453 g/mol) = 0.0094 M

Concentration at bottom = 428 mg/L / (1000 x 35.453 g/mol) = 0.012 M

Table 9-2-1. Coordinates of CTD-Scale simulation domain

E-W(m)	**N-S(m)**	**E.L.(m)**	
6522.7	**-68943.5**	**-250.0**	**Upper boundary**
6496.1	**-68795.9**	**-250.0**	**Upper boundary**
6397.7	**-68813.7**	**-250.0**	**Upper boundary**
6424.3	**-68961.3**	**-250.0**	**Upper boundary**
6522.7	**-68943.5**	**-350.0**	**Lower boundary**
6496.1	**-68795.9**	**-350.0**	**Lower boundary**
6397.7	**-68813.7**	**-350.0**	**Lower boundary**
6424.3	**-68961.3**	**-350.0**	**Lower boundary**

Table 9-2-2. Coordinates of monitoring section in Well 12MI33

Section ID	Top			Middle			Bottom		
	E−W(m)	N−S(m)	E.L.(m)	E−W(m)	N−S(m)	E.L.(m)	E−W(m)	N−S(m)	E.L.(m)
12MI33_P1	6445.46	−68845.50	−303.27	6445.30	−68844.80	−303.30	6445.19	−68844.00	−303.36
12MI33_P2	6448.96	−68864.90	−302.24	6447.30	−68855.70	−302.70	6445.63	−68846.50	−303.22
12MI33_P3	6452.81	−68886.20	−301.11	6451.00	−68876.00	−301.60	6449.13	−68865.80	−302.19
12MI33_P4	6454.62	−68896.30	−300.57	6453.80	−68891.80	−300.80	6452.98	−68887.20	−301.06
12MI33_P5	6456.34	−68905.80	−300.07	6455.60	−68901.50	−300.30	6454.78	−68897.20	−300.52
12MI33_P6	6464.16	−68949.20	−297.76	6460.30	−68928.00	−298.90	6456.50	−68906.70	−300.02

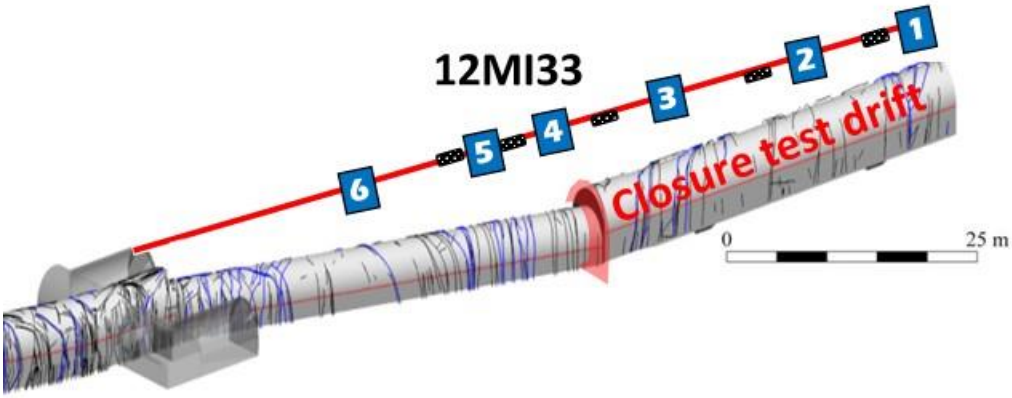

Figure 9-2-4. Schematic diagram showing the modeled part of the tunnel and the monitoring well 12MI33 with the monitoring sections

9.2.2.1.1 Homogenous model with Visualization Area domain simulation results

A steady state run was made to obtain initial pressure and chloride concentration conditions before the excavation progress was modeled. Representation of the inclined drift and the CTD in the model are shown in Figure 9-2=5. Figure 9-2-6 shows distributions of the steady state pressure and chloride concentration using the initial and boundary conditions described above. The figures show the pressure and concentration gradients as a function of depth.

Simulations of excavation progress were conducted using the steady state pressure distributions and constant pressure boundary conditions inside the tunnel. The DAKOTA-PFLOTRAN system described above was used to separately model excavation progress in the inclined drift and the CTD. The outputs were post-processed to evaluate inflow into the tunnel and pressure history at the observation points. Results of pressure and chloride concentration distributions at 173 simulation time are shown in Figure 9-2-7. The figures represent fluid flow and chloride transport into the tunnel as a result of the initial and boundary conditions. The left (south) side boundary conditions were set close to the inclined tunnel entrance, and the effect of that is shown in the figures. The left side of the figure in Figure 9-2-7 (b) shows high concentrations at the inclined tunnel entrance. Figures 9-2-8 and 9-2-9 show predicted pressure vs. time and chloride concentration vs. time at the selected monitoring points. Figure 9-2-8 shows higher pressure drawdown in Observation Section 6, which is closer to the inclined drift entrance (see Figure 9-2-4 for location of monitoring points). The figure shows the lowest pressure drawdown in Section 1, which is close to the edge of the CTD. This is in line with expectations as the inclined tunnel was open for a longer period of time and thus more inflow compared to the CTD.

The flow of water into the excavated space (inclined drift and CTD) was also predicted based on the excavation progress. The output of the simulation was post-processed to determine inflow rate. The resulting inflow into the tunnel (inclined drift and CTD) is shown in Figure 9-2-10. Task C project experimental data on inflow into the Inclined Drift and the CTD are given in Table 9-1-3. The recorded combined in flow is about 56 L/min, or 80.64 m^3/day. This data point is shown in Figure 9-2-10 at 173 days of excavation. The data point has lower inflow compared to the predicted inflow for the homogenous model with Visualization Area domain. The inflow is a function of the boundary and initial conditions as well as material properties selected. Any of these variables could influence the prediction.

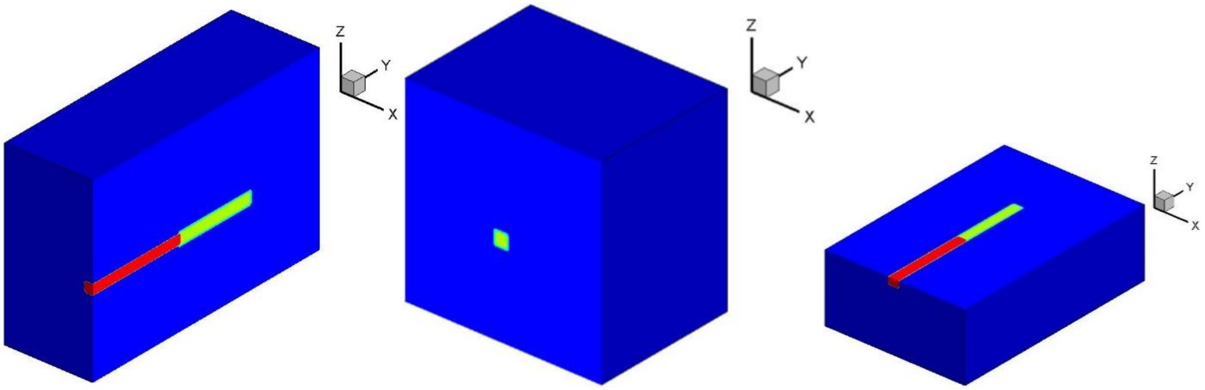

Figure 9-2-5. Placement of tunnel in simulation domain: Inclined Drift and CTD: Cross-section along a) x-axis, b) y-axis and c) z-axis

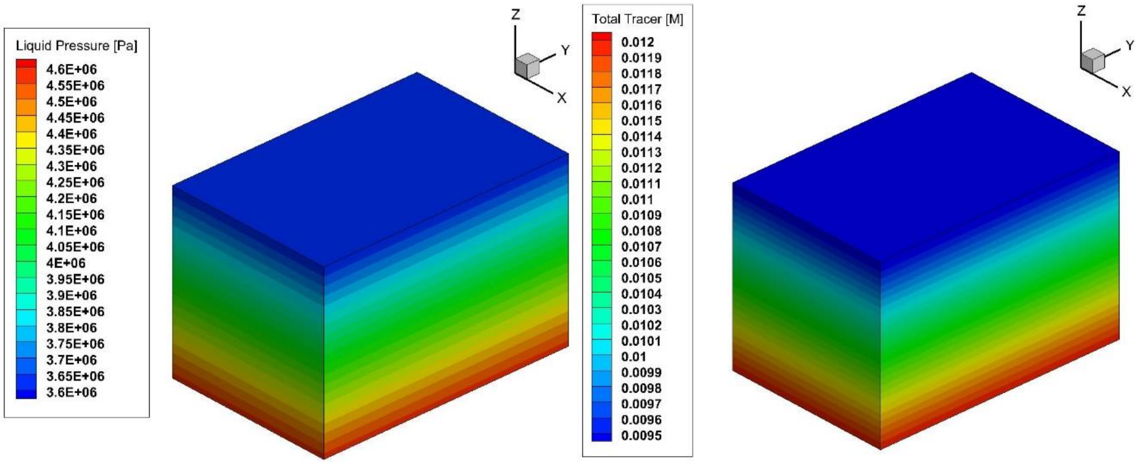

Figure 9-2-6. Steady state pressure and chloride concentration distribution (molarity units): homogenous system

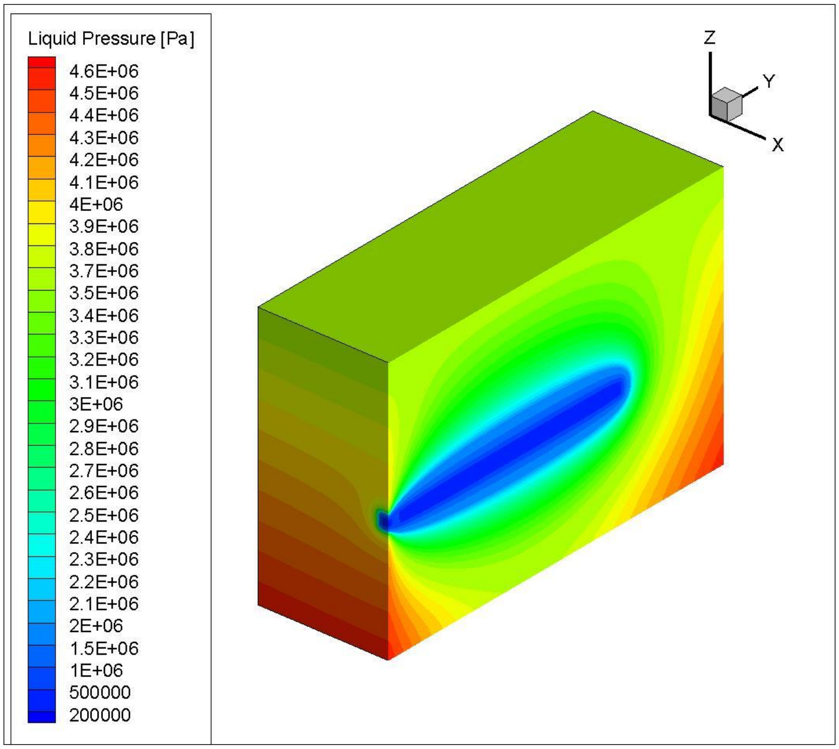

a) Pressure distribution: cross-section along the axis of the tunnel

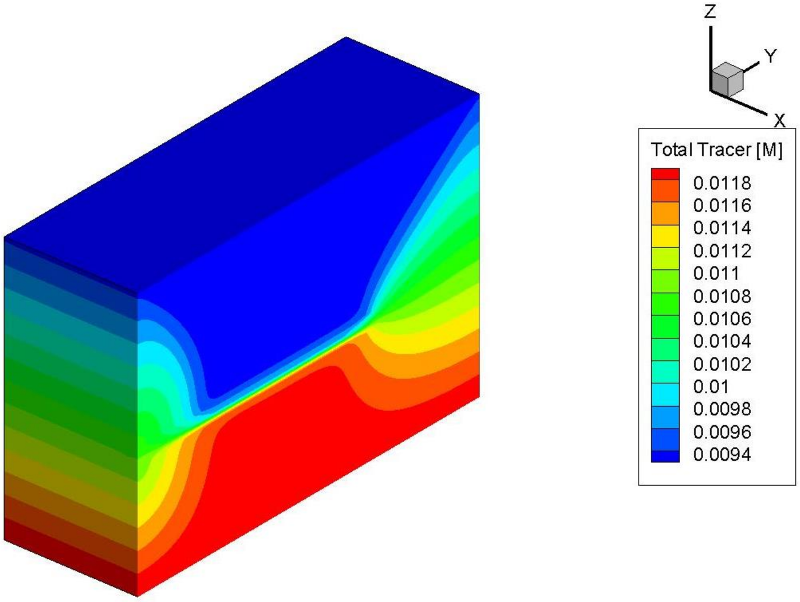

b) Chloride concentration distribution: cross-section along the axis of the tunnel

Figure 9-2-7. Predicted pressure and chloride concentration distributions after 173 days simulation time: homogenous system with visualization area domain

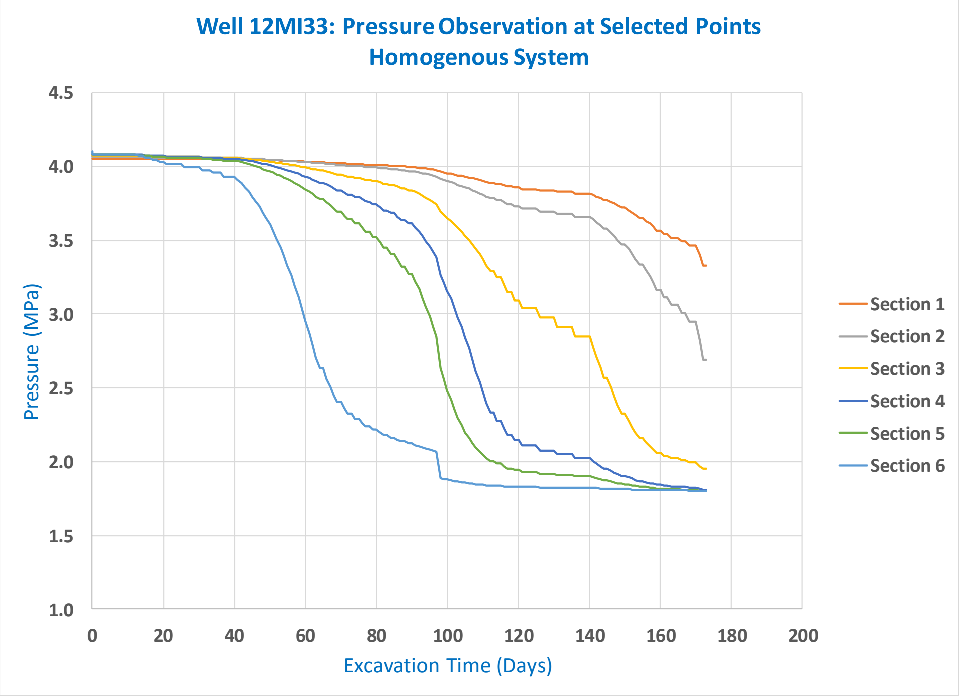

Figure 9-2-8. Predicted pressure history at observation points (in Well 12MI33) during excavation: homogenous system with Visualization Area domain

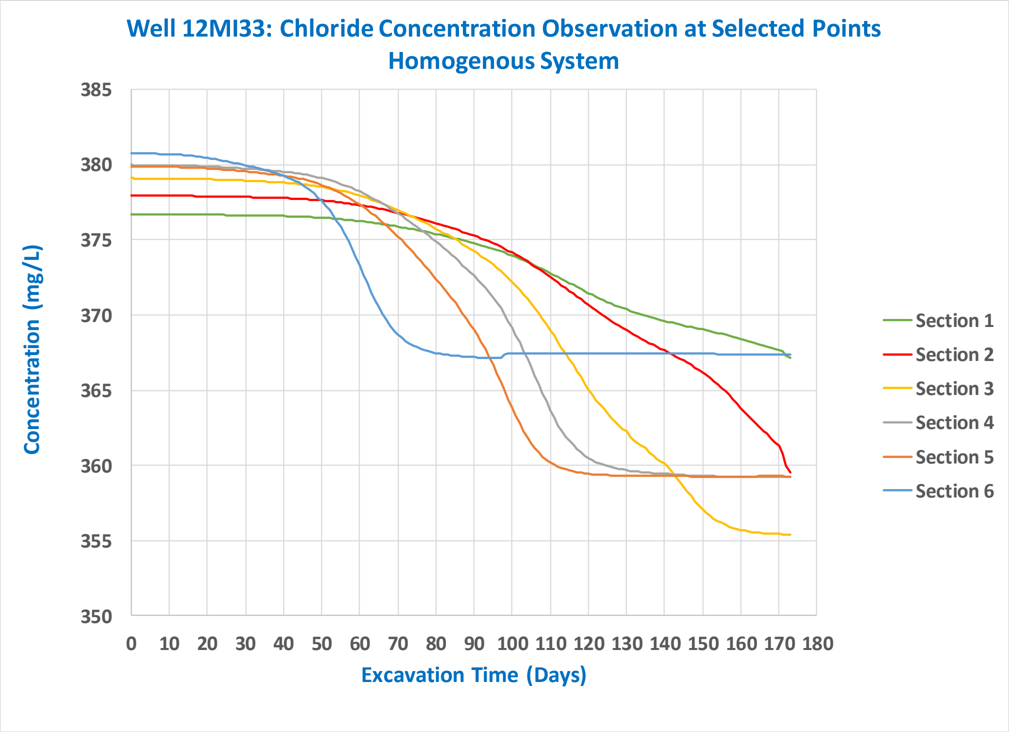

Figure 9-2-9. Predicted chloride concentration history at observation points (Well 12MI33) during excavation: homogenous system with Visualization Area domain

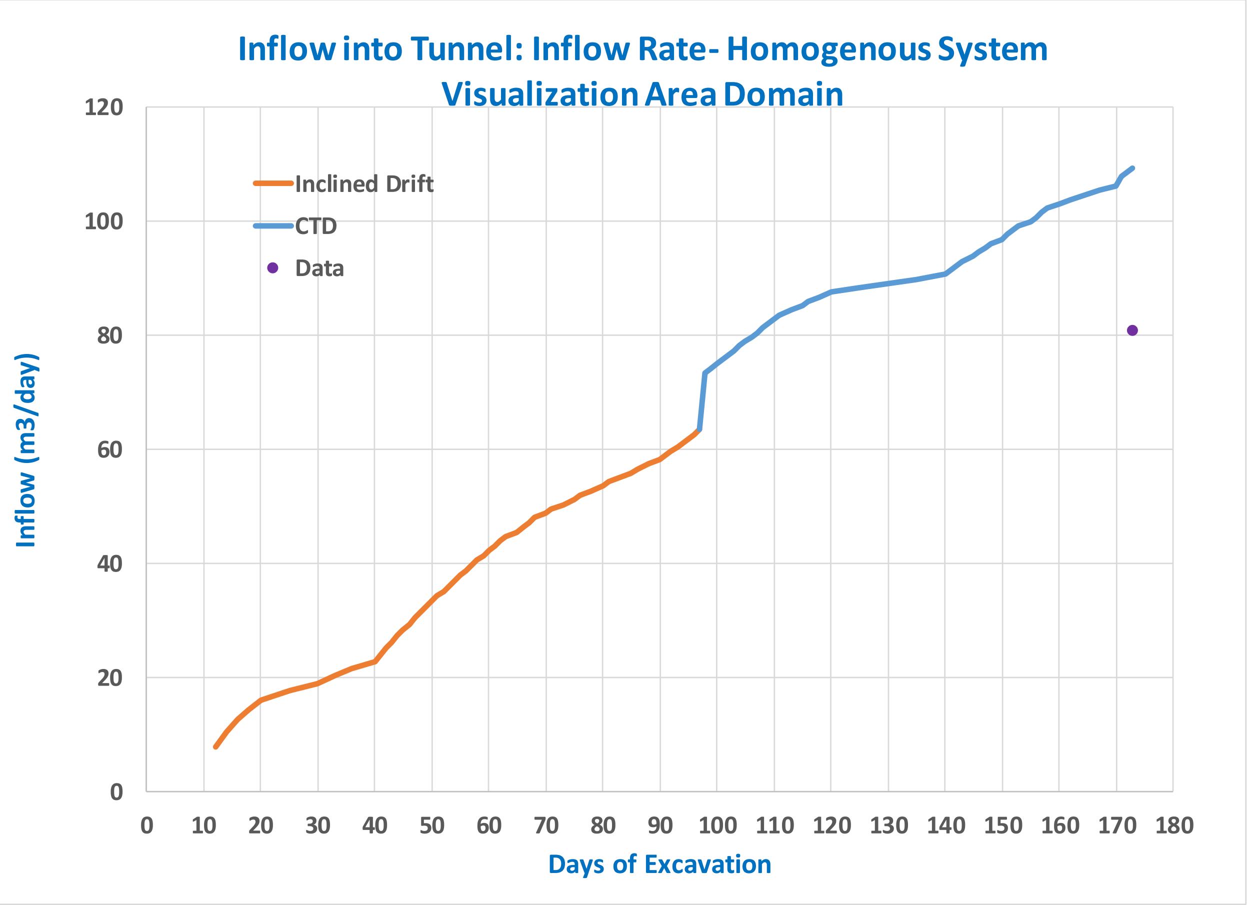

Figure 9-2-10. Predicted inflow into the Inclined Drift and CTD during excavation: Homogenous system, Visualization Area domain

9.2.2.2 Model with large domain

To study the effect of boundary conditions on the predicted output, a larger domain was selected. For the simulations a grid with 2080 m x 2130 m x 700 m in the x, y, and z directions was used. The same grid block size (i.e. 1 m x 1m x 1m) as the previous model was applied to the Visualization Area. Outside of the Visualization Area a progressive grid size was used. The new mesh size is 122 x 122 x 117 for a total 1,741,428 grid blocks. The larger domain mesh is shown in Figure 9-2-11. The same pressure and concentration gradient initial and boundary conditions as the previous model were applied. The same material properties were also used.

Simulations as described in Section 9.2.1.1 for the Visualization Area domain using the coupled DAKOTA-PFLOTRAN codes were conducted. Simulation results are shown in Figures 9-2-12 to 9-2-16. Figures 9-2-12 and 9-2-13 show pressure and concentration distributions, respectively, at 173-days simulation time. The results do not show effects of boundary conditions as those of Figure 9-2-7 for the Visualization Area domain. The boundary conditions imposed on the left boundary of the Visualization Area domain, that are more visible for chloride concentration (Figure 9-2-7b), are absent in Figure 9-2-13.

Predictions of pressure and concentration histories at observation points for the large domain case are shown in Figures 9-2-14 and 9-2-15, respectively. The pressure profiles at observation points are similar to those of the Visualization Area domain (Figure 9-2-8) but with larger drawdowns. The same trend is observed when comparing chloride concentration profiles.

The flow of water into the excavated space (inclined drift and CTD) was also evaluated for the large domain homogenous model. The resulting inflow into the tunnel (inclined drift and CTD) is shown in Figure 9-2-16 together with the results for the Visualization domain. Task C project inflow data point (for combined Inclined Drift and CTD) is also included. The data point is closer to the predicted inflow for the homogenous model with large domain.

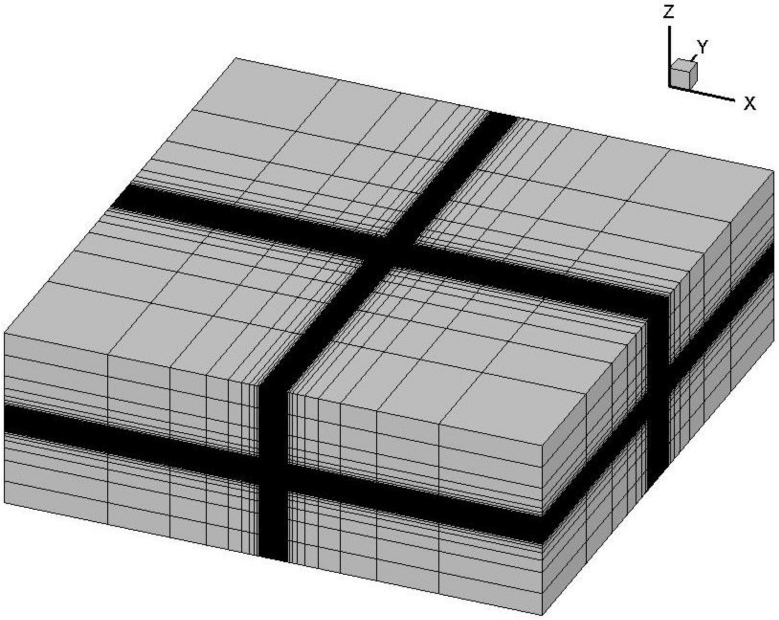

Figure 9-2-11. Grid for large domain

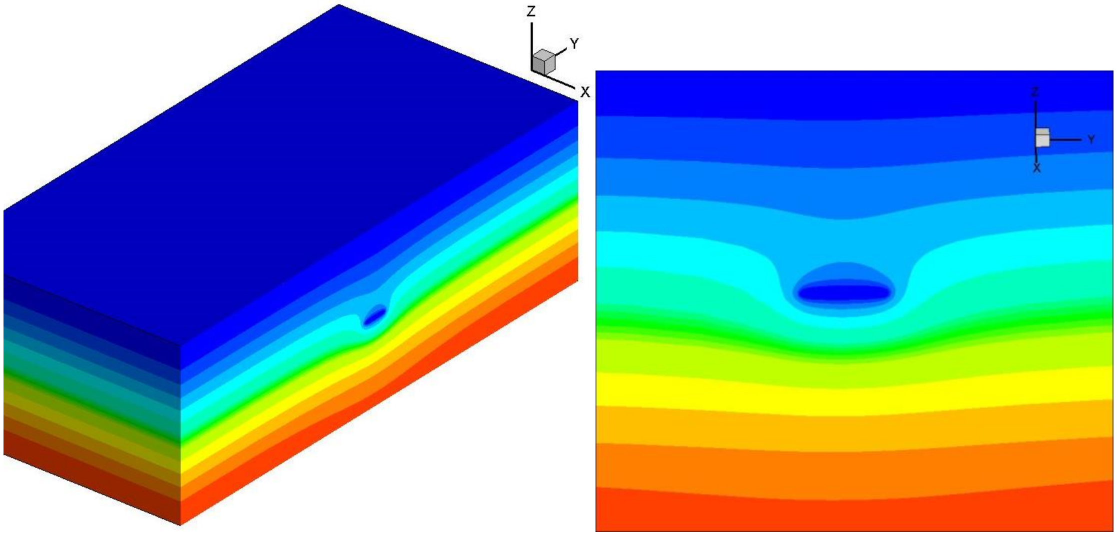

a) Cross-section along the axis of the tunnel

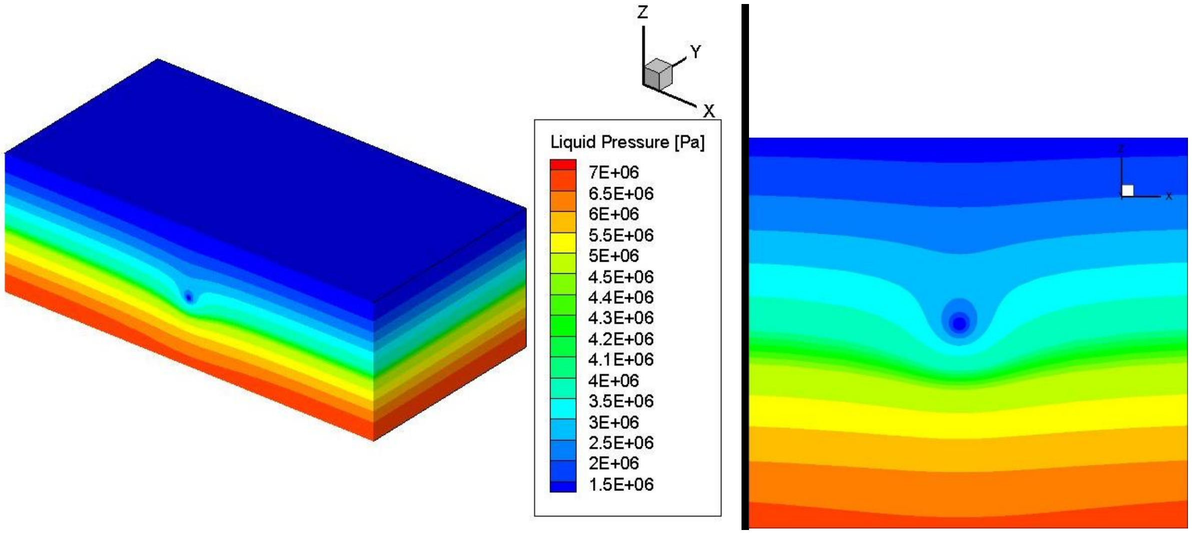

b) Cross-section perpendicular to tunnel axis

Figure 9-2-12. Predicted pressure distribution after 173-days simulation time: homogenous system with large domain

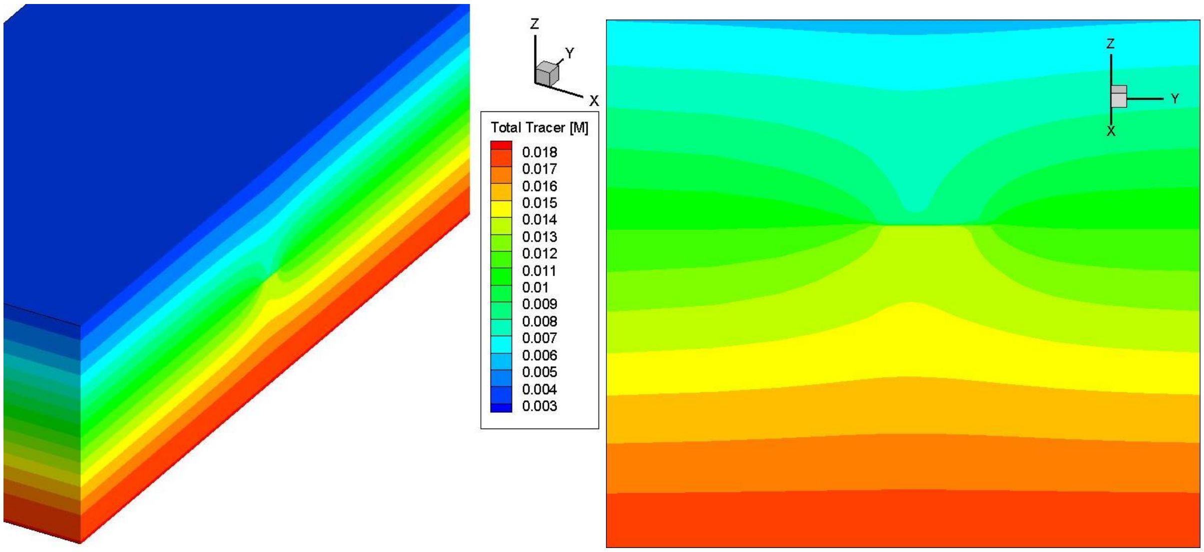

a) Cross-section along the axis of the tunnel

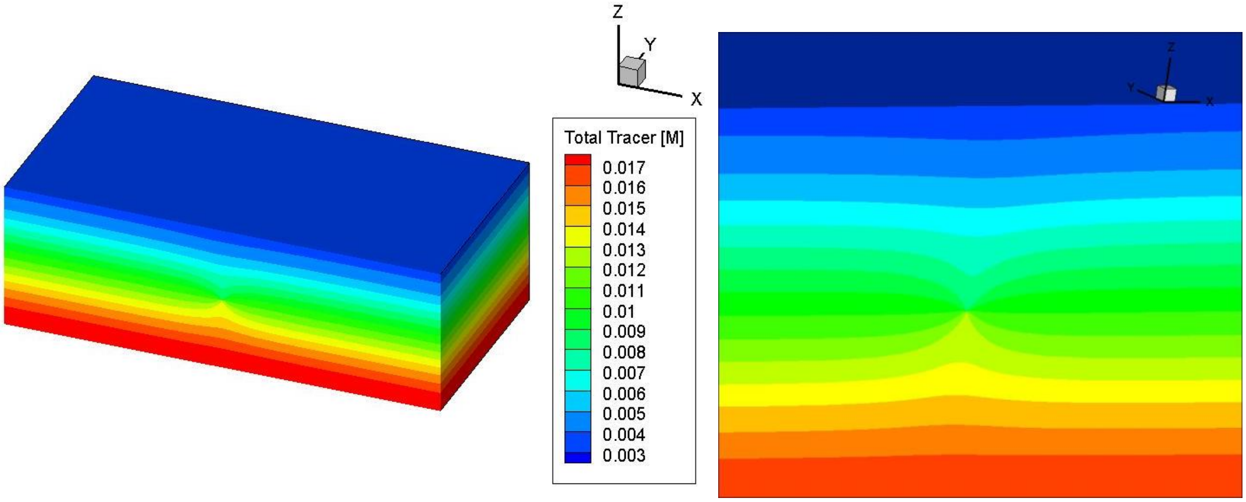

a) Cross-section perpendicular to tunnel axis

Figure 9-2-13. Predicted chloride concentration distributions after 173-days simulation time: homogenous system with large domain

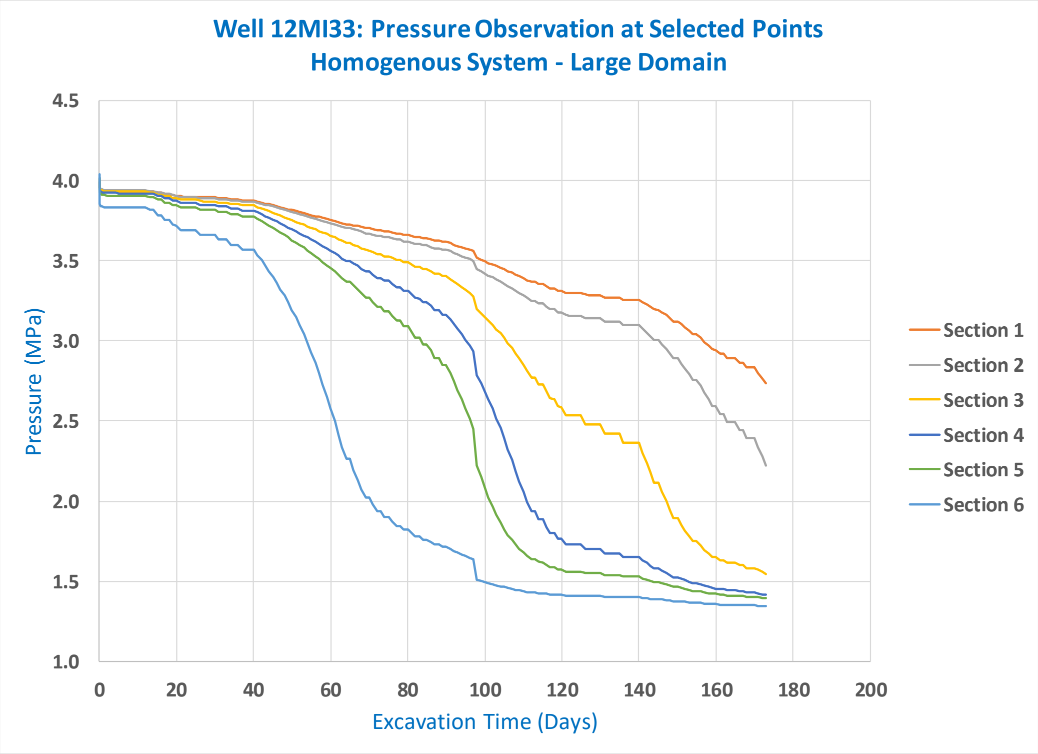

Figure 9-2-14. Predicted pressure history at observation points (in Well 12MI33) during excavation: homogenous system with large domain

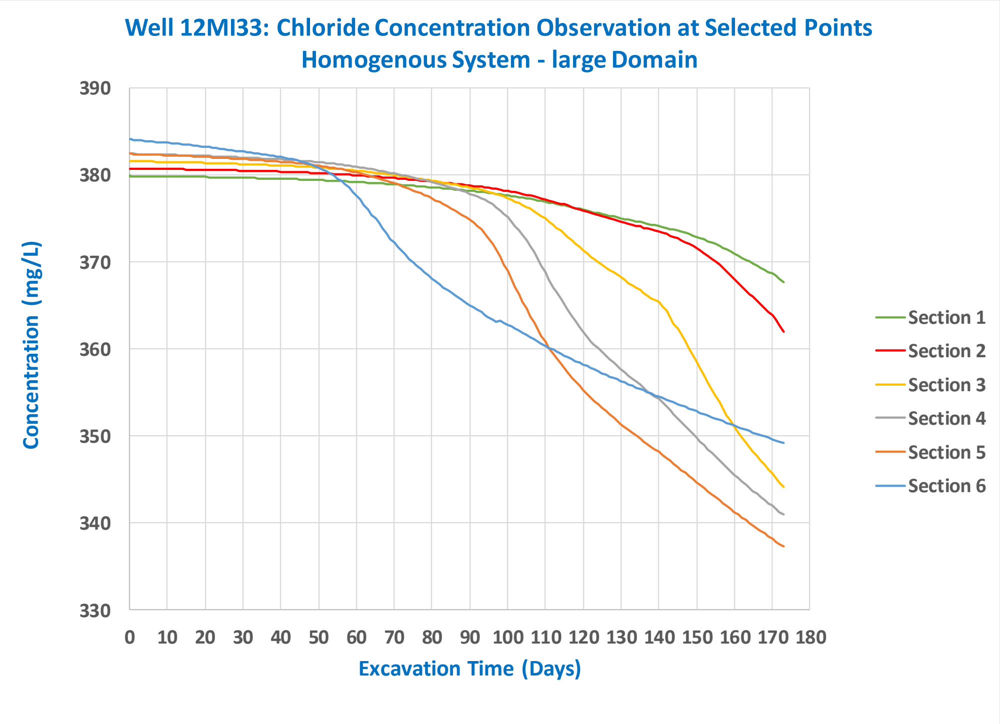

Figure 9-2-15. Predicted chloride concentration history at observation points (Well 12MI33) during excavation: homogenous system with large domain

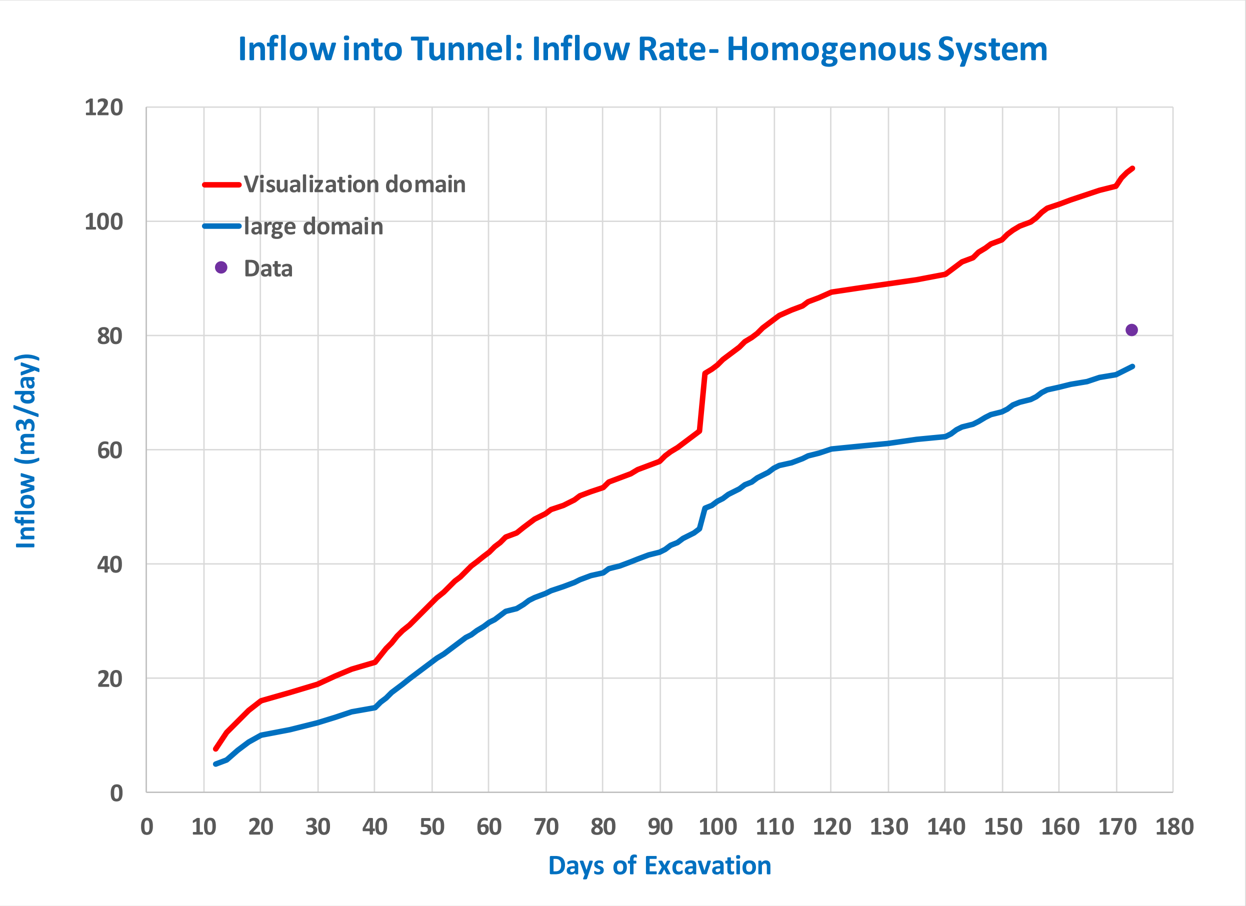

Figure 9-2-16. Predicted inflow into the Inclined Drift and CTD during excavation: Homogenous system.

9.2.3 Fractured System Model

Section 9.1 describes the fracture model development based on fracture data collected from the excavated areas and boreholes. The analysis produced up-scaled permeability and porosity data for flow and transport modeling of the excavation process. Permeability and porosity fields were obtained for one realization, for the Visualization Area domain. The matrix rock was assigned permeability of 10^{-19} m^2 and porosity of 0.001. Figure 9-2-17 shows the resulting permeability and porosity fields for the selected realization. An analysis was carried out to obtain the effective permeability for this realization. The same procedure described in Wang et al. (2016) was applied. Flow based effective permeability was calculated using Darcy's law and liquid flux at steady state:

$$q = \frac{-k_{eff}\Delta P}{\mu L} \tag{9.2.1}$$

where

q = flux,
k_{eff} = effective permeability,

ΔP = pressure difference between west and east faces (1000 Pa)
μ = dynamic viscosity
L = distance between west and east faces (100 m)

PFLOTRAN flow simulations were carried out using the permeability and porosity fields. A pressure gradient was imposed between the west and east faces of the Visualization Domain. Equation (9.2.1) was then used to estimate the effective permeability values using flux output on the east face, distance between west and east faces (100 m) and cross-sectional area (1.5×10^4 m^2). The resulting calculated effective permeability for this realization was 1.62×10^{-16} m^2. This value is an order of magnitude lower than the permeability of the homogenous model.

The same simulations as described in Section 9.2.1.1 for the Visualization Area domain using the coupled DAKOTA-PFLOTRAN codes were conducted. For the fractured system runs the permeability and porosity fields for Realization 1 were used. Simulation results are shown in Figures 9-2-18 to 9-2-22. Figures 9-2-18 and 9-2-19 show pressure and concentration distributions, respectively, at 173-days simulation time. The pressure distributions in Figure 9-2-18 indicate flow into the tunnel in a fractured system. It is evident that use of the Visualization Area domain resulted in boundary effects. The concentration distributions shown in Figure 9-2-19 are not as smooth as results of the homogenous model. The concentration gradient is affected by the porosity field.

Predictions of pressure and concentration histories at observation points for the large domain case are shown in Figures 9-2-20 and 9-2-21, respectively. The pressure profiles at observation points show larger pressure drawdowns when compared to those of the Visualization Area domain (Figure 9-2-8) and the large domain (Figure 9-2-14) homogenous models. Profiles of chloride concentration are very different from those of the homogenous model. As also shown in Figure 9-2-19, concentrations are highly affected by the fracture system.

The flow of water into the excavated space (inclined drift and CTD) was also evaluated for the fractured system, Realization 1. The resulting inflow into the tunnel (inclined drift and CTD) is shown in Figure 9-2-22 together with the results for the homogenous model. Task C project inflow data point (for combined Inclined Drift and CTD) is also included. The predicted inflow for the fractured system is lower than the other cases. Note that the results of the fracture system are for one realization only. Additional realizations would be needed to get better representation of the fractured system.

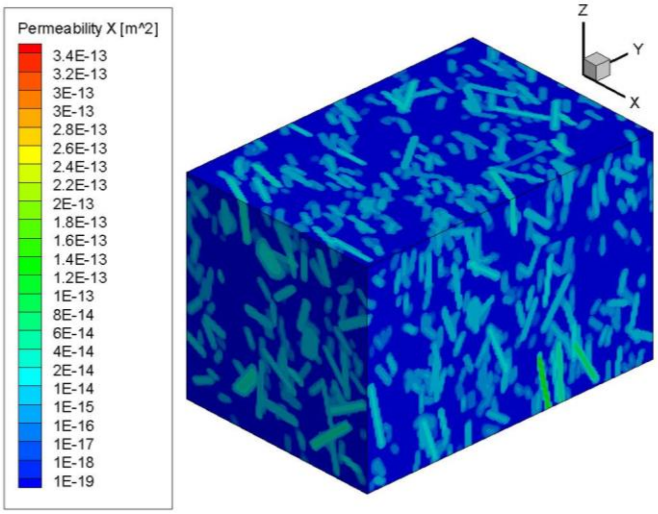

a) permeability

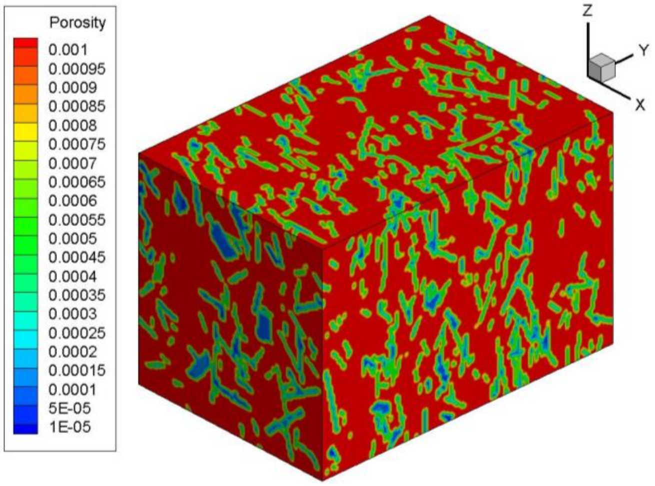

b) porosity

Figure 9-2-17. Fracture permeability and porosity for Realization 1: Fractured system with Visualization Area domain

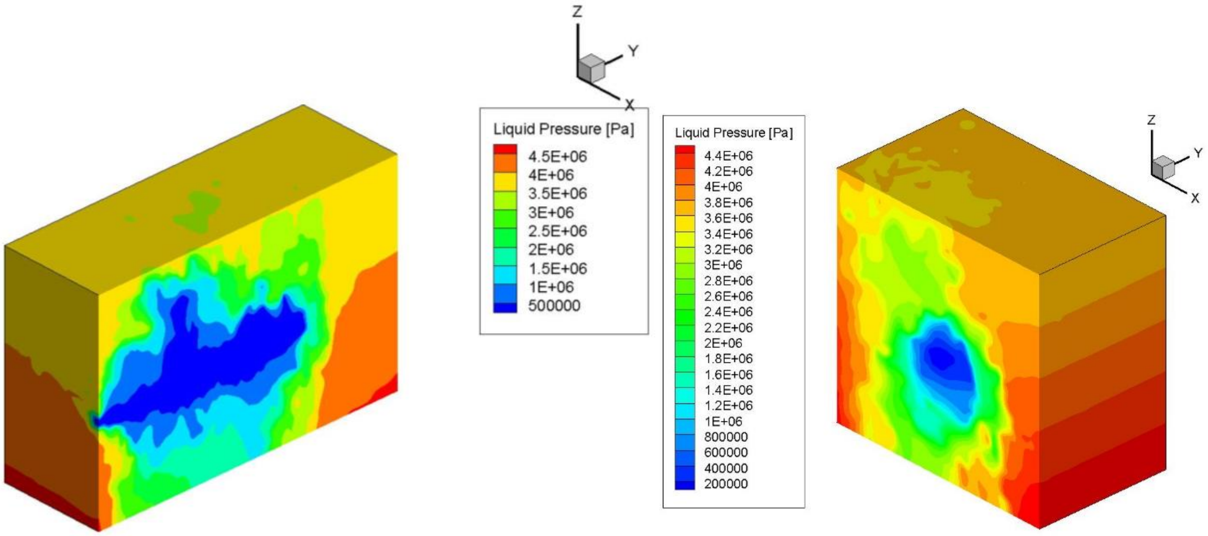

a) Cross-section along the axis of the tunnel b) Cross-section perpendicular to tunnel axis

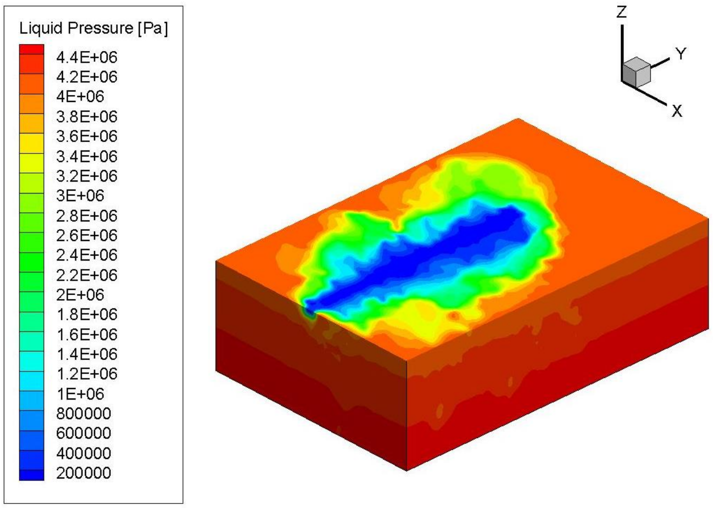

c) Vertical cross-section

Figure 9-2-18. Predicted pressure distribution after 173-days simulation time: fractured system with visualization area domain. Realization 1.

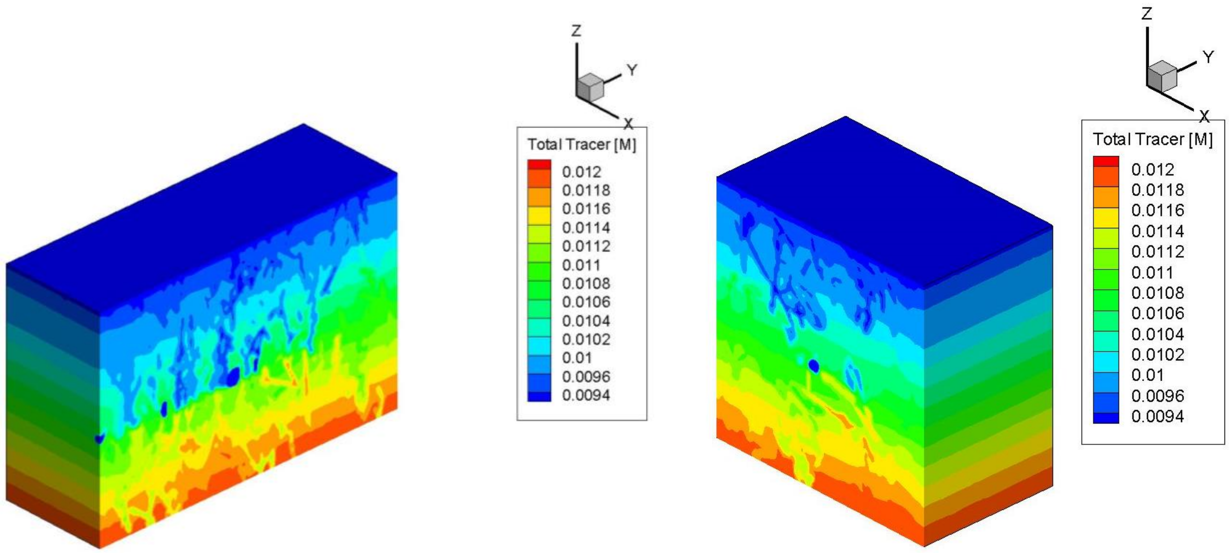

a) Cross-section along the axis of the tunnel b) Cross-section perpendicular to tunnel axis

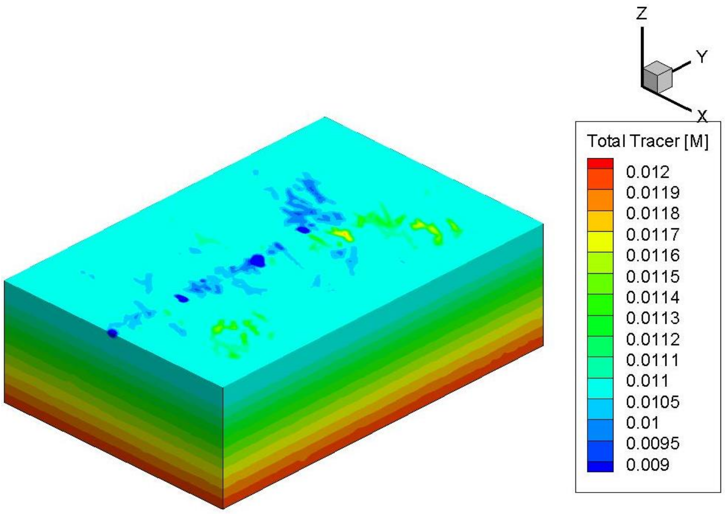

b) Vertical cross-section

Figure 9-2-19. Predicted chloride concentration distribution after 173-days simulation time: fractured system with visualization area domain. Realization 1.

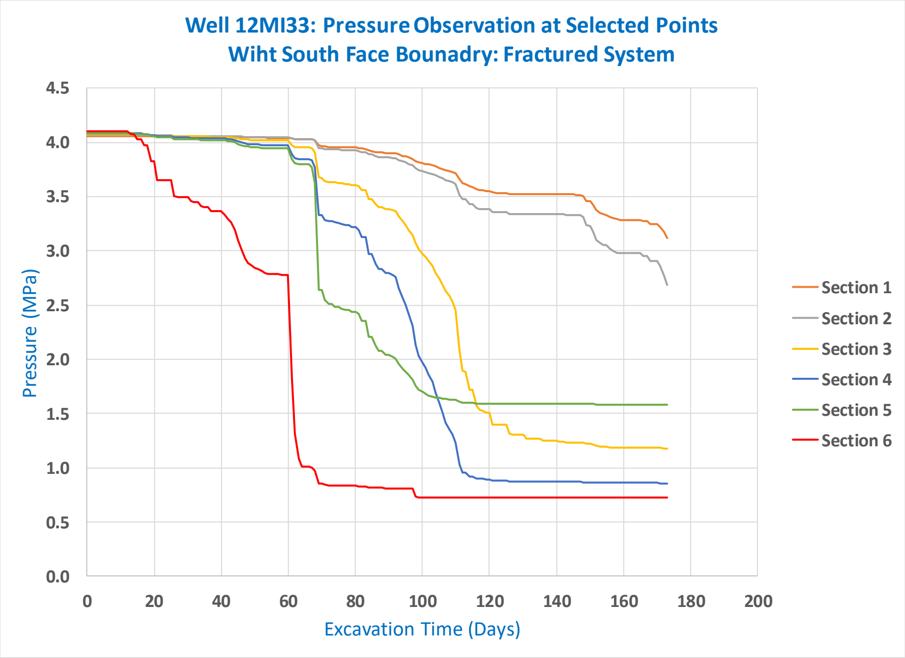

Figure 9-2-20. Predicted pressure history at observation points (in Well 12MI33) during excavation: fractured system with Visualization Area domain. Realization 1.

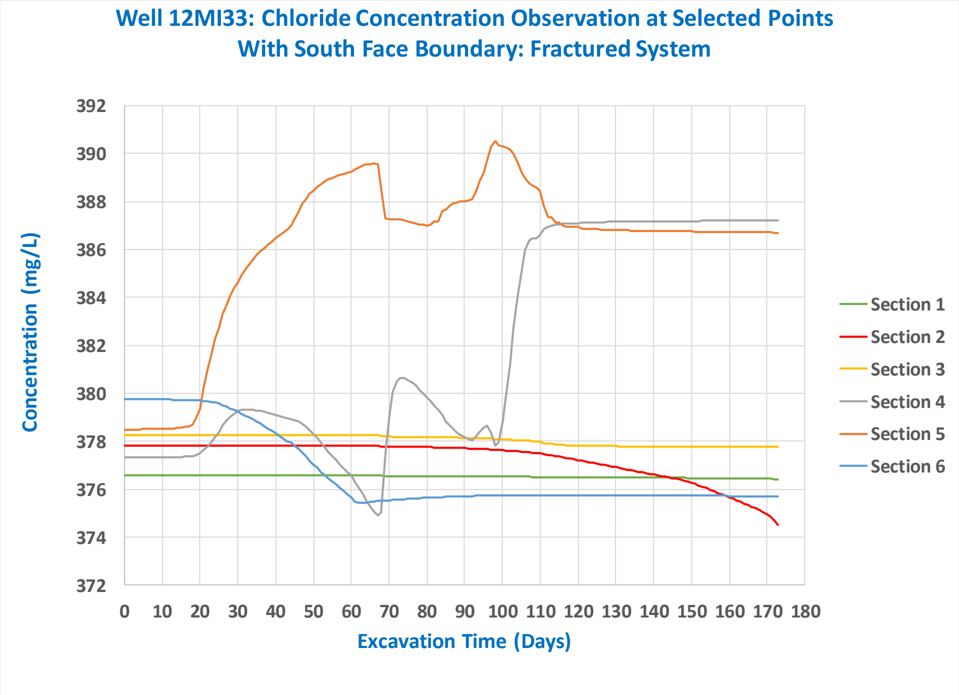

Figure 9-2-21. Predicted chloride concentration history at observation points (in Well 12MI33) during excavation: fractured system with Visualization Area domain. Realization 1.

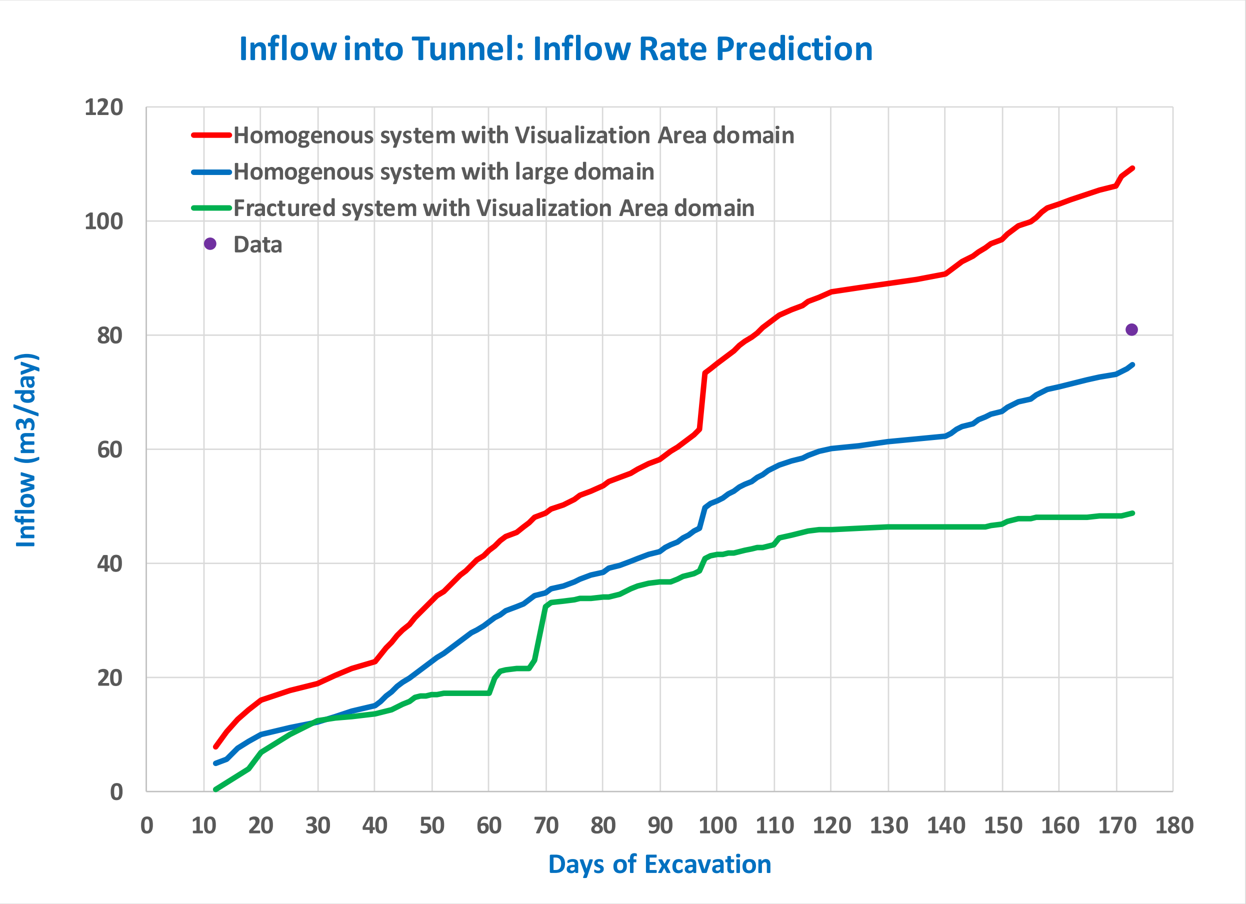

Figure 9-2-22. Predicted inflow into inclined drift and CTD: comparison of results of homogenous and fracture systems.

9.2.4 Summary

Preliminary modeling analysis was conducted at Sandia National laboratories as part of DECOVALEX19, Task C, Step 1. The analysis looked at use of a homogenous model with reference hydraulic conductivity, and a fracture model developed in Section 9.1 above. For the base case the CTD-scale Visualization area domain was used (100 m x 150 m x 100 m). Boundary and initial conditions specified by the project, based on data from wells, were applied to flow and transport. The data include head and chloride concentration at different parts of the modeling domain. Parameter data also obtained from wells were used. Data of excavation progress for the Inclined Drift and the CTD were also provided. A simulation method was developed to simulate excavation progress by continuously removing material from the excavated area. The DAKOTA statistical analysis and optimization code and the PFLOTRAN numerical flow and transport code were used. Simulations of flow and transport for the homogenous model with the Visualization Area domain indicated boundary effects at the Inclined Drift entrance. The boundary effects were caused by the application of side boundary conditions close to the tunnel entrance. To study the extent of the boundary effect a new grid was developed with a larger domain (2080 m x 2130 m x 700 m). Simulation results of the larger domain did not show the boundary effects, which would indicate the need to enlarge the boundaries of the CTD-scale model. The results of the larger domain also showed reasonable agreement between experimental inflow data and predicted inflow.

The modeling analysis also included use of a fracture model developed in Section 9.1. this allows realistic representation of the system in the excavated region. For the analysis permeability and porosity fields obtained for one realization were used instead of the constant permeability used in the previous simulations. The same simulation approach as the homogenous model were followed for the CTD-scale Visualization domain. The simulation results provided detailed flow and transport distributions in a fractured system. The results are preliminary output for a single realization. More realizations will be needed to obtain average representative output.

9.3 References

Adams, B. M. et al. (2017). Dakota, A Multilevel Parallel Object-Oriented Framework for Design Optimization, Parameter Estimation, Uncertainty Quantification, and Sensitivity Analysis: Version 6.6 User's Manual. SAND2014-4633. Updated May 9, 2017.

Ando, K., Tanaka, T., Hashimoto, S., Saegusa, H. and Onoe, H. (2012). *Study for establishment of the methodology for hydrogeological modeling using hydraulic discrete fracture networks (study on hydrogeology in crystalline fractured rock),* JAEA-Research 2012-022, 2012.

Baecher, G. B., Lanney, N. A., Einstein, H. H. (1977). *Statistical description of rock properties and sampling*, Proceedings, 18th US Symposium on Rock Mechanics, 1–8(5C1).

Bruines, P., Tanaka, T., Abumi, K., Hashimoto, S., Saegusa, H., Onoe, H., and Ishibashi, M. (2014). *Development and Application of the GeoDFN and HydroDFN at the Mizunami Underground Research Laboratory*, 8th Asian Rock Mechanics Symposium, October 14-16, 2014, Sapporo, Japan.

Butscher, Christoph (2012). *Steady-State Groundwater Inflow into a Circular Tunnel,* Tunnelling and Underground Space Technology, 32 (2012), pp. 158–167.

Golder Associates, Inc. (2017). *Interactive Discrete Feature Data Analysis, Geometric Modeling and Exploration Simulation*, FracMan Manual, April 6, 2017.

Hammond, G. E., Lichtner, P. C., and Mills, R. T., *Evaluating the Performance of Parallel Subsurface Simulators: An Illustrative Example with PFLOTRAN*, Water Resources Research, 50, doi:10.1002/2012WR013483 (2014).

Ishibashi, M. and Sasao, E. (2015). *Data on Fractures in the Toki Granite Based on the Deep Borehole Investigations*. Geoscientific Research Department, Tono Geoscientific Center, Sector of Decommissioning and Radioactive Waste Management, Japan Atomic Energy Agency, Akiyo-cho, Mizunami-shi, Gifu-ken, JAEA-Data/Code 2015-004, March, 2015.

Khanga, N.D., Watanabea, K., Saegusab, H. (2004). *Fracture Step Structure: Geometrical Characterization and Effects on Fluid Flow and Breakthrough Curve*, Engineering Geology, 75 (2004), pp. 107–127.

La Pointe, R.P. (2002). *Derivation of parent fracture population statistics from trace length measurements of fractal fracture populations*, International Journal of Rock Mechanics & Mining Sciences, 39 (2002), pp. 381–388.

Snow, D. (1969). *Anisotropic Permeability of Fractured Media*, Water Resources Research, 5 (1969), pp. 1273–1289.

Wang, Y., T. Hadgu, E. A. Kalinina, J. Jerden, J. M. Copple, T. Cruse, W. Ebert, E. Buck, R. Eittman, R. Tinnacher, C. Tournassat, J. Davis, H. Viswanathan, S. Chu, T. Dittrich, F. Hyman, S. Karra, N. Makedonska, P. Reimus, M. Zavarin, C. Joseph: Used Fuel Disposition in Crystalline Rocks : FY16 Progress Report, Fuel Cycle Research and Development, FCRD-UFD-2016-000076, SAND2016-9297 R. September 21, 2016.

Zhang, H.H. Einstein and Dershowitz, W.S. (2002). *Stereological relationship between trace length and size distribution of elliptical discontinuities*, Geotechnique, 52/6 (2002), pp. 419-433.

10. SUMMARY

Significant progress has been made in FY17 in both experimental and modeling arenas in evaluation of used fuel disposal in crystalline rocks, especially in model demonstration using field data. The work covers a wide range of research topics identified in the R&D plan. The major accomplishments are summarized below:

- **Model development for spent fuel degradation and its coupling with metal corrosion:** Both experimental and modeling studies show that H_2 plays an important role in determining the dissolution rate of UO_2 fuel, and that even moderate H_2 concentrations suppress the oxidative dissolution of spent fuel. The major source of H_2 within a breached waste package in low-oxygen environments will be anoxic corrosion of the various steels used as containers and structural components. The steel corrosion and H_2 generation reactions are coupled redox reactions that proceed at equal rates under anoxic conditions. Therefore, a steel corrosion model was added to the fuel matrix degradation (FMD) model to represent the primary kinetic source of H_2 (and Fe^{2+}) in a breached waste container. Once it is fully calibrated, the steel corrosion model can be used to calculate the corrosion rates of various metals under the environmental conditions in a breached waste package as a function of temperature, Eh, pH and solution chemistry to provide the H_2 concentrations controlling the fuel degradation rate. We identified the processes through which steel corrosion kinetics is coupled with the fuel degradation kinetics in the FMD model and summarized the sensitivity of the calculated fuel degradation rate to the range of corrosion rates that could occur for different steels expected to be present in a waste package. We also identified information gaps that need to be filled in order to further develop, parameterize, and calibrate the steel corrosion model for the range of environmental conditions that could occur in a breached waste package.
- **Model development for glass waste form degradation:** The reactivity of silicate glasses and minerals is important to numerous engineering applications including nuclear waste disposal. The dissolution process has long been considered to be controlled by a leached surface layer in which cations in the silicate framework are gradually leached out and replaced by protons from the solution. This view has recently been challenged by observations of extremely sharp corrosion fronts and oscillatory zonings in altered rims of the materials, suggesting that corrosion of these materials may proceed directly through congruent dissolution followed by secondary mineral precipitation. We have shown that complex silicate material dissolution behaviors can emerge from a simple positive feedback between dissolution-induced cation release and cation-enhanced dissolution kinetics. This self-accelerating mechanism enables a systematic prediction of the occurrence of sharp dissolution fronts (vs. leached surface layers), oscillatory dissolution behaviors and multiple stages of glass dissolution (in particular the alteration resumption at a late stage of a corrosion process). Our work provides a new perspective for predicting long-term silicate weathering rates in actual geochemical systems and developing durable silicate materials for nuclear waste disposal.
- **Understanding uranium interactions with bentonite materials:** This work is designed to test the effect of bentonite heating on U(VI) adsorption. U(VI) adsorption onto bentonite samples from the FEBEX *in situ* experiment, which were subjected to 18 years of heating at temperatures of 45-100 °C, was compared to adsorption onto original FEBEX bentonite and cold-zone FEBEX bentonite from the *in situ* experiment. The experimental results show that kinetics of U(VI) adsorption appear to be very fast, reaching equilibrium in less than 8 hours, while DIC concentrations reach equilibrium in 48 hours. U(VI) adsorption onto unpurified FEBEX bentonite samples which experienced sustained temperatures of approximately 95 °C was lower than adsorption onto original unheated and cold-zone (20 °C) FEBEX bentonite over a range of chemical conditions (pH 7-8, Ca = 0.1 and 2.0 mM) relevant to nuclear waste disposal. U(VI) adsorption

onto unpurified FEBEX bentonite which experienced more moderate temperatures (approximately 45 °C) was *not* lower than unheated FEBEX bentonite for the single chemical condition tested (0.05 M NaCl, pH 7.5, 0.1 mM Ca). The difference in U(VI) adsorption between heated (95 °C) and cold-zone (20 °C) FEBEX bentonite persisted over the range of chemical conditions tested when the bentonite samples were purified to remove mineral impurities such as calcite, quartz, and feldspars. This suggests that the decrease in U(VI) adsorption was due to alteration of the clay mineral structure, and *not* due to a change in the pore water chemistry or amount and type of accessory minerals. This may reflect illitization of the montomorillonite; however, further clay characterization is needed to verify this hypothesis. These results provide key information necessary for performance assessment of HLW disposal scenarios. The decreased adsorption observed in this study as a result of bentonite heating may impact the diffusion of U(VI) through engineered clay barriers. Because the decreased U(VI) adsorption was due to changes in the clay mineral structure and *not* to aqueous U(VI) speciation, other radionuclides may be similarly affected

- **Understanding radionuclide interactions with metal corrosion products:** The main interest in radionuclide sequestration by corrosion products stems from (1) the potential for this process to significant inhibit radionuclide release during canister breaching and (2) from the absence of such processes in most repository performance assessments. The objective of this work is to quantify radionuclide sequestration as a result of canister breaching and near field corrosion processes. We have evaluated this process from both an experimental and modeling perspective. Experimentally, we developed methodologies to grow various iron oxides phases (goethite, hematite, magnetite) in the presence of radionuclides. We performed a small number of binary (RN-mineral) coprecipitation experiments to test radionuclide (Pu, Am, Np, and U) partitioning. Experiments are aimed to quantify coprecipitation partitioning and also examine the effects of aging and the potential iron oxide recrystallization effects associated with the presence of aqueous phase Fe(II). The exprimental results reveal that (1) upon aging of a Pu-doped ferrihydrite precorsor into more crystalline phase, plutonium associates more strongly with goethite (FeOOH) than hematite (Fe_2O_3); and (2) the timing of Pu addition in the synthetic procedures affects the final form of plutonium associated with goethite.
- **Understanding colloid-facilitated Cs transport in granitic materials:** Transport experiments using two mini-columns were conducted to interrogate the colloid-facilitated transport of ^{137}Cs through crushed Grimsel granodiorite. Water from the Chancellor nuclear test cavity at the Nevada Nuclear Security Site was selected because ^{137}Cs is strongly associated with the colloidal fraction, and ^{3}HHO is present in high concentrations and therefore acts as a conservative tracer. Column eluent was measured for ^{3}HHO, ^{137}Cs, and turbidity (as a proxy for colloid concentration). After one pore volume eluted through the first column, both the ^{3}HHO and turbidity reached Chancellor water values, suggesting that no colloids were filtered by the granodiorite. ^{137}Cs breakthrough occurred concurrently with the ^{3}HHO and turbidity breakthroughs but in concentrations less than the injection solution. The initial breakthrough consisted almost entirely of colloidal ^{137}Cs. Solute concentrations of ^{137}Cs were negligible initially and rose steadily along with the colloid-associated ^{137}Cs until about 50 pore volumes, after which both solute and colloid-associated ^{137}Cs eluted through the column at the same concentration and partitioning as the injection solution, suggesting that the granodiorite's adsorption capacity had been exhausted. Eluent samples from the first ~26 pore volumes that were not used for analysis were combined and injected into a second column. Analyses indicated that the granodiorite in the first column had adsorbed most of the ^{137}Cs in the solute phase and over half of the ^{137}Cs that was associated colloids during the first 26 pore volumes. Thus, the injection solution into the second column consisted mainly of ^{137}Cs strongly bound to colloid surfaces that outcompeted the sites of the granodiorite. The results from the second column reflect the much stronger association between the ^{137}Cs and the strong sites of the colloids. In contrast to the results from the first column, where only about 45% of the ^{137}Cs

initially associated with colloids remained associated with colloids, about 90% of the colloid-associated ^{137}Cs remained associated with colloids in the second column. The results from both column experiments were simultaneously matched by a two-adsorption-site model in which the first site is weaker than the second but has greater abundance. These experiments demonstrate how the sequential column technique can provide well-constrained model parameterizations of the adsorption and desorption behavior of a radionuclide on colloids in the presence of competing immobile surfaces. The method is especially well suited to interrogate the slower desorption rate constants of radionuclides from colloids that will dictate the magnitude of colloid-facilitated radionuclide transport over the long time and distance scales relevant to nuclear waste repository systems.

- **Compaison of discrete fracture and equivalent continuum approaches for modeling flow and transport in fractured media:** One of the major challenges of simulating flow and transport in the far field of a geologic repository in crystalline host rock is related to reproducing the properties of the fracture network over the large volume of rock with sparse fracture characterization data. Various approaches have been developed to simulate flow and transport through the fractured rock. The approaches can be broadly divided into Discrete Fracture Network (DFN) and Equivalent Continuum Model (ECM). The DFN explicitly represents individual fractures, while the ECM uses fracture properties to determine equivalent continuum parameters. We compared DFN and ECM in terms of upscaled observed transport properties through generic fracture networks. The major effort was directed on making the DFN and ECM approaches similar in their conceptual representations. This allows for separating differences related to the interpretation of the test conditions and parameters from the differences between the DFN and ECM approaches. The two models were compared using a benchmark test problem that is constructed to represent the far field (1x1x1 km^3) of a hypothetical repository in fractured crystalline rock. The test problem setting uses generic fracture properties that can be expected in crystalline rocks. The models were compared in terms of the: 1) effective permeability of the domain, and 2) nonreactive solute breakthrough curves through the domain. The principal differences between the models are mesh size, network connectivity, matrix diffusion and anisotropy. We demonstrated how these differences affect the flow and transport. We identify the factors that should be taken in consideration when selecting an approach most suitable for the site-specific conditions.
- **Understanding solute dispersion and mixing in fracture networks:** Using the DFN model, we performed dispersion and mixing simulations on three dimensional fracture networks. The new capability was developed to calculate and analyze subsurface transport dispersion. We designed two synthetic networks to isolate the influence of structure and disorder at the macro-scale and then compared its importance relative to moderate levels of hydraulic heterogeneity. Our study shows that, as hydraulic heterogeneity increased, both longitudinal and traverse dispersion also increased; the less mechanical dispersion observed in the structured network appeared to be linked to the higher levels of connectivity than in the poorly connected random network; for moderate levels of hydraulic heterogeneity, fracture network structure is the principal control on transport times and dispersion within fracture networks. We applied a DFN model to interpret tracer diffusion data obtained from the Long Term Sorption Diffusion Experiments conducted in Sweden. Experiments were focused on tracer transport in the stagnant pore water of the rock matrix. Analyzing the shape of the tracer penetration profiles observed in the experiment and comparing it to the predicted general shape of a 1D diffusion model, vastly different behavior was observed for the natural fracture surfaces and for the unaltered rock matrix. The micro fractures were observed in different slices of the sample core. Several slices of the individual cores had micro fractures that were fresh and consequently they were likely newly formed, i.e. induced by drilling or stress release. Our study focuses on understanding how micro fractures, which provide faster transport paths, affect the penetration profile. The DFN model was used to investigate, how the thickness of fractured layer affects the penetration profile of tracer driven by pure diffusion. The obtained results

emphasize the importance of including heterogeneity into the simulation process. Micro fractured surface contributes to initial fast decrease of concentration followed by a slower penetration as tracer gets into homogeneous medium.

- **Synthesis of field data into a flow and transport model:** Through the Development of Coupled Models and their Validation against Experiments (DECOVALEX-2019) project, we obtained a comprehensive set of hydrologic and chemical data from a research tunnel at 500 m depth, at the Japan Atomic Energy Agency (JAEA) Mizunami Underground Research Laboratory (MIU). The objectives of this work is to develop a general workflow or methodology to synthesize field observations and measurements into a flow and transport model. Fracture data analysis and preliminary modeling analysis were performed. The fracture data analysis utilizes fracture data collected in the research tunnel and monitoring borehole 12MI33. A discrete fracture model was developed based on fracture orientation, size and intensity derived from the fracture data analysis. The discrete model was then upscaled to an effective continuum model that could be used for flow and transport simulations. A preliminary modeling analysis was conducted to predict inflows into the inclined drift and the Closure Test Drift (CTD) as a function of the extent of tunnel excavation. The predicted inflow rates are comparable to field measurements.